EXPERIMENTAL AND THEORETICAL INVESTIGATION OF TOP OF THE LINE CORROSION IN CO_2 GAS AND OIL ENVIRONMENTS

Khalid Abdulhussain Mohammed

Submitted in accordance with the requirements for the degree of

Doctor of Philosophy

The University of Leeds
School of Mechanical Engineering

Institute of Thermofluids

March 2018

The candidate confirms that the work submitted is his own and that appropriate credit has been given where reference has been made to the work of others.

Publication Statement

The candidate confirms that the work submitted is his/her own, except where work which has formed part of jointly-authored publications has been included. The contribution of the candidate and the other authors to this work has been explicitly indicated below. The candidate confirms that appropriate credit has been given within the thesis where reference has been made to the work of others.

Papers contributing to this thesis:

K.A. Mohammed, R. Barker, A. Neville, H.M.Thompson “Effects of water condensation rate and surface temperature on top of line corrosion of carbon steel in a CO_2 environment”, Electrochem Conference 2017, Birmingham, England.

The paper below, the primary author completed all experimental studies, evaluation of data and preparation of publications. All authors contributed to the proof reading of the articles prior to publication.

K.A. Mohammed, R. Barker, M. Al-Khateeb, A. Neville, H.M.Thompson “An experimental theoretical investigation of top line corrosion in a CO2 environment under dropwise condensation”.

Acknowledgements

First and foremost, I appreciate Almighty God for His mercy and kindness all through my life.

I would like to thank my academic supervisors, Professor Harvey Thompson and Dr Richard Barker for all of their supervision, enthusiasm, encouragement, advice, support in the lab, and when writing my thesis. They have been amazing and without their continued support, this work would not have been possible.

I would also like to express my sincere appreciation to Iraqi Higher Education Ministry and University of Dhi-Qar for their financial sponsorship of my PhD. I am extremely grateful to Professor Nik Kapor and Professor Anne Neville for allowing me to use the corrosion lab facilities. I'm so grateful to the technical staff, in particular, Jordan, Mick, Andrew and Mark for helping me with setting up my rig. I wish to thank all my colleagues in the School of Mechanical Engineering, both past and present for their tremendous support.

Finally, a big thank goes to my wife for all her support, encouragements and prayers. A massive thank you to my children, Tiba, Rand, Mosa and Maryam for believing in me and helping me cope with the stress of writing up.

Abstract

Top of Line Corrosion (TLC) occurs in the transportation of multiphase wet gas flow pipelines due to the condensation of water when there is a significant temperature difference between the produced fluids and the surrounding environment. If the gas/liquid flow is stratified, saturated water vapour condenses on the inside walls of the pipeline and forms small water droplets which become saturated with acidic gases e.g. CO_2, H_2S and CH_3CO_2H leading to severe corrosion.

In the oil and gas industry, a standard method for corrosion control is an injection of the corrosion inhibitors. The conventional corrosion inhibitors are non-volatile liquids and cannot easily reach the upper surface of the pipeline where the aggressive condensed water is formed and remain at the bottom of the pipe. Therefore, this mitigation technique is not successful for TLC prevention because the delivery of the corrosion inhibitor is governed by the flow regime. For better understanding the mechanism of CO_2-TLC and to predict the corrosion risk and develop improved corrosion mitigation techniques, an experimental and theoretical research on the influence of the environmental parameters on the corrosion at the top of the line is needed.

This study provides a comprehensive experimental investigation into the effect of condensation rate, surface temperature and iron carbonate saturation on TLC and $FeCO_3$ precipitation rate on carbon steel (X65) in a CO_2 environment. TLC is found to be governed by surface temperature regardless of water condensation rates (WCR) at a surface temperature below 32°C, whereas for temperatures above 32°C the WCR influences the TLC, precipitation rate and scale film formation. On the basis of the experimental data, a new empirical model to predict the TLC rate in the absence of $FeCO_3$ films is proposed. The post process observations on the morphology of the corrosion product films and the feature of the localized pits on the steel surface provide a useful insight into the mechanisms involved in the TLC processes.

To enhance our understanding of water condensation mechanism at top of the pipeline during gas and oil transportation, Zhang model (Corrosion, 2007.Vol 63, No.11) was implemented and developed at different flow conditions.

In this study, a mathematical model for the condensation of water vapour was developed for the prediction of the water condensation in a top of the line scenario at stagnant gas velocity. In this model, the heat and mass conservation equations are linked to account for the effect of all important heat and mass transfer resistances. A numerical method is proposed to solve the non-linear equation system and predict the condensation rate. The mechanistic model was validated with experimental results. The experiments are conducted in the unique setup developed to simulate the top of line corrosion at static conditions. The comparison of the experimental and the model results showed that the model was able to predict the condensation rate at static conditions reasonably well.

A mechanistic of the top of line corrosion has been implemented, which covers the processes of condensation, dropwise condensation, chemical reactions, electrochemical reactions at the steel surface and diffusion through condensed droplets. The model was validated against experimental data and used then to explore the influence of key parameters.

Table of Contents

List of Tables

List of Figures

Chapter 1. Introduction

1.1 Introduction

Based on their availability, and ability to meet many of the mechanical structural, fabrication and cost requirements, carbon steel alloys are continuously used in every part of the oil and gas industry starting from production and processing to transporting and distribution of the refined products [1]. Because of their significance in transporting oil and natural gas from production fields to refineries, power stations, and markets, across vast areas, pipelines are becoming central to the global oil and gas industry [2]. The integrity of the used pipelines is very important to ensure a safe working environment and continuous production. Unfortunately, internal corrosion of oil and gas pipelines is frequently reported in the petroleum industry. The internal corrosion in carbon steel pipelines is influenced by a number of parameters, for instance, temperature, CO_2 and H_2S partial pressure, water chemistry, flow velocity, oil and/or water wetting, the composition of the carbon steel alloy and the outside conditions of the pipeline [3]. Figure 1-1 shows the interconnected parameters that affect CO_2 corrosion of carbon steel pipeline.

The oilfield corrosion problem is predominantly associated with the presence of both common natural gas contaminants in oil reservoirs such as CO_2 (sweet corrosion) and H_2S (sour corrosion) which can be highly corrosive in combination with water [1, 4, 5]. The degradation of carbon steel is significantly decreased when a layer of corrosion product forms on the metal surface. In CO_2 –dominated environments, and at high temperature, a more dense and protective corrosion product film of iron carbonate ($FeCO_3$) is precipitated on the surface of the metal, but when H_2S is present in addition to CO_2, iron sulphide (FeS) may be formed instead of $FeCO_3$ at low temperature because FeS is thermodynamically more stable than $FeCO_3$ [3].

The corrosion product layer forms on the corroding surface preventing the underlying steel from further dissolution and acting as a barrier preventing the metal surface from direct contact with corrosive gases or solution. However, if there is any damage to the protective corrosion film, it may lead to serious localised corrosion problems by exposing the underlying metal to the aggressive corrosive environment resulting in a significant economic loss.

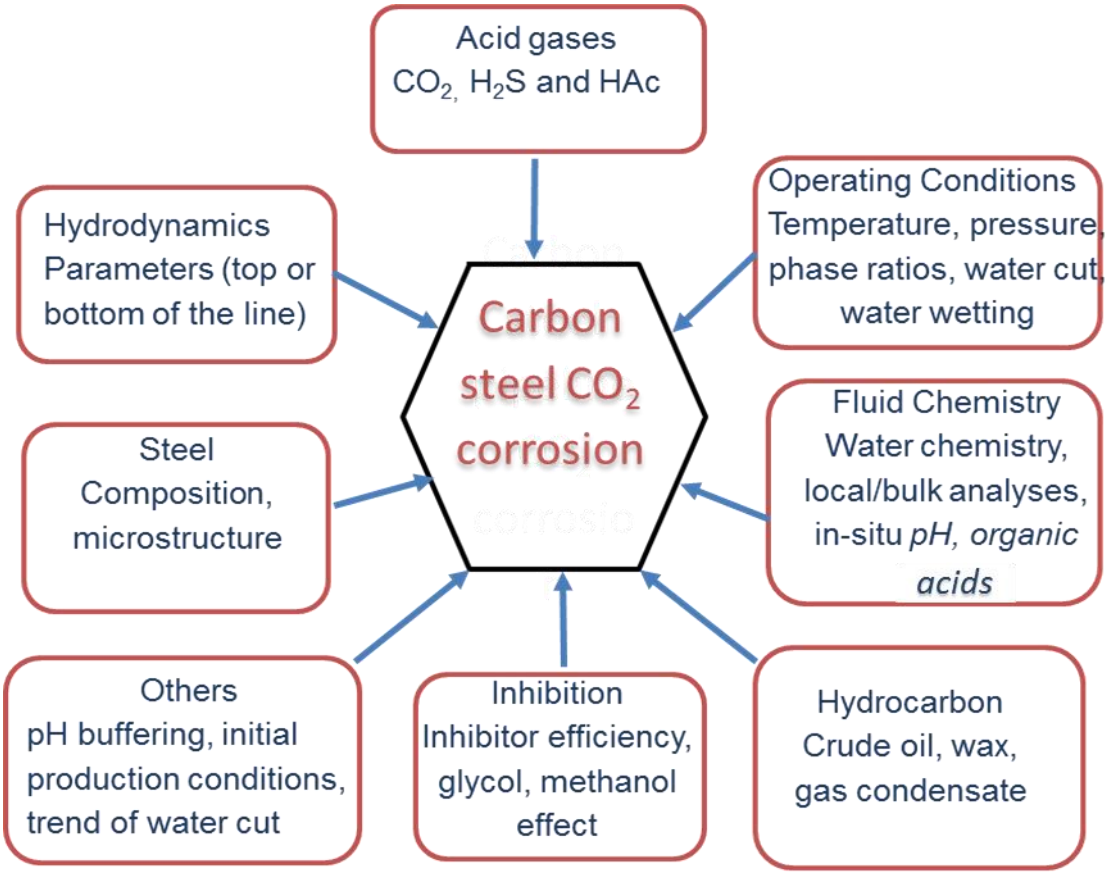

Figure 1-1. Interconnected factors affecting CO_2 corrosion of carbon steel pipeline [1].

At stratified gas flow regime which is common in most wet gas fields, water vapour in the gas phase condenses on the internal pipe surface when the environment outside the pipeline is cooler than the saturated vapour flowing inside the pipe. The condensed water is aggressive as it contains various corrosive species, such as CO_2 and H_2S, it attacks the pipe wall and causes

a severe corrosion problem resulting in specific corrosion phenomena related to the wet gas production, known as top-of-the-line corrosion (TLC) [6]. In other words, the phenomenon of TLC happens in gas and oil pipelines due to condensation of water vapour containing dissolved corrosive gases on the upper part of the pipe wall between the10 to 2 o'clock positions [7].

This type of corrosion is difficult to mitigate using conventional inhibitors. In stratified flow regime, non-volatile liquid inhibitors would be unable to reach the upper surface of the pipeline and remain at the bottom of the pipe. This leads to the formation of a protection layer around the bottom of the line, however, the top position of the pipe will be susceptible to pitting and localized corrosion. Therefore, TLC is a significant problem facing both the oil and gas industry and research laboratories globally as, to date, there are no effective solutions for combating this type of corrosion. The typical species that are present in pipelines both at the bottom and top of the line are shown in Table 1-1. From the table, it is clear that the chemical composition of condensed water at the top of the line (TOL) is different from the formation water at the bottom of the line (BOL). This is an indication that only volatile species and their derivatives are present at the top of the pipeline.

In all the reported cases of TLC, acetic acid gas (HAc) is present in the produced gas, and being volatile, transports in the gas phase and condenses along together with water, leading to an increase in the iron solubility which eventually increases the TLC. The presence of acetic acid not necessary increases the corrosion rate of carbon steel, at some specific concentrations acetic acid acts as an inhibitor [8]. Furthermore, the presence of the acetic acid would significantly reduce the pH of the condensed water compared to a solution containing only CO_2 gas [9].

Table 1-1. Typical species that are present in pipelines both at the BOL and TOL adapted from [10, 11].

Species	Name	Present at BOL	Present at TOL
CO_2	Dissolved carbon dioxide	✓	✓
H_2CO_3	Carbonic acid	✓	✓
HCO_3^-	Bicarbonate ion	✓	✓
CO_3^-	Carbonate ion	✓	✓
H^+	Hydrogen ion	✓	✓
OH^-	Hydroxide ion	✓	✓
Fe^{2+}	Iron ion	✓	
CL^-	Chloride ion	✓	
Na^+	Sodium ion	✓	
K^+	Potassium ion	✓	
Ca^+	Calcium ion	✓	
Mg^+	Magnesium ion	✓	
Ba^+	Barium ion	✓	
Sr^+	Strontium ion	✓	
CH_3COOH_3	Acetic acid	✓	✓
H_2S	Hydrogen sulphide	✓	✓
HSO_4^-	Bisulphate ion	✓	✓
SO_4^{2-}	Sulphate ion	✓	

TLC corrosion mechanisms have affected the oil and gas industry for several decades. Many studies have been conducted to investigate the parameters influencing (directly or indirectly) TLC which include the temperature of the gas bulk, the temperature of the pipe wall, the total pressure of the system, the partial pressure of CO_2, the gas velocity, solution pH, water wetting, concentration of dissolved corrosion product ($FeCO_3$), acetic acid, and the condensation rate [12, 13].

The focus of this research is to simulate the electrochemistry of carbon steel pipelines transporting wet gas, under controlled laboratory conditions, and to investigate the various parameters that influence CO_2-TLC such as temperature and water condensation rate. The aim is to obtain a better understanding of the corrosion mechanism and the factors which affect the TLC rate occurring in the pipeline transporting wet gas. A new apparatus was designed and manufactured for this research, which allows an investigation of TLC over a wide range of conditions as a function of time. Moreover, a semi-analytical model to predict water condensation during TOLC and a mechanistic model to predict TLC for static conditions were developed in this study.

1.2 The Cost of Corrosion

Failure due corrosion is one of the main threats in oil transportation pipelines; water present in the oil production process combined with other soluble corrosive gases such as carbon dioxide creates an environment which initiates the corrosion process [14]. Literature shows that between 1980 and 2006, about 50% of European, major incidents arising from technical plants failures were primarily due to degradation of plants caused by corrosion, erosion, and fatigue [15]. In 2002, the U.S. Federal Highway Administration (FHWA) released a study on the direct costs associated with metallic corrosion in nearly every U.S. industry sector. The study provides information on the overall cost of corrosion by analysing 26 industrial sectors in which

corrosion is known to exist and extrapolating the results for a nationwide estimate. Results of the study showed that the total annual estimated direct cost of corrosion in the U.S. amounted to $276 billion (3.1% of Gross Domestic Product (GDP)) [16]. The U.S. economy was divided into five major sectors of infrastructure, utilities, transportation, production and manufacturing, and government. When added together, the total direct losses attributed to corrosion for these sectors was $137.9 billion as shown in Figure 1-2. Economically, there are two types of cost caused by corrosion, direct and indirect losses [17].

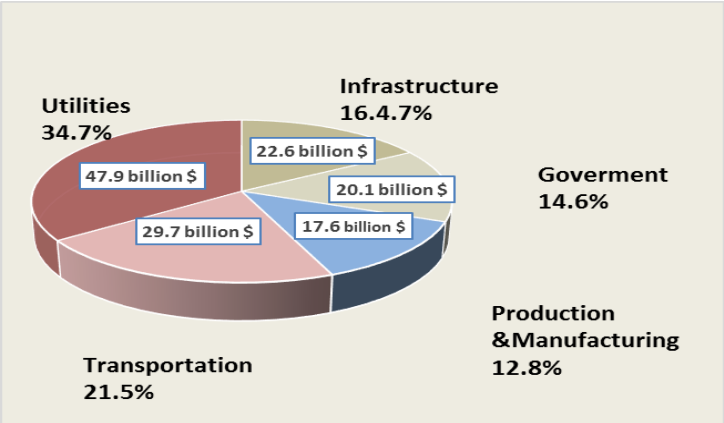

Figure 1-2. Percentage and dollar contribution to the total cost of corrosion for the five economic sectors in the U.S.A. [16]

1.2.1 Direct Cost of CO_2 Corrosion

Losses such as replacement costs, including parts and labour, and protection costs such as the cost of alloying, corrosion inhibitors, coatings, cathodic protection, and research & development can be accounted for direct losses [17].

1.2.2 Indirect Cost of CO_2 Corrosion

The indirect cost of corrosion is estimated to be equal to the direct cost [18]. It includes:

- Cost of labour attributed to corrosion management activities.
- Cost of the equipment required because of corrosion-related activities.
- Loss of revenue due to delays and disruption in the supply of product.
- Cost of loss of reliability.
- Contamination of product from spills, fires etc.

Every year corrosion phenomena cost the oil and gas industry tens of billions of dollars in lost income and treatment costs. The total annual cost of both the direct and indirect costs of corrosion was expected to exceed $1.1 trillion by the end of 2016 [19].

It should be noted that not only the oil and gas industry but also other major areas like building construction, transportation, production and manufacturing is damaged by corrosion. It was found that the sectors of drinking water and sewer systems ($36 billion), motor vehicles ($23.4 billion), and defence ($20 billion) have the largest direct corrosion impact. Within the total cost of corrosion, a total of $121 billion per year is spent on corrosion control methods and services [18]. Thus, research into the mechanisms that cause corrosion and determining how to treat forms of degradation effectively is essential to reduce both the impact on safety and the environment and the expenditure of industries. With the developing environmental awareness and imposed international laws, corrosion problems in the oil and gas industry are becoming increasingly important, highlighting the necessity of in-deep research [20].

1.3 Statement of the Research Problem

Economically, multiphase wet gases are now being sent unprocessed into pipelines rather than being separated and dried prior to transportation. Consequently, problems linked with the presence of water in the pipeline such as hydrate formation and internal corrosion of the pipeline can be

present. Corrosion inhibitors can effectively hinder the internal corrosion by forming a protective film on the steel surface. However, traditional non-volatile liquid inhibitors remain at the bottom surface of the pipeline and could not reach the corrosion-exposed area at the top of the surface of the pipeline. The insufficient concentration of the corrosion inhibitors at the top of the pipeline leads to continued TLC phenomenon. Accordingly, intensive research has been, and still is, carried out by the oil and gas industries to understand the problems related to the transport of unprocessed fluids produced from a well.

Since it is not possible to prevent TLC with the existing inhibition technologies and without high expenses and interruption of the production, it is of prime importance to understand the mechanisms involved during TLC and predict the conditions under which TLC is going to occur. The vital goal for the oil companies is to optimize the design of pipelines, for example by selecting corrosion resistant alloy, so that conditions leading to TLC can be avoided. For this purpose, the corrosion rate should be predicted in order to estimate the lifetime of the pipeline.

1.4 Objectives of the Research

The scope of this study will focus on achieving the following objectives:

- Investigate how the important parameters such as operating temperature, water condensation rate, wet gas velocity effect, and total and CO_2 partial pressure may affect TLC.

- Understand the mechanism behind the TLC and determine the actual relationship/synergy between the condensation rate and surface temperature and which is dominant under which conditions.

- Predict water condensation rate at static and flowing conditions accurately.

- Develop a mechanistic model to predict TLC to explore the influence of key parameters.

1.5 Structure of Thesis

The experimental work and theoretical study represent the general structure of this thesis. Eight chapters are presented in this thesis.

Chapter one briefly presents the corrosion problems encountered by the oil and gas industries and the costs of this problem. The objectives of this study are described in this chapter as well.

A description of the fundamental theories of the general CO_2 corrosion behaviour of the carbon steel and the different corrosion mechanisms and key factors influencing carbon dioxide corrosion are included in Chapter 2. Furthermore, this chapter presents and reviews a number of well-known mechanistic, semi-empirical and empirical models which can be used to help predict CO_2 corrosion rates.

Chapter 3 highlights TLC in particular. The condensation phenomenon description and water condensation modes are described in detail in this chapter. Additionally, this chapter discusses the relative effects of the key parameters (CO_2 partial pressure, pH, operating temperatures, etc.) and corrosion products formation on TLC. The most representative experimental studies, as well as some popular models, are presented are reviewed. Common mitigation and control techniques in the field are also mentioned in this section.

Chapter 4 covers in detail the experimental protocol, the new setup used in this project and measuring methods and instrumentations employed in this work.

Chapter 5 presents the experimental investigation of TLC exposed to the CO_2-saturated water phase. The effects of the condensation rate and the pipe surface temperature for 6 days duration are covered. A discussion of all the results presented, followed by analysis using SEM, XRD. Based on the comprehensive data was obtained from the experimental work, an empirical correlation between pipe surface temperature, water condensation rate and TLC rate was proposed in this chapter. The localised corrosion investigation under different conditions was identified using surface profilometry technique.

Chapter 6 describes a model for water condensation developed in this study, its validation against experimental data and a wider study of the influence of key parameters.

A numerical model developed for TLC prediction in CO_2 environments was is detailed in Chapter 7.

Chapter 8 outlines the main conclusions and the significance of the present work along with some recommendations for future work.

Chapter 2. Literature review I: CO_2 Corrosion in the Oil and Gas Industry

2.1 Definition of CO_2 Corrosion

The accepted broad definition of corrosion is material deterioration due to chemical or/and electrochemical reactions with its corrosive environment [21]. The mechanism of CO_2 corrosion is very complex and its understanding, prediction and control are important challenges [1].

CO_2 corrosion is a process involving three physicochemical processes occurring simultaneously. These processes are chemical reactions in the bulk solution, mass transport of aqueous species through the liquid boundary layer and electrochemical reactions at the metal surface [22]. The corrosion process is shown schematically in Figure 2-1.

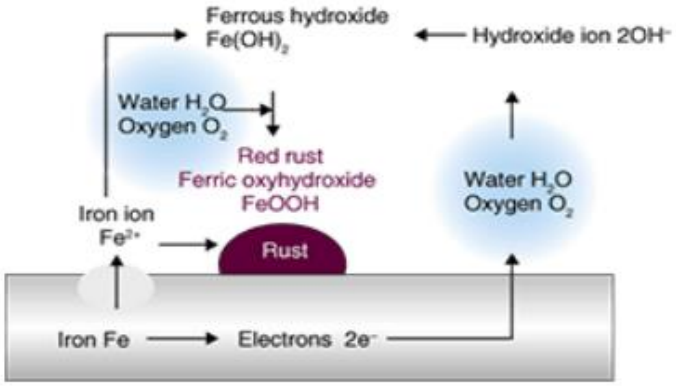

Figure 2-1. Corrosion mechanism of iron [23].

2.2 Top of Line Corrosion

Top of Line corrosion (TLC) occurs in stratified multiphase wet gas flow systems when water vapour contained in the gas phase condenses on the internal walls of a pipeline. Figure 2-2 shows a schematic diagram of the wet gas pipeline showing the case of TLC. This is due to strong gradients of temperature between the hot unprocessed well gases and colder outside

surroundings (seawater, river water, frozen areas or cold air) if the pipe is not thermally insulated or buried at an appropriate depth.

As the condensation process occurs, the condensed water then becomes enriched by corrosive species such as CO_2, H_2S and organic acids (mostly acetic acid) which exist naturally in the gas stream. The condensed liquid usually has a low pH because it does not contain any buffering species such as iron or bicarbonate. As seen in the previous chapter, the major concern is carbon dioxide (CO_2), which reacts with water to form carbonic acid (H_2CO_3), although hydrogen sulphide (H_2S) and acetic acid can also present serious challenges. Since TLC occurs in wet gas pipelines operated in stratified flow regimes, corrosion inhibitors or other corrosion protection chemicals such as mono-ethylene glycol (MEG) which are injected into the system remain at the bottom of the pipe and the upper part of the pipe stays remains unprotected.

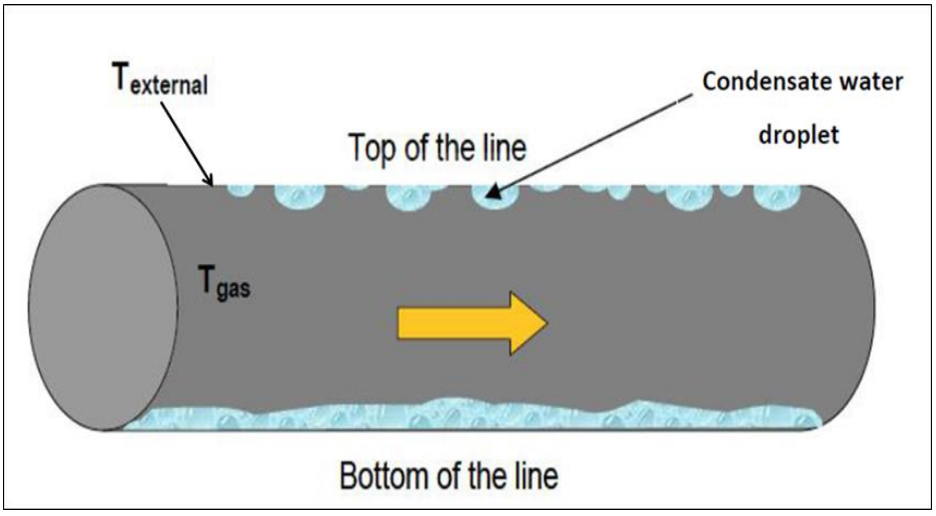

Figure 2-2. Schematic of top of the line corrosion at a stratified flow regime.

2.2.1 Pipeline Flow Regimes

Three main flow regimes may be encountered within the gas-oil-water three-phase flow or gas-liquid two-phase flow. Figure 2-3 shows a schematic of the flow regimes possible in a horizontal pipeline and the flow regimes under

which the top of the line corrosion is possible [24]. These flow regimes are described below:

- **Wavy or smooth stratified flow**: At low gas and liquid flow rates, the gas and liquid phases are segregated with gas at the upper level and the liquid at the lower level and the gas-liquid interface is smooth. This flow regime is subdivided into two sub-regimes: the Stratified-Smooth pattern, where the gas/liquid interface is smooth, and the Stratified-Wavy pattern, occurring at relatively higher gas rates, at which stable waves form at the interface. With increased liquid and gas velocity, waves will be initiated at the gas-liquid interface.
- **Slug or plug intermittent flow**: At higher liquid velocity, the tops of the waves can reach the upper surface of the pipe, and intermittent flow ensues with liquid slugs connecting the top and the bottom of the line. The Intermittent flow regime is subdivided into slug and plug regimes. The plug flow occurs at relatively low gas flow rates and in this case, the liquid slug is free of entrained bubbles. When the gas flow rate becomes higher, the front of the flow forms eddies and the flow converts to slug flow.
- **Annular flow**: When the gas phase velocity increases but the liquid phase velocity is kept low, the flow is annular. In annular flow, water droplets are transported to the upper part of the pipe forming a liquid film covering the whole pipe wall surface and the gas stays in the core.

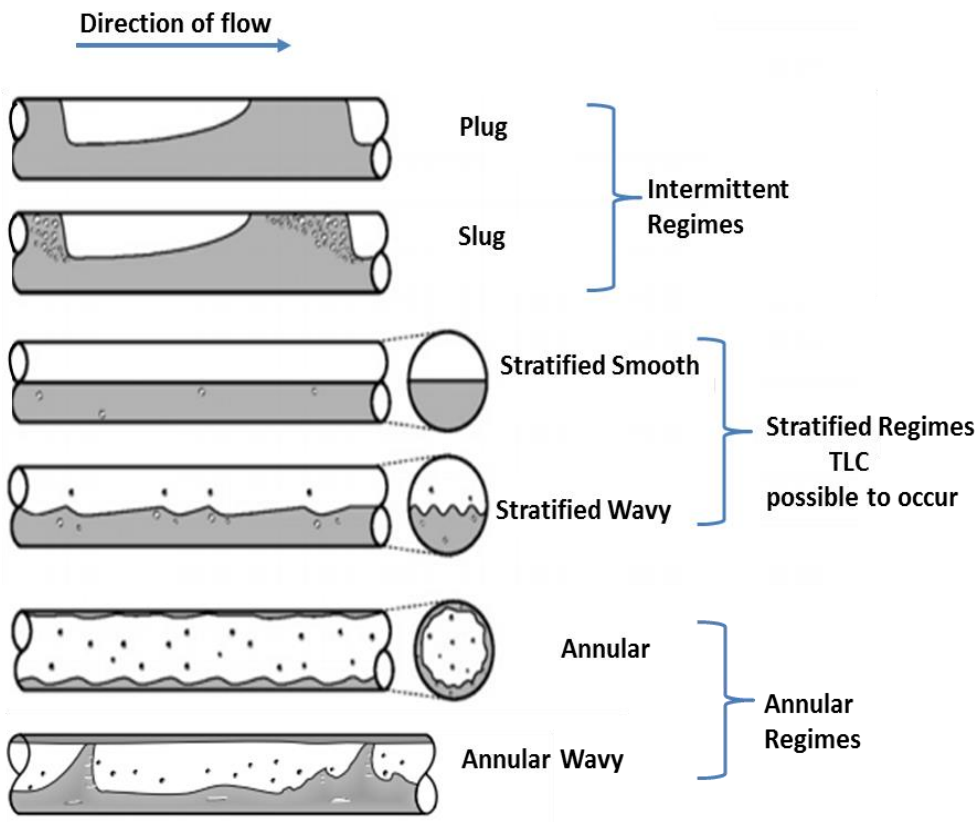

Figure 2-3. Different flow regimes possible for two-phase flow in the pipeline. Adapted from [24].

2.2.2 Condensation at the Top of the Line

Condensation is a complex process of converting a substance from a vapour phase to liquid phase. It results when the temperature of a condensing surface is lowered below the saturation temperature of the surrounding vapour or the vapour pressure of the material is increased above saturation values [25]. The liquid phase formation can be controlled by two key parameters, i.e. the temperature and the wetting properties of the condensation surface. These two parameters control the nucleation rate and growth of droplet patterns [26]. Condensation at the top of the pipeline is classified into two regimes: filmwise condensation and dropwise condensation.

2.2.2.1 Filmwise Condensation Regime

Filmwise condensation (FWC) happens when the condensate completely wets the condenser surface and the whole surface is covered by a condensate liquid film. The first analytical investigation was carried out by Nusselt in 1916. He developed the Nusselt condensation theory to calculate the heat transfer rate for a laminar film with stagnant vapour on a vertical plate. According to his theory, he calculated the heat transfer coefficient and the condensed film thickness. Nusselt confirmed that the liquid film represents a thermal resistance to heat transfer. In fact, Nusselt's filmwise condensation theory for a vertical plate offers a base-model to calculate the condensation rate, however, it is limited to pure water vapour condensation, which is not common in reality.

To introduce the effect of the velocity of the fluid on the condensation rate of the vapour phase, Chato in 1966 [27, 28], extended Nusselt's filmwise condensation theory to filmwise condensation with a turbulent film when Reynolds number exceeds 35,000. The author derived a correlation for the heat transfer coefficient. However, when a non-condensable gas is present, Nusselt theory and all its derivatives will over-predict the rates of condensation due to lack of presence of the non-condensable gas influence. In 1966, Minkowycz et al. [29] included the effect of the non-condensable gases and the effect of the velocity to find the heat transfer on a vertical isolated plate during the steam condensation process. They suggested that there was another boundary layer on the side of gas phase at the interface between the gas and the liquid beside the boundary layer on the liquid side. The authors proposed that the existence of the double boundary layers of gas and liquid phases act as heat and mass transfer resistances. In their investigation, it was found that the heat transfer flux reduced more than 50% for air mass fractions lower than 0.005 which confirmed how important the role played by non-condensable gases.

Recently, Vitse et al. [30] conducted an experimental and theoretical study to determine the parameters that affect the condensation and the corrosion rate in a horizontal pipeline in the presence of non-condensable gas. In their experiments, the effect of the gas velocity and partial pressure of CO_2 and of gas temperature which play an important role in the water condensation rate were investigated. However, this study was a major breakthrough in the understanding of the condensation and TLC processes mechanisms, but it is not valid when trying to predict the condensation rate at the top of the line where dropwise condensation takes place.

2.2.2.2 Dropwise Condensation Regime

In dropwise condensation (DWC) individual liquid droplets form rather than a continuous liquid film and the solid surface cannot be completely covered by droplets. In this process, very tiny droplets are formed at the nucleation sites then they grow as a result of continued condensation and coalescence together to form much bigger droplets, which are then swept down as a result of drag forces from the gas flow and of gravity force when they reach its maximum size. Figure 2-4 describes the mechanism of the formation of a single condensate droplet. As dropwise condensation occurs on a surface which is not completely covered by condensed liquid, the heat transfer coefficients in dropwise condensation can be between 4 to 8 times higher than those linked with filmwise condensation [25, 31].

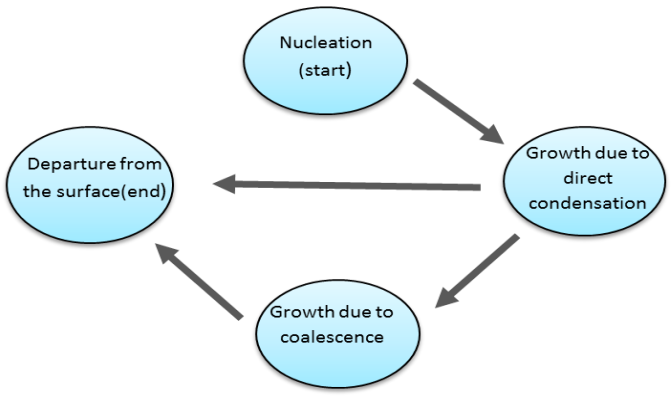

Figure 2-4. The Schematic process of dropwise condensation.

In the last decades, dropwise condensation in the presence of non-condensable gases has been documented by many researchers. In 1965, Tanner et al. [32] studied the effect of velocity and the existence of non-condensable gases on the dropwise condensation process. They found that the presence of even a small amount of non-condensable gas can considerably decrease the heat transfer coefficient.

Based on statistical analysis, Rose et al. [33] proposed the most used equation to find the droplet size distribution per square metre.

$$N(r)dr = \frac{n}{\pi r^2 r_{max}} [\frac{r}{r_{max}}]^{n-1} \quad 2.1$$

where $N(r)dr$ is the number of droplets with radii between r and r+dr, n is an exponent constant, normally 1/3, and r_{max} is the maximum droplet radius in m. In 1997, Abu-Orabi [34] calculated the total heat transfer in dropwise condensation through the integration of the heat flux of each droplet by considering a maximum droplet radius and the contact ngle of the droplet with the condensing surface. The results of his predicted models showed a good agreement when compared with the experimental results. However, his work was not validated in the presence of non-condensable gases, as the experiments were conducted in pure vapour systems.

2.2.3 The TLC Mechanism

The mechanisms of the top of line (TOL) corrosion fundamentally is similar to the bottom of line (BOL) corrosion mechanism. TLC involves three important processes that occur simultaneously: heterogeneous and homogeneous chemical reactions, electrochemical reactions at the surface of the pipeline and transport of species between the liquid droplet and the surface. The mechanism of CO_2 corrosion is complex and its understanding, prediction and control all present important challenges [1].

Most cases of TLC occur in stratified multiphase flow systems of wet gas transportation. It is linked to situations when a part of the pipeline is partially

or not completely thermal insulated from the upper section of the pipeline. Due to the large temperature gradients between the internal warm fluid and the cold surrounding environment, the water vapour condenses at positions between 10-2 o'clock of the pipeline. In these cases, the process of the hydration of acidic gases such as CO_2 takes place and this eventually leads to TLC. Figure 2-5 illustrates the schematic diagram of the cross-sectional wet gas transportation pipeline showing TLC.

Due to the effect of gravity, most of the condensate water drains to the bottom of the pipe leading to the bottom of the line corrosion (BLC). It is expected that the BLC is more severe than TLC, however, injection of corrosion inhibitors can mitigate the BLC cases effectively. Generally, TLC occurs in wet gas pipelines which are operated in stratified flow regimes, where corrosion inhibitors which are usually non-volatile in its nature remain at the bottom of the line and are not able to reach and protect the upper part of the line [35].

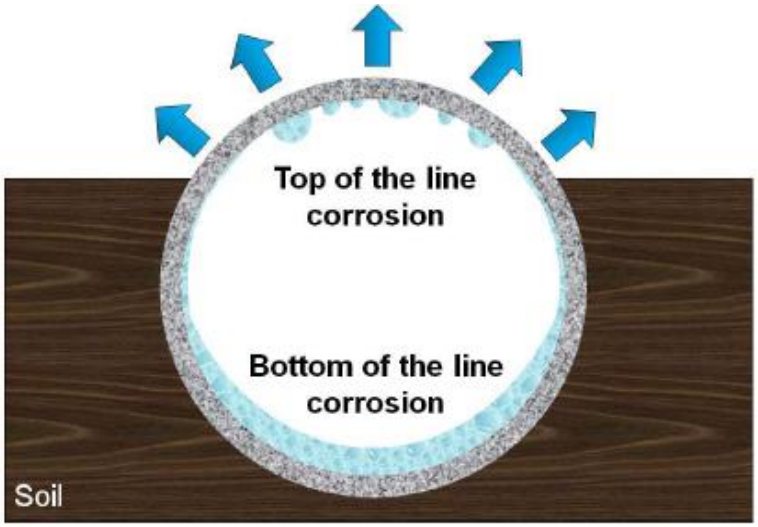

Figure 2-5. Schematic diagram of cross-sectional wet gas pipeline showing TLC occurred in a buried pipeline [36].

2.2.4 The Thermodynamics of CO_2 Corrosion

Metals and materials have a natural tendency to react with other chemical elements to return to their lowest energy state. To return to lower energy states, iron and steel frequently react with oxygen and water, both of which are present in most natural environments, to form hydrated oxide and in the case of iron, the iron oxide refers to “rust” [37]. The tendency for any chemical reaction to react, including the reaction of a metal with its environment (corrosion), is measured by the change in the Gibbs free energy, ΔG [38]. The value of ΔG indicates if the reaction tends to occur naturally or not. If the chemical reaction is spontaneous, and there is no external force applied to the system the system will tend to revert to its lowest energy state, then ΔG must be negative. While positive ΔG value means that reaction of the metal is not spontaneous and the system will require an energy input for the reaction to happen [21, 39].

Once the system reaches the lowest free-energy state, it remains in equilibrium. At this stage, there is no driving force for any further change from that state and the system is stable. These principles are illustrated in Figure 2-6 by a mechanical analogy.

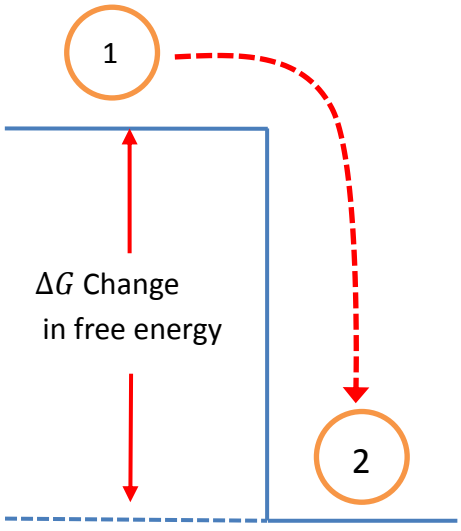

Figure 2-6. A mechanical analogy of free-energy change, adapted from [40]

Each metal surface has an inherent tendency to corrode or to react in an aqueous environment to produce metal ions and an electrochemical potential. Faraday found the relationship between free energy change (ΔG) and electrochemical potential (*E*) of the corrosion process [21].

$$\Delta G = -nFE \qquad 2.1$$

where ΔG is the free energy change for the corrosion reaction in kJ/mol, n is the number of electrons in the reaction and F is Faraday's constant=96500 Coulombs/mole, E is the electrochemical potential in Volts.

The Equation 2.1 can be re-written at standard conditions at a temperature of 273.15 K and pressure of 1 atmosphere.

$$\Delta G^o = -nFE^o \qquad 2.2$$

where ΔG^o and E^o represent the free energy change and electrochemical potential at standard conditions respectively. Table 2-1 provides values of E^o for several metals ranging` from 1.5 V for the reaction of gold ions to gold to a large negative value of –2.37 for the reaction of magnesium ions with magnesium. This wide range of potential values indicates a wide range in inherent tendencies to corrode, the more noble metals are at the more positive values. While, the more reactive metals, those suffer from corrosion, are at the more negative values and tend to be anodes [37].

The value of ΔG of a chemical reaction at any given temperature or concentration of reactants and products can be calculated using the Nernst equation.

$$\Delta G = \Delta G^o - RTln\frac{[a_{products}]}{[a_{reactants}]} \qquad 2.3$$

where R is the ideal gas constant= 8.134 $J.mol^{-1}.k^{-1}$, T is the temperature in K, $[a_{products}]$ and $[a_{reactants}]$ are the concentrations of all the products and reactants species, respectively [38, 41]. The Nernst equation gives an idea

of the different reactions to occur. However, other external parameters like water chemistry, the pH of solution, the temperature, the metal microstructure, the partial pressure of corrosive gases and the flow velocity will have an important influence on the corrosion processes.

Table 2-1. Standard electrode potential for selected metals at 273.15 K [37].

Electrode reaction	**Standard potential, V (E^o)**
$Au^{3+} + 3e^- \leftrightarrow Au$	1.500
$Ag^+ + e^- \leftrightarrow Ag$	0.800
$Cu^{2+} + 2e^- \leftrightarrow Cu$	0.337
$2H^+ + 2e^- \leftrightarrow H_2$	0.000
$Pb^{2+} + 2e^- \leftrightarrow Pb$	-0.126
$Ni^{2+} + 2e^- \leftrightarrow Ni$	-0.250
$Fe^{2+} + 2e^- \leftrightarrow Fe$	-0.440
$Zn^{2+} + 2e^- \leftrightarrow Zn$	-0.763
$Al^{3+} + 3e^- \leftrightarrow Al$	-1.660
$Mg^{2+} + 2e^- \leftrightarrow Mg$	-2.370

2.2.5 CO_2 Corrosion Electrochemistry

For any CO_2 corrosion to occur, there are four essential elements that must be available: anode, cathode, electrolyte and electronic path [37]. A schematic for an electrochemical corrosion cell is shown in Figure 2-7. The anode and cathode are connected to the solution by an electrolyte liquid (ionic current path), and they are connected through the metal by an electronic path.

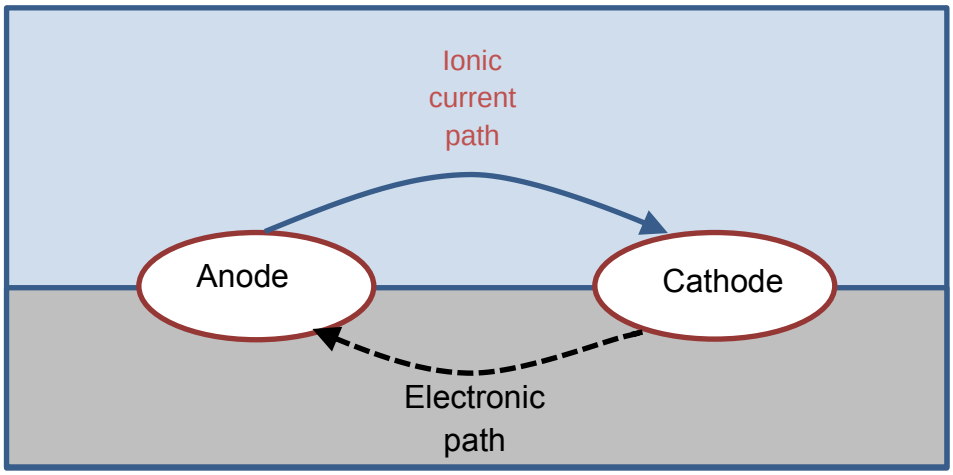

Figure 2-7. The four required components of an electrochemical corrosion cell [37].

2.2.5.1 Cathodic Reactions

Cathodic and anodic electrochemical reactions are established at the same time when a metal is exposed to the solution (carbon dioxide gas in combination with water), in other words, that the electrons released from the anode are consumed by the cathodic reaction [42]. The cathodic reaction is the hydrogen evolution reaction, the presence of CO_2 in an aqueous solution promotes the hydrogen ion consumption, leading to an increasing rate of corrosion of iron [39].

The CO_2 corrosion process starts by the dissolution of carbon dioxide in water to form aqueous carbon dioxide as shown in reaction 2.4 [43, 44].

$$CO_{2(g)} \leftrightarrow CO_{2(aq)} \quad 2.4$$

As aqueous CO_2 hydrates in water, it forms carbonic acid (H_2CO_3), a weak acid compared to mineral acids since it does not completely dissociate as represented by reaction 2.5 [1].

$$CO_{2(aq)} + H_2O \leftrightarrow H_2CO_{3(aq)} \quad 2.5$$

Carbonic acid dissociates in two steps to produce bicarbonate and carbonate ions as represented by reaction 2.6 and 2.7 respectively [1, 43, 45].

$$H_2CO_{3(aq)} \leftrightarrow H^+ + HCO_3^- \quad 2.6$$

$$HCO_3^- \leftrightarrow H^+ + CO_3^{-2} \quad 2.7$$

The main cathodic reactions are most commonly the reduction of hydrogen reaction 2.8 and the direct reduction of H_2CO_3 reaction 2.9 [1, 43, 45].

$$2H^+ + 2e^- \rightarrow H_2 \quad 2.8$$

$$2H_2CO_3 + 2e^- \rightarrow H_2 + 2HCO_3^- \quad 2.9$$

Also, it is believed that the direct reduction of water (reaction 2.10) can become significant and contribute to the overall reaction process under low partial pressure PCO_2 << 0.1 bar and pH > 6, but this reaction is very slow and can be neglected under other conditions [39].

$$2H_2O + 2e^- \rightarrow H_2 + 2OH^- \quad 2.10$$

2.2.5.2 The Anodic Reaction

The anode is the place at which metal is corroded, or at which metal dissolution processes takes place.

When the surface of a metal becomes exposed to the solution, metal is dissolved and transferred to the solution as metal ions. Positively charged

ions of metal tend to detach themselves from the metal surface and pass into the solution or electrolyte, leaving electrons behind on the metal. Through the metal surface, the electrons flow as an electrical current, to the cathode site where they are consumed. This process is known as oxidation [40].

The anodic dissolution of iron in aqueous CO_2 solutions is presented in reaction 2.11.

$$Fe \rightarrow Fe^{2+} + 2e^{-} \qquad 2.11$$

The electrons produced in the anodic processes are consumed in the cathodic processes. To create Fe^{2+}, Bockris et al [46] suggested the following steps:

$$Fe + H_2O \rightarrow FeOH + H^{+} + 2e^{-} \qquad 2.12$$

$$FeOH \rightarrow FeOH^{+} + e^{-} \qquad 2.13$$

$$FeOH^{+} + H^{+} \rightarrow Fe^{2+} + H_2O \qquad 2.14$$

During the pure CO_2 corrosion the concentration of iron ions increases, when the concentrations of Fe^{2+} and CO_3^{-} ions exceed the solubility limit, solid iron carbonate precipitates [47, 48].

$$Fe^{2+} + CO_3^{-} \rightarrow FeCO_{3(s)} \qquad 2.15$$

At the TOL, under certain conditions of temperature and solution pH, iron ions and carbonate ions can react to form an iron carbonate layer ($FeCO_3$) as shown in Equation 2.15, depending on various parameters, this layer can be protective or non-protective [49-51]. The formation of an iron carbonate layer at the surface of the metal can slow down the corrosion process by presenting a diffusion barrier and by covering a portion of the metal surface and hindering the underlying steel from further dissolution [52].

2.3 Types of CO_2 Corrosion

In CO_2 dominated environments, corrosion attacks appear in many forms that strongly depend on the inherent characteristics of the metal, the predominating environmental conditions and the corrosion kinetics. In the oil and gas industry, there are mainly two forms of corrosion namely uniform and localized corrosion.

2.3.1 Uniform Corrosion

Uniform corrosion, also known as general corrosion, happens uniformly over the entire exposed surface or across a large area of the steel surface [37, 53]. General corrosion development and progress are functions of the solution properties and the physical characteristics of the environment. The typical form of metal degradation from the surface due to general corrosion attack is shown in Figure 2-8.

Figure 2-8. General corrosion [54]

2.3.2 Localised Corrosion

Localised corrosion can be defined as a type of corrosion in which confined areas on the metal surface exhibits a metal loss greater than the rest of the

surface as shown in Figure 2-9. Usually, localised corrosion results in deep penetration of the metal surface. Mainly three forms of localised corrosion are generally encountered in carbon steel pipelines, pitting corrosion which is the most severe one, crevice corrosion and mesa attack [1, 55].

The corrosion phenomena are mostly associated with the formation of a film on the surface of the metal [1, 56, 57]. In certain conditions, the film passivity may be destroyed locally, which leads to localised corrosion/pitting corrosion.

It has been suggested that localised or pitting corrosion of carbon steel in CO_2 and CO_2-H_2S containing environments is often related to the formation of, and/or breakdown of (non-protective and protective respectively) $FeCO_3$ films and formation of semi-protective iron sulphide film respectively [58]. In fact, pitting corrosion of carbon steel can be complex and in the main unpredictable in nature with significant challenges that are usually associated with inhibiting pit propagation once it has initiated. It has been envisaged that factors such as temperature, *in-situ* pH, exposure time of metallic components to corrosive media and solution chemistry (e.g. chloride ion concentration) that can influence the CO_2 corrosion process along with associated film formation characteristics and morphology could also influence the tendency for pits to initiate and propagate on carbon steel materials [59-61].

In reality, localised corrosion or pitting corrosion is the main reason for corrosion failures of facilities encountered in oil and gas fields. This is mainly observed at low fluid velocities for flowing systems or in stagnant conditions. The reason behind that is that corrosion may be caused by a local electrochemical concentration cell between the pit cavity and the pipe surface [62, 63]

In the case of top of the line corrosion (TLC), a protective iron carbonate ($FeCO_3$) film can be formed under certain conditions. Inhibitors at the upper surface are not effective and mostly result in localised corrosion. A better

understanding of the TLC mechanism is achieved when the temperature of the inner wall of the pipe and the bulk gas temperature are put into consideration.

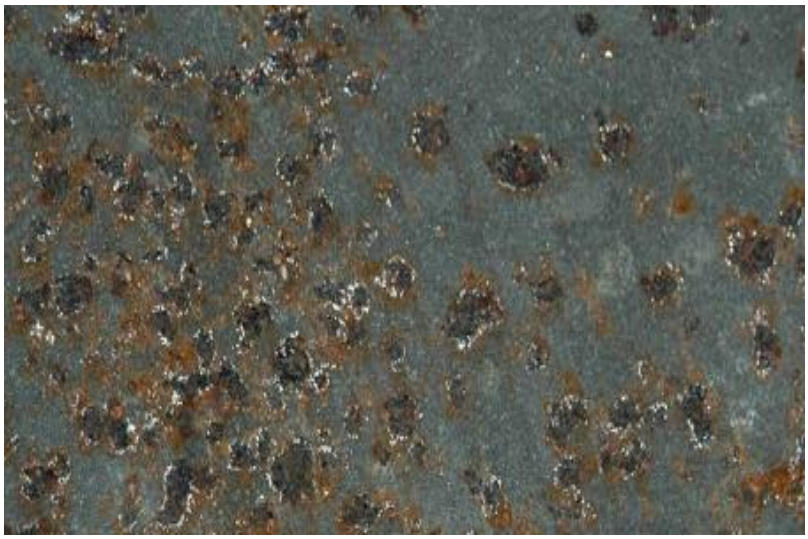

Figure 2-9. Localised corrosion [64]

2.4 Key Parameters Influencing TLC

A deep understanding of the influence of environmental factors on the rate of TLC is very important for corrosion prediction and mitigation strategies. Up to now, the progression in the study of the TOL corrosion in a CO_2 environment has led to the identification of several parameters affecting this corrosion processes namely, vapour and surface temperature, water condensation rate, water chemistry, CO_2 and H_2S partial pressure, flow velocity and organic acids concentration [1, 10, 65, 66]. The influence of these parameters is briefly discussed hereafter.

2.4.1 Effect of Operating Temperature

Gas and outer environment temperature have been considered to be the main factors affecting TLC because of both of its influence on the water condensation rate (WCR) and the nature of corrosion products formed, and ultimately the corrosion rate [67]. At higher gas temperature, the WCR is

expected to be higher and more water condenses on the top part of the pipeline. However, at low gas temperature, the WCR is likely to be relatively low, and as a result, the TLC is governed by the chemical and electrochemical reactions of the condensed water[67].

The effect of temperature is one of the crucial parameters influencing corrosion rate, particularly when working with carbon steel equipment as the formation of a protective film is highly temperature dependent [1, 65, 68].

Furthermore, in CO_2 corrosion environments, the two controlling reactions, named iron dissolution and iron carbonate precipitation Equations 2.16 and 2.17 respectively occur adjacent to the inner steel surface. [69, 70].

$$Fe \rightarrow Fe^{2+} + 2e^{-} \quad 2.16$$

$$Fe^{2+} + CO_3^{2-} \rightarrow FeCO_3 \quad 2.17$$

Hence, the kinetics and thermodynamics of these reactions are mainly governed by the temperature of the steel surface. An increase in temperature accelerates all the processes involved in corrosion such as electrochemical, mass transport etc. The Arrhenius equation describes the relationship between the temperature and reaction rate constants [71].

$$k = Ae^{-\frac{E_a}{RT}} \quad 2.18$$

where k is reaction rate constant, A is a pre-exponential factor, R is the universal gas constant, T is the absolute temperature in Kelvin and E_a is the activation energy for the reaction in Joule/mol (activation energy can be defined as the minimum energy required to start a chemical reaction).

In a case of low pH, the corrosion rate steadily increases with temperature when the precipitation processes of iron carbonate and other protective scales are not influential [10, 66]. When the pH increases, the solubility product of the species is more likely to be exceeded leading to the formation of a protective scale-film. In these particular conditions, increasing

temperature accelerates the kinetics of precipitation and protective scale formation, decreasing the rate of corrosion [10, 66]. Depending upon the water chemistry and flow behaviour, the corrosion rate peaks tend to occur between 60°C and 80°C [20].

The characteristics and morphology of the corrosion film are strongly affected by the operating temperature, it virtually reduces the film porosity and increases the adhesion and hardness of the protective film [1]. At a temperature between 60°C and 90°C, iron carbonate becomes more stable, denser and therefore, more protective over time [52, 72]. Figure 2-10 illustrates that the increase in temperature accelerates the iron carbonate film formation process, consequently, increases the surface coverage due to the higher precipitation rate and therefore, reduces the rate of corrosion [56].

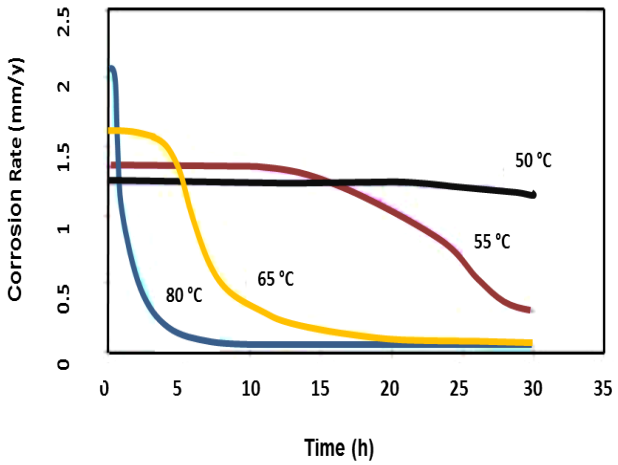

Figure 2-10. Predicted effect of temperature on the corrosion rate for pH 6.6, P_{CO2} 0.54 bar, [Fe^{2+}] 250ppm and V= 1m/s [56].

Therefore, it clearly appears that TLC rates are influenced by the counteracting actions of wall temperature and water condensation rate. Further details concerning the counteracting roles of these two parameters in sweet dewing conditions are presented in Chapter 5**.**

2.4.2 Effect of Condensation Rate

When transporting wet gas, due to significant heat exchange between the inside of the pipe and the outside environment, condensation of water vapour carried by the wet gas occurs on the internal pipe wall. Typically, the condensed water is pure and, due to the hydration of CO_2, the condensed water has a pH value approximately 3.8 [73]**.** This leads to the so-called top of line (TLC) scenario, as shown in Figure 2-11.

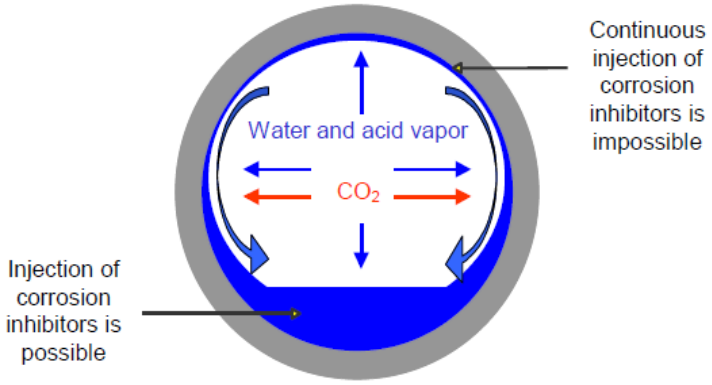

Figure 2-11.Schematic of the liquid condensation processes inside the pipe [73].

Large research efforts have been undertaken to study TLC and how the condensation rate can affect the TLC process [30, 67, 74]. All these studies report the effect of low and high water condensation rate on the corrosion process. If the rate of condensation is low, water droplets are not replenished quickly and flow down very slowly and the corrosion process can release sufficient iron ions (Fe^{2+}) to raise the pH and saturate the solution. Hence, iron carbonate corrosion products ($FeCO_3$) accumulate rapidly in the condensed water and increase the local pH until the water is saturated with iron carbonate. As saturation is reached, a precipitation reaction occurs and an iron carbonate protective scale will form. Therefore, the corrosion rate is controlled by the electrochemical reaction of the condensed water and the TLC rate is limited by the number of iron ions that can be released and transported through the condensed water.

In contrast, when the condensation rate is high, due to the rapid renewal of the water droplets the supersaturation of the condensed water droplets with respect to iron carbonate is difficult to achieve and an unprotective iron carbonate film will form leading to an increase in the corrosion rate ultimately.

The corrosion scale is often protective, however, incidents of localized attack in TLC were reported [10, 12]. In the stratified or stratified-wavy flow regime which is typical for TLC, the corrosion inhibitors cannot reach the upper surface of the internal pipe wall and protect it.

To describe the phenomenon of corrosion occurring at the top of the line qualitatively and quantitatively, a thorough investigation into the combined effect of the chemistry, hydrodynamics, thermodynamics, and heat and mass transfer in the condensed water is needed.

2.4.3 Effect of Solution Chemistry

The solution chemistry is probably one of the most influential factors affecting CO_2 corrosion. The composition of the solution can vary from very simple, for example, those found in gas condensate in the pipeline systems, to very complex, with numerous species in the solution such as formation water emerging together with crude oil [10].

In the oil field production scenarios, the water phase may be formed by condensation of water vapour, or due to the presence of formation water. In the latter case, the water contains significant amounts of salts (chloride, sodium and calcium ions are the most common species) these can adversely affect the solution pH value. Solution pH plays an important role in the corrosion processes of carbon steel by affecting both the electrochemical reactions that lead to iron dissolution and iron carbonate supersaturation which influences the formation of a protective film and has a direct effect on the corrosion rate [1, 10].

Any increase of the pH values promotes high iron carbonate supersaturation, which in turn, would lead to a reduction of the corrosion rate due to an increase of the film's precipitation rate [74, 75]. The study of Kermani et al. [1], has shown that increasing the pH of a solution from 4 to 5 decreases the solubility of Fe^{2+} by approximately a factor of 5. A further increase in pH from 5 to 6 reduces solubility 100 times. Supersaturation (SS) is defined as:

$$SS = \frac{[Fe^{2+}][CO_3^{2-}]}{K_{sp}} \qquad 2.19$$

where $[Fe^{2+}]$and $[CO_3^{2-}]$ are the concentrations of iron and carbonate species, respectively, and K_{sp} is the equilibrium solubility product for iron carbonate. The value of saturation (SS) has to be >1 to have supersaturation with respect to iron carbonate. Figure 2-12 illustrates the effect of pH solution and CO_2 partial pressure on the iron carbonate ($FeCO_3$) saturation level [76]. The figure shows that when the value of pH is high, the solubility of iron carbonate decreases corresponding to a higher precipitation rate leading to a higher scaling tendency.

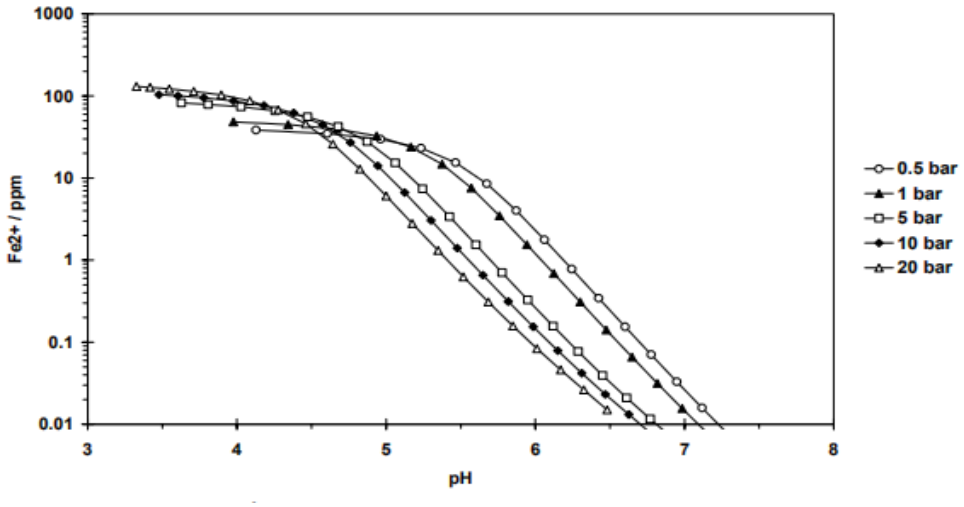

Figure 2-12. Fe^{2+} amount needed to be produced by corrosion to reach $FeCO_3$ saturation plotted as a function of pH [76].

In the case when the water formed as a result of condensation processes, there are no other species, such as from brine, the typical pH value of freshly condensed water is quite low and varies between 3 and 4 [7]. However, as the corrosion process takes place, and at a certain condition, divalent ions, such as iron ions, can react with the carbonate species, when present in the system, leading to increases in the pH value especially when the rate of condensed water renewal is low.

The presence of Oxygen (O_2) contamination is recognized as the main difficulty in investigating CO_2 corrosion in the laboratory. In real conditions in oil and gas fields, traces of O_2 may enter production equipment by injection of inhibitors and secondary recovery operations. The addition of O_2 (0.01ppm to 105ppm) results in a moderate increase in CR caused by an alternative cathodic reaction, increasing the overall corrosion rate [77]. However, O_2 also may promote the formation of protective corrosion product layers, retarding the corrosion attack [78].

Organic acids are also often present in oil and gas fields. The most common among them is acetic acid (CH_3COOH) [79]. It is understood that the presence of acetic acid leads to a considerable increase in the corrosion rate. Acetic acid acts as a provider of hydrogen ions and the cathodic reduction of the hydrogen ions is accelerated, increasing the rate of the anodic dissolution of iron and eventually enhancing the severity of the corrosion [79, 80].

2.4.4 Effect of CO_2 Partial Pressure

An increase of CO_2 partial pressure (P_{CO2}) leads to an increase in the TLC rates. This is usually true at low temperatures and high condensation rates or at high temperatures and low condensation rate. However, at high temperatures and high condensation rates, the effect of CO_2 partial pressure on the TLC can become more significant [30, 81]. Vitse et al.[82] confirmed in their study that the influence of CO_2 partial pressure is greater at high temperatures and high condensation rates. This behaviour can be attributed

to that at a low condensation rate it is easier to saturate the condensed liquid with corrosion products which inhibit the transformation of ions from and to the steel surface, leading to increasing solution pH and retarding the kinetics of the electrochemical reactions. While at a high condensation rate, it is difficult to saturate the condensed liquid with the products of corrosion and the pH of the condensed liquid could be more sensitive to the partial pressure of CO_2. Also, Son [83] reported that a high CO_2 partial pressure gives high corrosion rates by reducing the solution pH due to the supply of H^+ ions from carbonic acid and by increasing the rate of carbonic acid reduction to bicarbonates.

$$H_2CO_3 \leftrightarrow H^+ + HCO_3^- \qquad 2.20$$

Nyborg and Dugstad [84] studied the effect of CO_2 partial pressure on TLC. The authors observed that when the CO_2 partial pressure increases the iron solubility increases and thereby also the TLC rate increases. Table 2-2 illustrates their results, it clearly shows that an increase in P_{CO2} by a factor 20 provides an increase in the predicted TLC by a factor about 3. Accordingly, they concluded that the P_{CO2} has a less pronounced effect on TLC rates than variations in temperatures and water condensation rates.

Table 2-2. Variation in CO_2 partial pressure, iron solubility, WCR and TLC at 80°C [84].

CO_2 partial pressure bar	**Water condensation rate g/m²s**	**Iron solubility ppm**	**Top of line corrosion rate mm/y**
0.5	0.24	16	0.08
2	0.24	25	0.13
5	0.24	33	0.18
10	0.24	42	0.22

The above suggests that the TLC rate is sensitive to a change in P_{CO2} at high water condensation rates but is insensitive to such a change at low water condensation rates.

2.4.5 Effect of Gas Velocity

The hydrodynamics of the system plays an important role in TLC corrosion rates. At conditions not favourable to form iron carbonate films, increasing the fluid velocity enhances the diffusion rate of species towards and away from the steel surface, this fast movement of species increases the rate at which hydrogen ions are replenished and generated ferrous ions are removed from the steel surface, which in turn, leads to higher dissolution of the metal and an increase in the rate of corrosion [10, 65]. However, when a $FeCO_3$ protective film forms on the metal surface, the flow intensity can totally or partially remove the protective film. This local breakdown of the iron carbonate layer can also lead to localized corrosion, which has the potential to be more dangerous than uniform corrosion [85, 86]. Figure 2-13 describes the effect of the velocity on corrosion rate in a CO_2 corrosion system [87].

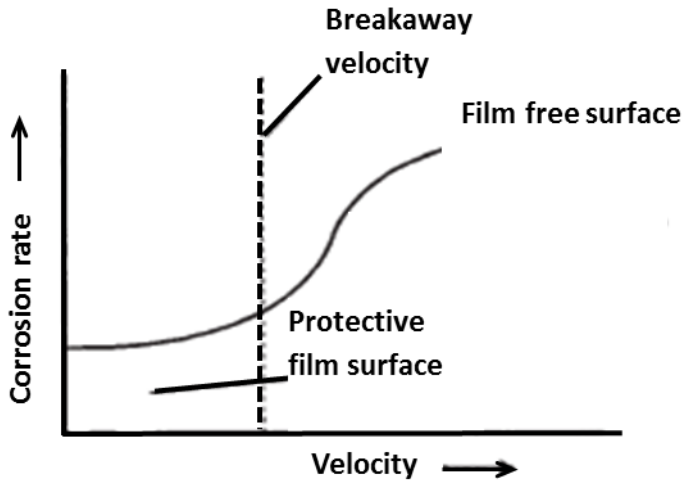

Figure 2-13. Schematic of the effect of velocity CO_2 corrosion [87]

Vitse et al. [30] gave some fundamental understandings of the significance of the gas velocity on the TLC. They observed that at a gas temperature of

90°C, increased gas velocity promoted water condensation but TLC rates remained relatively unchanged. However, when the temperature was 50°C, both the water condensation rate and the corrosion rate increased with increasing gas velocity. These results are shown in Figure 2-14. Also, they confirmed that mass transfer in the gas phase is less important at low gas velocities because there is less water available for condensation at the wall resulting in low heat loss thereby preventing the process of the phase change for the water phase. At the high temperature of 90°C, the corrosion rate remains unaffected by a change of gas velocity, and this is explained by the fact that at low water condensation rate, there is a tendency to reach saturation on time to form iron carbonate corrosion layer, which is only protective at high temperature.

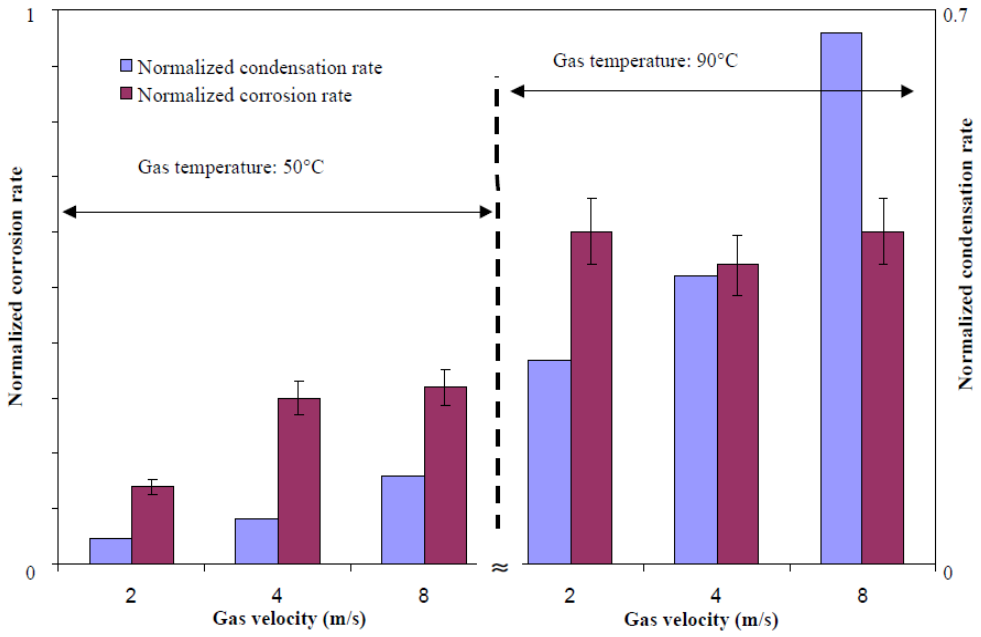

Figure 2-14. Influence of the gas velocity on the condensation rate [30].

The study by Singer and his co-workers [88] showed that at a low gas velocity, the gas starts to condense at the upper part of the pipe by forming stagnant droplets. A high supersaturation of iron carbonate is expected to be achieved in the condensed droplets leading to a dense corrosion protective layers. When the gas velocity increases, the condensation regime changes

gradually from a stagnant to sliding droplet. During the sliding droplet regime, the condensed liquid droplets flow along the upper surface of the pipe and can slide to the sides of the pipe, eventually accumulating in the bottom of the pipe. The authors found that the stagnant droplet forms a $FeCO_3$ protective layer, and due to the sliding droplets are not generally in contact with the pipe steel long enough to produce the $FeCO_3$ film, a non-protective Fe_3C film on the liquid pathways will form instead.

2.4.6 Effect of Organic Acids

In reality, TOL CO_2 corrosion is always associated with the presence of organic acids[89]. The main organic acids which are frequently present in formation water with its physical and chemical properties are listed in Table 2-3. Studies have found that the average quantity of organic acids in the formation water in the oil and gas system is in the range of 500 to 3000 ppm of which acetic acid contributes 50 to 90% of the organic acids [12, 90].

Table 2-3. List of some organic acids in formation water [11, 91, 92].

Acid	Formula	Concentration (mg/l)	Density (g/ml) at 20°C	Molecular weight
Acetic acid	CH_3-$COOH$	6.9	1.049	60.05
Propionic acid	CH_3-CH_2-$COOH$	113	0.996	74
Formic acid	$HCOOH$	14	1.22	46.03

Acetic acid which is commonly abbreviated as HAc is a volatile gas, so it can be easily transported in the gas phase and condenses with the water on the internal pipe surface. This can increase the concentration of acetic acid in the condensed droplets leading to an increase in the concentration of acetic

acid in contact with the metal surface which in turn increases the solubility of iron, in such case, the protectiveness of the corrosion products layers at the top of the line is reduced and the TLC rates increases eventually [90].

Since the 1980's, several studies have been conducted to investigate the effect of acetic acid on the corrosion rate of the carbon steel in the CO_2 environment [73, 93-96]. This literature reported that the presence of HAc even in small amounts in unprocessed oil and gas fluid could significantly increase the corrosion rate of carbon steel. They attributed that to the fact that the acetic acid has the ability to decrease the solution pH and increase the solubility of the iron ions due to the effect of undissociated acetic acid on the cathodic reactions of the corrosion process. As the solubility of the iron ions increases, the thickness of the protective iron carbonate layer decreases at the top or bottom of the pipe.

Through their experimental study, Okafor et al. [90] proposed a mechanism for CO_2 corrosion of carbon steel corrosion under liquid droplets containing acetic acid. Okafor and his co-workers proposed that the initiation of localized corrosion is due to the presence of protected and non-protected regions under dropwise condensation. They assumed that galvanic cell forms between the unprotected regions, with those regions covered by an iron carbonate corrosion product film. Also, Okafor et al. further reported that an increase in acetic acid concentration leads to an increase in the corrosion rate at the top of the line due to an increase in the concentration of undissociated acetic acid in the condensed droplet and thus increases the concentration of acetic acid in contact with the pipe surface. Figure 2-15 shows how the corrosion rate increases with an increase the concentration of the acetic acid [90].

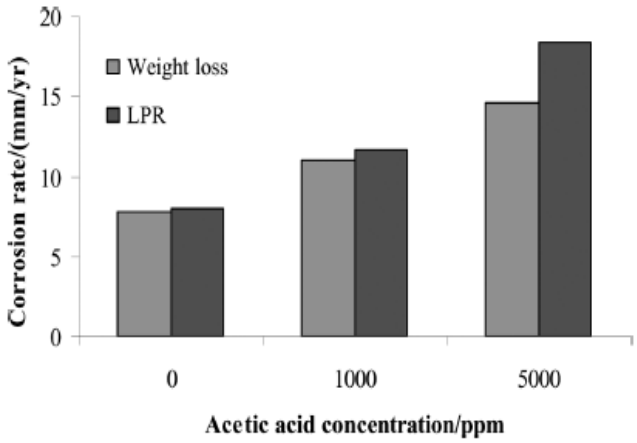

Figure 2-15. Variation of corrosion rate with acetic acid concentration from LPR and mass loss methods[90].

Hinkson et al. [97] investigated the effect of the presence of acetic acid on the TLC through determining the concentration of acetic acid in the condensed water. Their results showed that the total acetic acid in the condensed water decreased with an increasing water condensation rate. Also, they assumed that the corrosion process produces Fe^{2+} which can increase the condensed water pH due to the consumption of hydrogen ions and, this can lead to more acetic acid dissociation, and reduce the acetic acid concentration.

2.4.7 Effect of the Steel Composition and Microstructure

In the oil and gas industries, the mechanical properties, such as hardness, mechanical resistance, weldability, and toughness, and corrosion resistance are strongly governing the design criteria of pipeline materials [98]. Indeed, the mechanical properties of pipeline materials are mainly dependent on microstructure, which is determined by its chemical composition and heat treatments [99].

Most carbon steel alloys are heterogeneous in nature, and often composed of two or more different metallic elements, to give greater strength or resistance to corrosion. Each of these elements has a different structure,

chemical composition, and mechanical properties, the different structures would then behave in a different way in a corrosive environment. [87]. Also, studies [77, 100-102] have shown that the effect of chromium (Cr) content of the iron carbonate ($FeCO_3$) layer and found that additional amount of Cr can improve the protective properties of mild steel against corrosion attack. For example, Edmonds et al. [103] stated that adding 3% chromium to the carbon steel can reduce the corrosion rate by a factor of 10. If the chromium percentage is further increased to 12%, a thin chromium oxide layer, which is highly resistant to CO_2 corrosion, is formed and improves the protective properties of the steel surface.

The steel microstructure is considered to have an important effect on how firmly the corrosion scale sticks to the steel surface. The adherence of the corrosion product film, and hence its protectiveness, has often been related to the presence of iron carbide and its morphology (laminar, globular, etc.) [100, 104]. The idea is that the iron carbide can strengthen the film and can anchor it to the steel substrate, then the size and distribution of these carbides become very important [105, 106]. However, the accumulation of carbides in the corrosion product has been seen as the cause of increasing corrosion rate over time of exposure for ferritic perlitic steels [107, 108]. In TLC conditions, as corrosion proceeds, ferrite, which has higher energy and electric potential, corrodes and dissolves into the condensed liquid while the perlite phase remains on the surface [108, 109]. The latter being electrically conductive forms galvanic coupling with the remaining ferrite and acts as an additional cathode [107, 110].

2.4.8 Effect of CO_2 Corrosion Product Films

In sweet corrosion environments, previous research indicate that iron carbide (Fe_3C) and iron carbonate ($FeCO_3$) are the two main corrosion product scales [1, 111].

2.4.8.1 Iron Carbide (Fe_3C) Formation

Iron carbide or cementite (Fe_3C) component is a naturally occurring in ferritic-pearlitic carbon steels. The characteristics Fe_3C film are brittle and porous and therefore, very susceptible to flow conditions, or it can be a tough cementite network in acidic solutions [1].

Studies [1, 111-113] have proposed that the Fe_3C is capable of acting as an electrical conductor which can accelerate the corrosion rate of carbon steel by forming a galvanic effect on the surface and acting as a favourable cathodic site for hydrogen evolution. As corrosion proceeds, the iron carbide film formation can increase the rate of corrosion by a factor of 3 to 10 in some instances by playing a number of roles including galvanic coupling and/or creation of micro-galvanic corrosion cell on steel surfaces, as well as internal acidification of anodic regions within the layer [1, 114].

2.4.8.2 Iron Carbonate ($FeCO_3$) Film Formation

Iron carbonate film formation can reduce the corrosion process by either forming a diffusion barrier for the reactive species involved in the corrosion processes or by covering an area of the metal surface and preventing it from further dissolution [1, 10, 52, 68, 115, 116].

The iron carbonate corrosion products form when the carbonate anions (CO_3^{2-}) which form by the carbonic acid dissociation processes as described in Equation 2.7 reacts with dissolved ferrous ion Fe^{2+} [113, 117].

$$Fe^{2+} + CO_3^{-2} \rightarrow FeCO_{3(s)} \qquad 2.21$$

The iron carbonate precipitates heterogeneously at the metal surface, and its protectiveness from corrosion strongly depends on the precipitation rate, which in turn, depends on both the carbon steel characteristics (chemical composition, microstructure, heat treatment) and environmental factors such

as solution pH, temperature, CO_2 pressure, solution composition, flow rate, etc.[1].

As the metal corrosion process develops, the metal is attacked and dissolved, leaving gaps in the surface and corrosion continuously undermines the $FeCO_3$ layer. If the formation and precipitation rate of the corrosion products on the steel surface exceeds the corrosion rate (dissolution of iron), an adherent and dense $FeCO_3$ layer can form on the metal surface sometimes very thin (1 μm) but still protective. Conversely, when the corrosion process attacks the new corrosion products faster than the precipitation process, a porous and non-protective scale forms (which could be very thick about 100 μm). [10, 68, 107, 118, 119].

Figure 2-16 [51, 95, 120, 121] shows an example of a protective scale and the thickness of protective corrosion layer and the gaps and porous layer underneath the film. The main parameter affecting iron carbonate formation is the supersaturation value which can be found by Equation 2.19.

The formation of iron carbonate scales strongly connect with the operating temperature. At low temperature, the precipitation process is slow and even at high supersaturation values, a non-protective film will be formed.

When increasing temperature, for example, beyond 60°C, even for lower supersaturation values, the precipitation process proceeds rapidly due to a reduction in the solubility of $FeCO_3$ and, then dense and very protective scales can be formed [10].

The importance of $FeCO_3$ formation was perhaps first suggested to be important in TLC conditions by Olsen et al. in 1991 [81]. The precipitation of $FeCO_3$ requires the film or droplets of water on the steel surface to be highly saturated with respect to $FeCO_3$ to facilitate the formation of a protective film. Olsen et al. found that protective films were generated at a high gas temperature of 70˚C and a low condensation rate. However, it has also been observed by Olsen et al. [81] that the protectiveness of this layer is affected

by the WCR, but supported by the Fe^{2+} dissolution rate. Furthermore, Singer et al. [88] also commented that the very aggressive localised corrosion can be initiated and sustained if the local protection afforded by $FeCO_3$ is compromised. The main threats to this are high WCR and the extent to which the condensate promotes $FeCO_3$ breakdown/dissolution. Both Pots et al.[122] and Vitse et al.[28] performed extensive tests in CO_2 TLC conditions and identified that $FeCO_3$ formation, highlighting the competition between iron dissolution and condensation rate, while also demonstrating that the protective layer was favoured by increasing temperature.

The solution chemistry (pH) is one of the most influential factors affecting iron carbonate formation. Increasing the solution pH would lead to a decrease in the solubility of the iron carbonate film, therefore increasing precipitation which could lead to a reduction of the general rate of metal corrosion [1].

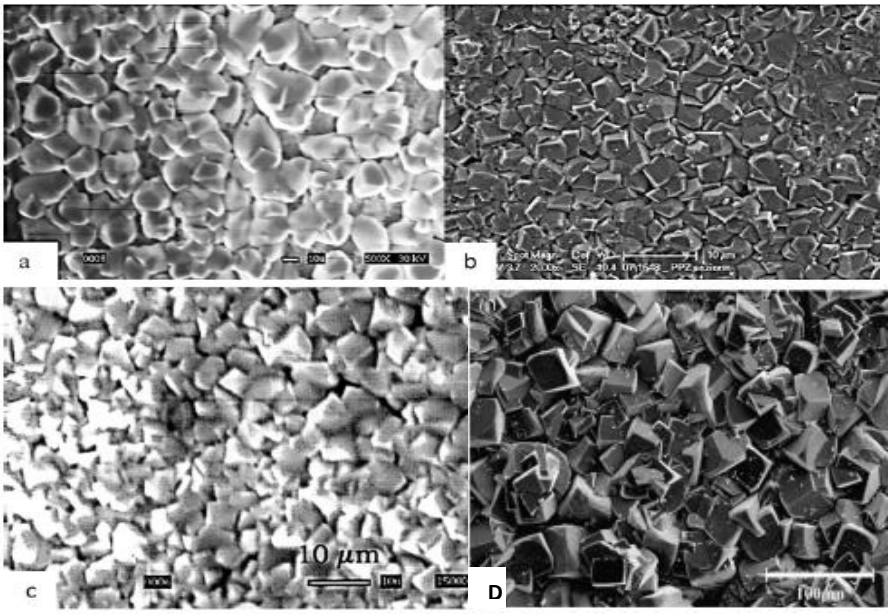

Figure 2-16. Different SEM images of iron carbonate film: a) at pH 6.6, Fe^{+2} concentration 10 ppm, saturation ratio 30, T 80°C, stagnant conditions [120]. b) at pH 6.6, T 80°C [121]. c) at pH 6.6, T 80°C, Fe^{+2} concentration 50 ppm, saturation ratio162 [95]. D) at T 75°C, pH 6.5 and P_{CO2} 10 bar [51].

2.5 Control and Mitigation Techniques for TLC

The severity of the TLC phenomenon is the result of complex interactions between all parameters affecting TLC such as vapour and surface temperature, water condensation rate, CO_2 and H_2S partial pressure, flow velocity and organic acid concentration, and any effective mitigation strategies would require a good understanding of the mechanisms involved [88].

In order to prevent and mitigate TLC phenomena, many control techniques have been developed and used in oil and gas industry. The techniques are:

- Thermal insulation and protective coatings.
- Chemical inhibition.
- Increase fluid pH.
- Selection of more corrosion-resistant metals and alloys.
- Cathodic protection.

2.5.1 Thermal Insulation and Protective Coatings.

Applying thermal insulation technique is the most common choice to reduce the water condensation rate and thereby reduce the TLC rate [36]. Not only the temperature and the gas flow rate govern the water condensation rate, but also the type of pipeline insulation and the coating has an important role to influence the water condensation rate. Nyborg and Dugasted [84] reported that different types of pipeline coating with different thermal insulation properties can give large differences in the water condensation rate and hence a large variation in the predicted top of line corrosion rates for similar cases. Their results show that the heat transfer coefficient is dependent on the coating type of the pipeline and the actual thermal conductivity of the different materials. They found that increasing the coating thickness for example, from 4 mm to 8 mm decreases the heat transfer coefficient from 53 to below 30 $W/m^2.K$.

Table 2-4. Different water condensation rates and top of line corrosion rates for different types of pipeline coating [84].

Coating	Overall heat transfer coefficient ($W/m^2.K$)	Condensation rate ($g/m^2.s$)	TLC (mm/y)
0.5 mm fusion epoxy	283	1.26	0.74
6 mm coal tar enamel	100	0.46	0.25
4 mm 3-layer polypropylene	53	0.24	0.13
8 mm polypropylene	28	0.13	0.07
4 mm PP + 40 mm concrete	21	0.10	0.05

2.5.2 Injection of Chemical Inhibitors

Internal corrosion in carbon steel pipelines transporting carbon dioxide and/or hydrogen sulphide containing gases can be prevented by drying it prior to transport it in transportation pipelines. However, the high cost of dehydration units represents a big barrier to use these units currently [123]. Accordingly, the use of the continuous injection of chemical corrosion inhibitors into the produced fluid has been the commonly used method in the oil and gas industry.

Corrosion inhibitors are chemical substances which, when added in small quantity to a corrosive environment, significantly decreases the rate of attack by the environment without a significant change in the concentrations of corrosive species in the environment [11, 124, 125]. In recent time, amine and imidazoline derivatives are the most commonly used commercial inhibitors with success to slow down carbon steel corrosion in oil and gas industry because of their good solubility, high stability, and low toxicity[11]. A corrosion inhibition method is based on the assumption that corrosion protection is achieved by surface coverage, i.e. that the inhibitor adsorbs

onto the reacting surface and slows down one or more electrochemical reactions. The protection degree is directly proportional to the fraction of the reacting surface covered by the inhibitor [10].

The continuous injection of inhibitors is an efficient method where the inhibitor can remain in contact with the steel surface. However, in a scenario of the TLC where the flow type is stratified, there are no means for the inhibitor present in the bulk liquid phase at the bottom of the line to reach the top of the pipe, since the inhibitor is generally non-volatile and does not condense at the top of the pipe.

Consequently, this method is ineffective for TLC mitigation, unless the chemical inhibitor has some volatile properties and can evaporate and then condense together with the water at the top of the line. Research has been conducted to develop and use the Volatile Corrosion Inhibitor (VCI) for field application and some limited success has been obtained and an acceptable protection level was achieved in the laboratory [126, 127].

2.5.3 Increase of the Fluid pH Technique

Studies have shown that an increase in fluid pH has a greater impact on the protective $FeCO_3$ film formation due to the fact that solution pH is directly related to the carbonate (CO_3^{2-}) concentration which in turn influences the iron carbonate saturation level, and this generally leads to a reduction of the corrosion rate by slowing down the rate of the electrochemical mechanisms [3, 13, 128, 129].

The fluid pH can be increased in wet gas pipelines by adding pH stabilizers of alkaline chemicals such as sodium hydroxide (NaOH) or methyl di-ethanolamine (MDEA) to any corrosive medium in order to increase the solution pH and thus improve the protective corrosion layer properties [13].

Recently, Pojtanabuntoenga et al [130] investigated the effect of n-methyl di-ethanolamine pH on corrosion behaviour of carbon steel (X65) at 10°C.

Figure 2-17 shows corrosion rates obtained by linear polarisation measurements as a function of pH and MDEA concentration. The corrosion rate was the maximum value before using any pH adjustment, and the solution pH was 4.44. By adding MDEA the corrosion rate slightly decreased to 0.10 mm/y and the pH increased to 6. Their results also showed no dramatic difference in corrosion rate when pH increased from 6.5 up to 8.5. The authors proposed that the addition of MDEA amount increased the solution pH and reduced corrosion rate and the optimum pH range which gave a balance between corrosion rate reduction and the required MDEA concentration was 6.5–7.

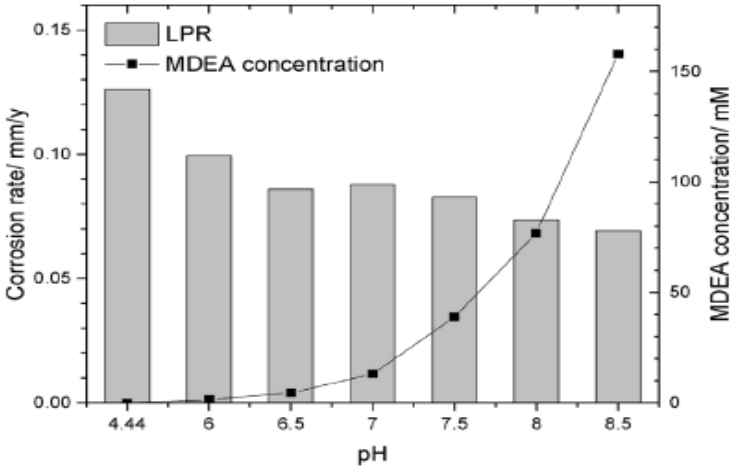

Figure 2-17.Corrosion rate obtained from linear polarisation measurements and the MDEA concentration at different pH [130].

2.5.4 Selection of Corrosion-Resistant Metals and Alloys.

in oil and gas industry, selection of more corrosion-resistant alloys (CRA) such as stainless steel, copper-base alloys and nickel-base alloys which are generally immune to well fluid with high CO_2, H_2S and high brine concentrations can control and mitigate TLC [11, 131]. The CRA sections can be specially designed to enhance cooling and promote water vapour condensation on these sections [132].

The CRA applications are nevertheless still limited to highly corrosive environments in petroleum industry due to their cost impact [133]. However, this solution is only economically feasible on short pipelines, and severe corrosion problems exist at the connection areas between CRA and carbon steel lines [124].

Also, in some practical situations, non-metallic materials can be used, however, this can damage the mechanical properties of facilities particularly under extreme conditions of temperature and pressure. The use of metallic materials is therefore recommended in such conditions [133].

2.5.5 Corrosion Monitoring and Management

Visual inspections and periodic check-ups for material degradation is the best way to check corrosion [134]. Though it may be possible to check the material condition externally, it is difficult to check the internal surfaces. One of the corrosion monitoring methods is to do on-stream inspection through periodic wall thickness measurements on fixed and vulnerable locations on equipment and pipelines to assess material conditions and corrosion rates. But, the limitation of this method is the checkpoint under investigation may show a level of corrosion lower than that at some other point, which may be heavily corroded and go undetected [134]. Another method to monitor the corrosion is by placing electronic probes in the pipelines and by measuring the change in the electric resistance in the probe[135].

Intelligent pigging operations such as magnetic flux or ultrasonic pigs are normally used to check pipelines networks. These operations will detect the internal conditions of the pipeline and corrosion conditions on the pipe wall thickness and will indicate the thickness available on the pipe wall[134].

2.6 Summary

The corrosion process occurs naturally and affects many petroleum applications such as oil and gas transportation, production systems and refineries, etc. Top of line corrosion is becoming more concerning and affecting the oil and gas industry. This is due to the conventional non-volatile organic corrosion inhibitors that have been effective at mitigating BLC could not protect the upper part of the pipeline because of the difficulty involved in transporting the inhibitor molecules to this position of the pipeline.

In this chapter, the current understanding of CO_2 corrosion mechanisms for carbon and low-alloy steels in hydrocarbon production has been described. The two main corrosion forms, namely uniform corrosion and localised corrosion, occur when CO_2 corrosion dominates in various oilfield environments.

In order to understand CO_2 corrosion, the electrochemical process of iron dissolution in CO_2 solutions has been reviewed. Key parameters which influence TLC in CO_2 environments, for instance, pH, temperature, partial pressure, gas flow, steel composition, and vapour condensation have been studied. The formation of iron carbonate scale process has been identified and the impact of various parameters on it has been described. It was identified that the conventional non-volatile corrosion inhibitors that have been effective to mitigate bottom of line corrosion could not be effective at the top of the line because of the difficulty involved in transporting the inhibitor molecules to the 10-2 o’clock positions of the pipeline.

Chapter 3. Literature Review II: Experimental and Theoretical TLC Studies

3.1 The history of TLC

The first case of TLC failure was reported by Estavoyer [136, 137] in 1960, at the Lacq sour gas field in France. Estavoyer reported that the TLC happens at low gas velocities with stratified or stratified-wavy flow regimes. The author confirmed that there is no corrosion at the top of lines when the flow was under an annular regime. After that, many incidences of TLC have been reported by different operators in several locations like Crossfield in Canada [138, 139], where the failure was in 6" internal diameter pipeline transporting wet gas containing 5.9% of CO_2 and 0.3% H_2S at a total pressure of 68 bars. Due to the condensation of water vapour at the upper part of the pipeline in the presence of acidic gases, in the absence of hydrocarbon condensate, the corrosion mechanism was identified as TLC.

Thereafter, in 1996, several cases of TLC in gas pipelines in the Tunu field which is situated in the delta of Mahakam River on Borneo were detected [140]. It was reported that factors such as extreme gas cooling due to a high-temperature gradient between the inside flowing gas and external temperature, high rates of water condensation due to high inlet gas temperatures, and lack of the effective thermal insulation due to pipe coating damage were responsible for corrosion failures at the top of the line.

TLC not only takes place in oil and gas pipelines. In 2003, Babaker and Barromove reported cases of TLC failure in wastewater treatment pipeline systems due to multiple pinhole leaks [141].

3.2 Experimental Studies of TLC

Since it was first identified in the 1960s, extensive experimental studies have been carried out to investigate the key parameters influencing TLC such as

temperature, the pressure of acid gases, total pressure, fluid velocity and the effect of acetic acid [35, 73, 81, 88, 122, 142, 143].

One of the earliest attempts to model the corrosion at the top of the line was made in 1991 by Olsen et al. [81]. They conducted an experiment work to investigate the parameters influencing TLC, the impact of the temperature on the product of corrosion is of first interest in their work. The authors confirmed that the relationship between the water condensation rate and the corrosion rate controlled by iron carbonate ($FeCO_3$) saturation level which in turn eventually can affect the corrosion rate. They found that a dense and protective $FeCO_3$ is formed at high temperature (>70°C) and low condensation rate. They stated that at high condensation rate, the saturation in $FeCO_3$ is difficult to obtain due to the rate of fresh water renewal.

The effect of the gas velocity on the corrosion rate also was studied by Olsen and his co-workers [81]. They observed that the higher the gas velocity, the higher the rate of corrosion. Also, they found that an increase in gas velocity would lead to an increase in water condensation rate as the heat transfer coefficient increases with gas speed. Accordingly, it can be concluded that the gas velocity affects the water condensation rate, which in turn influences the corrosion rate. Their study on the parameters influencing TLC provides an important database on TLC. However, they did not suggest any correlation to relate the corrosion rate with temperature, condensation rate, or gas velocity.

A first complete description of a sweet TLC case (CO_2 dominated) was made by Gunaltun et al. in 1999 [140]. They describe in detail a case of CO_2 TLC that happened in a wet gas pipeline in Indonesia. Throughout their inspection and visual observation, three different locations with different types of corrosion were identified along the flow pipeline:

- The bottom of the line, this part of the pipeline is subject to uniform corrosion and the rate of corrosion can be lowered by injecting inhibitors.
- The top of the line, several deep pits are found due to the water vapour condensation at the upper surface of the pipeline. This section of the pipe is covered by a protective $FeCO_3$ layer.
- The side of the pipe, also the corrosion is uniform but much higher than at the bottom. The authors explained that as the condensed water drains to the bottom of the pipe due to gravity, this would leave this area of the pipe without any protective iron carbonate layer or inhibitors.

In 2002, Vitse and his co-workers [30] made a major breakthrough in the understanding of the mechanism of TLC through an experimental and theoretical study to investigate the influences of gas temperature, CO_2 partial pressure, gas velocity, and water condensation rate. The experiments were conducted in a flow loop using a pipeline of 4″ internal diameter. They concluded that TLC increased by increasing the gas temperature up to 70°C, and decreased when the temperature of the gas exceeds 80°C. When the gas temperature is between 50°C and 90°C the condensation rate is lower than a critical value of 0.25ml/m^2.s, CO_2 partial pressure has a minor influence on TLC rate due to $FeCO_3$ precipitation. In their study, the authors assumed that a continuous film of liquid covers the steel surface at the upper surface of the pipeline (filmwise condensation). However, theoretical studies and experiments have revealed that filmwise condensation at the top of the line is not common. Rather, dropwise condensation is the predominant condensation mechanism at the top of the line between the 10 and 2 o'clock position. Filmwise condensation is possible along the sides and bottom of the pipe.

The presence of acetic acid in oil and gas systems can increase the corrosion rate in both top of line (TOL) and bottom of line (BOL) [122, 142, 144]. To study the mechanism of TLC in the presence of acetic acid and carbon dioxide, Singer in 2004 [73] used a flow loop of 4" internal diameter and high-pressure stainless steel, the schematic setup is shown in Figure 3-1. They successfully measured the corrosion rate of the carbon steel sample at 40°C gas temperature and found that the general corrosion rate remains constant at a low value throughout the test compared to the gas temperature of 70°C. The interesting thing about their results was that the corrosion rate at the BOL was 10 times higher than at the TOL. At the upper surface of the pipeline, a dense $FeCO_3$ protective film was found, whereas, at the bottom of the line there was no precipitation process detected.

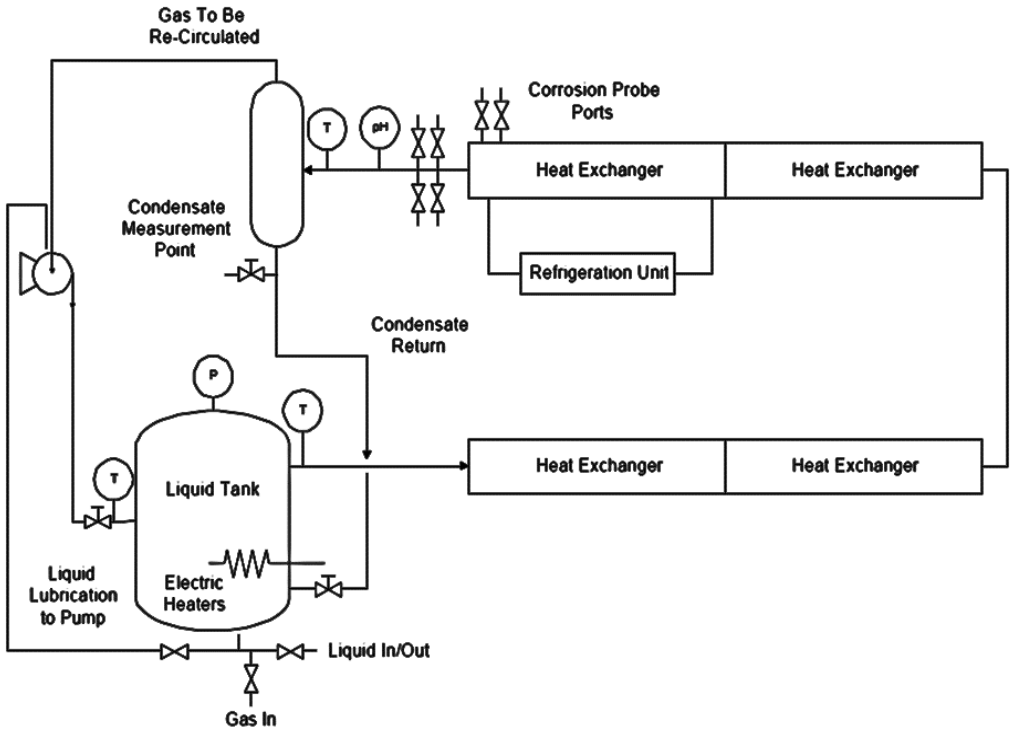

Figure 3-1. Schematic of the large-scale flow loop in Singer and his co-workers' study [28].

The problem of TLC in a sour environment occurs when the wet gas in the pipeline contains water and hydrogen sulphide H_2S. This problem is now a

growing concern for both onshore and offshore oilfields. In fact, the presence of H_2S gas in the oil and gas industry poses more problems than CO_2 because of its high toxicity. Also, H_2S leakage should be avoided because at a concentration of H_2S higher than 100 ppm it is very hazardous to health [145]. The sour corrosion mechanism is known to be different from that of sweet corrosion mechanism. In pure CO_2 corrosion environments the main formation scale is the iron carbonate ($FeCO_3$), however, many types of iron sulphide may form (FeS) in H_2S environments, such as amorphous ferrous sulphide (FeS), smythite ($Fe_{3+x}S_4$), greigite (Fe_3S_4), and pyrite (FeS_2). The presence of trace amounts of H_2S reduces the initial average corrosion rate compared to a pure CO_2 environment. Another difference is that despite the fact that solubility of H_2S gas in water is almost three times higher than CO_2 gas, the acid created by the dissociation of H_2S is about three times weaker than carbonic acid[146].

Many studies have been carried out to determine the influence of the presence of H_2S in TLC [147-150] . In 2007, the result of Singer et al.[151] showed that even presence of trace amounts of H_2S (0.004 bar) in the CO_2 environment sharply decreases the corrosion rate by two orders of magnitude. They found that when H_2S partial pressure is increased to 0.13 bar, the trend is reversed and the general corrosion rate increase by an order of magnitude. A FeS film, protective at low H_2S partial pressure covers the surface. They concluded that at higher H_2S content, the scale seems to break easily due to internal stresses and the steel is not evenly corroded.

Pugh et al. [149] in 2009, performed experiments to determine the influence of temperature, water condensation rate and organic acid on TLC. The experiments were conducted at a range of temperatures from 25°C to 55°C and at condensation rates of 0.002 ml/m^2.s and 0.1 ml/m^2/s and using an acid gas concentration of 1 % H_2S and 2.4 %CO_2, the test duration was 6 to 10 weeks. Their results showed that at a lower wet gas temperature of 25°C and lower water condensation rate of 0.002ml/m^2.s, the TLC was higher than

at higher temperature (55°C) and condensation rate (0.1ml/m^2.s). They found that in both cases, the iron sulphide (FeS) film was formed on the steel surface. However, the scale film had different characteristics, at low temperature, the film was very thin, porous and unprotective with a grain size of 500 nm, whereas, when the temperature was 55°C, the film was denser, had a grain size 10 microns and was protective. The authors proposed that, unlike sweet TLC, the temperature is the key parameter while the water condensation rate is of secondary importance.

In 2009, Camacho [148] conducted a series of long-term experiments (up to three weeks) in 4"ID flow loops (CO_2 dominated) to study TLC. This study investigated the effect of the most influential factors which determine the severity of the corrosion. This included evaluation of the condensation rate, the gas temperature, the gas velocity, the partial pressure of CO_2 and the presence of organic acid. The work by Camacho et al. highlighted that $FeCO_3$ precipitation can reduce corrosion rates. However, the development of such a layer is also intrinsically linked to the initiation and propagation of localised corrosion.

In 2010, Gunaltin and his co-workers [127] proposed a new glass cell design shown in Figure 3-2. The system is composed of a glass cell used to generate vapour and weight loss sample and Electrical resistance (ER) probe. The online corrosion measurement ER technique is more suitable for TLC experiments since it does not need a lot of water as an electrolyte. Though, ensuring complete coverage of the ER probe is fundamental for precise measurement of corrosion rate. Another limitation of this technique is that the condensed water accumulating on the surface of the corrosion sample could not be collected for any chemical analysis.

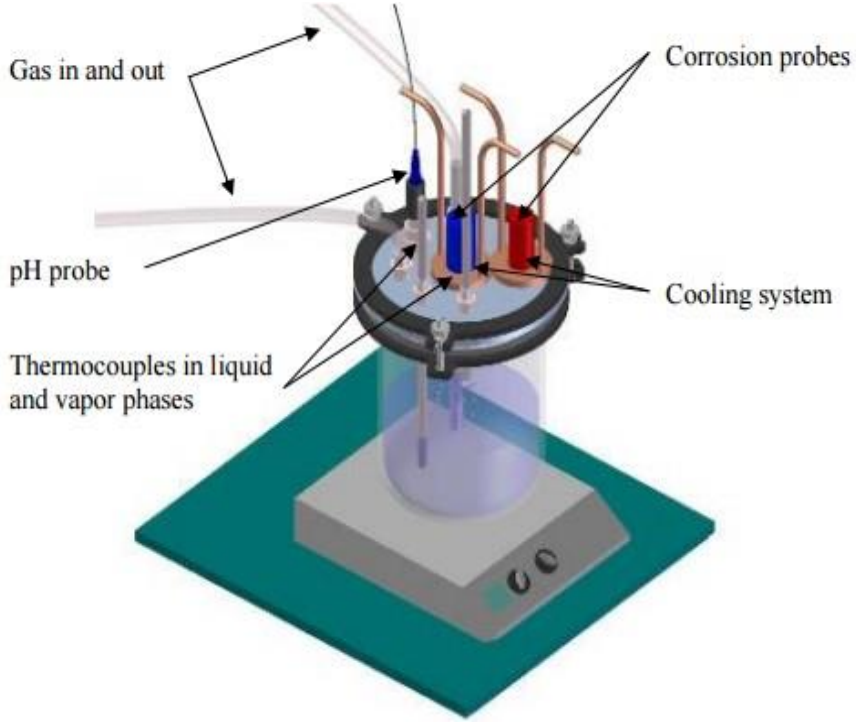

Figure 3-2. Experimental set-up of Gunaltin and his co-workers (2010) [127].

In oil and gas production, a proportion of the hydrocarbons will condense along with water and form two condensed immiscible liquids, each with different wettability on the surface and different levels of corrosivity. Wettability can be defined as the tendency for one immiscible fluid to spread on or adhere to a solid surface in the presence of another immiscible liquid [152]. Emulsion fluid (a mixture of oil and water) formation during oil and gas transportation can have either a positive or negative influence on the protective layer on the steel surface. If the water/hydrocarbon ratio in the pipeline is low, the water can be emulsified in the crude oil resulting in an oil-wet steel surface, a lower corrosion rate and vice versa. In 2011, Pojtanabuntoeng et al. [153] carried out experiments to clarify the role of the presence of hydrocarbons on TLC, Figure 3-3 shows their experimental setup. They confirmed that in the presence of hydrocarbons, the condensation rates of water had less effect on the rates of TLC. Also, they observed that the protective $FeCO_3$ film was formed only in the co-condensation (the condensation of the hydrocarbons and water vapour)

scenario, suggesting a change of the chemistry of condensed water when the hydrocarbons are present. The investigators stated that processes of condensation of two immiscible liquids are complicated due to the preferential wetting of each liquid on the steel, which is normally referred to as wettability.

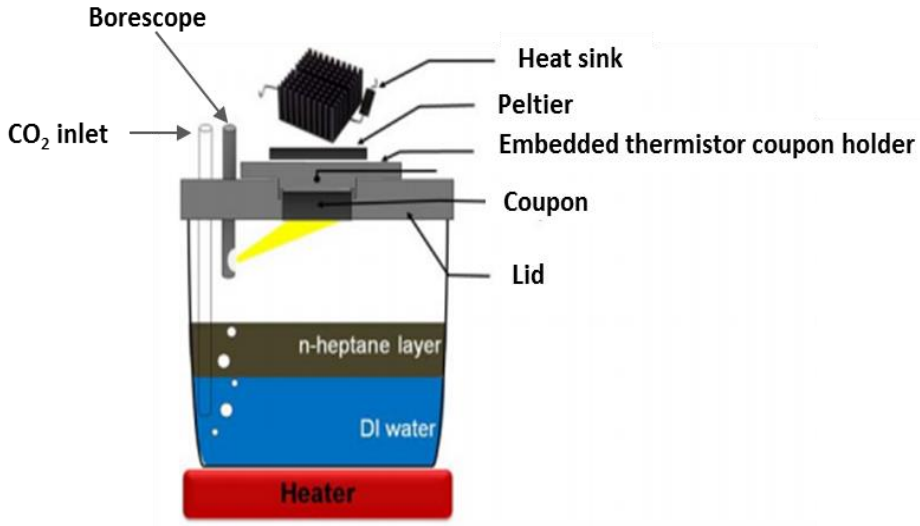

Figure 3-3. Schematic of the experimental setup used in the study of Pojtanabuntoeng et al.[154].

In 2012**,** Asher et al. [155] conducted experiments to study the influence of condensation rate, temperature, the partial pressure of acid gases, detailed water chemistry, and flow characteristics on TLC in a CO_2 environment. They study the effect of pipe surface temperature on TLC based on their TOL corrosion prediction model at a constant condensation rate of 0.1 ml/m^2.s. Their study reported that with increasing wall temperature from 25°C to 90°C a declining trend of TLC rate was observed.

Qin et al. [156] in their study of TLC at low pipe temperature showed that at a gas temperature of 45°C, the TLC values decreased slightly with an increasing pipe temperature from 5°C to 20°C. They explained that at low pipe temperature, slow electrochemical reactions take place, however, by increasing temperature to 40°C, corrosion rate reduced sharply due to low

water condensation rate associated with higher scale formation tendency, their results are summarised in Figure 3-4.

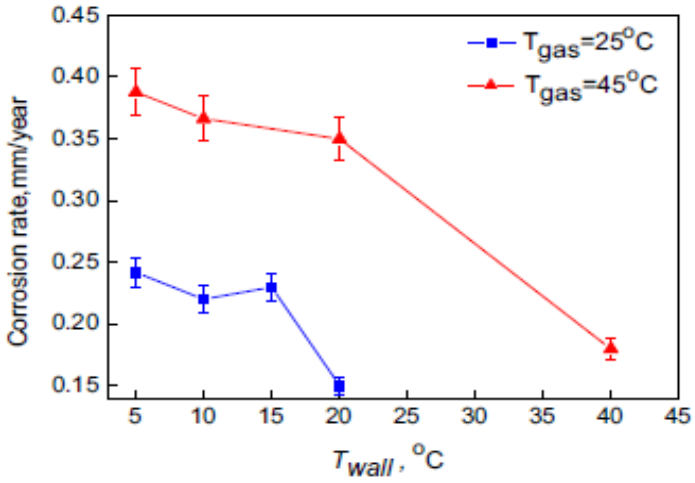

Figure 3-4. Effect of the pipe wall temperature on the corrosion rate of X70 steel at T_g=25°C, 45°C [156].

In 2013**,** Singer et al. [88] performed an experimental study in a large flow loop to study the effect of flow parameters such as CO_2 partial pressure water condensation rate, gas temperature, organic acid concentration, and gas velocity on the type of the TLC, which was either localised or uniform corrosion. The results showed that the $FeCO_3$ precipitation on the metal surface can decrease significantly the average corrosion rate. However, the protectiveness of the $FeCO_3$ layer is controlled by the water condensation rate and the overall corrosivity of the environment (CO_2 content, acetic acid concentration). Also, the study of Singer et al. [88] proposed that when the water condensation rate is low, there is high tendency to reach $FeCO_3$ supersaturation, which can lead to formation of iron carbonate scale in the stagnant condensed droplets encouraging the formation of dense protective layers. While higher water condensation rates also prevent the formation of a stable corrosion product layer, aggressive localized corrosion can be initiated and sustained.

More recently, in 2016, Islam et al. [157]] investigated the effect of pipeline surface temperature and droplet retention time on TLC, supersaturation of the condensed water with respect to iron carbonate and scaling tendency of carbon steel under condensation conditions. Their results showed that at very low surface temperatures (15°C) the TLC was mainly governed by the surface temperature regardless of the value of the water condensation rate. Also, they found at surface temperatures greater than 30°C, both the surface temperature and water condensation rate affect TLC. Figure 3-5 shows TLC obtained at different surface temperature conducted by Islam et al. [157]. According to their experimental data and water chemistry calculations, they reported that the kinetic behaviour of iron carbonate formation at TOL is different from that at the bottom of the line. They also proposed a new kinetic constant for the calculation of iron carbonate formation rate at the TOL. However, the authors did not present any correlation between the governing parameters and they did not mention whether localised or general corrosion form occurred in their work.

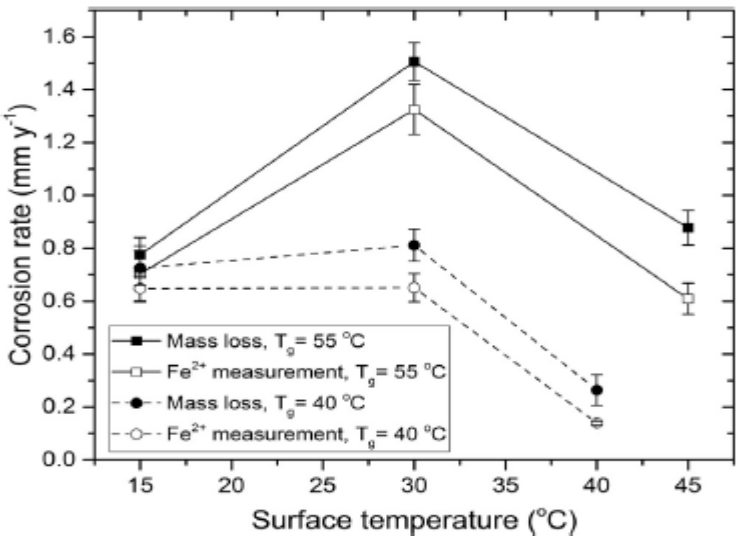

Figure 3-5. TLC obtained from mass loss and dissolved iron (Fe^{2+}) measurements at 55°C and 40°C gas temperature and different surface temperature [157].

3.3 Theoretical studies of TLC

To provide further insight into TLC phenomena, many predictive models of TLC have been proposed.

3.3.1 Corrosion Prediction Models

Corrosion rate prediction models have an important role to support critical decisions at several stages of any project, from materials selection and corrosion allowance to optimization of corrosion mitigation methods to installation of corrosion monitoring probes [158]. During the last two decades, the number of these prediction models has grown considerably. In 2010, Nyborg published a review paper in which he discussed the performance of the most commonly-used CO_2 corrosion predictive models for the oil and gas industry [159]. The corrosion prediction models can be divided into three main types of model:

- Empirical models.
- Semi-empirical models.
- Mechanistic models.

In fact, all these types of models predict the corrosion rate in e.g. mm/year, but the scientific frameworks behind the models are completely different.

3.3.1.1 Empirical Models

Empirical corrosion models are correlations of measured corrosion rate in the laboratory or field to a number of different operating parameters such as pressure, temperature, velocity, and solution pH. The drawbacks of this type of prediction models are that they limited to the conditions under which they were developed and extrapolation outside these conditions gives unreliable results. The empirical models always need to be updated and require recalibration when adding new data. Although the models have little or no

relation to the underpinning physics, these models have won acceptance in the oil and gas industry since they can be useful.

3.3.1.2 Semi-Empirical Models

These types of models also rely on experimental data, but the difference is that chemical and physical processes are represented, but some parameters are unidentified and must be fitted to measured corrosion rate data. Their simplicity and the little work required to evaluate the corrosion rate are the main benefits of these kinds of models. While the drawbacks of the semi-empirical models are the same as the empirical models. The fitted data do not give information on the mechanism of the system, however, the extrapolation can lead to unreasonable results and sometimes physically unrealistic results.

3.3.1.3 Mechanistic Models

Mechanistic models account for the chemical reactions, electrochemistry and physical mechanisms occurring at the metal surface.

In a mechanistic model for CO_2 corrosion the CO_2 gas dissolves and hydrates in the liquid phase producing a carbonic acid (H_2CO_3) which then dissociates to form bicarbonate (HCO_3^-) and carbonate (CO_3^{2-}). Carbonic acid diffuses to the pipe surface and precipitates in cathodic reactions at the surface and produces HCO_3^- and H_2 as mentioned earlier. The above reactions only continue if electrons are supplied by other reactions. The anodic process supplies the electrons by dissolution of iron. The chemical and electrochemical reactions that take place during CO_2 corrosion process are given in chapter II. Figure 3-6 illustrates the principles of the CO_2 corrosion mechanistic models.

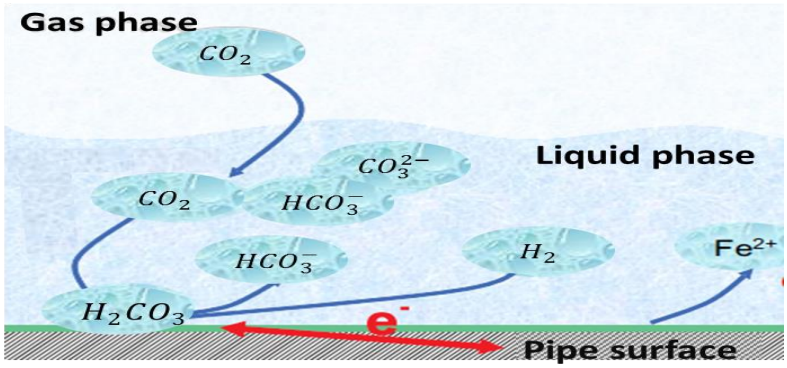

Figure 3-6. Principles of CO_2 corrosion mechanistic models [160].

The species produced from the above electrochemical processes transfer away from the pipe surface. Depending on the environmental conditions such as temperature and solution pH, iron carbonate ($FeCO_3$) precipitates on the pipe wall and may form a corrosion protective layer. This corrosion layer of $FeCO_3$ acts as a diffusion barrier leading to a lower reaction rate due to lack of the carbonic acid (H_2CO_3) which reduces the electron transfer process and the rate of iron dissolution [161]. Figure 3-7 shows how the CO_2 corrosion mechanism occurs in the presence of the $FeCO_3$. Due to the complexities involved, the development of a predictive corrosion rate model for TLC at conditions where $FeCO_3$ scale formation takes place is outside the scope of this thesis.

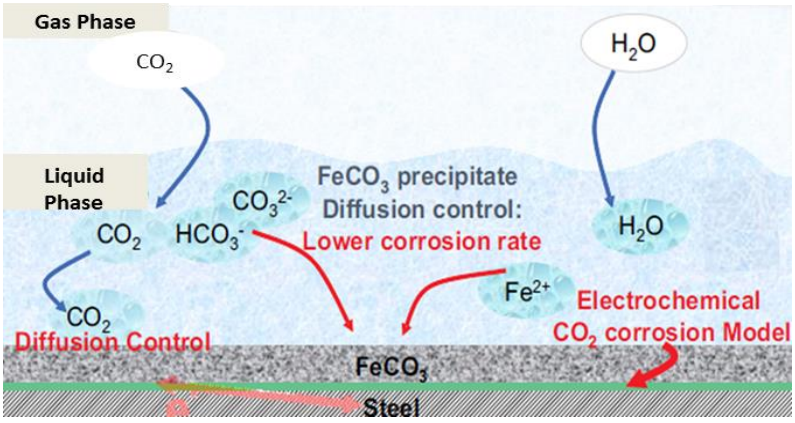

Figure 3-7. CO_2 corrosion mechanism in the presence of the $FeCO_3$ adapted from [160].

3.3.2 Top of Line Corrosion Models

Numerous mechanistic, empirical and semi-empirical models have been proposed in the literature to predict the TLC in CO_2 environments.

De Waard and Milliam's empirical model [162] is perhaps one of the most reliable and referenced models by corrosion engineers. According to their experimental results, in 1975, De Waard et al. introduce an empirical correlation allowing them to predict the CO_2 corrosion rate in natural gas pipelines.

Later in 1993, De Ward and Lotz [163] developed an empirical model to calculate the corrosion rate for a system operating under dewing conditions. The authors proposed correction factors to include the influence of environmental parameters such as condensation rate, CO_2 partial pressure, and temperature. To apply this to the case of TLC, they proposed a correction factor (F_{cond}) of 0.1 when the condensation rate less than 0.25 ml/m^2.s. The correlation suggested by De Ward and his co-workers is listed below:

$$\log(CR) = 5.8 * \log F_{cond} - \frac{1710}{273+T} + 0.67 * \log p_{CO2} \qquad 3.1$$

where:

p_{co2} is the partial pressure of CO_2, bar

T is the temperature, K

$F_{cond}$is the correction factor = 0.1

CR is the corrosion rate (mm/year).

It is worth noting that the De Ward's correlation depends exclusively on the gas temperature and the partial pressure of CO_2 and there is a serious lack of understanding of the mechanism behind the phenomenon of TLC.

Figure 3-8 shows the predicted TLC rates by De Waard model and experimental corrosion rates results. It is not surprising that the results are very inaccurate since the same constant correction factor (F_{cond} = 0.1) was used for all operating conditions.

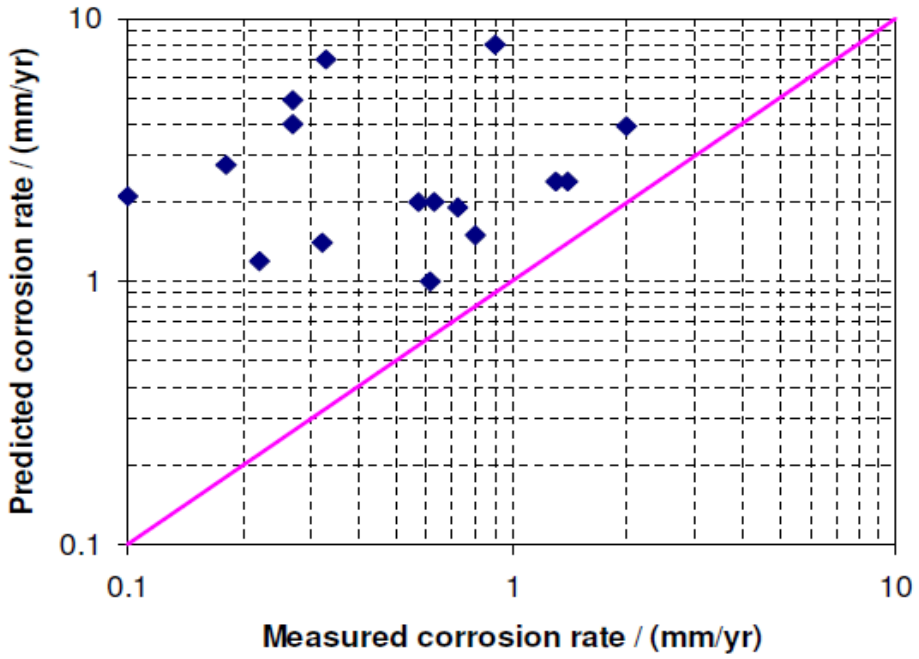

Figure 3-8. comparison between experimental TLC results and predictions by De Waard model [164].

One of the earliest attempts to model corrosion at the top of the line was made by Olsen et al. [81] in 1991. In their study, they confirmed that the relationship between the water condensation rate and the corrosion rate is controlled by the iron carbonate saturation level which in turn can affect the corrosion rate. They found that a dense and protective $FeCO_3$ film is formed at high temperature (>70°C) and low condensation rate. They stated that at high condensation rate, saturation in $FeCO_3$ is difficult to obtain due to the high rate of fresh water renewal.

In 1996, Van Hunnik et al. [74] observed that the CO_2 corrosion models often over-predict the corrosion rates in wet gas and oil transportation systems. The authors suggested that the reason for this is that the formation of corrosion product scales is not taken into account in the models. They developed an equation (Equation 3.3) which is specific to the situation where ($FeCO_3$) scaling governs the rate of the top of line corrosion. However, Equation 3.3 is no longer valid at very high condensation rates because under this condition, the fresh condensed water will dissolve the formed iron carbonate layer.

$$C_r = f_{cor} * V_{cond} * [Fe^{2+}]_{sat} \quad 3.3$$

where C_r is the corrosion rate in mm/y, f_{cor} is the correction factor to convert one mol of Fe^{2+} per litre into mm/y corrosion, V_{cond} is the condensation rate in L/s.m^2, $[Fe^{2+}]_{sat}$ is the ferrous ion concentration in the condensed water at $FeCO_3$ saturation, mol/L.

By taking into account the relation between the precipitation rate of iron carbonate and the condensation rate, in 2000, Pots and Hendriksen [122] published a paper focusing on TLC prediction**.** They proposed the so-called iron supersaturation model to describe the evolution of the corrosion rate as a function of the iron discharge via the condensation rate model. Their model uses the equation developed by Van Hunnik et al. [74] to calculate the precipitation rate. The corrosion rate CR is expressed as:

$$CR = \frac{M_{Fe}*10^6*24*3600*365}{\rho_{carbon\ steel}} * \frac{[Fe^{2+}]_{sat}*WCR}{\rho_{water}} \quad 3.4$$

where:

CR: Corrosion rate (mm/y)

WCR: Water condensation rate (ml/m^2.s)

ρ_{water}: Water density (g/m^3)

[Fe^{2+}]: Iron concentration (mol/l)

M_{Fe}: Iron molecular weight (55.847 g/mol)

$\rho_{carbon\ steel}$: Density of carbon steel (7.85 g/m^3).

Pots et al. [122] compared their model results with the experimental data obtained from Olsen and Dugstad [81], and also with the field data from Gunaltun [140]. Their calculated results were reasonably good agreement in both cases. The authors insisted on the importance of the role played by the condensation rate to predict the corrosion rate. However, it remains unclear as to how they calculated the heat transfer coefficient and then the water condensation rate.

In 2007, Nyborg and Dugstad [84] proposed through their experimental work an empirical equation to predict TLC. The model takes into account the water condensation rate, the iron carbonate solubility and a supersaturation factor. They stated that the iron solubility in the condensed water is a function of temperature and CO_2 partial pressure. Their model is limited only when the concentration of acetic acid is lower than 0.001 mol/litre and CO_2 partial pressure more than 3 bars and free of H_2S. The empirical model is listed below:

$$CR = 0.004 * R_{cond} * [Fe^{2+}] * (12.5 - 0.09 * T) \qquad 3.5$$

where CR is the TLC in mm/y, R_{cond} is the condensation rate in ml/m^2.s, $[Fe^{2+}]$ is the concentration of iron ions at $FeCO_3$ saturation (ppm$_{wt}$) and T is the temperature in °C. The authors confirmed the importance of accurately predicting WCR to calculate TLC, however, they did not provide details on how WCR was calculated.

In 2007, Zhang et al. [7] published the first fully mechanistic model for TLC. The three main processes were all accounted for: dropwise condensation, chemical reactions in the condensed water and corrosion at the steel surface.

The authors adapted the theory of dropwise condensation in the presence of non-condensable gases to a pipeline case where the droplets of condensed water are believed to condense between the 11-1 o'clock positions while the rest of the pipeline surface is covered by a condensed water film. To calculate the water condensation rate, Zhang added the heat and mass transfer equations as follows:

$$WCR = \rho_g \beta_g * \left(x_b^g - x_i^g\right) = \rho_g \beta_g * \frac{M_w}{P_T M_g} \left(P_{sat}\left(T_b^g\right) - P_{sat}(T_i^g\right) \quad 3.6$$

where WCR is the water condensation rate, ρ_g and β_g is the gas density and the gas mass transfer coefficient respectively, x_b^g and x_i^g is the mass fraction of water vapour in the bulk gas flow and at the gas-liquid interface respectively, M_w and M_g is the molecular weight of the water and the gas mixture, P_T is the total pressure and P_{sat} is the saturation pressure at a certain temperature. Also, Zhang simulated the droplet growth by calculating the maximum droplet size based on a force balance on a single droplet.

However, in their experimental and theoretical work the various factors that influence the CO_2-TLC such as, gas velocity, gas temperature, CO_2 partial pressure and acetic acid concentration are discussed. The effect of surface temperature is calculated implicitly when water condensation rate is calculated.

In 2008, Remita et al.[165] extended the work proposed by Vitse et al.[30] and developed a model of the physicochemical processes occurring during CO_2 corrosion of steel covered by a thin water film exposed to the atmosphere. They introduced a covering factor θ (coverage ratio of the steel surface by corrosion product scale) in order to take into account the effect of $FeCO_3$ film formation. The model follows a mechanistic approach for the chemical and electrochemical processes but assumed a homogeneous composition within the film.

To address the occurrence and prediction of localized corrosion in the upper part of the pipeline during wet gas transportation, Amri et al [166] in 2008 published the first study focusing on localized corrosion linked to TLC phenomena. Their result showed that the corrosion potential increases with increasing acetic acid (HAc) concentration and depletion of HAc inside the pit can increase the pit growth. They proposed a model of pit propagation and growth in the presence of HAc, however, more experimental validation was needed because the experimental work was not conducted in an apparatus designed to simulate a top of line corrosion environment.

3.4 Gaps in the Current Literature

Since the 1960's where the first TLC failure was reported in an oil and gas field, extensive related studies and experiments have been conducted.

The literature review revealed that the physical mechanisms controlling TLC are still unclear and there is a need to develop a better understanding of the mechanisms of TLC in CO_2 environments to provide more accurate predictions of the onset and severity of the corrosion attack. This would have direct implications for the gas and oil transportation.

Even though great efforts have been made over the past years in the understanding of the condensation process, none of the models proposed so far tackles the condensation prediction at stagnant conditions and low velocities.

Since most of the previous experiments lasted no more than 3 days, the corrosion rates were not stable and the results of localized corrosion were not conclusive in these studies. TLC should be studied for a longer time to understand the influence of the environmental parameters on CO_2 top of line corrosion in order to improve an understanding of the physical mechanisms.

Chapter 4. Experimental Study

4.1 Introduction

In order to model the top of line corrosion process that takes place during the oil and gas transportation, many experimental approaches have been made.

In 2000, Pots and Hendriksen [122] designed the apparatus shown in Figure 4-1 for top of line (TLC) experiments, comprising of a carbon steel tube mounted on a heat exchanger and placed inside an atmospheric box containing saturated water vapour and CO_2 gas. The water vapour condensed on the cooled steel tube at a rate controlled by the cooling water flow rate. In their setup, the condensed water was collected in a container underneath the sample, allowing the measurements of the condensation rate and the condensed water chemical analysis (pH solution and iron ion concentration).

Although the apparatus was designed to simulate TLC on a laboratory scale, its main limitation was that the total corrosion rate could be affected by corrosion that takes place at the outer diameter of the sample. Although this device was designed to analyse the condensed water, the composition of the condensed water may have been affected by re-evaporation inside the apparatus.

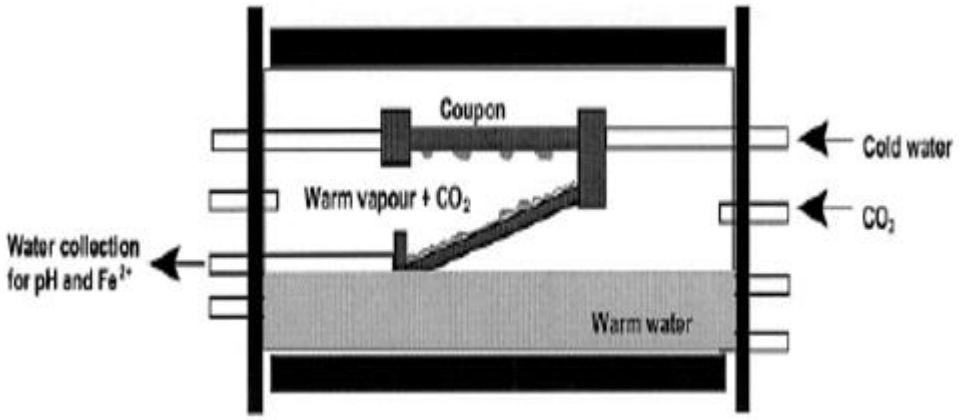

Figure 4-1. TLC experimental device in Pots and Hendriksen [122].

In 2009, Singer [88] conducted a series of long-term experiments (up to three weeks) in 4” internal diameter flow loops (CO_2 dominated) to study the TLC phenomenon. This study investigated the effect of the most influential factors on which the severity of the corrosion attack depends, such as the condensation rate, the gas temperature, the gas velocity, the partial pressure of CO_2 and the presence of organic acids without mention of the direct effect of surface temperature.

More recently in 2011, Rotimi et al.[167] conducted a series of long-term experiments (six weeks) in an autoclave especially designed for TLC study. In their work, the effect of water condensation rate and gas temperature were evaluated under different CO_2 partial pressures. They argued that the top of line corrosion decreased by more than a factor of two as the gas temperature increased from 25°C to 40°C, and an additional decrease in corrosion rate to half of its initial value was observed when the gas temperature was increased from 40°C to 55°C (highest temperature in their study) due to the formation of a more protective iron carbonate ($FeCO_3$) layer. However, no information was reported about the direct effect of the inner surface temperature on TLC.

Hence, for the top of line corrosion, the question is, what is the relationship/synergy between the condensation rate and surface temperature and which is dominant under which conditions? One of the main objectives of the work presented in this study is to find the actual relation between the different factors that determine and affect TLC.

The water condensation rate (WCR) and the surface temperature (Ts) control both the dissolution rate of the steel and dictate whether the condensate becomes saturated with $FeCO_3$, facilitating the precipitation of $FeCO_3$ onto the steel surface which is capable of suppressing the dissolution of the steel [81, 88]. Both $FeCO_3$ formation and steel dissolution thermodynamics are governed by surface temperature (T_s). Most models of TLC are based on the assumption that the gas temperature, T_g, is the main parameter controlling WCR and then either calculate T_s implicitly using heat and mass transfer

across the pipe wall or ignore its influence completely [30, 168]. A key challenge in understanding TLC is isolating the most influential parameters, understanding of which would lead to an improvement in prediction models.

In CO_2 environments, the top of line corrosion process can be affected by iron carbonate dissolution, which occurs in two steps; iron dissociation and iron carbonate formation which can be re-written in Equations 4.1 and 4.2 respectively.

$$Fe \rightarrow Fe^{2+} + 2e^{-} \quad 4.1$$

$$Fe^{2+} + CO_3^{2-} \rightarrow FeCO_3 \quad 4.2$$

Both these reactions occur adjacent to the inner steel surface, so the kinetics and thermodynamics of these reactions are governed by the temperature of the steel surface rather than the gas temperature [69, 70]. Therefore, it is important to study how both water condensation rate and surface temperature affect the TLC.

In this work, a new TLC rig design is presented, which is able to measure T_s, T_g and WCR, as well as enabling the corrosion rate of X65 steel coupons to be determined via gravimetric analysis. Additionally, the development of this setup holds many advantages as it involves very versatile and low-cost systems and the issue of re-evaporation has been tackled. Safety concerns related to high pressure and temperature setups are also avoided.

4.2 Methodology and Experimental Design

4.2.1 Experimental Setup

A set of three glass cells, each containing two carbon steel samples was used to conduct experiments at atmospheric pressure. A schematic diagram of one glass cell set-up is provided in Figure 4-2. The two X65 carbon steel coupons are flush mounted into the lid of each glass cell. To achieve condensation conditions, copper cooling coils were placed around each

sample and water circulated therein in order to cool the sample holder to the desired level. To achieve the desired gas temperature, a hot plate was used to heat the bottom solution. The bulk aqueous fluid comprised of a CO_2-saturated distilled water which was purged with CO_2 for 24 hours prior to separate vessels prior to commencing experiments to reduce the dissolved oxygen content. The solution was then transferred to the test cell prior to the start of each test. Condensed water was collected in a collection cup immediately below one sample and diverted into a sealed collection vessel saturated with CO_2, which was maintained at the same temperature as the sample surface (T_s) to determine the condensation rate and the pH of the condensed water. The pH of the collected condensed water was measured periodically prior to removal of the solution for condensation rate analysis. For each test condition, pH and WCR measurements were performed twice a day over a total test period of 168 hours.

Due to the challenges associated with performing electrochemical measurements in TLC conditions such as the low conductivity of the condensed water and the discontinuity of the water phase specially under a low condensation rate [169], the mass loss technique was implemented in this instance to measure corrosion rates. This imposes a limitation in that the mass loss technique adopts an integral approach, meaning that unlike electrochemical tests, real-time corrosion rates are not provided. However, to address the issue of not recording the real-time transient response of corrosion rate in these tests, samples were left in the test system for different durations of time (24, 48, 72, 96, 120, 144 and 168 h) to understand the corrosion rate behaviour with time.

To ensure reliability and the accuracy of the results, the experiments were repeated a minimum of three times with error bars on each graph illustrating the maximum and minimum values obtained under each test condition.

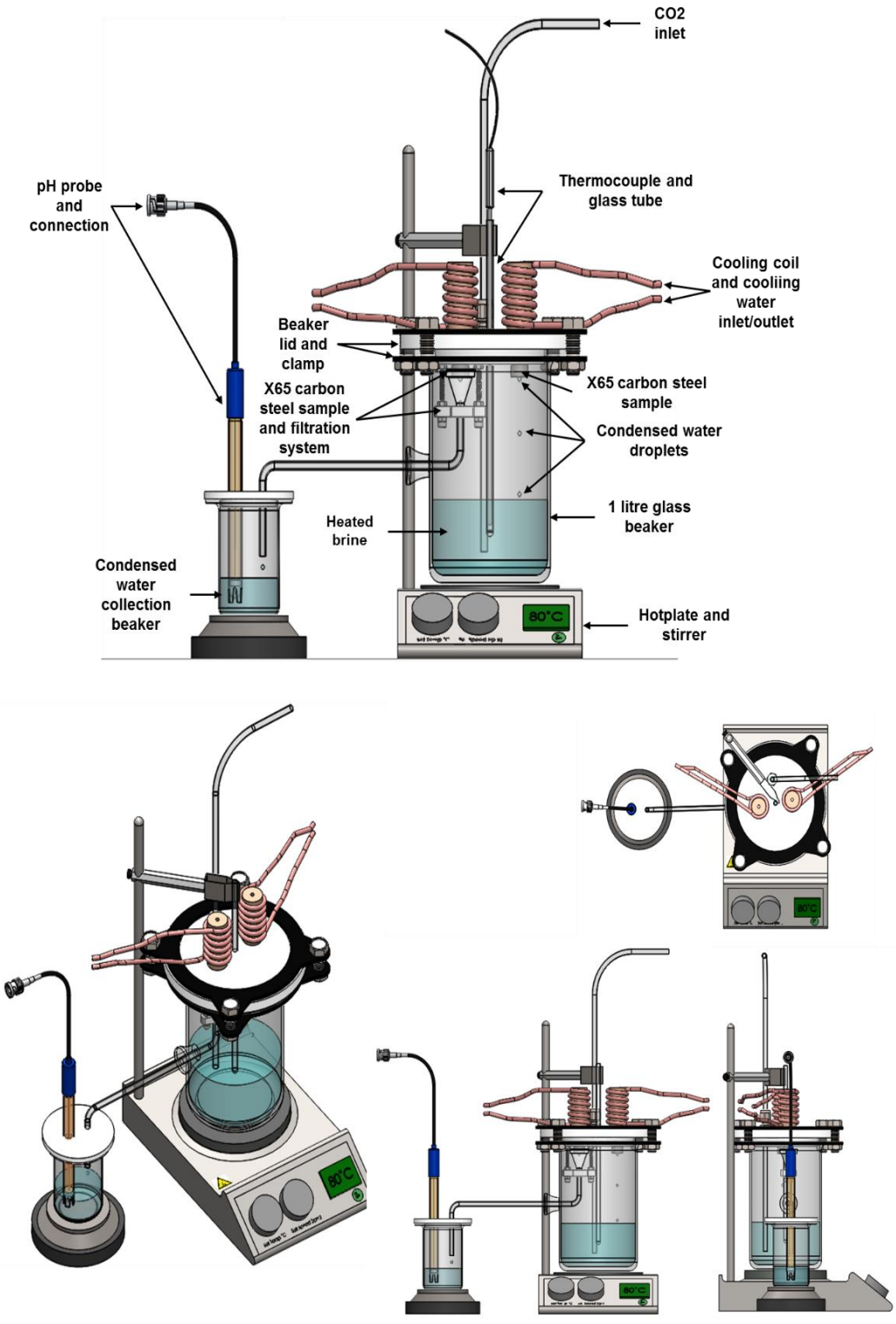

Figure 4-2. Schematic of the glass cell experimental set up used in experiments.

4.2.1 Materials

The material evaluated in this study is X65 carbon steel with the chemical composition shown in Table 4-1. This material comprised of a ferrite-pearlite microstructure, ferrite is the light phase and pearlite is the dark phase, as shown in Figure 4-4.

This alloy is selected due to its common usage within oil and gas transmission pipelines. The samples themselves consisted of cylindrical coupons (2.2 cm diameter and 1.2 cm thickness), with an area of 3.8 cm^2 exposed to the test solution per sample as shown in Figure 4-3. A hole of 2 mm diameter was drilled through the center of the sample holder to within 1 mm of the surface exposed to the test solution for a temperature probe to be inserted to measure T_s. A drop of oil was placed into the bottom of the hole to provide consistent surface temperature readings. To avoid any galvanic effect resulting in from the direct contact the samples and the sample holder, the specimens were coated on the sides and top with a Teflon paint leaving one surface exposed to the test environment.

Table 4-1. X65 Carbon steel composition (wt %) [170].

C	Si	Mn	P	S	Cr	Mo	Ni
0.12	0.18	1.27	0.008	0.002	0.11	0.17	0.07
Cu	**Sn**	**Al**	**B**	**Nb**	**Ti**	**V**	**Fe**
0.12	0.008	0.022	0.005	0.054	0.001	0.057	Bal

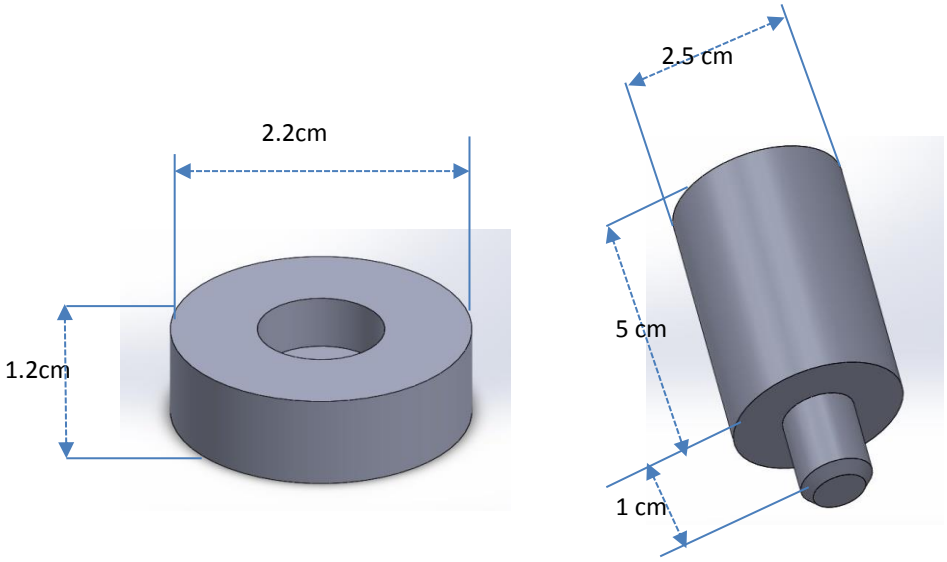

Figure 4-3. X65 sample coupon and a sample holder for TLC experiments.

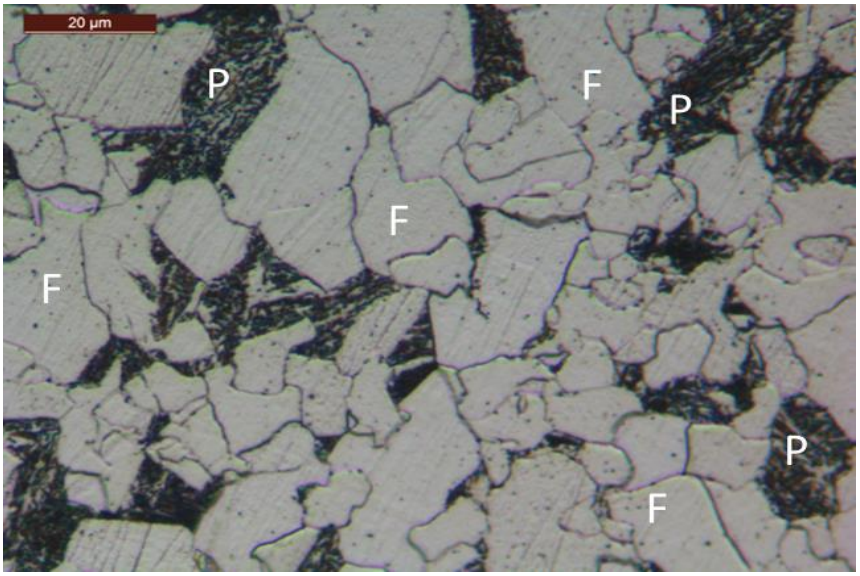

Figure 4-4. Microstructure of X65 steel polished and etched in 2% nital solution for 10 seconds indicating ferrite (lighter) and pearlite (darker) microstructure [39].

4.3 Experimental and Analytical Procedures

4.3.1 Test procedure for Determining Condensation and Corrosion Rates

Before starting each experiment, the exposed surface of the weight loss coupons (X65 carbon steel) was wet-ground using silicon carbide (SiC) abrasive papers of up to 1200 grit, cleaned with distilled water and ethanol and dried with compressed air. Each sample was then carefully coated on its top and outer edges. Following curing of the protective coating, the prepared samples were wet-ground again, weighed (mass m_1) by using a digital scale with a resolution of 0.1 mg before being mounted into the vessel lid using a specially designed holder containing the copper coil. The bottom solution used to generate water vapour consisted only of distilled water deoxygenated with CO_2. CO_2 gas was also continuously bubbled into the bulk solution during the experiments to maintain saturation. The cooling chamber was used to provide and maintain the desired inner surface temperature. This was achieved by adjusting both the cold water temperature and cooling water flow rate through the copper coils around each sample. A schematic illustration of the overall set up for the top of line corrosion testing is shown in Figure 4-5.

The condensed water drops which fell into the collector fitted directly under the sample were transferred immediately to the condensate collector for pH and WCR measurement. The water condensation rate was calculated by using the following equation

$$WCR = \frac{V_w \rho_w}{S_t t_c} \tag{4.3}$$

where WCR is the condensation rate (g/m^2.s), V_w the volume of condensed water (ml), ρ_w is the density of water (g/cm^3), t_c is the duration time (s), and S_t is the surface area of the sample (m^2).

The inner surface temperature of the sample was measured continuously through the experiment by placing a thermocouple on the outside of the steel sample through the hole in the sample holder.

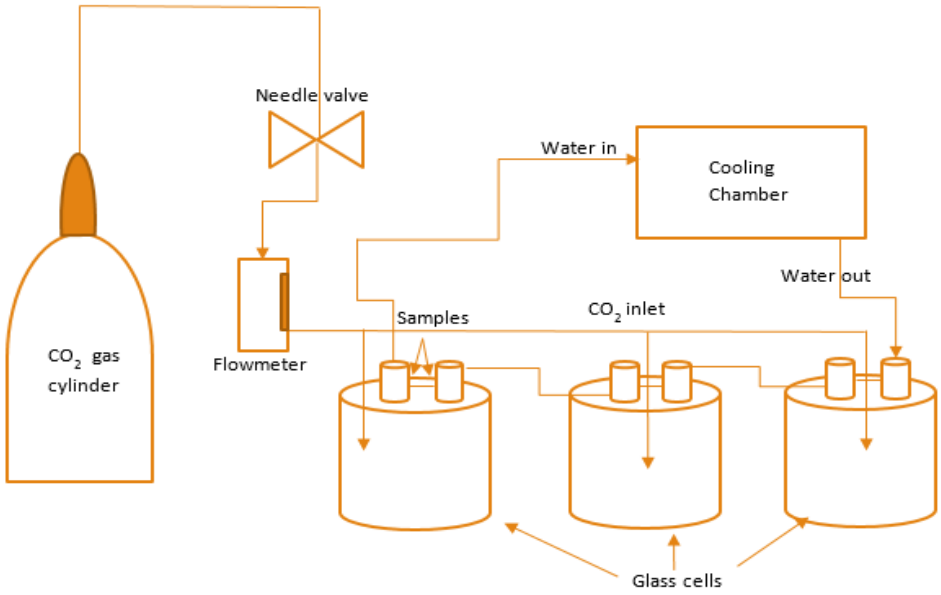

Figure 4-5. Schematic illustration of the overall set up for the top of line corrosion set up.

After each experiment was completed, the samples were removed from the system, rinsed with distilled water and acetone and dried using compressed air. Samples were then reweighed (mass m_2) before the corrosion product was removed using Clarke's solution (chemical composition as shown in Table 4-2 [171]. Samples were then weighed a final time to determine the mass in the absence of corrosion products (mass m_3) if any existed on the steel surface.

The average corrosion rate of the steel sample over the duration of the experiment was calculated using the following expression:

$$CR = \frac{\Delta WL}{\rho_{FE} * A * t} * 10 * 365 * 24 \qquad 4.4$$

where CR is the corrosion rate from weight loss, in mm/y; ΔWL is the difference in weight of carbon steel sample before the test (m_1) and after

removing of any attached corrosion products with Clarke solution (m_3), in grams; ρ_{Fe} is the density of carbon steel sample, in g/cm^3 (7.85 g/cm^3); t is the duration test time, in hours; A is the surface area of carbon steel sample, in cm^2.

Table 4-2. Composition of Clarke's solution [171].

Component	Amount
Hydrochloric acid (HCl, sp gr 1.19)	1000ml
Antimony trioxide (Sb_2O_3)	20 grams
Stannous chloride ($SnCl_2$)	50 grams

4.3.2 Determination of Corrosion Product Precipitation Rates

Although similar chemical reactions take place in the CO_2 environment at the top of the line (TOL) and bottom of the line (BOL) there is a significant difference in dissolution behaviour and the precipitation kinetics of corrosion products and the overall mechanism. Although the fresh condensate can have a relatively low pH (because it is pure water saturated with CO_2) the corrosion process causes the Fe^{2+} concentration in the condensate to rise quickly, resulting in an increase in pH. A combination of the corrosion rate, condensation rate, and the droplet size dictates whether iron carbonate ($FeCO_3$) saturation is met, and if so, at what rate. The formation of a protective $FeCO_3$ film was suggested to play a key role by Olsen and Dugstad [81]:

$$Fe^{2+}_{(aq)} + CO^{2-}_{3\,(aq)} \rightarrow FeCO_3 \qquad 4.5$$

The precipitation of $FeCO_3$ is influenced by the saturation ratio (S_{FeCO_3}), which is defined as:

$$S_{FeCO_3} = \frac{[Fe^{2+}][CO_3^{2-}]}{K_{sp}} \quad 4.6$$

where K_{sp} is the solubility product of $FeCO_3$ and $[Fe^{2+}]$ and $[CO_3^{2-}]$ are the iron and carbonate concentrations in the droplet, respectively.

High levels of saturation could lead to the formation of dense and protective films. There is, therefore, competition between $FeCO_3$ formation kinetics and the WCR. At a high WCR, the $FeCO_3$ formation is more difficult to obtain.

This study considers the boundaries between protective film-formation and non-film formation experiments. Further work was conducted to understand and investigate the precipitation process in more detail in conditions where film formation was recorded, both experimental corrosion scale formation rate ($PRexp$) and theoretical corrosion layer accumulation rate ($PRtheo$) where calculated. ($PRexp$) was determined experimentally using the following equation:

$$PRexp = \frac{(m_2 - m_3)}{1000 * MW_{FeCO3} * A * t} \quad 4.7$$

where $PRexp$ is the experimental precipitation rate (kmol/m^2.s), m_2 is the combined mass of corrosion product layer and steel sample (g) immediately after the experiment, m_3 is the mass of the steel sample after the removal of corrosion products using Clarke's solution (g), MW_{FeCO3} is the molecular weight of $FeCO_3$ equal to 115.8 g/mol, A is the surface area of the sample (m^2) and t is the experimental duration time (s). In some instances, the corrosion product was not removed from samples as they were evaluated using scanning electron microscopy (SEM) and x-ray diffraction (XRD).

While $PRtheo$ is calculated by using the empirical expression proposed by Nesic et al. [52].

$$PRtheo = K_r K_{sp}(SS - 1) \quad 4.8$$

where $PRtheo$ is the precipitation rate kmol/m^2 .s; K_r is the kinetic constant in m^4/kmol.s; K_{sp} is the solubility product constant of iron carbonate in (kmol/m^3)^2 and it's a function of temperature and ionic strength; SS is the supersaturation ratio of iron carbonate.

The kinetic constant K_r can be calculated by using the Equation 4.9 [52]:

$$K_r = e^{A-\frac{B}{RT_k}} \quad 4.9$$

Where A=28.2 and B=64851in J/mol; *R* is the gas constant=8.314 J/mol.K and T_k is the surface temperature in Kelvin where the reaction takes place.

The solubility product constant of $FeCO_3$ can be found by using the equation presented by Sun et.al.[172] :

$$log_{10}K_{sp} = -59.3498 - 0.041337T_k - \frac{2.1963}{T_k} + 24.5724log_{10}T_k \quad 4.10$$

The supersaturation ratio SS was calculated by using Equation 4.11 [173]:

$$SS = \frac{[Fe^{2+}][CO_3^{2-}]}{K_{sp}} \quad 4.11$$

where $[Fe^{2+}]$is the iron ion concentration in the condensed water in kmol/m^3 and can be calculated by using the following relation:

$$[Fe^{2+}]_{bulk} = \frac{[Fe^{2+}]_{corr} - [Fe^{2+}]_{prod.layer}}{Vol.of\ cond.} \quad 4.12$$

where $[Fe^{2+}]_{corr}$ is the ferrous concentration resulting from corrosion process and can be calculated by using equation 4.13.

$$[Fe^{2+}]_{corr} = \frac{CR*A*\rho_{Fe*}*t}{10*MW_{Fe}} \quad 4.13$$

where *CR* is the corrosion rate in mm/y, A is the exposure surface area of the sample in cm^2, ρ_{Fe*} is the iron density = 7.85g/cm^3, t is the time of

exposure in years, MW_{Fe} is the molecular weight of iron in g/mol, the $[Fe^{2+}]_{prod.layer}$ is the concentration of iron ions in the corrosion product layer in kmol/m^3 while $Vol.of\ cond.$ represent the volume of the condensed water accumulated on the test sample in m^3.

The carbonate ion concentration $[CO_3^{2-}]$ can be calculated by using the equilibrium bulk concentration for CO $_2$ saturated solution.

Firstly, from Henry's Law, the amount of CO_2 dissolved in water under atmospheric pressure can be found.

$$K_{sol} = \frac{[CO_2]}{[pCO_2]} \qquad 4.14$$

where is $[CO_2]$ concentration of dissolved CO_2 in moles/litre, P_{CO_2} is the partial pressure of CO_2 in bar and can be found by using Antoine equation[174]:

$$P = A - \frac{B}{C+T} \qquad 4.15$$

where P is the vapour pressure in bar, T is temperature in °C and *A*, *B* and *C* are component-specific constants, A=8.07131, B=1730.63 and C=233.426.

K_{sol} is solubility constant of the CO_2 gas moles/(litre. bar). The empirical expression suggested by Oddo and Tomson[175] can be used to find K_{sol}.

$$K_{sol} = \frac{14.5}{1.00258}\ 10^{-\left(2.27+0.00565T_f-8.06\times10^{-6}T_f^2+0.075I\right)} \qquad 4.16$$

T_f is the inside sample temperature in degrees Fahrenheit and I is the ionic strength in mole/litre. CO_2 dissolved and hydrated in water to give carbonic acid H_2CO_3 and the equilibrium constant for the reaction can be written as:

$$K_{hy} = \frac{[H_2CO_3]}{[CO_2]} \qquad 4.17$$

where K_{hy} is the equilibrium hydration constant and it does not change significantly within the temperature range of 20 °C -100°C, it is equal to 2.58 × 10^{-3} according to Eldik and Palmer's work [176]. $[H_2CO_3]$ is the initial concentration of H_2CO_3 in moles /litre. Carbonic acid dissociates into bicarbonate ions (HCO_3^-) and hydronium (H^+). The equilibrium constant for this reaction is known as the carbonic acid dissociation constant denoted by Kca , as Equation (4.18) shows [43, 175, 177].

$$K_{ca} = \frac{[H^+][HCO_3^-]}{[H_2CO_3]} \quad 4.18$$

The dissociation constant K_{ca} is estimated as follows:

$$K_{ca} = 387.6\text{x}10^{-(6.41-1.594*10^{-3}*\text{Tf}+8.52*10^{-6}*\text{T}f^2*-3.07*10^{-5}*\text{p}-0.4772*\text{I}^{0.5}-0.118*\text{I})} \quad 4.19$$

where *P* is total pressure in psi. The hydronium concentration $[H^+]$ is determined from solution pH using the equation 4.20

$$pH = -\log[aH^+] \quad 4.20$$

where aH^+ = γ.$[H^+]$, with γ assumed to be =1

Hence, the bicarbonate ion concentration can be calculated.

From the bicarbonate ion step dissociation, the concentration of carbonate can be calculated. Bicarbonate ion dissociates into carbonate (CO_3^{2-}) and hydronium (H^+) and the equilibrium reaction of this reaction can be stated as:

$$K_{bi} = \frac{[H^+][CO_3^{2-}]}{[HCO_3^-]} \quad 4.21$$

K_{bi} is known as the bicarbonate dissociation constant and can be determined using the Equation 4.22 [44].

$$K_{bi} = 10^{-(10.61-4.97*10^{-3}*T_f+1.33*10^{-5}T_f^2-2.624*10^{-5}p-1.166I^{0.5}+0.3466I)} \quad 4.22$$

As $[CO_3^{2-}]$, $[Fe^{2+}]$ and K_{sp} are calculated the supersaturation of the water condensate and theoretical corrosion layer accumulation rate $PRtheo$ can be determined according to the equations (4.11) and (4.8) respectively.

The iron carbonate scaling tendency (ST) which represents the protectiveness of the corrosion product layer is determined experimentally and theoretically by using equations 4.23 and 4.24 respectively [178].

$$ST_{exp.} = \frac{PRexp}{CR} \quad 4.23$$

$$ST_{theo.} = \frac{PRtheo}{CR} \quad 4.24$$

where $ST_{exp.}$ and $ST_{theo.}$ are the experimental and theoretical scaling tendency respectively.

4.4 Test Matrix

The test matrix for the experiments is shown in Table 4-3. Tests were from 24 to 168 hours duration with a total pressure of 1 bar and gas temperature ranged from 30°C to 60°C and surface temperature between 5°C and 50°C.

Table 4-3.Test matrix for the effect of temperature/water condensation rate on top of line corrosion rate.

Test material	**X-65 carbon steel**
Total pressure (bar)	1
Gas temperature (°C)	30-60
Inner steel temperature (°C)	5-50
Condensation rate (mL/m^2/s)	0.115-1.712
Test duration	168 hours
pH	5.06 - 5.93
TLC mm/y	0.224 - 1.520
Bottom solution	Distilled water
O_2 concentration	≈10 ppb

4.5 Experimental Post Processing

At each set of experimental conditions, half of the total samples were generally used for weight loss measurements, the others were preserved for further corrosion product evaluations. Before the corrosion production layers were removed, the steel samples were analysed by SEM (Scanning Electronic Microscope), EDX (Energy Dispersive X-ray Spectroscopy and XRD (X-ray diffraction). These techniques are extremely useful for studying and characterising the morphology of surface corrosion films or cross-section corrosion films. SEM analysis was used to study the corrosion product morphology while EDX and XRD were used for chemical analysis and identification of the crystal structure presented on the surface of the specimens.

4.5.1 Scanning Electron Microscopy (SEM) and Energy Dispersive X-ray Analysis (EDX)

SEM is a technique used for examining and imaging the surface of materials at a higher magnification and resolution compared to the optical microscope, images magnification ranging from 10 to 10,000x [179]. Energy Dispersive X-Ray analyses (EDX) was conducted, in order to determine which type of scale deposit is dominant on the surface of the sample. In this study, the topography of the corrosion product was observed with a Scanning Electron Microscope (SEM) 15 VP SEM Carl Zeiss EVO MA15 SEM. Figure 4-6 shows the SEM and EDX machine which used in this study. Energy Dispersive X-Ray analyses (EDX) were used to analyse the elemental components of the corrosion products and allow the characterisation of the distribution of individual elements of the corrosion products on the surface. This apparatus can give the elemental composition of any point of the sample. Figure 4-7 shows an example of EDX results where the peaks show the elements of corrosion product.

Figure 4-6. Carl Zeiss EVO MA15 Scanning electron microscopy and energy dispersive X-ray analysis setup

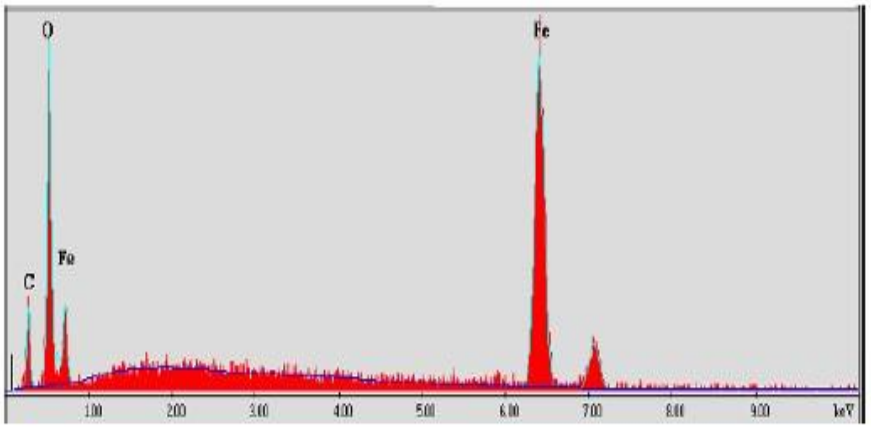

Figure 4-7. Example of EDX analysis [180]

4.5.2 X-Ray Diffraction Analysis

To determine if the scale formed on the surface of the metal sample was an iron carbonate or not, X-Ray Diffraction analysis has been used. Based on the intensity of the diffracting ray and its diffracting angles, X-ray diffraction (XRD) is able to identify the crystalline structure of materials. As indicated in the literature [28, 95, 181], the main peaks of intensity and diffracting angle which showing the iron carbonate formation are found at 25,32,42,46,51 and

53° Two-theta angle as shown in Figure 4-8. Moreover, a specific iron peak is presented at an angle of 45° 2-theta.

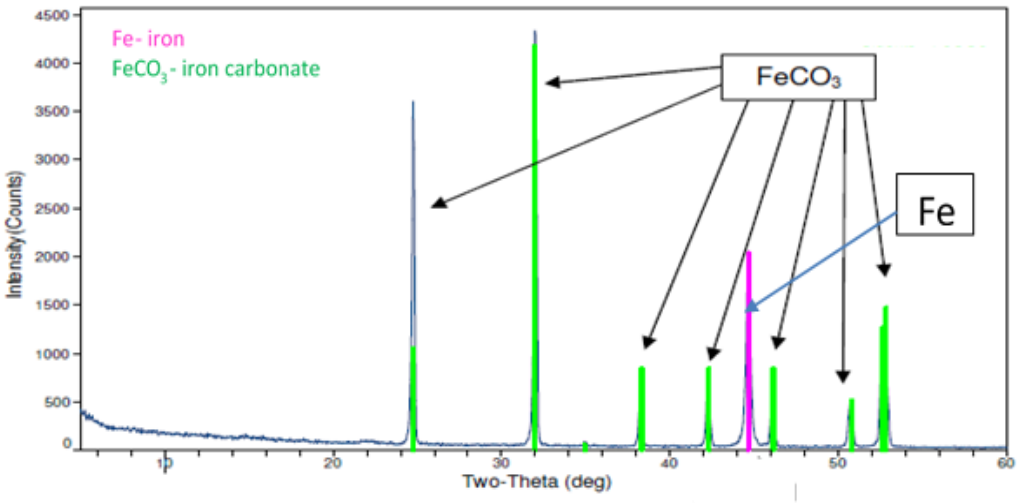

Figure 4-8. Typical X-ray Diffraction (XRD) spectrum obtained for the corrosion scale [181]

4.5.3 Surface Interferometry Analysis

The main aim of using interferometry analysis is to determine the type of corrosion occurring on the surface of the sample. Before the analysis, and to ensure that the all traces of corrosion products were removed from the surface, the samples were cleaned thoroughly by using Clarkes' cleaning solution [182]. In this study, a non-contact NPFLEX 3D Surface Metrology System profiling system was used. An image of the 3D NPFLEX apparatus in use is shown in Figure 4-9. For each sample, four chosen regions were selected (scanning a 3 mm x 3 mm area at a time). The objective used 2.5X with an approximately 3.5mm working distance.

NPFLEX 3D rapidly and accurately measures and provides three types of information on surface characterisation for pitting corrosion damages:

- The maximum and average pit depths, pit diameter, pit volume.

- The quantification of the number of deep pits.
- A 3D image of the attacked sample (for an easier viewing of the surface aspect).

The interferometer simply acts as an optical device that divides a beam of light by the beam splitter into two beams and then recombines them in order to extract information about the original state of the source waves and to create an interference pattern.

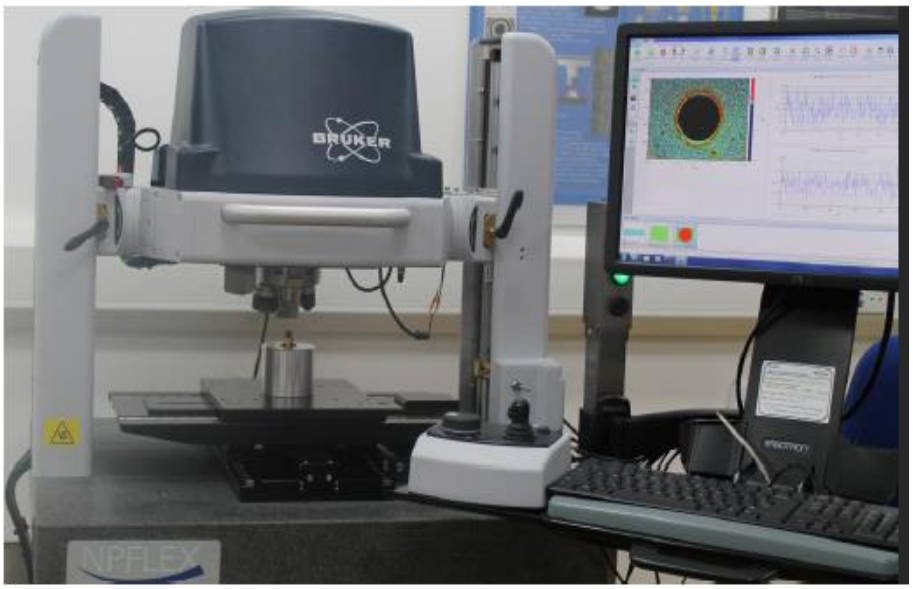

Figure 4-9. The NPFLEX 3D Surface Metrology Setup.

4.6 Summary

This chapter describes all the experimental methodologies and set up used in this thesis. The glass cell set up and experimental techniques and methods of analysis described in this chapter make it possible to conduct a comprehensive investigation into the top of line corrosion of carbon steel X65 material along the period of time lasted seven days.

To get a good understanding of the relation between iron dissolution resulting from the corrosion process and the corrosion product layer which formed on the top of the steel surface, a mass balance was done by comparing the: total mass of iron ions loss from the corrosion process, mass of iron ions in

the corrosion product layer, and mass of iron ions in condensed water. The different surface analysis of the tested samples makes it possible to observe and characterise what is taking place on the surface of a metal and provides an understanding of the mechanism of top of line corrosion. Figure 4-10 demonstrates the map of the overall procedure of experimental work outlined in this project.

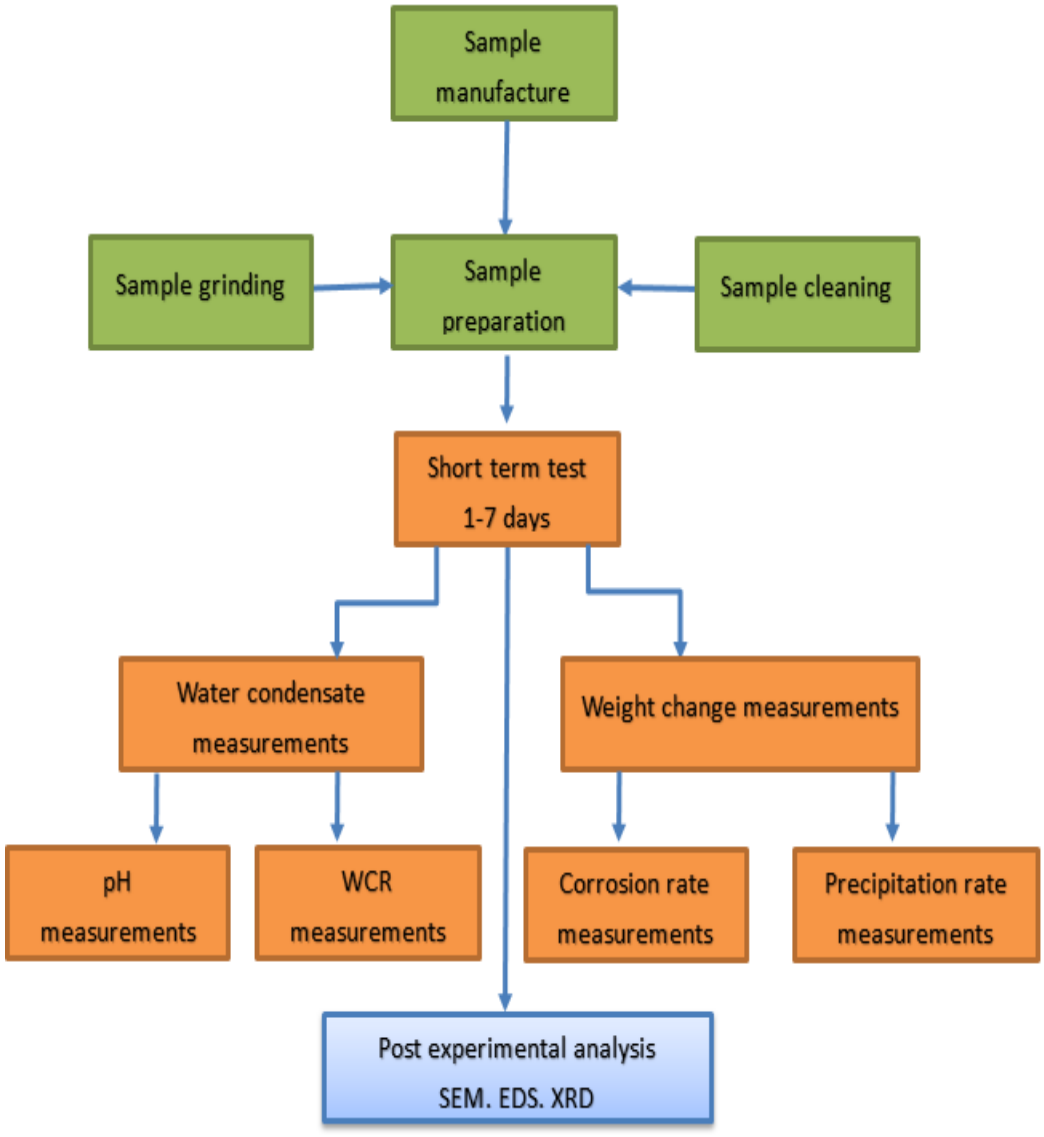

Figure 4-10. Map of experimental work outlined in this study.

Chapter 5. Experimental Results and Analysis

Since the first case of TLC was recorded in the 1960's at the sour Lacq field in France [183], several theoretical and experimental studies have been conducted to predict and understand the TLC [7, 66, 67, 74, 81, 88, 122, 167, 184]. Most of these investigations express TLC as a function of gas temperature (T_g) and condensation rate (WCR) with the surface temperature (T_s) being taken into account implicitly through heat and mass transfer across the pipe wall when WCR is calculated.

The three parameters of WCR, T_g and T_s are regarded as the most influential and interrelated factors. These factors control both the dissolution rate of the steel and dictate whether the condensate becomes saturated with iron carbonate (a protective corrosion product). The implication of saturation in the condensate is that it facilitates the precipitation of $FeCO_3$ onto the steel surface which is capable of suppressing the dissolution of the steel but is also believed to initiate localised corrosion in the upper portion of the pipe in some circumstances [81, 88]. Consequently, understanding the kinetics of film formation and conditions whereby $FeCO_3$ formation may be anticipated is an important step towards identifying whether localised corrosion is likely to occur.

$FeCO_3$ formation and steel dissolution thermodynamics and kinetics will inevitably be governed by surface temperature (T_s). However, most studies and prediction tools address TLC phenomena by correlating with T_g, and calculating T_s either implicitly using heat and mass transfer across the pipe wall or not at all [30, 168]. This is essentially related to the fact that T_g is believed to be the main parameter controlling WCR. An additional challenge associated with experimentally evaluating TLC is individually isolating the numerous interrelated parameters. If such parameters could be isolated and evaluated, it would inevitably lead to a better understanding of TLC and an improvement in prediction models.

In this study, a TLC rig design is presented which is able to measure T_s, and WCR, as well as allowing sampling of the condensate to be performed. A parametric approach is adopted by systematically varying T_g and the external sample temperature to produce 23 different conditions. For each set of conditions, the corrosion rate of the steel sample is evaluated using mass loss measurements at times of 24,48,72,96,120,144 and 168 hours over a range of T_g from 30 to 60^{o}C and T_s from 5 to 52^{o}C. An empirical correlation is established between the conditions where no scale formation or no significant change in corrosion rate was observed over the duration of the experiment. This enabled the effect of T_s and WCR to be isolated from one another and their contributions to be quantified.

Numerous experiments were done for variable time periods of 24, 48, 72, 96, 120, 144, and 168 hours for inner surface temperature ranged between 5°C and 52°C and gas temperature of 30, 40, 50 and 60°C. At the end of each time period, the weight change measurements of each specimen and the pH of the water condensate and water condensation rate were measured. Surface analysis from SEM and corrosion scale composition from EDX and XRD was conducted to support the observed trends and the results. Also, NPFLEX machine was used to provide information on surface characterisation for pitting corrosion damages.

The results are presented in three categories; condensation rate results, pH measurement results and the weight change results. In order to fulfil the repeatability of the results, experiments were usually conducted three times for each set of gas and inside surface wall temperature. Based on the experimental results a new empirical correlation to calculate corrosion rate at the top of line by taking into account the effect of most important variables condensation rate and inner steel temperature has been suggested.

5.1 Condensation Rate Results

WCR was measured at gas temperatures (T_g) ranging from 30˚C to 60˚C while the steel temperature (T_s) was controlled to values between 5˚C and 52˚C.

Table 5-1 summarises the entire series of experiments performed, complete with the initial (24 h) and final (168 h) corrosion rates recorded, as well as observations of film formation.

A subset of results for the measured in situ WCR are shown in Figure 5-1, Figure 5-2, Figure 5-3, Figure 5-4 and Figure 5-5, the results in all cases of experiments illustrate that the WCR is roughly constant throughout the experiments, with typical variations of less than 5 %.

Figure 5-6 provides the full set of average WCR values as a function of T_g and T_s over the duration of each 168 hours experiment.

Considering Figure 5-6, as expected the highest WCR was observed for the highest temperature difference between the steel surface and the bulk gas (at T_g= 60˚C and T_s=15˚C, the WCR was 1.718 ml/m^2.s). The lowest WCR of 0.116 ml/m^2.s was recorded when T_g=30˚C and T_s=25˚C. It can be clearly seen that the condensation rate is strongly dependent on the temperature of the gas phase. As the temperature increases, the condensation rate also increases since the humidity levels increase with gas temperature (the amount of water available for condensation is larger), thereby enhancing heat and mass transfer according to Nusselt's theory of condensation [185, 186].

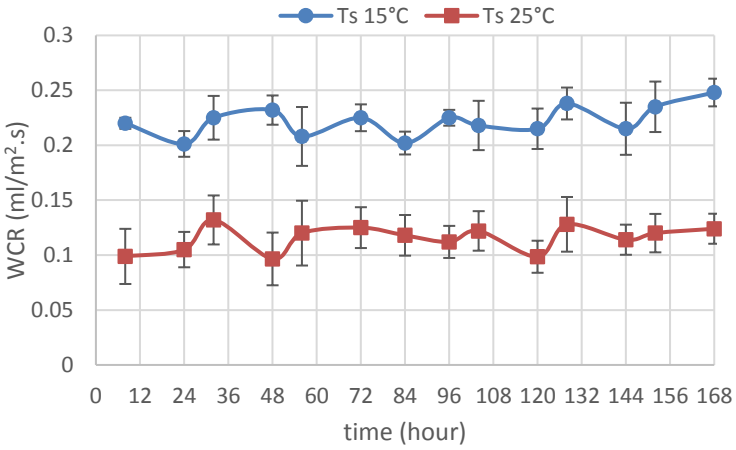

Figure 5-1. Condensation rate WCR as a function of the time at gas temperatures 30°C and surface temperature of 15 and 25°C.

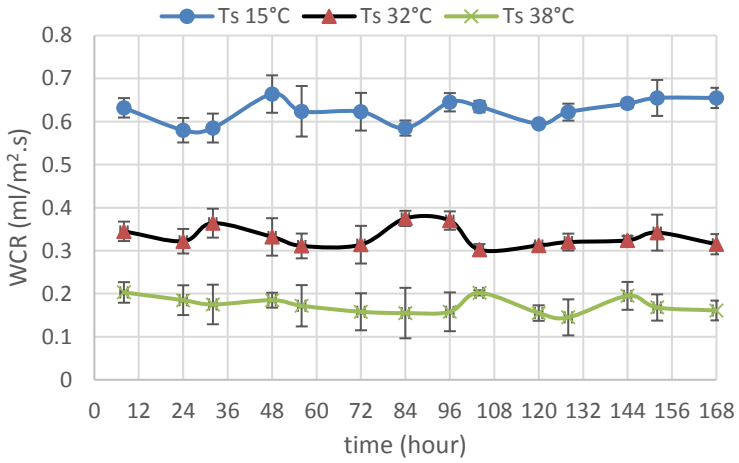

Figure 5-2. Condensation rate WCR as a function of the time at gas temperatures 40°C and different surface temperatures at a total pressure of 1 bar.

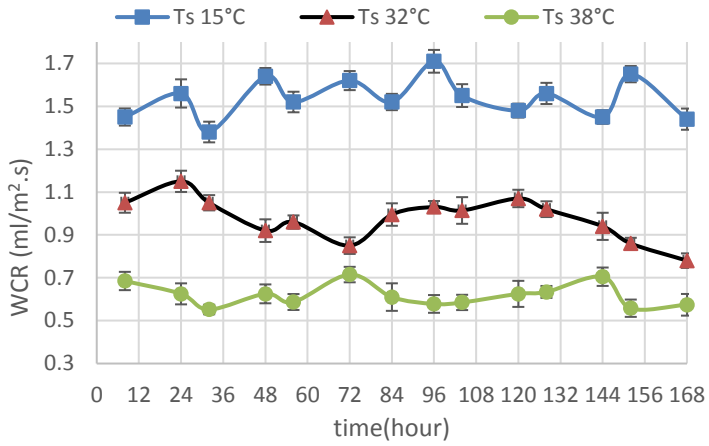

Figure 5-3. Condensation rate WCR as a function of the time at gas temperatures 50°C and different surface temperatures at a total pressure of 1 bar.

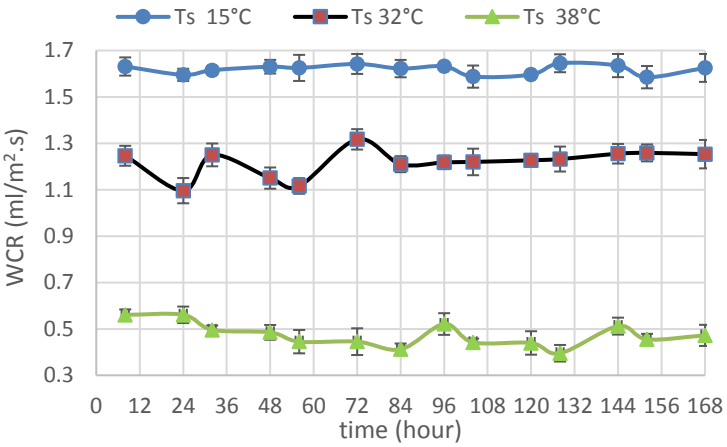

Figure 5-4. Condensation rate WCR as a function of the time at gas temperatures 55°C and different surface temperatures at a total pressure of 1 bar.

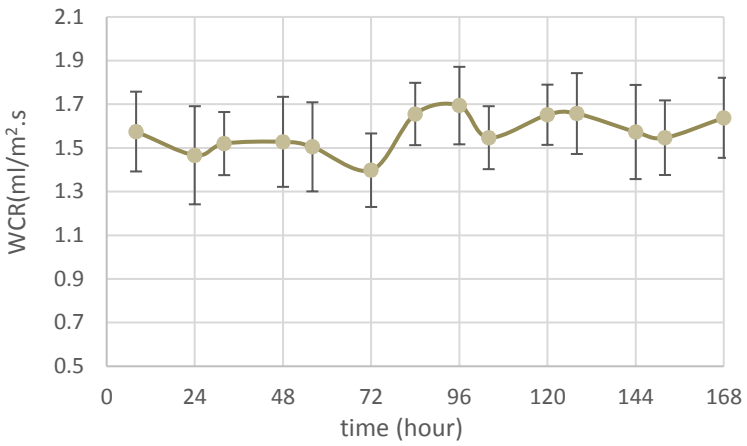

Figure 5-5. Condensation rate WCR as a function of the time at gas temperatures 60°C and surface temperature 20°C and at a total pressure of 1 bar.

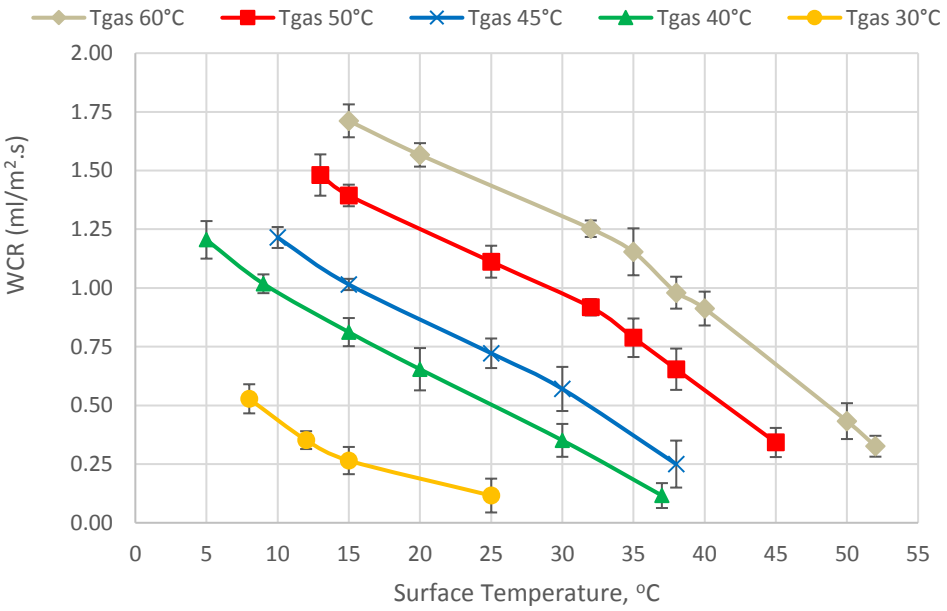

Figure 5-6. Condensation rate (WCR) versus surface temperature (T_s) for different gas temperatures (T_g). Error bars represent the standard deviation based on multiple measurements in different cells and at different times.

5.2 Corrosion Rate and pH Analysis

5.2.1 Corrosion Rate vs Time – for Film Forming and Non-Film Forming Conditions

The water condensation rate and temperature are believed to be two key factors affecting the top of line corrosion rate [73, 84]. Consequently, both of these parameters were varied to determine their effect on the corrosion rate of carbon steel as a function of time.

The results are displayed in a series of graphs from Figure 5-7 to Figure 5-22. It should be mentioned that all the corrosion rates were measured using weight loss technique of coupons made of carbon steel. Mass loss measurements were recorded for samples after 24, 48, 72, 96, 120, 144 and 168 h in every experiment.

5.2.1.1 The Inside Surface Temperature Effect

Across all experiments, either one of two distinct trends was observed in the corrosion rate response. Either the corrosion rate increased dramatically with time, or the corrosion rate response remained stable, followed by a slow decline. The responses within Figure 5-7 and Figure 5-8 provide a selection of results which depict both scenarios. These results correspond to the same conditions previously provided for WCRs shown in

Figure 5-6. For T_g = 40°C in Figure 5-7, the corrosion rate rises with time at T_s =15°C and 32°C, with similar values of corrosion rate being observed in each test (an increase from ~0.52 to ~0.95 mm/y). This behaviour can be attributed to the presence of an un-protective iron carbide (Fe_3C) scale, SEM images Figure 5-9, confirmed the presence of the iron carbide layer. Iron carbide is one of the most common corrosion products found in CO_2 corrosion of mild and low-alloy steels [28, 113]. EDX spectra of the samples after 168h of exposure Figure 5-10 shows low-intensity peaks of carbon in comparison to that of iron which indicates the presence of iron carbide.

Iron carbide is the part of the steel microstructure and its amount increases with the carbon content of the steel [113], and it is more difficult to dissolve than the ferrite phase (α-Fe) and it is often found left on the metal surface as a result of the corrosion process. Since Fe_3C is an electronic conductor, it is believed that its presence increases the corrosion rate by causing galvanic effect and acting as a cathodic site for the hydrogen evolution reaction[98, 187]. Hence, as the corrosion process continues, more iron carbide forms, increasing the cathodic reaction and therefore the corrosion rate.

At T_s = 38°C for T_g=40°C a significantly lower initial corrosion rate is observed (0.2 mm/y) which can be attributed to a reduction in WCR. In this test, the CR shows signs of reduction after ~100 hours. Similar observations were recorded at T_g = 50˚C in Figure 5-8, however, the increase in corrosion rate at T_s = 15°C and 32ºC was more dramatic, and the reduction in corrosion rate at T_s = 38˚C was more significant. The reduction in TLC rates can be explained by the fact that the $FeCO_3$ protection film forming on the steel surface was porous and not dense to protect the steel surface, this is confirmed by SEM image and XRD analysis provided in Figure 5-11 and Figure 5-12 respectively.

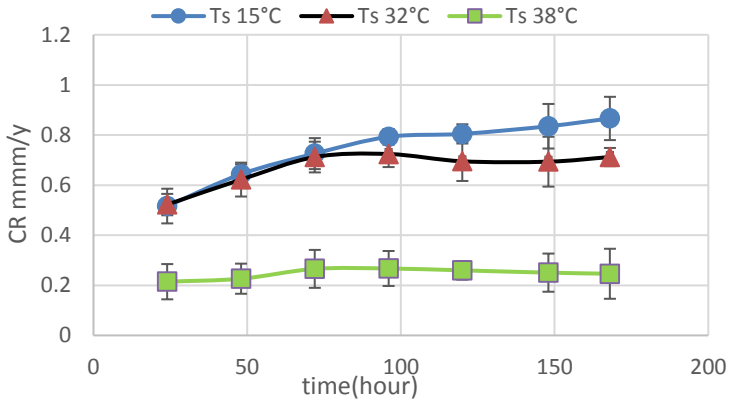

Figure 5-7. Corrosion rate vs time on at 40˚C gas temperature. Influence of the inner surface temperature.

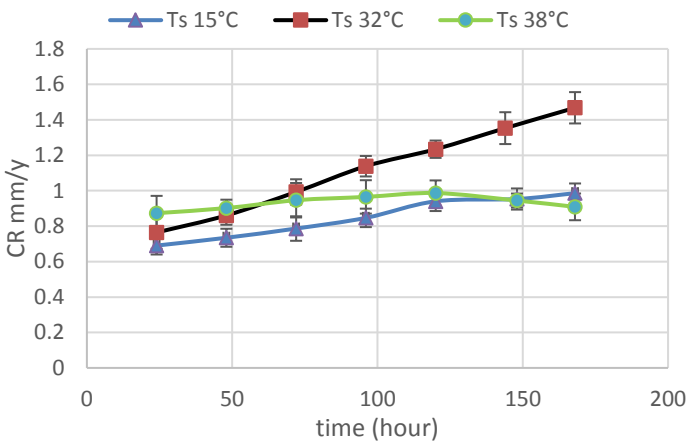

Figure 5-8. Corrosion rate vs time at 50˚C gas temperature. Influence of the inner surface temperature.

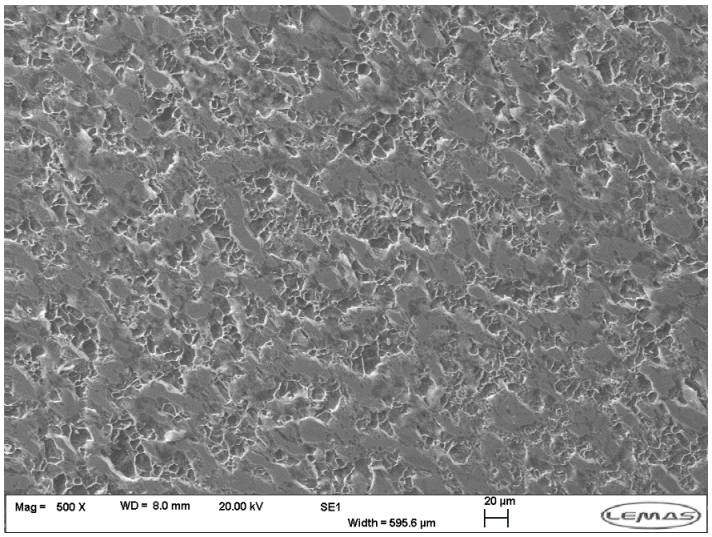

Figure 5-9. SEM image of the sample after 168h of exposure at 50°C gas temperature and 15°C surface temperature. Presence of an un-protective iron carbide (Fe_3C) scale.

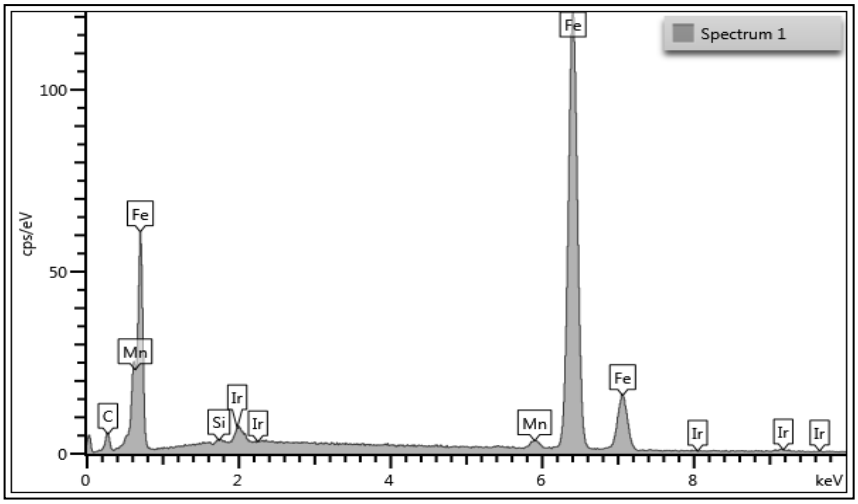

Figure 5-10. EDX spectra of the samples after 168h of exposure at 50°C gas temperature and 32°C surface temperature and WCR of 0.98 ml/m^2.s. Presence of an un-protective iron carbide (Fe_3C) scale.

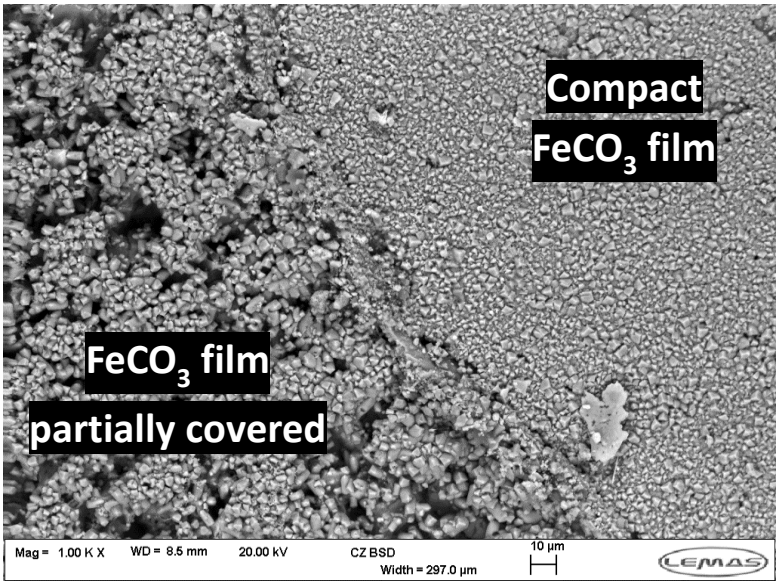

Figure 5-11. SEM image of the samples after 168 h of exposure at T_g of 50°C and T_s of 38°C and WCR of 0.622 ml/m^2.s. $FeCO_3$ partial covered the steel surface.

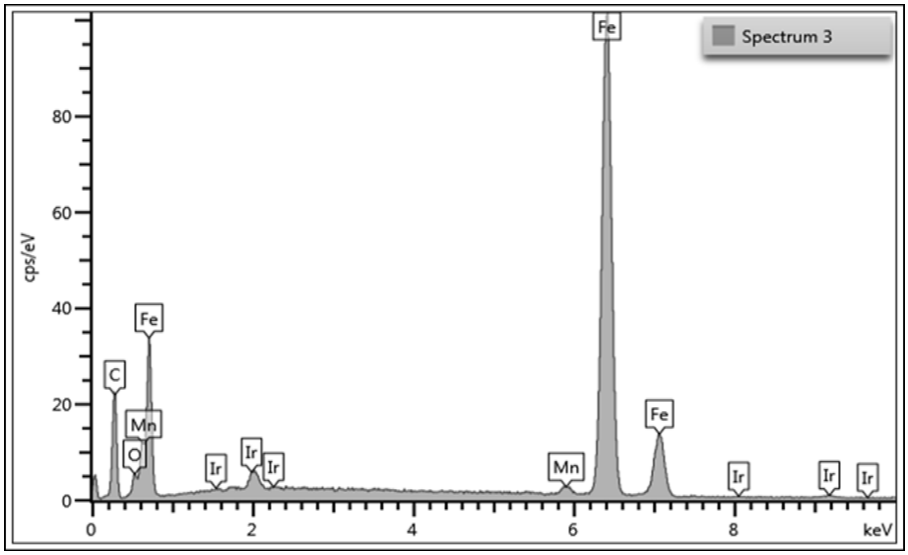

Figure 5-12. EDX spectra of the corrosion product layer on the coupon surface and cross-section analysis after 168 hours of exposure at 50°C gas temperature, 38°C inner surface temperature, pressure= 1 bar and WCR 0.622 ml/m^2.s. $FeCO_3$ partial covered the steel surface.

At T_g is 60°C and T_s is 50°C the behaviour of corrosion is qualitatively different. As shown in Figure 5-13, the TLC rate decreased gradually throughout the experiment to around 0.63 mm/y at the end of the test after 168 hours which was approximately two-thirds of its initial value 0.91mm/y. This due to the forming more protective and denser layer of corrosion product of $FeCO_3$ since the kinetics of iron carbonate precipitation is faster at higher surface temperature [43]. The iron carbonate covered the entire surface and its crystals are clearly visible in the SEM image shown in Figure 5-14. Also, EDX spectra Figure 5-16 shows the high-intensity peak of oxygen in relation to that of iron and carbon, this means the presence of iron carbonate scale [188-190]. XRD analysis in Figure 5-15 ,which can be compared to the reference patterns of Fe, Fe_3C and $FeCO_3$ in Figure 5-17, clearly confirmed the $FeCO_3$ formation at these particular conditions.

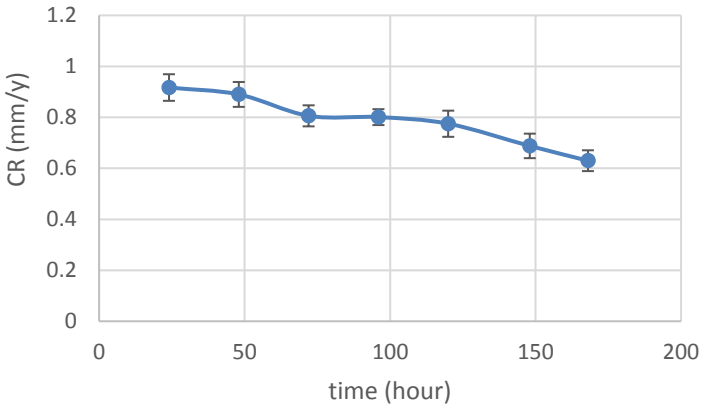

Figure 5-13. Average top of line corrosion rate at 60°C gas temperature and surface temperature of 50°C and WCR of 0.264 ml/m^2.s.

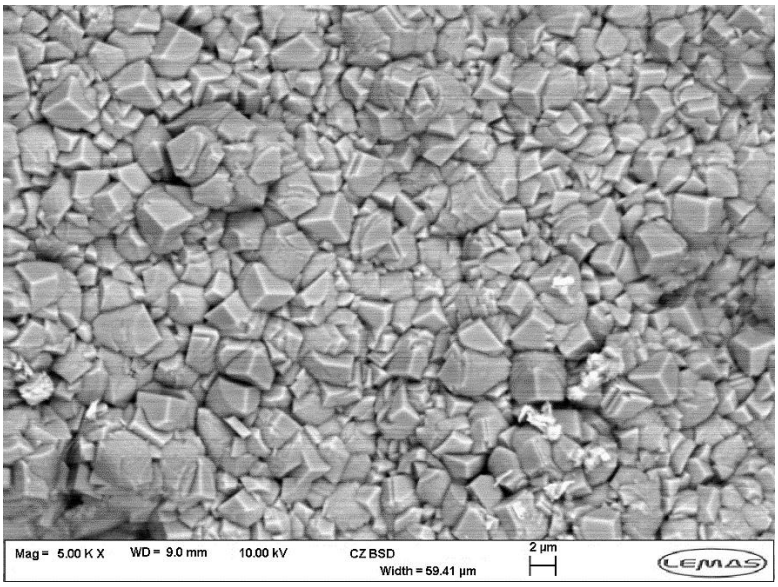

Figure 5-14. SEM of the sample after 168 h of exposure at T_g of 60°C, Ts 50°C and WCR of 0.264 ml/m2.s. Full coverage of $FeCO_3$.

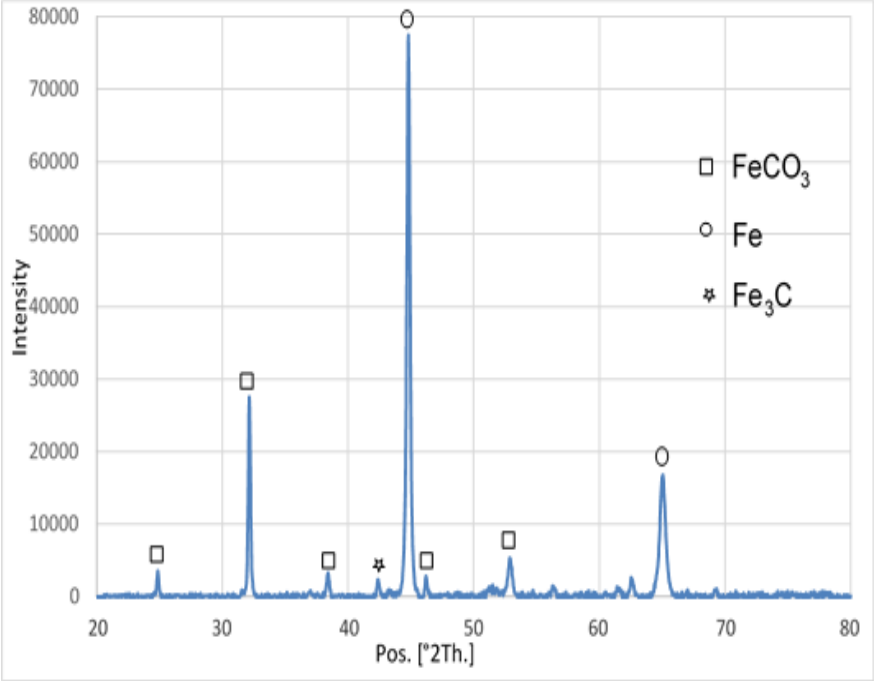

Figure 5-15. XRD pattern for corrosion product layer on X65 coupon at gas temperature of 60°C and surface temperature 50°C. The image is for a test duration of 168 hours.

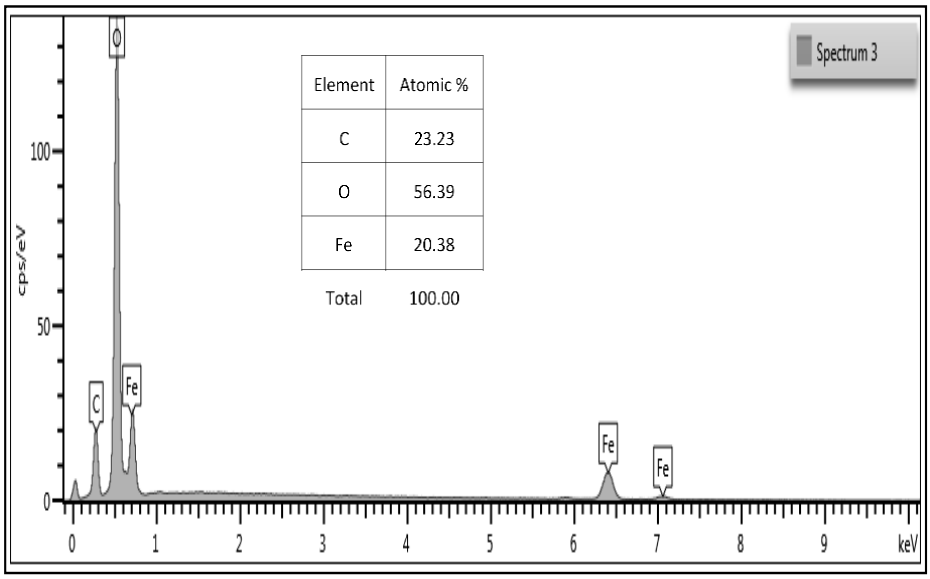

Figure 5-16. EDX spectra for corrosion product layer on X65 carbon steel gas temperature of 60°C and surface temperature 50°C. The image is for a test duration of 168 hours.

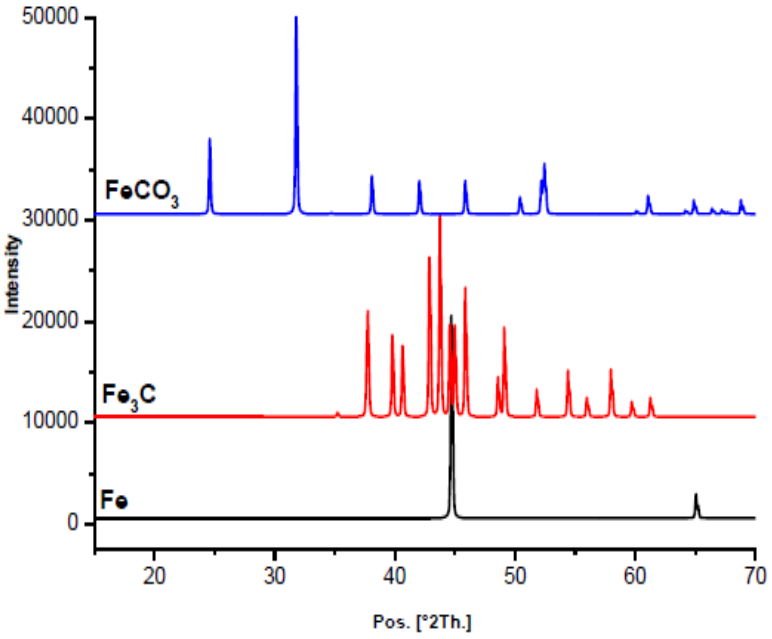

Figure 5-17. Reference XRD patterns for Fe, Fe_3C and $FeCO_3$ [188-190].

Based on ex-situ analysis of samples at the end of each 168 h experiment and the corrosion rate response, each experiment was categorised as either $FeCO_3$ film-formation or non-film-forming over the 168 hour time period of the experiments. It is recognised that protective films may eventually form on the surface after 168 hours, but these conditions are not considered here.

Table 5-1 summarises the entire series of experiments performed, complete with the initial (24 h) and final (168 h) corrosion rates recorded, as well as observations of film formation. In addition, Figure 5-9 and Figure 5-11 provide two typical images contrasting the visual appearance of the surface in the presence and absence of $FeCO_3$.

At this stage, it is perhaps important to mention that the use of the mass loss technique to determine the corrosion rate at a particular instant in time adopts an integral approach, considering the average corrosion rate response prior to each point of measurement. Therefore, when corrosion rates are rising with time, the mass loss technique underestimates the ‘real-time’ corrosion rate, and when corrosion rates reduce with time, the ‘real-time’ corrosion rate

is overestimated. This point will be considered further in a subsequent section.

Table 5-1. Initial (24 h) and final (168 h) corrosion rates recorded from mass loss measurements in a parametric study of the CO_2 top of line corrosion. All conditions are under atmospheric pressure.

Gas Temperature T_g (˚C)	**Surface Temperature T_s (˚C)**	**Condensation rate (ml/m^2/s)**	**Corrosion rate after 24 hours (mm/y)**	**Corrosion rate after 168 hours (mm/y)**	**$FeCO_3$ Film formation observed?**
30	8	0.528 ± 0.08	0.511± 0.08	0.588± 0.02	No film
30	15	0.265 ± 0.04	0.697± 0.1	0.663± 0.08	No film
30	25	0.116 ± 0.02	0.562± 0.05	0.522± 0.05	No film
40	5	1.080 ± 0.108	0.812± 0.1	0.764± 0.1	No film
40	9	0.915 ± 0.1	0.721± 0.09	0.755± 0.1	No film
40	15	0.812 ± 0.08	0.516± 0.06	0.866± 0.1	No film
40	20	0.654 ±0.04	0.528± 0.05	0.882± 0.1	No film
40	32	0.288 ±0.01	0.522± 0.08	0.712± 0.08	No film
40	38	0.116 ±0.01	0.214± 0.02	0.246± 0.02	No film
50	15	1.394 ±0.152	0.690± 0.04	0.986± 0.1	No film
50	25	1.112 ±0.12	1.062± 0.12	0.953± 0.08	No film
50	32	0.918 ±0.08	0.765± 0.06	1.165± 0.15	No film
50	35	0.788 ±0.06	1.120± 0.15	1.020± 0.1	No film
50	38	0.774 ±0.04	0.873± 0.06	0.906± 0.09	No film
60	15	1.712 ±0.14	0.824± 0.08	1.050± 0.1	No film
60	20	1.566 ±0.155	0.774± 0.1	0.936± 0.1	No film
60	32	1.340 ±0.122	1.421± 0.16	1.520± 0.18	No film
60	40	0.912 ±0.08	1.330± 0.14	1.224± 0.12	No film
60	52	0.326 ±0.02	1.122± 0.11	0.606± 0.03	Film formed
60	50	0.433 ±0.02	0.917± 0.1	0.630± 0.06	Film formed

5.2.1.2 The Water Condensation Rate Effect on TLC.

In this study, the effect of the condensation rate during top of line corrosion has been widely investigated theoretically as seen in chapter 6. However, it seems from the previously documented experimental information [73, 84, 169] that the role of the condensation rate is essential in the determination of the corrosion rate during TLC. Thus, the influence of the condensation rate on the TLC rate is studied experimentally in this chapter.

The effect of WCR on TLC rate was tested under three of surface temperature 15°C, 32°C and 38°C.

Since the rate of the renewal of the water droplets is faster at a higher WCR, the CR rate is expected to be highest at the highest WCR as shown in Figure 5-19 when the surface temperatures are 32°C and 38°C. However, this is not always true, when the T_s is relatively low at 15°C, there is no significant change in TLC rate when the WCR increased above the 1.2 ml/m^2.s as illustrates in Figure 5-18.

It is worth noting from Figure 5-18 that at low T_s (15°C), increasing the WCR from 0.772 to 1.712 ml/m^2.s i.e. increasing the gas temperature from 40°C to 60°C has not significantly affect corrosion rate even though WCR increased more than double. Whereas, at high surface temperature T_s=32°C and 38°C Figure 5-18, the corrosion rate values increased considerably by increasing gas temperature and increasing WCR. The experimental result shows at surface temperature of 32°C, increasing the WCR from 0.288 ml/m^2.s to 1.34 ml/m^2.s led to significant increase in CR from 0.712 to 1.52 mm/y. Similarly, at surface temperature of 38°C, CR increased considerably from 0.246 to 1.224 mm/y by increasing WCR from 0.116 to 0.912 ml/m^2.s. Hence for the higher surface temperatures, higher WCR plays a crucial role in increasing CR.

From the brief description presented above, it is clear that if the steel temperature is less than 32˚C, the extent of corrosion at the top of the line can be correlated to the steel temperature, not the WCR. The kinetics of any chemical or electrochemical reaction slows down at low temperature including iron dissolution process and $FeCO_3$ precipitation. Due to slow iron dissolution, the Fe^{2+} concentration in the condensed liquid remains low resulting in very low supersaturation and very low or no accumulation of corrosion products on the steel surface. Therefore, at low surface temperature, the corrosion reaction should be controlled by the temperature at which it happens, i.e., the steel temperature rather than the gas temperature, which can be completely different.

In general**,** the lowest average corrosion rate at the top of the line was recorded at the lowest condensation rate (Figure 5-18). This observation can be explained by the fact that the formation of the corrosion product layer ($FeCO_3$) was influenced by the water condensation rate as the saturation of $FeCO_3$ is easier to reach when droplets of condensed water remain attached to the metal surface for a longer time. Therefore, at higher condensation rates, when the renewal of condensed water droplet is faster, supersaturation of condensed water with $FeCO_3$ reduces and the steel corrosion rates become higher, and vice versa.

Figure 5-19 shows that the effect of WCR becomes more important at a surface temperature above 32°C when iron carbonate formation becomes favourable. The higher surface temperature may increase the iron dissolution rate. In addition, at low condensation rate droplets can attach to the inner metal surface for enough time to achieve favourable conditions for forming an iron carbonate film in the droplets. In consequence, the high surface temperature and the long droplet lifetime promoted the formation of iron carbonate on the surface.

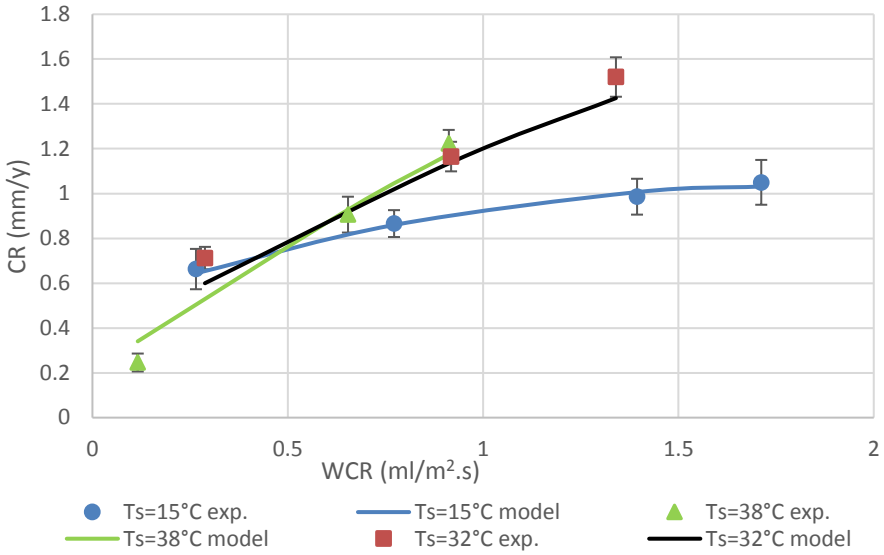

Figure 5-18. Influence of the condensation rate on the top line corrosion rate at 15°C surface temperature after 168 hours exposed.

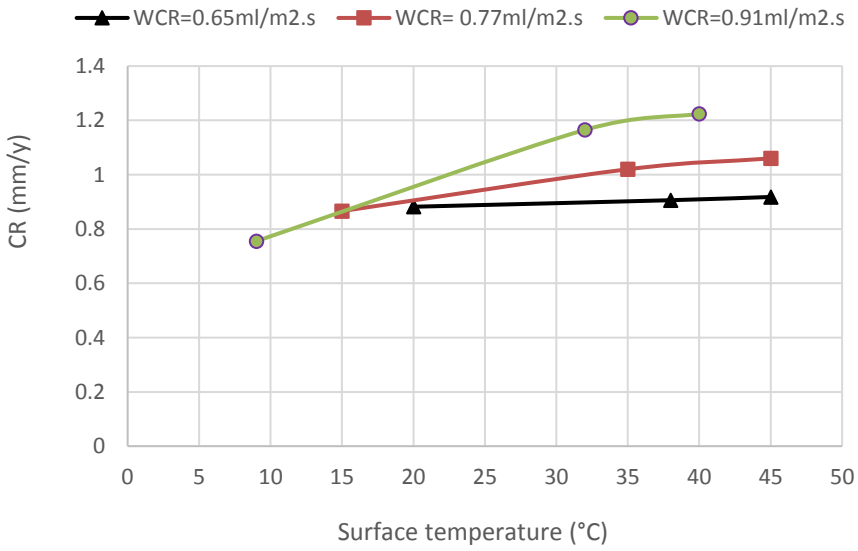

Figure 5-19. Influence of inner surface temperature on the top line corrosion rate at different water condensation rates.

5.2.2 Water Chemistry (pH) Results

Selected pH measurements were conducted to assist in both understanding protective film formation and correlating pH measurement with corrosion rate responses. Figure 5-20 and Figure 5-21 show the pH measurements from the condensate as a function of time for T_g of 40 and 50˚C and T_s values of 15, 32 and 38˚C. Again, these results can be compared with Figures Figure 5-7 and Figure 5-8. Through this comparison, it is possible to see that the pH and corrosion rate responses follow similar trends. When corrosion rate increases with time for a constant WCR, the concentration of dissolved iron in each droplet increases with time.

It can be seen that the pH of the collected condensed water varies between 5 and 6 depending on experimental conditions at T_g = 50˚C. The results of the pH measurements reveal that the trend of pH closely matches the trend of corrosion rate because the concentration of iron ion (Fe^{2+}) governs the pH of the condensed water to balance the charges. As stated by the electro-neutrality equation (Equation (5.1)), the sum of positive charges is equal to that of negative charges.

$$2[Fe^{2+}] + [H^+] = [HCO_3^-] + [OH^-] + 2[CO_3^-] \quad 5.1$$

In the condensed water, dissolved iron (Fe^{2+}) is also present which needs to be taken into account in the electro-neutrality equation and results in increased pH to maintain a total net charge of zero.

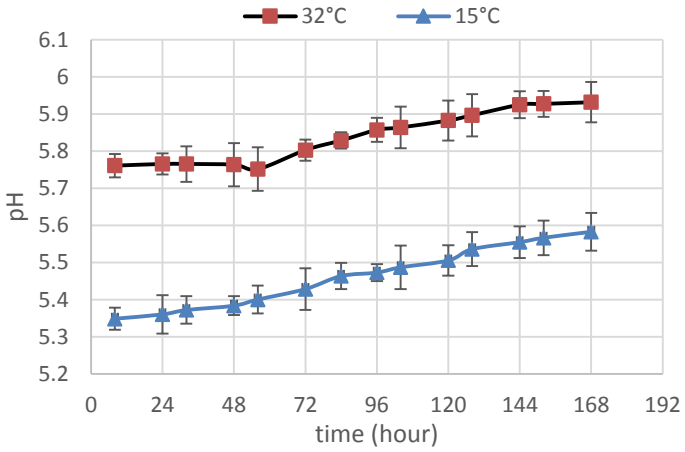

Figure 5-20. Measured pH at the condensed water as a function of the time at 40°C gas temperature. Influence of inner surface temperatures.

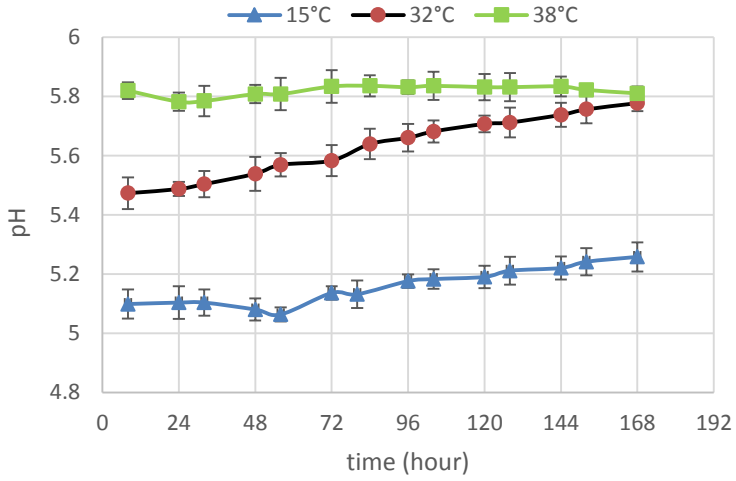

Figure 5-21. Measured pH at the condensed water as a function of the time at 50°C gas temperature. Influence of inner surface temperatures.

The typical pH value of freshly condensed water with acid gases dissolved in is between 3.5 and 4.5 [169]. However, as the corrosion process takes place, with accompanying dissolution of ferrous ions into the condensed water, pH increases. It should be highlighted that the water at the top of the line entirely comes from the condensation process, as a result of the gradient between gas and surface temperature. Therefore, the value of the

condensed water pH at the surface is only a function of the condensation and TLC process.

5.3 The 'real-time' Corrosion Rate Measurements

5.3.1 CO_2 Corrosion of Carbon Steel and $FeCO_3$ Precipitation

Studies have demonstrated that the presence of $FeCO_3$ is one of the main influential factors on the corrosion rate [191-196] since the presence of $FeCO_3$ can provide corrosion protection and may reduce corrosion rate. Therefore, it is very important to study the kinetics of iron carbonate scale formation on to carbon steel pipelines during CO_2 corrosion.

The experimental results showed that the top of line corrosion is controlled by both surface temperature and water condensation rate. To study the formation and precipitation of $FeCO_3$ with time, the test was carried out at a surface temperature of 50°C and a gas temperature of 60°C, these conditions provided WCR about 0.264 ml/m^2.s.

The main source of ferrous ions forming iron carbonate scale comes from the corrosion process of the steel surface. Thus the corrosion rate has a significant effect on the scale precipitation rate of iron carbonate scale.

As mentioned earlier the use of a mass loss technique to determine the corrosion rate at a particular time gives inaccurate real-time corrosion rate. Therefore, using a change in mass loss over time equation, from one period to the next one, allows for a more accurate calculating of corrosion rate over the time, for this purpose the Equation (5.2) was used.

$$CR = \frac{\Delta m}{t * A * \rho_{Fe}} * 8760 \qquad 5.2$$

where CR is the corrosion rate (mm)/y, Δm is the change in mass loss from one time interval to the next (g), t is the time interval in between

measurements (24 hours), A is the exposed sample area (m^2) and ρ_{Fe} is the density of the sample (kg/m^3).

Several experiments were carried out to measure TLC for various time periods of 0-24, 24-48, 48-72, 72-96, 96-12, 120-144 and 144-168 hours. The change in the weight of the sample was determined at the end of each time period. From Figure 5-22, which shows the corrosion rate results obtained from equation 5.2 at each time step over the total time of 168 hours, it can be seen that the initial corrosion rate at the very beginning of the test (first 24 hours) is the highest value over the whole time period of the test, this is because the freshly condensed water is very corrosive. The corrosion rate decreases dramatically from 1.21mm/y to 0.76 mm/y after 24 hours from the test starting. As the protective corrosion scale grows and becomes denser, the corrosion rate is decreased gradually and reached its lowest value 0.24 mm/y at the end of the test.

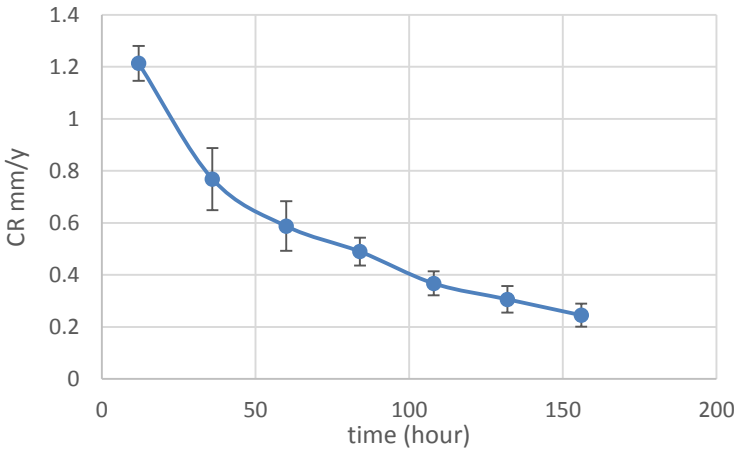

Figure 5-22. CR based on the difference in the mass of the sample at each time step (Δm /Δt) at a gas temperature of 60°C and surface temperature 50°C and WCR 0.264 $ml/m^2.s$

To gain a better understanding of the TLC mechanism, the precipitation rate was calculated from the mass gain measurements according to Equation (5.3) from one period to the next one until covering the whole experiment time, each time step was 24 hours.

$$PR = \frac{\Delta m_{film}}{MW_{FeCO3} * t * A * 3600000} \quad 5.3$$

where PR is the precipitation rate in (kmol/m^2.s), Δm_{film} is the change in mass gain from one time interval to the next in (g), MW_{FeCO3} is the molecular weight of iron carbonate (115.8 g/mol), t is the time interval between measurements (hours) and A is the exposed sample area (m^2).

The mass gain was experimentally determined for a time period of 0-24, 24-48, 48-72, 72-96, 96-120, 120-144 and 144-168 hours, this means the time interval t was 24 hours. The procedure of the experiments under this range of time has been explained previously in section 4.3.2. In these tests, the samples were re-used for several times. After each experiment, the sample was re-ground with using silicon carbide (SiC) abrasive papers of up to 1200 grit, cleaned with distilled water and ethanol and dried with compressed air.

Figure 5-23 shows the mass gain for each individual time period of 24 hours over the total time of exposure (seven days). Due to higher corrosion rate at the earlier time periods, the results show that the mass gain is higher at the very beginning of the test. It may be observed from the same figure that the weight of the gained mass decreased steadily over the time periods and follow the same trend of the corrosion rate. It starts with 10.88 mg and decreases gradually to reach 2.87 mg after seven days.

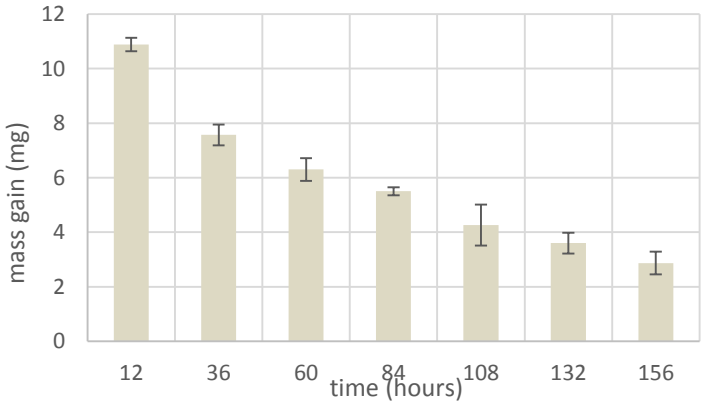

Figure 5-23. The measured mass gain due to $FeCO_3$ precipitation over variable time periods, at T_g 60°C and T_s 50°C.

5.3.2 Comparison of Precipitation Rate and Corrosion Rate

In order to get a further understanding of TLC phenomenon, both of the two dominant processes i.e. the precipitation rate and corrosion rate obtained by the weight change method over time were plotted and described in the same molar unit. Thus, to understand and compare how much amount of corrosion product scale that precipitated as $FeCO_3$ on the steel surface ($FeCO_3$) and iron ion (Fe^{2+}) is lost due to the corrosion on the steel surface with a surface area of one m^2 in a second, both processes were converted into reaction rates expressed in units of $mol/m^2.s$. The corrosion rate in $kmol/m^2.s$ can be obtained by converting the corrosion rate in mm/y from Equation 5.2 by Equation (5.4).

$$CR = \frac{CR_w * \rho_{Fe}}{MW_{Fe} * 8760 * 3600 * 1000} \quad 5.4$$

where:

CR_w = Corrosion rate from weight loss method at each time step (mm/y)

ρ_{Fe} = density of iron (equal to 7850 kg/m^3)

MW_{Fe} = molecular weight of iron (equal to 55.85 g/mol)

Figure 5-24 shows a direct comparison between the corrosion rates (CR) and the precipitation rates (PR) at the end of each time period at the surface temperature of 50°C and gas temperature of 60°C. The error bars represent the standard deviation of the measured corrosion and precipitation rates.

The precipitation rate decreased considerably with the increase of reaction time during the first three days, then the rate of decreasing in precipitation rate at the period from 3-5 days became less than the first three days because of the reduction in corrosion rate at this period, as a consequence of this CR reduction, the releasing of Fe^{2+} decreased and as a consequence decreased of supersaturation in the bulk of the solution causing decreasing in PR at the end. From 5-7 days, the precipitation rate decreased slowly. This is due to the slow change in mass gain over this period of time.

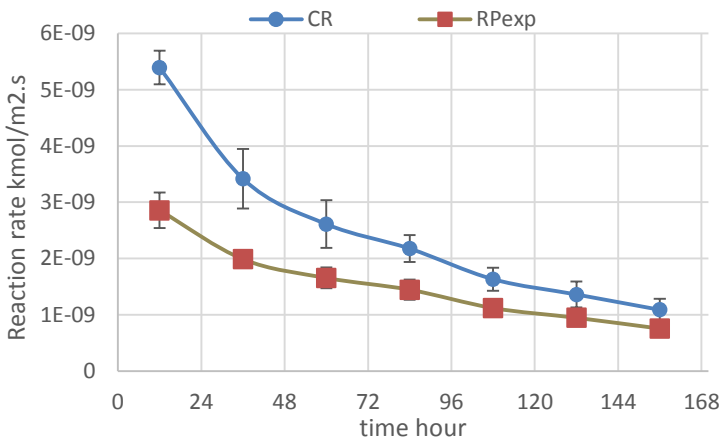

Figure 5-24. Comparison of corrosion rate and precipitation rate calculated according to equations 4.2 and 4.3 at surface temperature of 50°C and gas temperature of 60°C.

Comparison of the corrosion rate with precipitation rate in the same units (mol/m^2.s) shows that the corrosion rate is slightly higher than the precipitation rate in the first two days. After two days, the difference between the precipitation and corrosion rate is decreased and become lower than at the beginning of the test, while, after seven days of exposure the difference was reduced to the minimum value. The source of Fe^{2+} forming iron carbonate scale is released from the steel surface due to the corrosion process. Hence, the corrosion rate has a significant effect on the precipitation rate of iron carbonate scale $FeCO_3$.

The comparison indicates that both the corrosion rate and scale precipitation rate decreased over the time of the experiments, however, the corrosion rate is always higher than the scale precipitation rate. For bulk fluid flow, Nesic and Sun [178] proposed that not all corrosion product scale resulting from corrosion process precipitates on the steel sample but is also deposited elsewhere in the test system. They showed that from 40% to 72% of the ferrous ions consumed by the corrosion process end up as corrosion scale while the rest is lost to the solution. While at TLC scenario the iron ions may fall down with the droplet prior to precipitation with the iron carbonate.

5.3.3 Scaling Tendency of Top of the Line

The protectiveness of the corrosion product layer is measured by using scaling tendency which is can be described as follows [178]:

$$ST = \frac{PR}{CR} \quad 5.5$$

where PR is the precipitation rate of iron carbonate calculated based on experimental data using Eq 5.3, CR is the corrosion rate of the steel calculated from Eq 5.4. For ST <<1 porous and unprotective films are likely to form, and conversely for ST equal or greater than unity, conditions become favourable for formation of dense protective iron carbonate films [197]. However, Pots et al. [122] proposed that the critical ST, at which effective corrosion reduction by corrosion product formation can vary between 0.4–1 depending on carbon content in the steel.

The scaling tendency was calculated by using the same molar units (kmol/ m^2.s) for precipitation rate and the corrosion rate as shown in Figure 5-25. The experimental conditions were surface temperature of 50°C, gas temperature of 60°C and the test duration was 168 hours. As shown in Figure 5-25, the scaling tendency changes with time as the corrosion and precipitation rates change (varying from 0.54 to 0.71). When the exposure time increases from 24 hour to 72 hour, the scaling tendency increases by 0.07. This suggest that more iron ions (Fe^{2+}) fall down with the condensed water from the steel surface than precipitating on the steel surface.

While, at the later time periods from 72 hours until the end of the experiment, the scaling tendency is higher than the first three days of exposure. This is due to more Fe^{+} settling down on the steel surface rather than diluting in the water droplets. Consequently, it leads to increasing the precipitation rate forming a protective film, increasing the scaling tendency and decreasing the corrosion rate. From abovementioned, it can be concluded that in TOL scenario, the value of 0.5 to 0.7 of scaling tendency is sufficient to form a protective iron carbonate film.

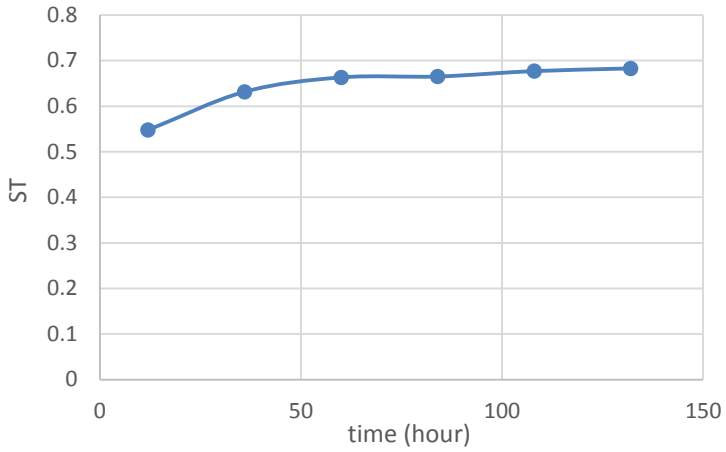

Figure 5-25. Scaling Tendency versus exposure time at surface temperature of 50°C and gas temperature of 60°C.

5.4 Analysis of Kinetic Constant of TLC vs BLC

In order to gain a better understanding of the TLC behaviour, precipitation rate values from the weight change measurements were compared with the precipitation rate proposed by Sun and Nesic [52] discussed previously in Chapter Three. The equation can be re-written as:

$$PR = K_r K_{sp}(S_s - 1) \quad 5.6$$

Where the kinetic constant K_r is calculated according to Equation 5.7 [52]

$$K_r = e^{A - \frac{B}{RT_k}} \quad 5.7$$

Where A = 28.2 and B = 64851 J/mol; R = 8.314 J/ mol.K and T_k is the surface temperature in K. In this work the kinetic constant 'K_r' has been recalculated based on A= 25.75 instead of 28.2 to match the $PR_{theo.}$ with experimental value PR_{exp}. The new constant is more appropriate to obtaining the precipitation rate as it is fitted with the experiment data as seen in Figure 5-26.

Figure 5-26 shows a comparison of the precipitation rate measured based on weight change method and precipitation rate calculated based on

Equation 5.7 with A=25.75 at each time interval (24 hours) over seven days of exposure. The comparison shows a close correlation between the two results obtained through both methods.

Figure 5-27 shows the comparison between the experimental data and the precipitation rate determined in the current work and the precipitation rate calculated based on Sun and Nesic [52]. The same was observed by Islam et al.[157]. The calculated results of precipitation rate obtained by using the Sun and Nesic kinetic constant overestimated the magnitude of the experimental precipitation rate by a large margin, while a good agreement is observed by using the new constant.

Based on the above observations, it can be concluded that the kinetic constant A presented by Sun and Nesic [52] cannot be applied to a TLC scenario. This is due to the difference between top of line corrosion mechanism and bottom of line corrosion mechanism.

It is well known and has been found that the condensed water droplets do not attach to the steel surface for a constant period of time. At the top of line corrosion conditions, as corrosion proceeds, iron concentration in the droplet varies from its minimum to maximum value. In contrast, the larger volume of liquid in the bottom of the line prevents the fluctuation of iron concentration due to corrosion. This represents a significant difference in precipitation kinetics at top of line and bottom of line though similar reactions are taking place in the CO_2 environment.

Figure 5-26. Comparison of experimentally measured precipitation rate and calculated precipitation rate which was calculated by using the empirical expression proposed by Sun and Nesic with the modified kinetic constant =25.75 at gas temperature 60°C and surface temperature 50°C.

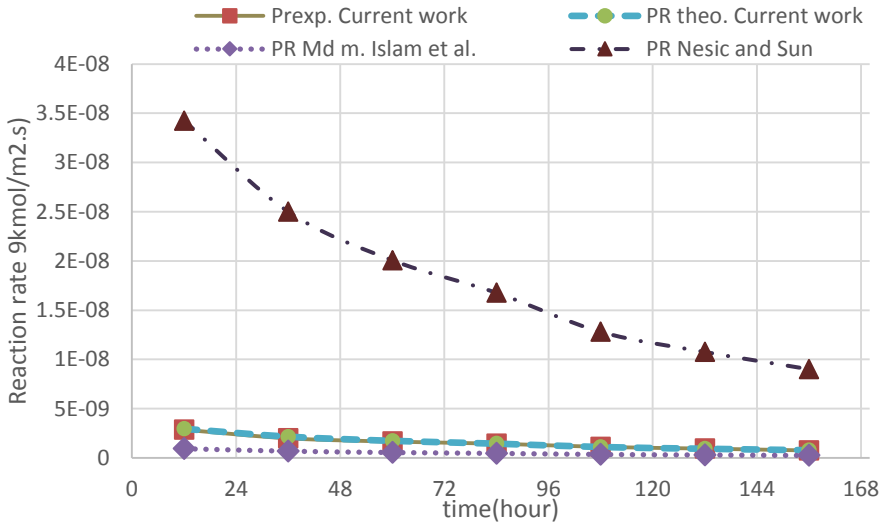

Figure 5-27: Comparison of experimentally measured precipitation rate and calculated precipitation rate using various kinetic constants K_r at gas temperature 60°C and surface temperature 50°C and WCR 0.264 ml/m^2.s.

5.5 Localised Corrosion Behaviour of Carbon Steel as a Function of Surface Temperature and Water Condensation Rate at the Top of Line

Considering the literature relating exclusively to CO_2 TLC, the general consensus is that $FeCO_3$ formation is pivotal in influencing the steel corrosion behaviour; a lack of protective formation results in high general corrosion rates, while the presence of the film is capable of suppressing corrosion rates significantly under the correct conditions. However, if the film protectivity is compromised locally, significant mesa-attack may occur.

This section presents the relationship between the pitting corrosion behaviour of carbon steel under different surface temperatures and water condensation rate in CO_2 saturated environments at the top of line scenario. In this section, the discussion is concentrated on the effect of the surface temperature on the localised corrosion behaviour of carbon steel materials in CO_2 environments.

Surface profilometry was conducted to review the pitting corrosion behaviour of carbon steel under different surface temperatures and water condensation rate in CO_2 saturated environments at the top of line scenario. Samples analysed using profilometry were first cleaned thoroughly with Clarke's solutions to remove any traces of corrosion product that may prevent the pits from being detected and accurately quantified. The pit depth analysis was conducted in alignment with ASTM Standard [198]. The standard stipulates that an average of the 10 deepest pits and the maximum pit depth should be used for pit damage characterisation of the sample area.

5.5.1 Localised Corrosion Behaviour of Carbon Steel at Surface Temperature of 32°C

At conditions favourable to form a partial iron carbonate ($FeCO_3$) protective layer, a set of experiments was conducted over 168 hours at surface temperature =32°C and WCR= 0.326 ml/m^2.s to investigate the behaviour of the localised corrosion at the top of the wet gas transportation pipeline. Through the course of the experiments, relatively continuous pit growth was observed, from maximum depths of ≈ 7µm after 24hours, up to ≈ 25 µm after 168 hours, as shown in Figure 5-28.

Also, the results showed that the pit depth increased with exposure time indicating that the presence of amorphous $FeCO_3$ has little or no effect in terms of inhibiting pit propagation. Instead, there is a possibility that the Fe_3C layer may even promote pitting corrosion on other localised anodic regions through a galvanic effect.

It is worth noting that the pit depths presented in Figure 5-28 are depths relative to the corroded surface. Thus, if general corrosion rate increases and pit growth remains constant, the relative growth of pits will appear to be reducing. Consequently, the increase observed could be related to galvanic effects between Fe_3C and the steel surface, as suggested by Crolet et al [112]. From Figure 5-28, it is obvious that the localized attack depth measured after 168 hours of exposure is almost 3.5 times higher than the one measured after 24 hours of testing. The hypothesis here is that TLC may have significantly slowed down. Figure 5-29 presents a 3D and 2D image and profile of the deepest pit on the entire exposed steel surface at 32°C after 168 hours.

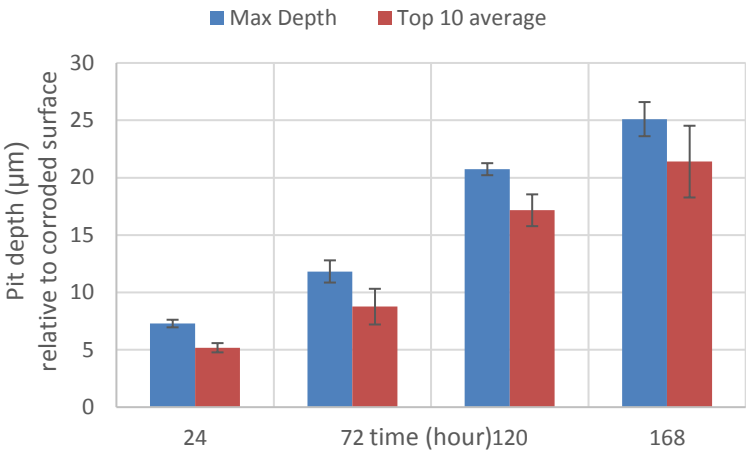

Figure 5-28. Plot depicting the variation of relative pit depth (maximum and top 10 average) with time at 32°C and WCR=0.362 ml/m^2.s, over a duration of 168 hours in a CO_2 corrosion at the top of line case. Error bars represent the standard deviation based on the average measurements.

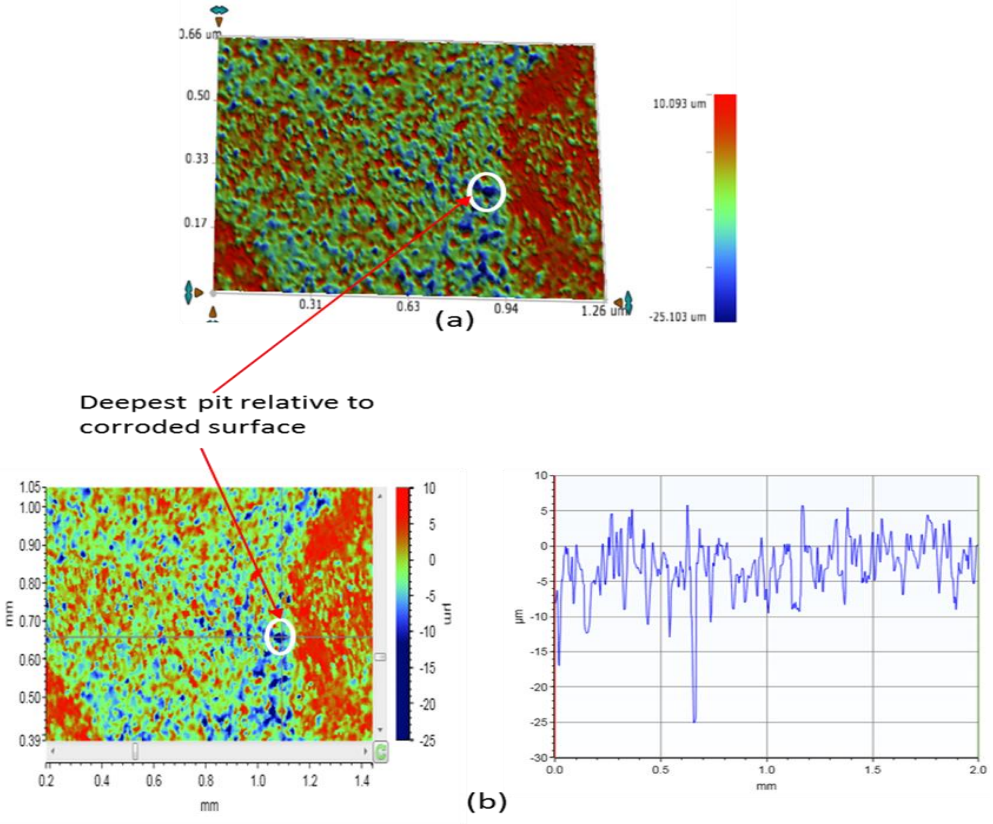

Figure 5-29. 3D and 2D profiles of measurable maximum pits on the surface of X-65 carbon steel; (a) 3D and (b) 2D at 32°C after 168 hours exposed.

5.5.2 Pitting Corrosion Behaviour of Carbon Steel at 42°C

According to Figure 5-30, it is clear that a steady and linear pit growth rate occurs from about 9 µm after 24 hours up to 42 µm after 168 hours. Figure 5-31 provides 3D and 2D images of the deepest pit on an entire sample surface after 168 hours in this condition. Interestingly, despite the evidence of the formation of a protective iron carbonate($FeCO_3$) layer, the role of this particular corrosion product morphology on reducing general corrosion rate appears not to have the same influence on the ability of pits to propagate. The reason behind the continuity of pit growth may be due to the non-uniformity of the coverage of $FeCO_3$ film on steel surface and therefore, the semi-protective nature of the corrosion product layer at this temperature.

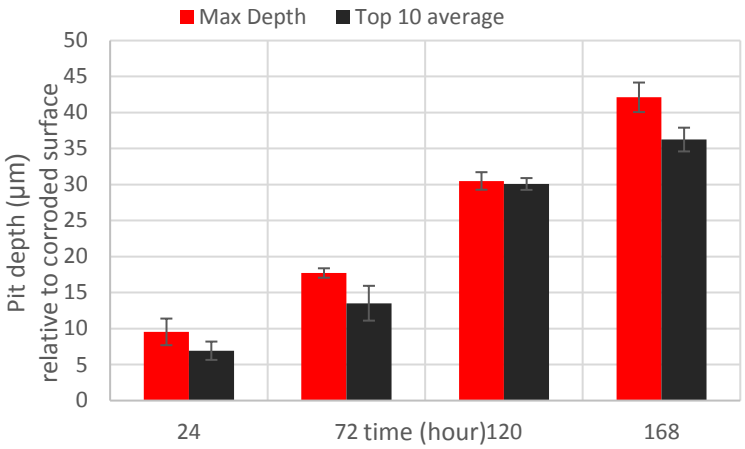

Figure 5-30. Variation of the relative pit depth (maximum and average) with time at T_s=42°C, WCR=0.342 ml/m^2.s over a duration of 168 hours.

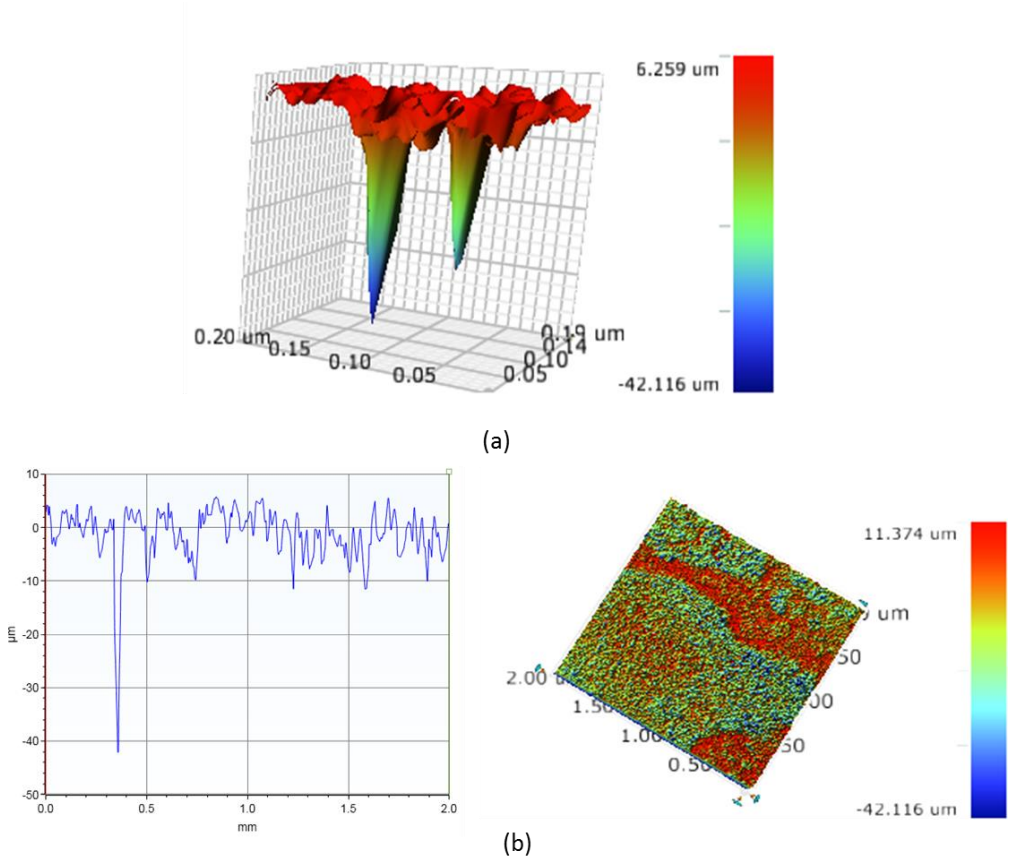

Figure 5-31. Examples of 3D and 2D profiles of measurable maximum pits on the surface of X-65 carbon steel; (a) 3D and (b) 2D at 42°C after 168 hours.

5.5.3 Pitting Corrosion Behaviour of Carbon Steel at 52°C

A shown in Figure 5-32 once pits initiated, a steady growth of pits was observed between 24 and 72 hours. At this period of time, the nature of the corrosion product layer comprises from Fe_3C and very small crystals of $FeCO_3$. After 72 hours, a slightly decreased pit growth rate was observed. Referring to Figure 5-22, the corrosion rate decreases dramatically between 36 and 72 hours as the protective corrosion scale grows and becomes denser. This may indicate that the presence of $FeCO_3$ crystals may be playing a major role in the reduction of both the growth of pits and general corrosion rate.

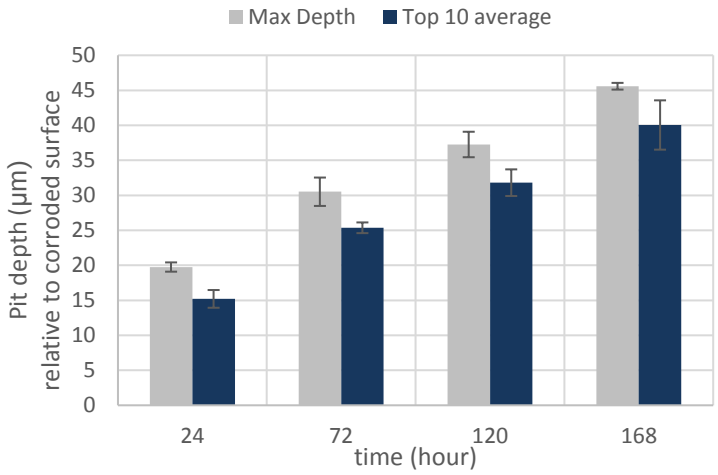

Figure 5-32. Variation of relative pit depth (maximum and average) with time at 52°C, over a duration of 168 hours.

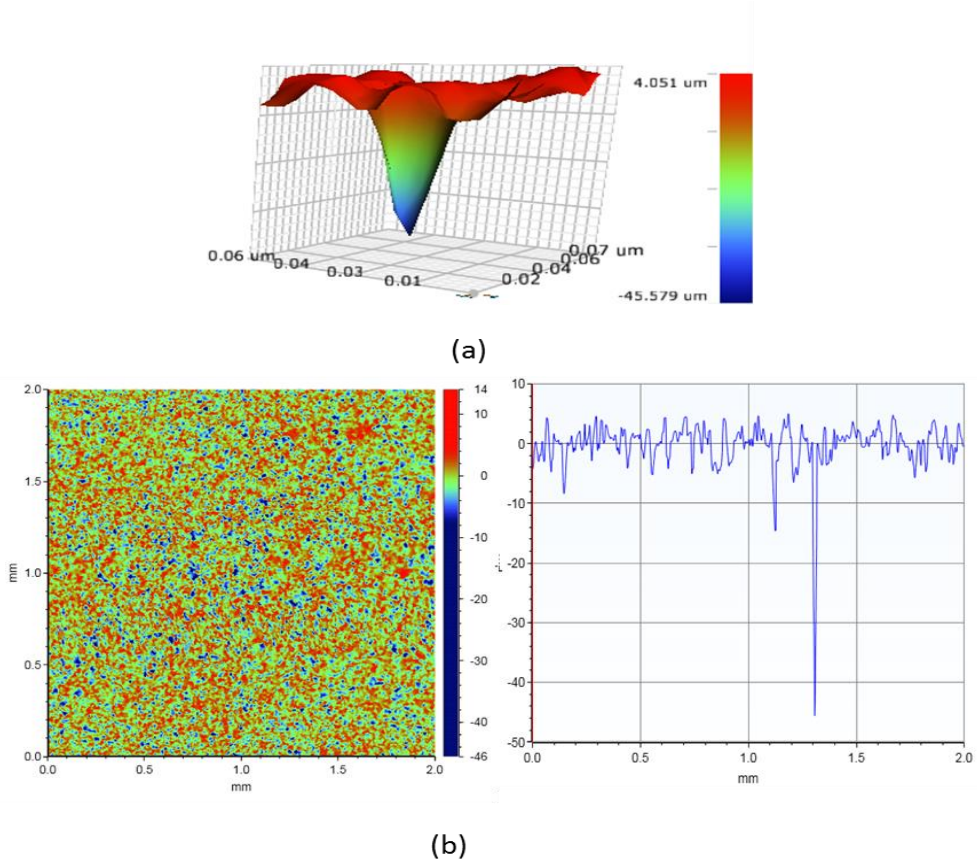

Figure 5-33. 3D and 2D profiles of measurable maximum pits on the surface of X-65 carbon steel; (a) 3D and (b) 2D at 52°C after 168 hours.

According to Figure 5-34, the depth of initiated micro pit generally increases with increasing temperature over a whole time of experiments.

In order to understand the CO_2 corrosion process of carbon steel, the typical microstructure of X65 pipeline should be taken into consideration prior to corrosion process. As mentioned in section 4.2.1 earlier, a common X65 pipeline steel constitutes irregular ferrite and pearlitic grains. The pearlite phase in carbon steel microstructure is formed by layers of ferrite and cementite (Fe_3C) with 88 wt.% of the ferrite phase [199]. Studies [1, 107, 200, 201] have shown that ferrite preferentially dissolves from the steel surface during corrosion reaction of steel in CO_2 saturated environments, hence, an un-corroded cementite (Fe_3C) phase is left behind as a result of the anodic dissolution of ferrite and becomes preferential sites for cathodic reduction reactions of H_2CO_3 and HCO_3^- to take place[1, 107]. This presents the overall corrosion behaviour; general and pitting corrosion, of carbon steel materials exposed to CO_2 environments.

Most of the chemical, electrochemical and transport processes occurring in the system; such as H^+ reduction, H_2CO_3 and HCO_3^- reduction is known to accelerate by increasing temperature, which in turn, increases cathodic and anodic reactions [202, 203]. Therefore, any potential galvanic effects between Fe_3C regions and exposed areas of localised pores and the associated corrosion kinetics would be enhanced by the higher temperature, leading to the more substantial pit growth process at 52°C compared to 42 and 32°C. This trend is consistent with the results reported by Papavinasam and his co-workers [58]. In their study, it was reported that pitting corrosion rates increased from 10 mpy at ≤ 25°C to 80 mpy at ≥ 50°C.

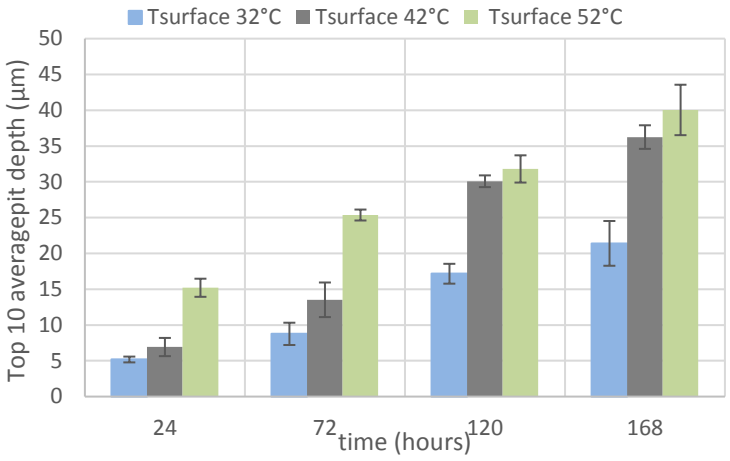

Figure 5-34. Plot depicting the variation of relative pit depth (maximum and average) with time at 32, 42 and 52°C, over a duration of 168 hours.

5.6 Development of the Correlation

One of the main goals of this study was to establish an empirical correlation to calculate corrosion rate in the top of the line by taking into account the effect of most important variables condensation rate and inner steel temperature. From an initial analysis of the corrosion rate responses in Figure 5-35, the effect of each individual parameter is obscured by the interplay between them. To decouple these variables from one another and evaluate the individual effect of WCR and T_s, on corrosion rate, an empirical model was developed based on the database of 23 sets of corrosion rate data for non-film-forming conditions. To obtain the correlation, the average corrosion rate over 168 hours was used. Design Expert version 10 software was used to help in analysis and interpretation of the collected data. The experimental data cover the inner surface temperature range of 5°C to 40°C and WCR range from 0.116 to 1.712 ml/m^2.s.The correlation can be written as:

$$CR=0.36+0.34*WCR +0.008*T_s+0.014*T_s*WCR-0.16*WCR^2- 0.000133*T_s^2 \quad 5.8$$

where WCR is the condensation rate in ml/m^2.s, T_s is the temperature of the inner pipe surface in °C and CR is the top of line corrosion rate in mm/y.

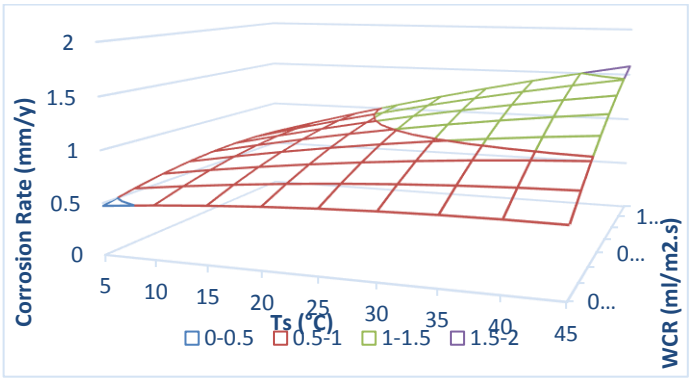

Figure 5-35. A combination effect of surface temperature and water condensation rate on TLC rates.

5.6.1 Comparison of the Experimental and Calculated Data

Experimental data at different gas and pipe temperatures and water condensation rates were compared with the calculated results. It has been found that the top of line corrosion rate predicted by the present correlation is in good agreement with the experimental results as seen in Figure 5-36.

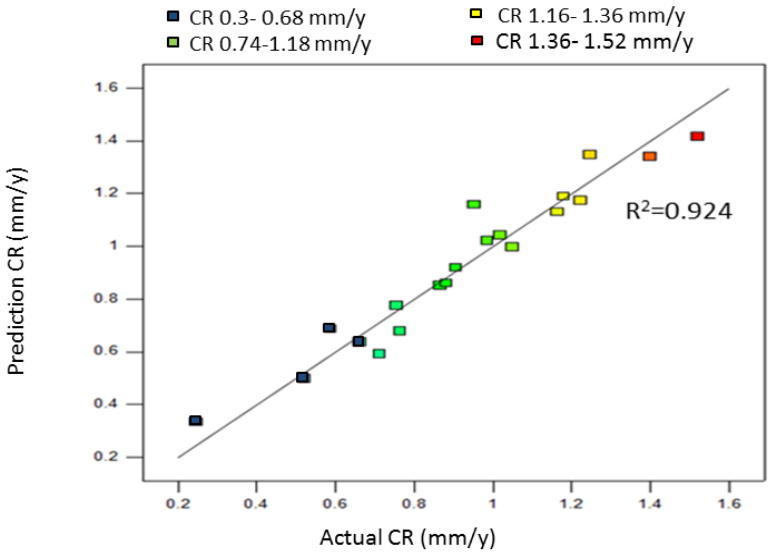

Figure 5-36. Comparison of calculated and experimental TLC rates at 1 bar total pressure.

5.6.2 Empirical Model Verification

The predicted values using the new Equation 5.7 were compared with the experimental results provided by Islam Md et al [157]. It was found that the calculated values at different surface temperatures are in very good agreement with the experimental data Figure 5-37.

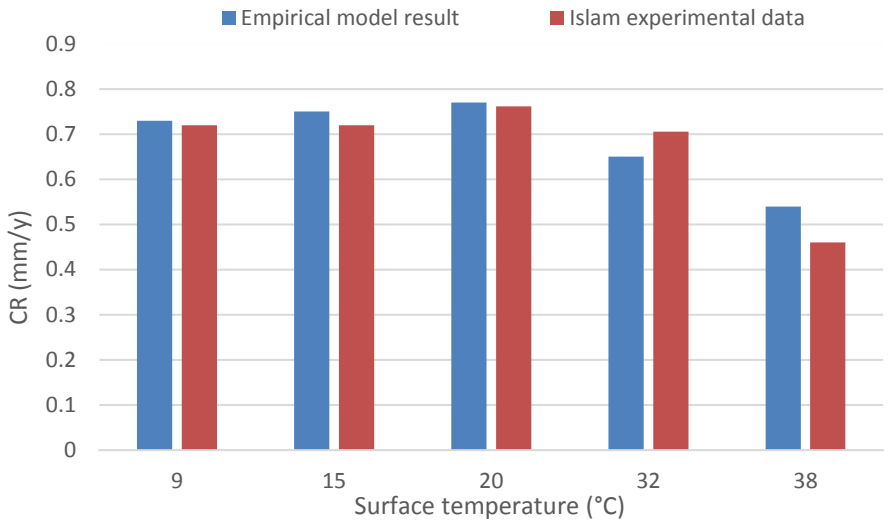

Figure 5-37. Comparison of the experimental result after 168 hours provided by Islam et al. [157] and the calculated TLC by using the empirical model at 1 bar pressure and 40°C gas temperature.

5.6.3 Empirical Model Implementation

The results of the implementation of this model are shown in Figure 5-38 and Figure 5-39. Figure 5-38 illustrates how the calculated corrosion rates vary with water condensation rate at different pipe surface temperature at atmospheric pressure. The water condensation rate has a significant effect on the corrosion rate for both of the surface temperatures 15°C and 40°C. One interesting observation is that the TLC rates at the surface temperature of 40°C are higher than at wall temperature of 15°C for all values of WCR. This due to the fact that the corrosion rate is enhanced at higher temperatures. Figure 5-39 shows the effect of the pipe surface temperature on the TLC rates at different water condensation rate. It can be seen that the

average TLC rate is generally the lowest at the lowest condensation rate. The reason for this is probably that there is more fresh liquid available at higher condensation rate. Additionally, at lower condensation rate the droplet grows slower and is refreshed in less frequency. Therefore, the saturation of iron carbonate ($FeCO_3$) is easier to achieve when there is less liquid available.

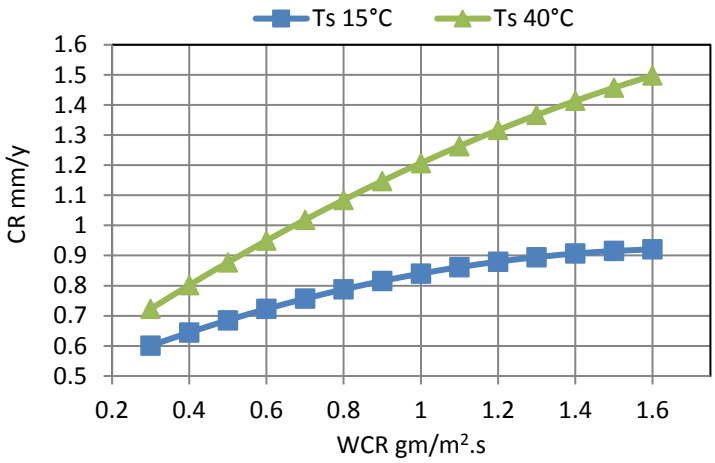

Figure 5-38. TLC rate verses WCR at surface temperatures of 15°C and 40°C and 1 bar total pressure obtained by the model.

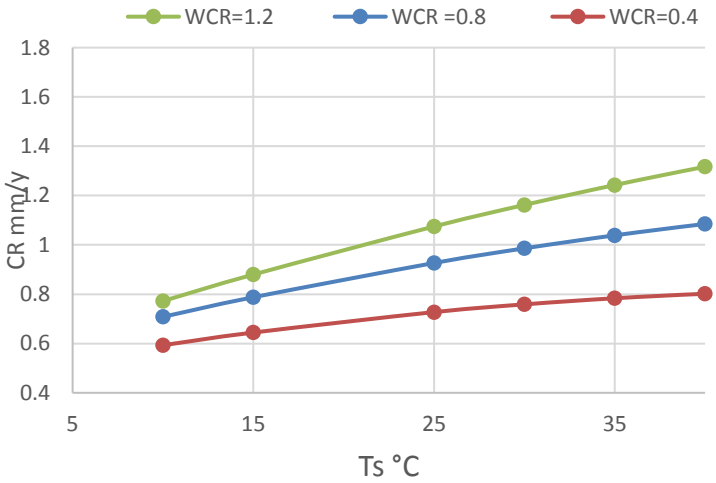

Figure 5-39. The effect of the condensation rate on the general corrosion rate at the top of the pipe at atmospheric pressure.

5.6.4 The Model Limitations

As mentioned previously the model is based on experimental data with no H_2S present in the system. There are strong indications that trace amounts of H_2S have a positive effect on reducing the corrosion rate as the sulphides improve the protectiveness of the film on the surface [148]**.** Therefore the correlation cannot be used in sour corrosion systems where H_2S is dominated or in systems with high contents of organic acids and the application of the model is only valid for conditions when CO_2 dominates. Since the experiments have been conducted at atmospheric pressure the model is only valid for total system pressure of 1 bar.

5.7 Summary

A comprehensive experimental investigation into the effect of condensation rate, surface temperature and iron carbonate saturation on TLC and $FeCO_3$ precipitation rate on carbon steel (X65) in a CO_2 environment was carried out using a combination of weight change and post-experiment surface analysis techniques.

In this study, a new design of the TLC setup was designed, the setup is capable of measuring real T_s and T_g, also it suitable to collect the condensed water and in-situ measure the pH of the solution.

The extensive data obtained in this study gave a better understanding of the TLC mechanism. TLC is found to be governed by surface temperature regardless of water condensation rates (WCR) at a surface temperature lower than 32°C. The results also show that WCR influences the TLC, precipitation rate and scale film formation at a surface temperature higher than 32°C. At surface temperatures greater than 32°C, both of the surface temperature and water condensation rate effect TLC.

On the basis of the experimental data, a new empirical model to predict the TLC rate in the absence of iron carbonate films is developed. The model can

predict the uniform corrosion rate at the top of line at different WCR rates and surface temperatures. Through comparisons with experimental data found in open literature, the model shows reasonable performance in the prediction of TLC.

A new kinetic constant for the calculation of iron carbonate precipitation rate under condensing condition at the top of the line is proposed.

By the processes of the surface analysis of the sample, the evolution of the film formation process has been clarified. Besides, SEM and EDX results have shown that different films are formed at the sample surface. It confirmed that the protective film at the top of the line is made up of iron carbonate crystals ($FeCO_3$).

According to the calculated and experimental precipitation rate, it has been concluded that the kinetic behaviour of $FeCO_3$ films formation at the top of the line is different from that at the bottom of the line.

The relationship between the pitting corrosion behaviour of carbon steel under different surface temperatures and water condensation rate in CO_2 saturated environments at the top of line scenario was investigated. It was concluded that the depth of the initiated pit generally increases with increasing temperature over a whole time of experiments.

Chapter 6. A Mechanistic Model of Dropwise Condensation at Top of the Line in Presence of Non-Condensable Gases

6.1 Introduction

Studies of top line corrosion showed that the corrosion process occurring at the top surface of the pipe is directly affected by water condensation rate and iron solubility in the condensed water. Hence, there is a need to have a full understanding of the mechanism of water condensation from the vapour phase as related to hydrodynamic, thermodynamic, and heat and mass transfer between the interface of the pipe wall and the outside environment.

Condensation is the process by which a water vapour phase converts into a liquid phase. It happens whenever water vapour comes into contact with a surface at a temperature below the saturation temperature corresponding to its vapour pressure[204]. The nature of condensation depends upon whether the liquid thus formed wets or does not wet the solid surface. Condensation may take place in two possible modes:

- Filmwise condensation.
- Dropwise condensation.

In the case of filmwise condensation, the condensate forms a continuous film, and the surface is completely wetted by the condensate. Whereas, in dropwise condensation, the vapour forms droplets instead of a continuous film and the surface cannot be completely wetted. Figure 6-1 shows the two modes of condensation.

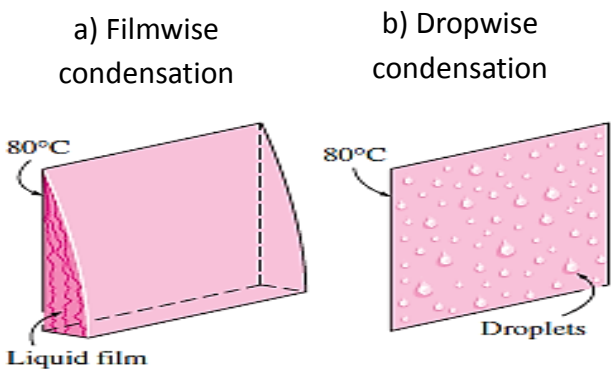

Figure 6-1. Modes of condensation [204]

The report on field cases presented by Gunaltun in 1999 [140] has clearly shown that the condensation type in the top of the line corrosion (TLC) is dropwise condensation [205]. In addition, the theoretical study in dropwise condensation which was done by Yu-Ting Wu et al. [206] showed that dropwise condensation processes occur repeatedly on the condensation surface. They proposed in dropwise condensation processes that primary droplets are first formed at nucleation sites, then the droplets grow by condensation until coalescence occurs between the neighbouring droplets, and then a new generation of drops is formed at sites exposed by coalescence. These again grow to be followed by a third generation and so on until a falling drop sweeps the entire field and the process starts again.

Moreover, the experiments in this study include *in-situ* visual observations shown in Figure 6-2 and support the view that the condensation mode at the top of line corrosion is dropwise.

Basically, dropwise condensation is a heat exchange process if the vapour phase is stagnant and without any non-condensable polluting gases. However, these are not the conditions found in wet gas pipelines, in which the vapour gas is a mixture of condensable and non-condensable gases. The sources of these non-condensable gases in the production and transportation of oil and gas equipment are usually from the gases associated with production gas. Just small amounts of water vapour are

available in the natural gas with a lot of non-condensable and condensable hydrocarbon fractions. In these cases, dropwise water condensation depends on heat exchange as well as mass exchange and hydrodynamics.

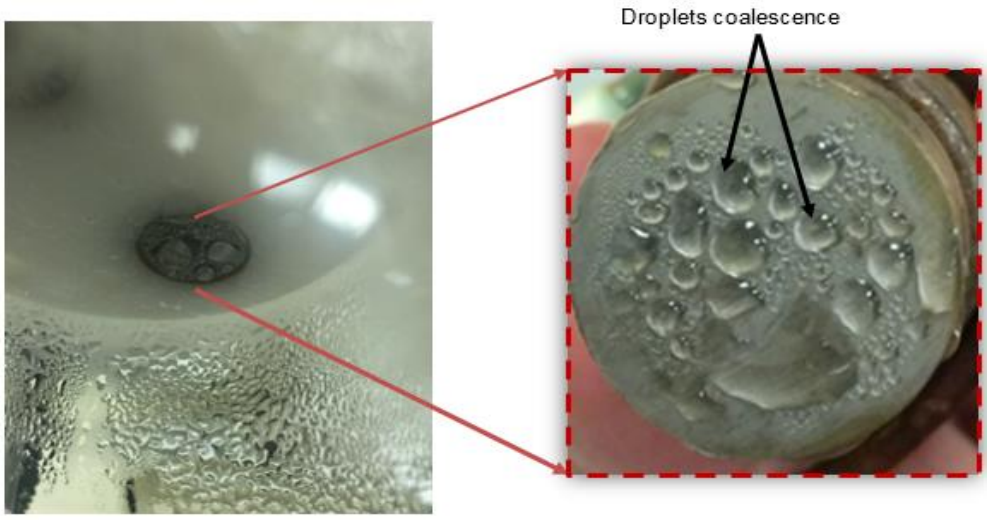

Figure 6-2. Dropwise condensation our direct observations (Nucleation, Growth and Coalescence).

In both theoretical and experimental studies on condensation and corrosion, most researchers did not take the existence of a non-condensable gas into consideration in dropwise modelling, since they postulated that the vapour phase was pure, which is not the real situation seen in the gas and petroleum industry, although, this assumption is sometimes acceptable i.e. for some simple heat transfer system. Until now, very few researchers have mentioned the issue related to the presence of non-condensable gases, such as Gener et al.[207], Wang et al. [208] and in 2004 Shixue et al [209], they observed that about 10% of non-condensable gas can decrease the heat transfer rate by approximately 60% and 500 ppm of nitrogen gas in the vapour ethanol mixture could reduce the heat transfer by nearly 50%. However, these researchers did not propose a physical mechanism from their tests.

In fact, the presence of non-condensable gases in the working fluid reduces the heat transfer rate [210-213]. The two regimes of condensation, namely filmwise and dropwise condensation, are affected by the presence of the

non-condensable gases in the vapour, but it is more significant for the case of dropwise condensation than the filmwise mode. This is due to the fact that the non-condensable gases carried to the condenser surface by the condensing vapour accumulate and cause a reduction in heat transfer coefficient by reducing the vapour partial pressure. This reduction might be large enough to reduce the rate of dropwise condensation.

In the present study, the mechanistic model of dropwise condensation established by Zhang *et al*. [7] was replicated and implemented into a python program to predict the condensation rate at different conditions in the presence of non-condensable gases in the vapour phase. In this model, heat exchange and droplets distribution equations from the model of pure vapour dropwise condensation were modified by including heat conduction resistance through the droplets and vapour-liquid interfacial resistance. The association between heat exchange and mass exchange balance conditions was built up through those mass exchange and heat transfer coefficients in the hydrodynamic part of the investigation.

Additionally, in this thesis, Zhang et al.'s model was modified, the domain of calculation had to be adapted to the static state scenario to take into account the buoyancy-driven effect. The maximum droplet diameter was also determined based on a force analysis on a single droplet. Since the droplet lifetime has a significant effect on the corrosion rate, scale precipitation rate, and iron carbonate supersaturation [10, 91, 143, 146, 154], a useful modification procedure to calculate the droplet lifetime was established. The modified model has been validated against experimental results and used to analyse the factors affecting the corrosion rate, such as temperature and CO_2 partial pressure.

6.2 Zhang et al.'s Condensation Rate Model

To predict the amount of water vapour condensing at the inner surface of the pipe, one needs to find two things: the critical droplet diameter and the heat

and mass transfer through each droplet (from the gas bulk to the gas-liquid interface). As the water vapour condenses on the wall, it forms a family of droplets with different sizes. A force analysis on this droplets must be conducted to predict their diameters. Once temperature profile and the droplet size are known, the heat transfer through the condensed water droplet can be predicted.

6.2.1 Heat Transfer in Dropwise Condensation

The heat transfer process in the wet gas pipeline is influenced by a number of variables, including environmental, physical, and metallurgical parameters as illustrated in Figure 6-3. The identified parameters affecting heat transfer at dropwise condensation include:

- Inner wall and gas temperature.
- Non-condensable gas concentration.
- Gas pressure.
- Gas velocity.
- Condenser thermal conductivity.
- Inside pipe diameter.
- Surface structure properties.

6.2.2 Drop-Size Distribution Function

For dropwise condensation process the drop size distribution must be specified. The high magnification visual observations of the condensation process at any time show that there is a range of droplets with different sizes on the condenser surface [33, 214-217].

To calculate the droplet size distribution, Zhang et al (2007) used the Rose and Glickman [33] expression:

$$N(r)dr = \frac{n}{\pi r^2 r_{max}} \left(\frac{r}{r_{max}}\right)^{n-1} dr \qquad 6.1$$

where:

$N(r)dr$: Number of drops per area with radius, r, over one m^2 surface area, m^2

r_{max}: Maximum radius of dropthe let, m

n: Exponent constant, the alue of n is usually taken to 1/3.

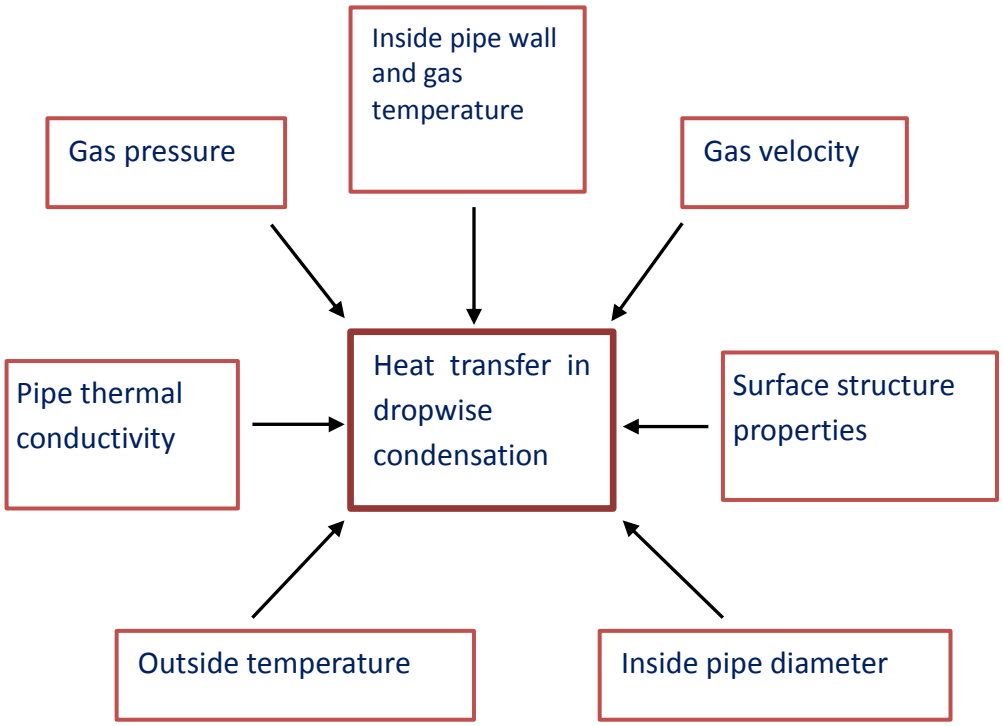

Figure 6-3. The common factors that influence dropwise condensation in the wet gas pipeline plants.

6.2.3 Heat Flux through a Single Droplet in Dropwise Condensation

To build up a model of heat transfer throughout a single droplet one needs to first identify all contributing thermal resistances between the saturation temperature of the vapour and the temperature of the outer insulation layer.

The overall heat flux through a single droplet during the dropwise condensation process can be divided into several stages in which several thermal resistances are connected in series [34, 218, 219]. For the purposes of this model, all resistances ($R_w, R_l, R_d, R_c \; and \; R_i$) will be presented as the temperature drop (ΔT).

The thermal resistances shown in Figure 6-4 are composed of:

- Drop curvature resistance. This is important especially for small droplets since the most of the heat is transferred through these small droplets, ΔT_c.
- The vapour/liquid interface resistance, ΔT_i
- Heat conduction resistance through a hemispherical droplet itself, ΔT_d
- Heat conduction resistance through the pipe wall and the protection layer to the outside environment, ΔT_w and ΔT_lrespectively.

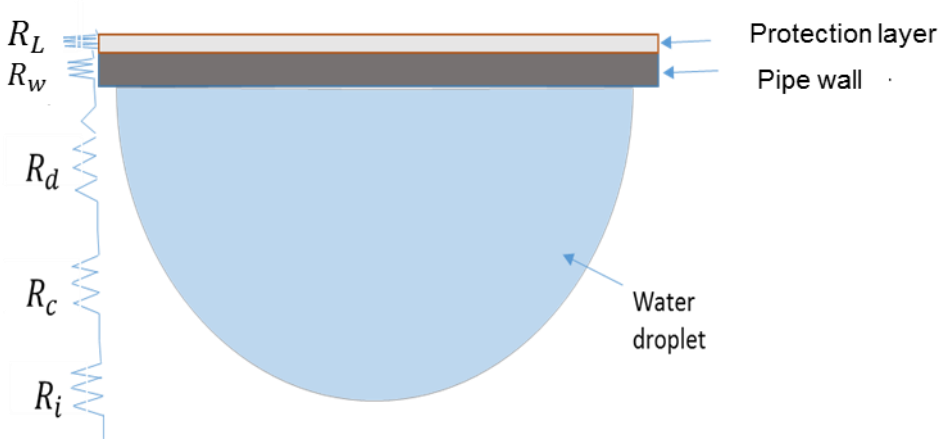

Figure 6-4. Droplet thermal resistances through one condensed water droplet.

6.2.4 Heat Balance in the Presence of Non-condensable Gases

It has been stated that during the dropwise condensation (DWC) process the main resistance for heat transfer comes from the existence of non-condensable gas [208, 220, 221].

The presence of non-condensable gases, such as air, carbon dioxide, or light hydrocarbons in a condensing environment reduces heat and mass transfer during the condensation process. The accumulation of non-condensable gases even in a small amount near the condensing surface acts as a barrier and prevents the diffusion of the vapour from the bulk mixture to reach the condensing surface and offers an extra thermal resistance and decreases the heat and mass transfer coefficients.

Due to the fact that DWC is a stochastic process, the approach to find total heat transfer is to calculate the heat transfer through a single droplet of a particular size and then the total heat transfer is determined by integrating over the distribution of sizes.

$$Q_T = \int_{r_{min}}^{r_{max}} q(r)N(r)dr \qquad 6.2$$

where:

Q_T: Total heat flux between the gas phase and the droplets (W/m^2).

$q(r)$: Heat flux through one droplet of radius r, (W/m^2).

$r_{min}\ and\ r_{max}$: Minimum and maximum droplet radius respectively, m.

The total heat transfer (Q_T) includes the heat transfer resulting from the presence of non-condensable gas and phase change can be written as:

$$Q_T = Q_g + Q_c \qquad 6.3$$

where $\mathrm{Q_c}$ is the heat flux is released from the condensation of water vapour at the droplet surface (latent heat flux) in W/m^2 and $\mathrm{Q_g}$ is the heat flux through the gas boundary layer to the liquid interface in W/m^2.

In a fully developed gas flow $\mathrm{Q_g}$ can be given by:

$$\mathrm{Q_g} = h_g(T_b^g - T_i^g) \quad 6.4$$

While the latent heat flux $\mathrm{Q_c}$ can be calculated by:

$$\mathrm{Q_c} = \dot{\mathrm{m}}\, H_{fg} \quad 6.5$$

The total heat flux is given by:

$$Q_T = h_g\left(T_b^g - T_i^g\right) + \dot{\mathrm{m}} H_{fg} \quad 6.6$$

where:

$\dot{\mathrm{m}}$ is the condensation rate of water, ml/m^2.s.

H_{fg} is the latent heat of vaporization/condensation of water vapour, J/k$_\mathrm{g}$.

h_g is the heat transfer coefficient in the gas phase estimated from the following correlations, W/m^2/K

T_b^g is the gas bulk temperature, K

T_i^g is the gas droplet interface temperature, K

By assuming the shape of the condensed droplet is hemispherical, the temperature gradient inside the droplet can be represented as shown in Figure 6-5.

The equation of Dittus-Boelter [222] can be used to calculate the heat transfer coefficient (h_g) of the gas boundary layer for a long pipeline under flowing conditions.

$$h_g = Nu * \frac{k_g}{D} \quad 6.7$$

where:

Nu is the Nusselt number $= 0.023Re^{0.8}Pr^{0.4}$, dimensionless number.

Re is the Reynolds number = $\frac{v_g \rho_g D}{\mu_g}$, dimensionless number.

Pr is the Prantdl number = $\frac{C_p \mu}{k_g}$, dimensionless number.

C_p = Specific heat capacity, J/K.kg.

D = Pipe diameter, m.

k_g = Thermal conductivity of gas phase, W/m.K.

v_g = Gas velocity, m/s.

ρ_g = Gas density, kg/m^3.

μ_g = Gas viscosity, Pa.s.

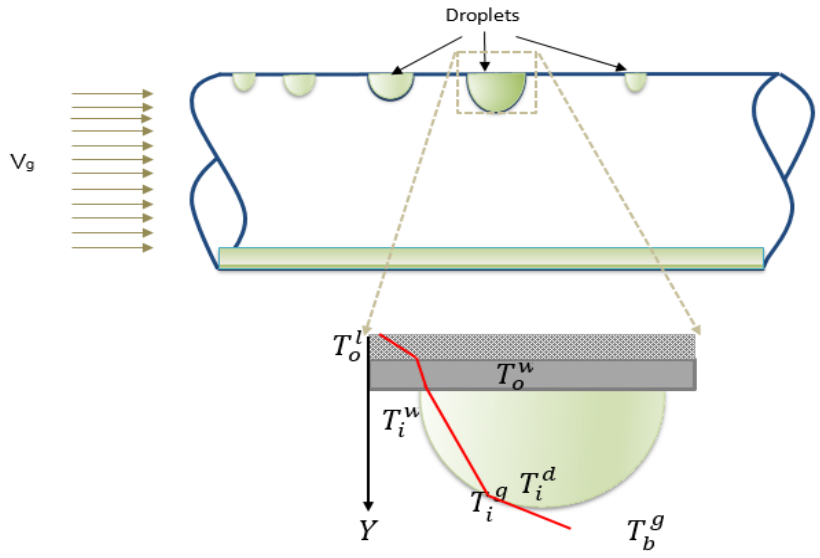

Figure 6-5. Temperature difference in a single droplet: T_i^w is the inner wall temperature, T_o^w is the outer wall temperature, T_i^d is the interfacial temperature in the liquid side, T_b^g is the bulk vapour temperature, T_i^g is the gas droplet interface temperature and T_o^l is the outer insulation layer temperature. Adapted from [7].

6.2.5 Temperature Difference through a Droplet

To calculate the condensation rate, the total heat transfer should be calculated by finding the gas droplet interface temperature T_i^g. By taking into consideration that the heat transferred from the gas to the droplet passes through the droplet, the pipe wall and insulation layer to the outside environment T_i^g can be determined as shown in Figure 6-5. The total temperature difference between the vapour and the pipe outside environment ΔT_t can be stated as;

$$\Delta T_t = T_i^g - T_o^l = \Delta T_c + \Delta T_i + \Delta T_d + \Delta T_w + \Delta T_l \qquad 6.8$$

where:

ΔT_c is the temperature drop at the interface due to droplet curvature and can be calculated as [34]: $\Delta T_c = \frac{2\sigma T_i^g}{\mathrm{H_{fg}}}$ 6.9

ΔT_i is the temperature difference due to vapour/liquid interfacial resistance (T_i^g-T_i^d) in K can be also calculated through [223]:

$$\Delta T_i = \frac{q(r)}{4\pi r^2 h_i} \quad 6.10$$

The heat transfer coefficient at the droplet interface h_i can be calculated as [34]:

$$h_i = \frac{2\alpha}{2-\alpha}\left(\frac{M_{H_2O}}{2\pi R T_{sat}}\right)^{0.5} \frac{{H_{fg}}^2}{T_{sat} V_g} \quad 6.11$$

where:

α: The condensation coefficient is defined as the ratio between the number of the molecules condensed on the liquid surface and the number of the molecules falling on it (it is taken as unity).

M_{H_2O}: The molecular weight of water =18 g/mol.

R: Gas constant=8.31 J/kmol/K.

T_s: Saturated temperature in K.

V_g: Specific volume of water vapour in m^3/k_g.

ΔT_d is the temperature drop due to the heat conduction through a hemispherical droplet ($T_i^d - T_i^w$), K, and can be re-written as [214]:

$$\Delta T_d = \frac{q(r)}{4\pi r^2 \mathrm{k_{H_2O}}} \quad 6.12$$

ΔT_w is the temperature drop due to the heat conduction through the pipe wall ($T_i^w - T_o^w$), K, and can be determined by Equation 6.13 [34]:

$$\Delta T_w = \frac{q(r) d_w}{4\pi r^2 k_w} \quad 6.13$$

ΔT_l is the temperature drop due to the heat conduction through the insulation layer ($T_o^w - T_o^l$), K, can be calculated through [34]:

$$\Delta T_{l=} \frac{q(r)d_l}{4\pi r^2 k_l} \quad 6.14$$

where:

r: radius of the droplet, m.

σ: vapour/liquid surface tension, N/m.

h_i: heat transfer coefficient at the droplet interface, W/m^2.K.

$\mathrm{k_{H_2O}}$: thermal conductivity of the water, W/m/K.

d_w: thickness of pipe wall, m.

k_w: thermal conductivity of the steel pipe wall, W/m/K.

d_l: thickness of the insulation/protection layer, m.

k_l: thermal conductivity of the insulation/protection layer, W/m/K.

Finally, by substituting all of the equations 6.9, 6.10, 6.12, 6.13, 6.14 into Equation 6.8 the total heat flux through a single droplet of radius r $\mathrm{q_{(r)}}$ can be determined as:

$$T_i^g - T_o^w = \frac{2\sigma T_i^g}{H_{fg}} + \frac{q(r)}{4\pi r^2 h_i} + \frac{q(r)}{4\pi r^2 \mathrm{k_{H_2O}}} + \frac{q(r)d_w}{4\pi r^2 k_w} + \frac{q(r)d_l}{4\pi r^2 k_l} \quad 6.15$$

Equation 6.15 can be re-written as:

$$\mathrm{q_{(r)}} = \frac{\left[T_i^g\left(1-\frac{2\sigma T_i^g}{H_{fg}}\right)-T_o^w\right]4\pi r^2}{\left[\frac{2}{h_i}+\frac{\mathrm{r}}{\mathrm{k_{H_2O}}}+\frac{d_w}{k_w}+\frac{d_l}{k_l}\right]} \quad 6.16$$

For the condensing surface which is covered by a large number of droplets of various sizes the total heat transfer per unit area Q_T can be calculated by substituting the $\mathrm{q_{(r)}}$ from Equation 6.16 into equation 6.2.

$$Q_T = \int_{r_{min}}^{r_{max}} q(r) N_{(r)} d_r = \int_{r_{min}}^{r_{max}} \frac{\left[T_i^g\left(1-\frac{2\sigma T_i^g}{H_{fg}}\right)-T_o^w\right]4\pi r^2}{\left[\frac{2}{h_i}+\frac{\mathrm{r}}{\mathrm{k_{H_2O}}}+\frac{d_w}{k_w}+\frac{d_l}{k_l}\right]} N_{(r)} d_r \qquad 6.17$$

The two heat flux equations 6.6 and 6.17 have three unknowns $\mathrm{Q_T}$, $\mathrm{T_i^g}$ and $\dot{\mathrm{m}}$, to calculate these unknowns a further mass balance equation can be used. The presence of the non-condensable gases affects not just the heat transfer through the droplet boundary layer but the mass transfer can be affected as well. Therefore, the mass and heat transfer should be coupled and solved simultaneously. The condensation rate $\dot{\mathrm{m}}$ can be written as:

$$\dot{\mathrm{m}} = \rho_g \beta_g (x_b^g - x_i^g) \qquad 6.18$$

where:

ρ_g is the gas density, kg/m^3

β_g is the mass transfer coefficient in the gas boundary layer, m/s.

x_b^g is the mass fraction of water vapour in the bulk gas flow, $\mathrm{kg_v/kg_g}$.

x_i^g is the mass fraction of water vapour at the gas-liquid interface, $\mathrm{kg_v/kg_g}$.

If assuming that the pressure inside the pipe is known, then the mass fraction of water vapour x (T) in a saturated gas mixture depends only on the gas temperature and can be calculated according to:

$$x(T) = \frac{P_{sat}(T) M_{water}}{P_{tot} M_{gas}} \qquad 6.19$$

where:

$P_{sat}(T)$ is the saturation pressure in (kPa) and can be calculated by Antoine's equation as:

$$P_{sat}(T) = \frac{10^{(a-b)/(c+T)}}{760} \qquad 6.20$$

where :

T is the gas temperature in degrees centigrade

a, b and C are specific constants

P_{tot} is the total pressure, KPa and M_{water} and M_{gas} are the molecular weights of the water and the gas mixture respectively, g/mol.

Now the mass fraction of the water vapour in the gas phase and at the gas-liquid interface can be rewritten as:

$$x_b^g = x\left(T_b^g\right) = \frac{P_{sat}(T_b^g)M_{water}}{P_{tot}M_{gas}} \quad 6.21$$

$$x_i^g = x\left(T_i^g\right) = \frac{P_{sat}(T_i^g)M_{water}}{P_{tot}M_{gas}} \quad 6.22$$

Stephan [186] stated an equation which can be used to estimate the mass transfer coefficient β_g in the gas , as follows:

$$\rho_g \beta_g = \frac{h_g}{C_p} Le^{-\frac{2}{3}} \quad 6.23$$

where:

Le is the Lewis number = $\frac{K_g}{\rho_{gas} C_p D_v}$, dimensionless;

D_v is the diffusivity factor of water vapour in the gas phase, m^2/s and K_g is the thermal conductivity, W/m.k.

By substituting 6.21, 6.22 and 6.23 in 6.18, the condensation rate can be rewritten as:

$$\dot{m} = \left(\frac{h_g}{C_p} Le^{-\frac{2}{3}}\right)\left(\frac{P_{sat}\left(T_b^g\right) - P_{sat}(T_i^g)\, M_{water}}{P_{tot} \qquad M_{gas}}\right) \quad 6.24$$

Now equation 6.6 can be rewritten as:

$$Q_T = h_g\left(T_b^g - T_i^g\right) + H_{fg}\left(\frac{h_g}{C_p} Le^{-\frac{2}{3}}\right)\left(\frac{P_{sat}\left(T_b^g\right) - P_{sat}\left(T_i^g\right) M_{water}}{P_{tot} \qquad M_{gas}}\right) \quad 6.25$$

To solve equations 6.25 and 6.17 one needs to find r_{max} and r_{min}. The minimum radius of the droplet that can be formed at a given sub-cooling surface can be calculated as [219]:

$$r_{min} = \frac{2T_s\sigma}{H_{fg}\rho\Delta T} \quad 6.26$$

where ΔT is the wall sub-cooling temperature and T_s represents the vapour saturation temperature both of these temperatures being in K.

Zhang et al. [7] developed the calculation of the maximum radius of the droplet by applying a forces balance on a single droplet, which is shown in Figure 6-6.

All the forces acting on a single droplet at the top of the pipe which shown in Figure 6-6 can be expressed as:

$$F_D^x = \frac{1}{2} C_D * \rho_g * V_g^2 * A \quad 6.27$$

$$F_f^x = K_f * \sigma * r \quad 6.28$$

$$F_g^y = \frac{4}{6} \rho_{water} \pi g r^3 \quad 6.29$$

$$F_D^y = \frac{1}{2} F_D^x \quad 6.30$$

$$F_\sigma^y = 2\sigma\pi r \quad 6.31$$

$$F_b^g = \frac{4}{6} \pi \rho_g r^3 \quad 6.32$$

When the surface tension force and the buoyancy forces exceed the gravity and downward drag forces, the droplet will fall. However, the critical droplet radius (maximum radius) can be calculated when:

$$F_{\sigma}^{y} + F_{b}^{g} = F_{D}^{y} + F_{g}^{y}$$

$$C_D * \rho_g * V_g^2 * A = \frac{8}{3}\pi g r^3 \left(\rho_{water} - \rho_g\right) - 2\sigma\pi r$$

Therefore:

$$r_{max} = \frac{3(C_D * \rho_g * V_g^2 * A + 2\sigma\pi r)}{8\pi\sigma} \qquad 6.33$$

While the sliding maximum radius can be found when $F_D^x = F_f^x$, and can be calculated as:

$$\frac{1}{2} C_D * \rho_g * V_g^2 * A = K_f * \sigma * r$$

$$r_{(\max)slid.} = \frac{C_D * \rho_g * V_g^2 * A}{2K_f\sigma} \qquad 6.34$$

$$A = \frac{\pi(r_{max})^2}{2}$$

where:

C_D is the drag coefficient.

A is the frontal area of the droplet, m^2.

V_g is the velocity of the flowing gas, m/s.

K_f is the coefficient of friction, which is a function of the roughness of the inner surface.

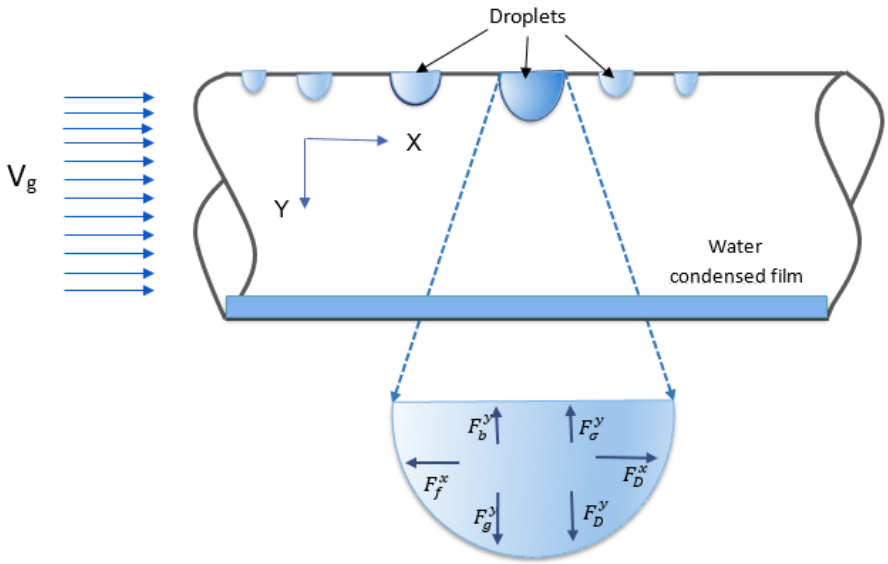

Figure 6-6. Single droplet goes through the following forces: F_b^y=gas buoyancy, F_σ^y=surface tension force, F_g^y =gravity force, F_D^y=flow drag force in y-direction, F_f^x=friction force between the liquid droplet and solid wall, F_D^x=flow drag force in x- direction, V_g=gas velocity. Reproduced from [7].

6.3 Validation of the Zhang's Condensation Model for Pipe Flow Conditions

Any predictive model should be carefully validated against experimental data if possible. To date, even in the original reference, there has not been any comprehensive comparison between the predicted and actual condensation rates using the model of Zhang et al. [7]. In this study, the validation used a variety of experimental and real field data which were found in the open literature. The real field data used to validate the model are diverse and range from low pressure to high pressure, low velocity to high velocity and various realistic temperatures in the field. Table 6-1 shows the data used for verification, the effect of the inlet gas velocity is used as a key parameter to compare the predicted condensation rate using the Zhang model and field and experimental data.

Table 6-1. Condensation rate comparison.

Temperature (°C)	Velocity (m/s)	Pressure (bar)	Condensation rate by using Zhang et al. model (ml/m^2.s)	Condensation rate from literature (ml/m^2.s)	(%) Deviation in predicted condensation
77	1	100	0.36	0.22 [117]	63.0
66	2.4	28	0.54	0.50 [224]	8.8
50	3.2	32	0.27	0.25 [224]	8.0
40	5	3	0.46	0.50 [7]	8.0
90	8.7	28	4.05	3.40 [224]	19.0

The first data row in Table 6-1 is from Svenningsen and his co-workers [117], which uses very high pressure 100 bar and very low velocity 1 m/s. The 2nd, 3rd and the fifth row of data are real field data, available from the Bongkot gas field in the Gulf of Thailand which was published in Gunaltun et al work[224]. The Bongkot field has eleven different flow lines (Line A to line K) operating at various operational conditions, the data used in this comparison is from line A, B, and C. The fourth row of experimental information are from Zhang et al study [7].

The calculated condensation rate from the model and condensation rate which obtained from open literature are plotted against the inlet gas velocity in Figure 6-7. From this figure, it can be seen that generally a reasonably good agreement is achieved between the model prediction and field data at velocities more than 1 m/s. It can be observed that in a range from 2.4 to 8.7 for the gas velocity, the values of the discrepancy of the real and experimental and predicted condensation rate is 8.8%, 8% and 9% for gas

velocities 2.4, 3.2, and 5 m/s respectively, and it becomes about 19% when the gas velocity is increased to 8.7 m/s.

While, at very low velocities (<1 m/s), the model over-predicts the condensation rate significantly, and the deviation percentage of the calculated condensation rate is about 63%. This relatively high value of discrepancy may be due to the fact that, at low velocity and steady conditions, the heat transfer in the vapour phase has a significant contribution from natural convection, not only by forced convection. The convection heat transfer coefficient is a strong function of velocity, which means, the higher the velocity, the higher the convection heat transfer coefficient [225]. Therefore, the heat transfer coefficients encountered in natural convection are usually much lower than those encountered in forced convection. Consequently, the calculated condensation rate should be significantly lower. As the model is established for forced convection conditions, it is unable to correctly predict the condensation rate and the calculated water condensation is higher than the accurate value.

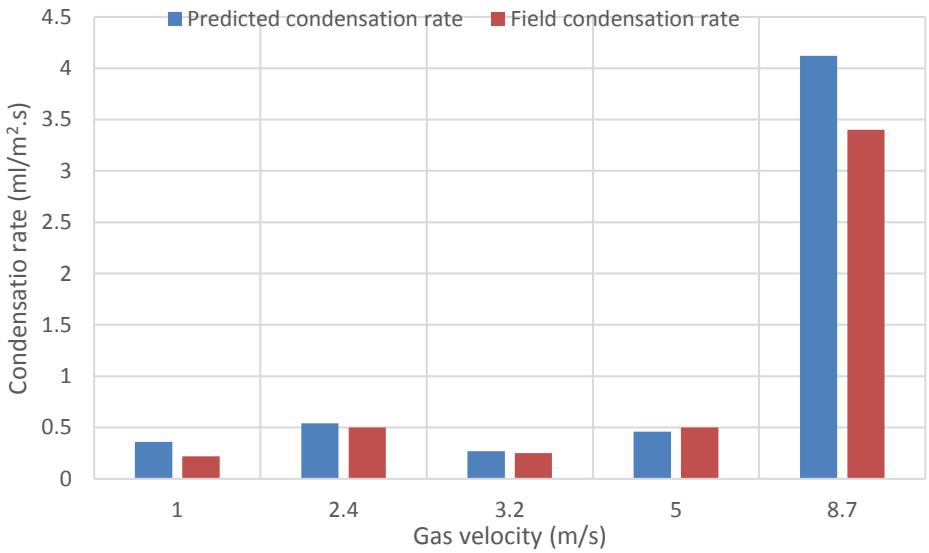

Figure 6-7. Comparison of condensation rate between calculated and real oilfield condensation rate available in the open literature. At 1m/s from [117], 2.4, 3.2 and 8.7 m/s from [224] and 5 m/s from [7].

6.4 Model Results and Parametric Study for Pipe Flow Conditions

The mechanistic model of Zhang and his co-workers' has been implemented in the Python programming language. It can predict the condensation rate for varying input parameters of velocity, gas and pipe temperature, internal pipe diameter and total pressure. The performance of the model has been validated through comparison with experimental and real field data which is available in the open literature [117, 224] and against experiments with a specially designed rig for static flow conditions, the test section design shown in Figure 4-2. In this chapter, a method to calculate a droplet lifetime based on condensation rate at static state is presented.

6.4.1 Influence of the Gas Phase Temperature on the Predicted Condensation Rate

The calculated water condensation rates according to Zhang's model at 1 bar total inlet gas pressure are plotted against the inlet gas temperature in Figure 6-8. It can be seen that the condensation rate is strongly dependent on the inlet temperature of the gas phase. For example, increasing the temperature difference between the inlet gas and outside environment temperature from 20°C to 60°C leads to a 12-fold increase in condensation rate, from 0.0883 ml/m^2.s to 1.05 ml/m^2.s and a further increase in temperature difference from 60°C to 90°C leads the condensation rate to increase 3.5 times. This further confirms that the condensation rate is highly dependent on the inlet gas temperature. This observation can be explained as follows:

Figure 6-9 represents schematically the basic outline of water phase diagram. It is clear from the phase diagram that at a higher temperature the amount of water vapour in the gas phase is larger according to the thermodynamics of vapour-liquid equilibrium. The amount of water available for condensation is, then, larger [226].

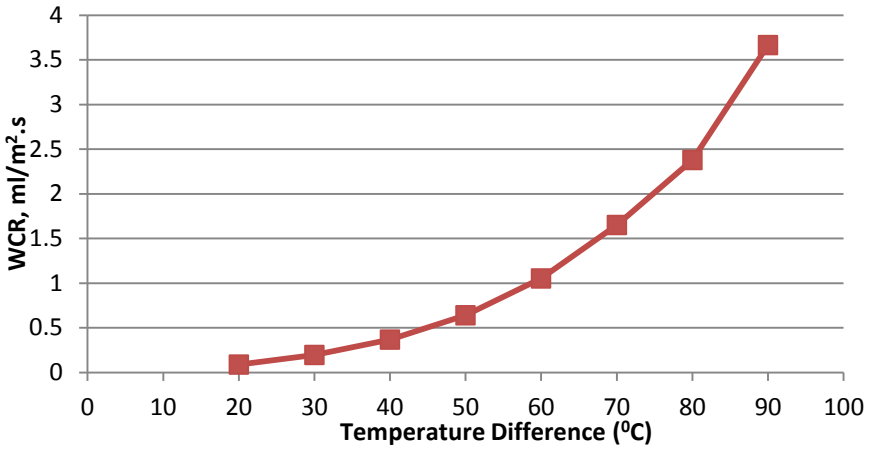

Figure 6-8. The effect of the inlet gas temperature on predicted water condensation rate at inlet total gas pressure =1 bar.

The second explanation is that, at a higher temperature, the difference in temperature between the gas phase and the cooled wall is greater, thus enhancing heat and mass transfer according to Nusselt's theory of condensation [185] later modified by Stephan [186].

The influence of the gas temperature on the condensation rate was studied at a range of total system pressure from 1-10 bars. The results are plotted in Figure 6-10. From this figure, it can be seen that, at a specific gas temperature, as the total pressure increased the condensation rate decreased. For example, at a gas temperature of 50°C, the condensation rate decreased from 0.64 ml/m^2.s at 1 bar to 0.45ml/m^2.s at 2 bar and to 0.203 ml/m^2.s at 10 bar. This can be explained by the fact that as a total system pressure increases the molar fraction of water present in the gas phase decreases, then the amount of vapour gas available to condensation process decreases. From Figure 6-10, it is interesting to see that, the influence of the pressure on the condensation rate at a gas temperature more than 50°C is more obvious than at temperatures less than 50°C. This is due to the calculated condensation rate values being higher at a higher temperature.

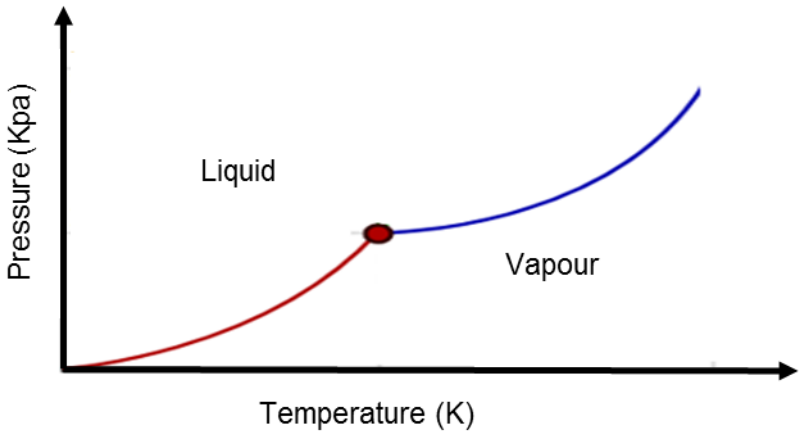

Figure 6-9. A typical schematic phase diagram of water. [226]

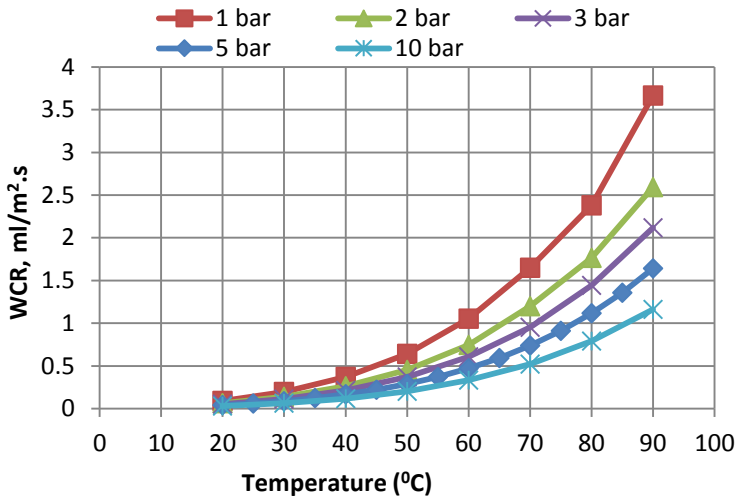

Figure 6-10. The effect of the inlet gas temperature on the predicted water condensation rate at different inlet gas pressure.

6.4.2 Influence of the Absolute Pressure on the Condensation Rate

The effect of the total pressure on the calculated condensation rate has been investigated over a wide range of pressure from 1 bar to 100 bar and inlet gas temperature of 25°C as shown in Figure 6-11. It can be observed that increasing the total pressure does not significantly affect the predicted water condensation rate. The reason for this behaviour is the fact that, theoretically, the thermodynamic equilibrium of the liquid and vapour phases is greatly

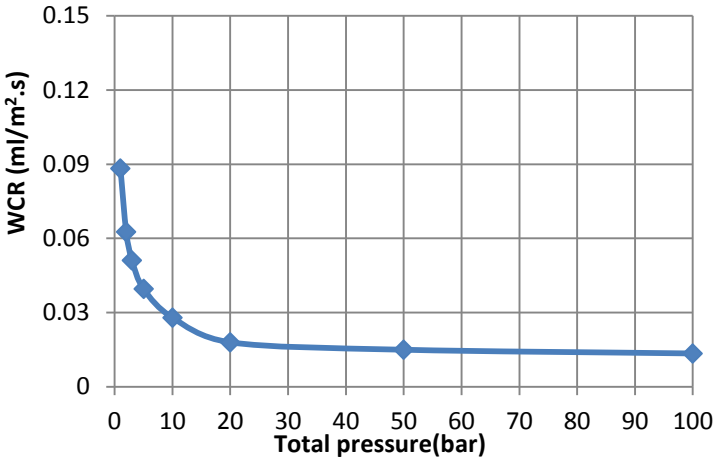

Figure 6-11. The effect of the gas pressure on predicted water condensation rate at inlet gas temperature = 25°C.

dependent on the pressure as is clear from Figure 6-9. The higher the pressure, the lower is the molar fraction of water vapour available in the gas phase. Consequently, less water vapour is available for condensation, this leads to decrease the condensation rate. From another hand, the pressure is involved in the heat and mass transfer in the gas phase as well. At higher pressure, the heat and mass transfer increase because the gas phase becomes denser. This means that at higher pressure, the gas density is higher and according to equation 6.35 the Reynolds number (Re) becomes greater.

$$Re = \frac{\rho_g * V_g * D}{\mu_g} \qquad 6.35$$

Increasing the Reynolds number leads to an increase in the heat transfer coefficient (h_g) according to Dittus and Boetler equation [222]:

$$\frac{h_g * D}{\lambda_g} = 0.023 * Re^{0.8} * Pr^{0.3} \qquad 6.36$$

As a result, the heat transfer coefficient (h_g) increases in the gas phase as the pressure increases. This implies more heat can transfer through the pipe, which allows a larger amount of water to condense. Additionally, the heat

transfer coefficient increases the mass transfer coefficient according to Equation 6.37

$$\rho_g * \beta_g = \frac{h_g}{C_{pg}} * Le^{2/3} \quad 6.37$$

where Le is the Lewis number and can be calculated as:

$$Le = \frac{D*\rho_g*C_{pg}}{\lambda_g} \quad 6.38$$

In conclusion, as the pressure increases, the mass transfer of water vapour from the gas bulk to the wall increases, so that the condensation rate should also increase. Thus, these two opposite impacts of the pressure on the condensation rate calculation may be the explanation for the question why there is no significant change in the range of the investigated pressure.

Figure 6-12 shows the effect of the gas pressure on predicted water condensation rate at different inlet gas temperatures. It is worth noting from this figure that, the pressure change has only a small influence on the calculated water condensation rate at the lower temperatures. However, when the temperature increases the effect of the pressure becomes more noticeable. Earlier it was mentioned that the dropwise condensation process is a mixed process of heat and mass transfer. Every factor which could either increase driving forces (density difference for mass transfer and/or temperature difference for heat transfer) or decrease the respective transfer resistances (in heat and/or mass) can promote the condensation process. Since the driving force due to the water vapour density difference increases with increasing gas temperature, the condensation process will be increased.

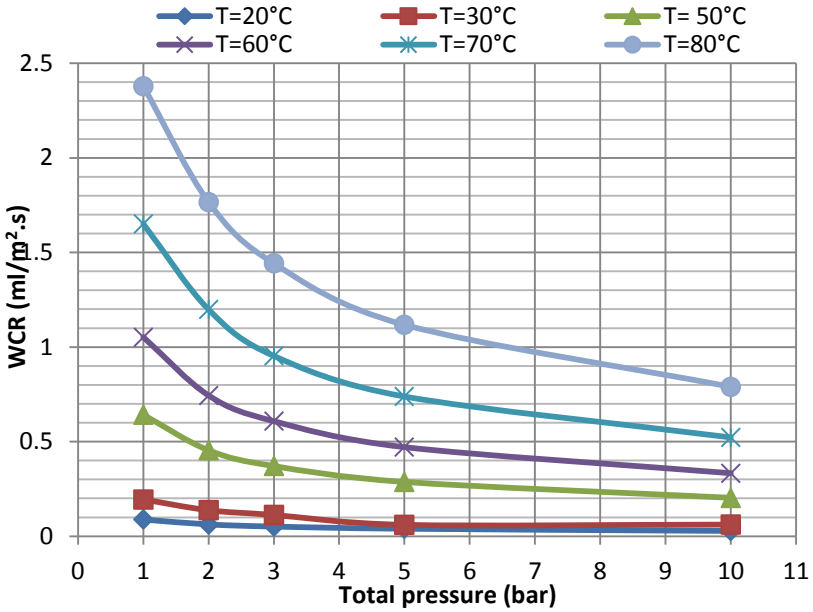

Figure 6-12. The effect of the gas pressure on predicted water condensation rate at different inlet gas temperatures.

6.4.3 Effect of the Gas Velocity on the Condensation Rate

The influence of gas velocity on condensation rate was studied under a wide range of gas temperatures and pressures as illustrated in Figure 6-13 and Figure 6-14 respectively. The results show the proportional relationship between the gas velocity and condensation rate, it can be seen clearly that as the gas velocity increases the condensation rate increases under all conditions of temperature and pressure. The presence of non-condensable gases can effectively reduce the rate of heat and mass transfer [29, 32, 211, 212, 227]. Hence, an increase in the gas velocity leads to remove the non-condensable gases and to reduce the thermal resistance of the condensed water, this, in turn, will increase the heat and mass transfer coefficients and thus increase the condensation rate. Another possible explanation for increasing the condensation rate by increasing the gas velocity is that, clearly obvious from Equation 6.35, 6.36 and 6.37 that the heat and mass transfer in the gas phase is related to the gas velocity. At a higher gas velocity, the Reynolds number is greater and a more turbulent flow is expected. In the turbulent flow, the heat and mass transfer from the gas to the pipe wall is

more efficient, which respectively increases the water phase change and the amount of water vapour available in the pipe wall for the process of condensation. Figure 6-13 confirms the fact that at the higher gas temperatures (higher sub-cooling temperatures), the condensation rate values are higher, and this is due to the fact that more water vapour is available for the condensation process in these conditions.

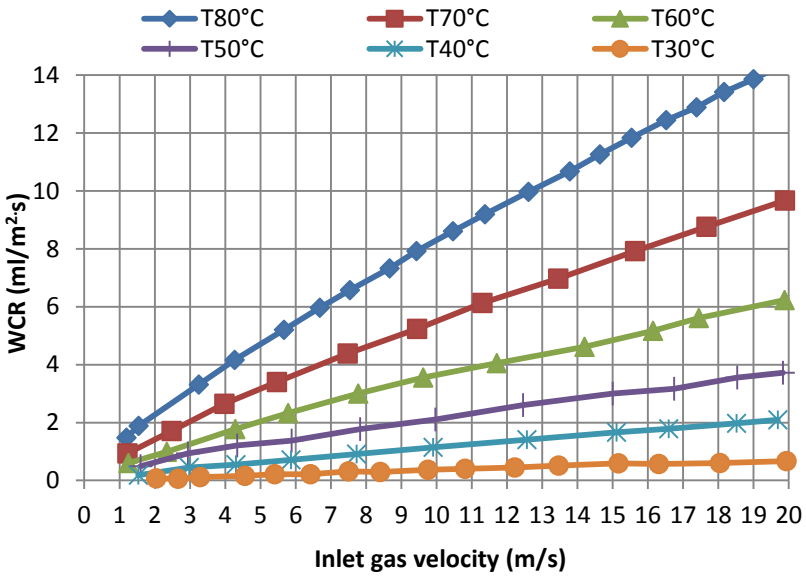

Figure 6-13. The effect of the inlet gas velocity on predicted water condensation rate at different inlet gas temperature and 1 bar total pressure.

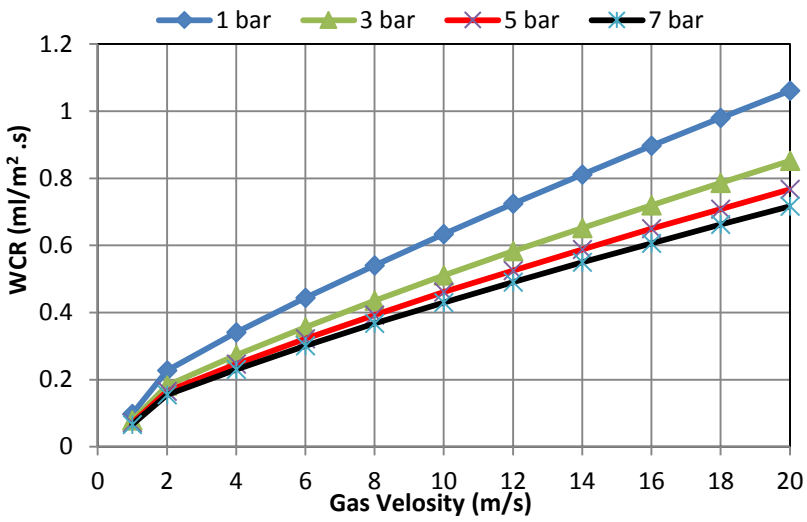

Figure 6-14. The effect of the inlet gas velocity on predicted water condensation rate at different inlet gas pressure and at an inlet gas temperature of 30°C.

6.4.4 Critical Droplet Diameter

In order to calculate the droplet lifetime, the droplet size and the motion of the condensed droplet (whether falling or sliding along the pipe) at different conditions, the effect of the most important factors that influence the droplet size including gas temperature, gas velocity, and the total gas pressure were examined through implementing Zhang model numerically by using the Python software. The results are shown in Figure 6-15 and Figure 6-16.

From Figure 6-15 it can be seen that at gas velocities lower than 8 m/s, the influence of the gas velocity on the droplet size is minor. At these velocities (8 m/s or lower), the droplet lifetime ends up due to falling under gravity. The increased gas density at high gas velocity makes the drag force increase dramatically. Thus, the force balance in the horizontal direction can be established at lower gas velocities. Hence, when the gas velocity increases, the condensed liquid droplets are pushed by flowing gas to slide along the pipe surface.

The Zhang model is used to find the effect of both total pressure and gas temperature on the droplet size and motion. Figure 6-15 shows the effect of the total gas pressure on the maximum droplet size, it is clear that the gas pressure has a significant influence on the droplet motion and droplet size. The sliding droplet happens at a lower gas velocity at higher gas pressure and vice versa. This can be explained by the fact that, increasing gas pressure leads to increasing gas density, the increased gas density at high gas velocity makes the drag force increase dramatically. Therefore, the force balance in the horizontal direction can be reached at lower gas velocities. However, from Figure 6-16, it is clear that the gas temperature has an insignificant effect on the maximum droplet size and droplet motion. This is due to the fact that, from field data, the change in the gas temperature is rather small, for instance from 30°C to 80°C whereas, the gas pressure can be changed by two orders of magnitude for example from 1 bar to 100 bar.

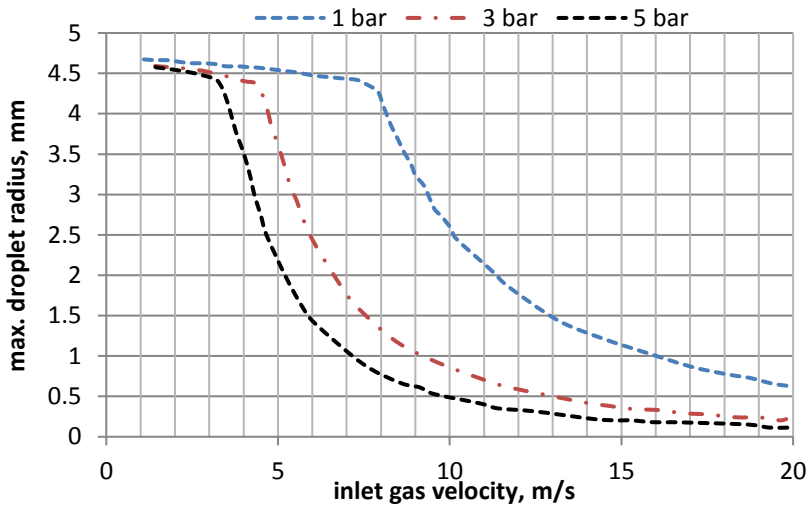

Figure 6-15. The effect of the inlet gas velocity on predicted maximum droplet radius at different inlet gas pressure and at a gas temperature of 30˚C.

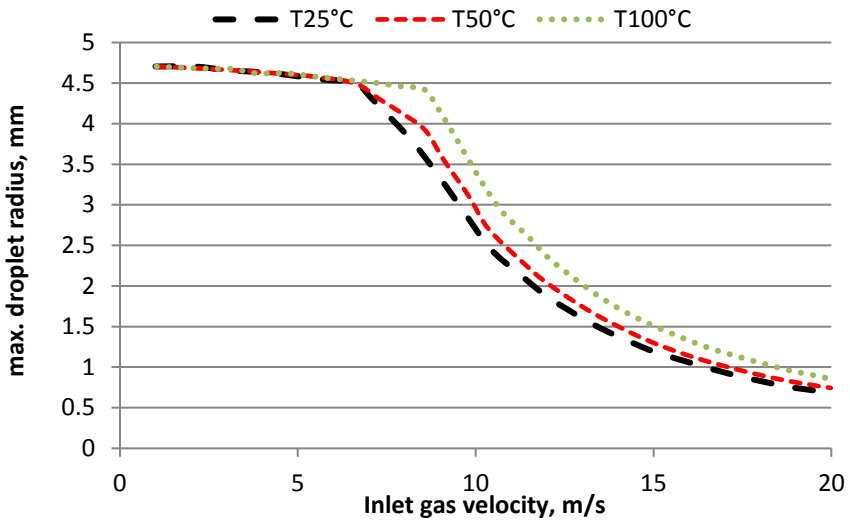

Figure 6-16. The effect of the inlet gas velocity on predicted maximum droplet radius at different inlet gas temperature and at a total gas pressure =1 bar.

6.5 Static TLC Conditions: Heat Transfer Due to Natural Convection

6.5.1 Buoyancy-driven heat transfer

The heat transfer coefficient has a strong relationship with the gas velocity, the higher the gas velocity, the higher the convection heat transfer coefficient and vice versa [228]. However, when the fluid velocity reduces to 1 m/s or less, the fluid motion is not noticeable because of the low velocities involved and the system can be considered under a natural convection [228]. The flow system in natural convection conditions is governed by the ratio of the buoyancy force to the viscous force acting on the fluid which is called the Grashof number.

For the abovementioned reason, the buoyancy-driven flow should be taken into account in water condensation rate prediction when it becomes very low (under 1 m/s). In this study, the Zhang et al's model is modified to involve the influence of the buoyancy-driven flow for more accurate water condensation prediction.

6.5.2 Condensation Rate under Buoyancy–Driven Force

At conditions of very low gas velocities 1m/s or less, when the temperature of any fluid changes the fluid density changes as well, then a flow can happen due to a buoyancy effect due to the density variations.

The heat transfer coefficient can be correlated by an equation containing three dimensionless numbers, the Nusselt, the Grashof number and the Prandtl number [32] as presented in Equation 6.39 [229].

$$Nu = a(Gr * \mathrm{Pr})^{b} \tag{6.39}$$

$$\mathrm{Nu} = 0.54(\mathrm{Gr}\ \mathrm{Pr})^{0.25} \quad \text{for laminar flow } (10^5 < \mathrm{Gr}\ \mathrm{Pr} < 10^7) \tag{6.40}$$

Where:

$$Gr = \left(\frac{\mathrm{D_o^3 \rho_v{}^2\ \beta g \Delta T}}{\mu^2}\right) \tag{6.41}$$

Gr = Grashof number, dimensionless

$$\mathrm{Pr} = \left(\frac{\mathrm{C_p\ \mu_f}}{\mathrm{k_f}}\right) \tag{6.42}$$

Pr = Prandtl number, dimensionless

D_o = Diameter of a pipe, in m

$\mathrm{k_f}$ = Thermal conductivity of vapour phase, in W/m/K

ρ_v = Density of vapour phase, in kg/m^3

β = Coefficient of thermal expansion, defined as a measure of the change in volume of a substance with temperature at constant pressure. The volume expansion coefficient β can be expressed approximately by replacing differential quantities by differences as:

$$\beta = \frac{1}{\rho}\frac{\Delta\rho}{\Delta T} = -\frac{1}{\rho}\frac{(\rho_l - \rho_v)}{(T_s - T_v)} \quad 6.43$$

where:

ΔT = Temperature difference between outside of a pipe and fluid distant from surface, in K

μ_f = Viscosity of vapour phase, in Pa.s

c_p = Specific heat capacity of vapour phase, in J/kg.K

ρ_l= liquid density, in kg/m^3

T_s =wall temperature, in K

T_v=water vapour temperature, in K

6.5.3 Minimum and Maximum Droplet Radii at Low Velocities and Static Conditions

The minimum radius of the droplet that can be formed at a given sub-cooling surface can be calculated as [219]:

$$r_{min} = \frac{2T_s\sigma}{H_{fg}\rho\Delta T} \quad 6.44$$

where ΔT is the wall sub-cooling temperature and T_s represents vapour saturation temperature both of these temperatures, K.

If the gas velocity dropped to be 1 m/s or lower, the dominant force acting on the water droplet is gravity, surface tension force and the buoyancy force. The net of the forces which act on the single droplet is shown in Figure 6-17.

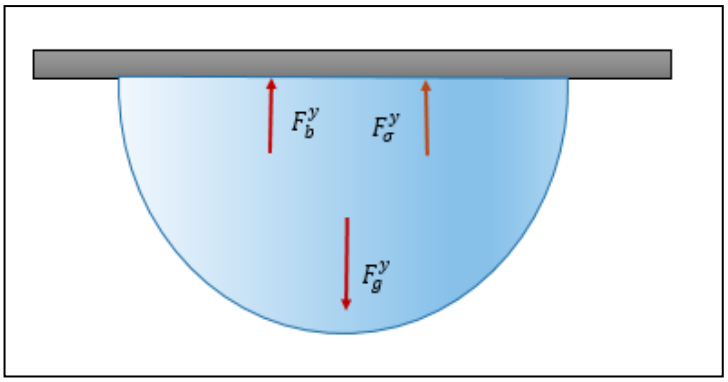

Figure 6-17. Force balance on a single droplet at static conditions.

Once the droplet reaches its maximum radius, the force balance in the y-direction is reached and the droplet will fall down and the maximum radius of the droplet can be found as:

$$F_\sigma^y + F_b^g = F_g^y \tag{6.45}$$

$$2\sigma\pi r + \frac{4}{6}\pi\rho_g r^3 = \frac{4}{6}\rho_{water}\pi g r^3 \tag{6.46}$$

$$r_{max} = \sqrt{\frac{3\sigma}{2g(\rho_{water} - \rho_{g)}}} \tag{6.47}$$

6.5.4 Validation of the Modified Model

The accuracy of the model for static conditions was checked by comparing the calculated values of the condensation rate with corresponding experimental data. This was done over a range of surface temperatures from 8°C to 38°C and at a gas temperature of 30°C - 50°C.

The results of the comparison are presented in Figure 6-18, Figure 6-19 and Figure 6-20, it can be seen that a good agreement is achieved between the model prediction and experimental data. The maximum value of the discrepancy of the experimental and predicted condensation rate at gas temperature 30°C is 26% at surface temperature of 8°C and about 20% when the gas temperature is 40°C at a surface temperature of 32°C, whereas,

when the gas temperature is 50°C the highest value of discrepancy is 16% at 38°C surface temperature.

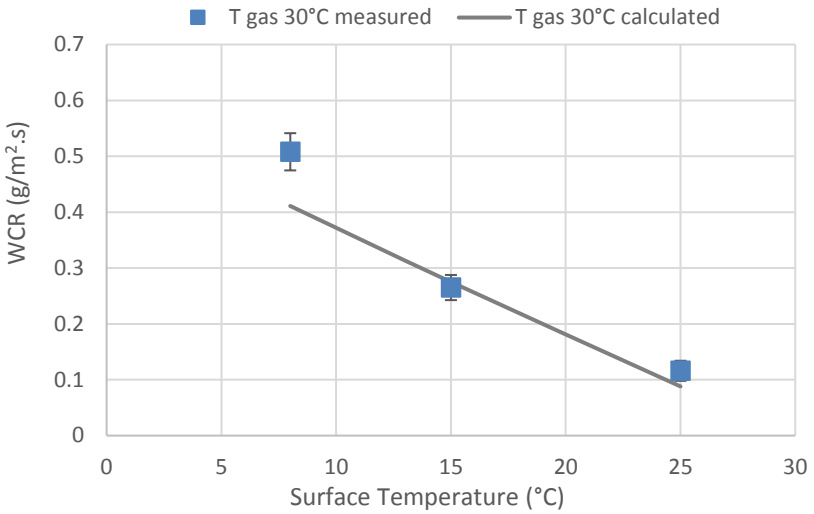

Figure 6-18. Calculated condensation rates versus experimental condensation rates at surface temperatures of 30°C at atmospheric pressure and stagnant conditions.

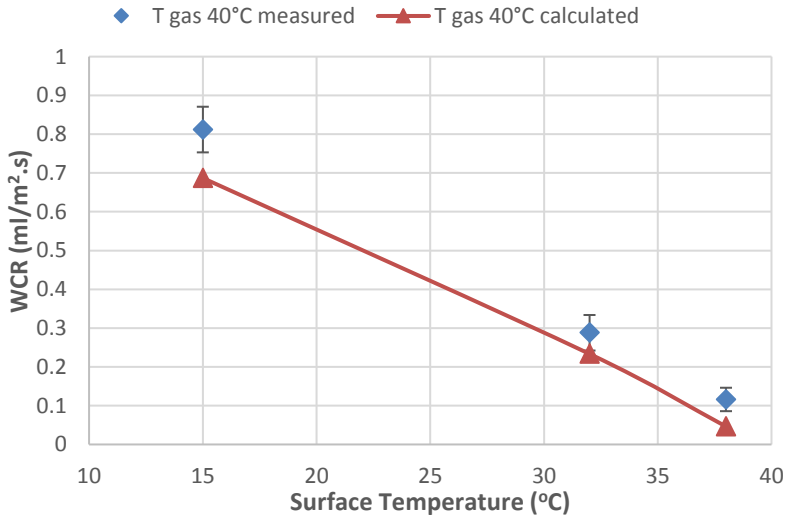

Figure 6-19. Calculated condensation rate versus experimental condensation rate at surface temperatures of 40°C and atmospheric pressure and stagnant conditions.

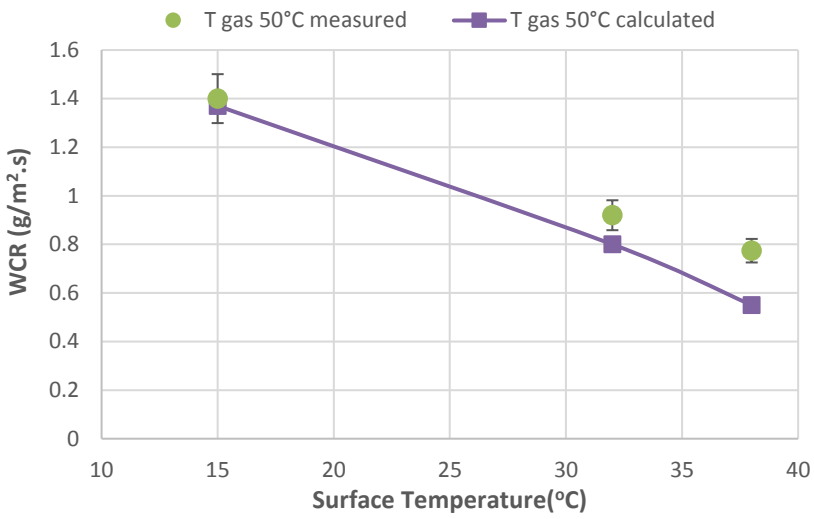

Figure 6-20.Calculated condensation rate versus experimental condensation rate at surface temperatures of 50°C and atmospheric pressure and stagnant conditions.

6.5.5 Condensation Rate under Natural Convection

Figure 6-21 shows the result of water condensation rate at different gas temperatures when the developed model was implemented. It can be seen that the water condensation increases as the temperature difference between the inlet gas temperature and pipe wall increases. It is well known under the natural convection mechanism, any fluid motion occurs by buoyancy force. The buoyancy force is proportional to the density difference, which is proportional to the temperature difference at constant pressure [225]. Thus, the larger the temperature difference between the fluid adjacent to a hot or cold surface and the fluid away from it, the larger the buoyancy force and the stronger the natural convection currents, and thus the higher the heat transfer rate. These, in turn, affect the heat transfer coefficient in the gas phase and leads to an increase in the water condensation rate according to equations 5.35, 5.37, 5.39.

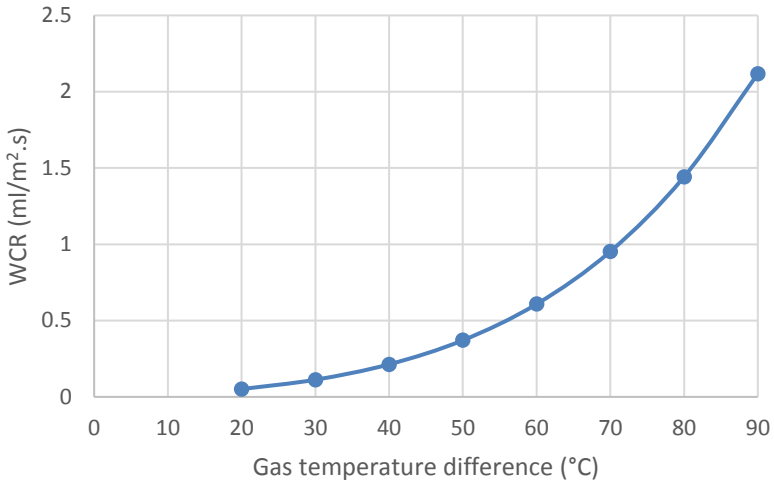

Figure 6-21. Effect of inlet gas temperature at stagnant conditions at a constant pressure is 1bar, on condensation rate.

6.6 Method for Calculation of the Droplet Lifetime

The experimental results of the tests which have been done in this study show that the precipitation rate PR is a function of iron carbonate supersaturation (SS). In turn, the iron carbonate saturation level strongly depends on the water condensation, which continuously supplies new and acidic condensed water. The chemistry in the condensed water (pH and $FeCO_3$ saturation level) and the protectiveness of the $FeCO_3$ are greatly influenced by the cycle of droplet renewal. The saturation of $FeCO_3$ is easier to achieve when the droplets of the condensed water remain attached to the steel surface for a longer time and vice versa. Therefore, for accurate prediction and calculation of precipitation rate and corrosion rate, the droplet lifetime should be determined precisely.

By using a borescope, Pojtanabuntoeng et al. [154] detected the condensation patterns in a water-hydrocarbon co-condensation system, however, the lifespan of the droplet at different condensation rates was not reported. Islam et al. [157] measured the lifetime of condensed droplets experimentally. They used an extra thermocouple to measure the droplet

temperature by placing it exactly beneath the sample surface. At the beginning of the condensation process, the thermocouple records the gas temperature, as the droplet formed and grew, the reading of the thermocouple decreased, and the lowest reading obtained when the droplet reaches its maximum volume. The fluctuation of the temperature readings represents the droplet lifetime.

In this study, based on the water condensation rate, a simplified method to calculate the condensed droplet lifetime has been developed. The detailed procedure of the calculation is as follows:

1. Calculate the liquid condensate volume using the Equation 6.48

$$cond.\ vol = \frac{WCR*A*t}{2.77*\rho_w}\text{, } ml \qquad 6.48$$

where WCR is the condensation rate in ml/m^2.s, A is the condensation surface area in cm^2 , ρ_w is the water condensate density in g/cm^3 and t is the exposure time in hours.

2. Find the number of droplets;

$$No.drops = \frac{cond.vol}{drop\ vol.} \qquad 6.49$$

where $droplet\ vol$ is the maximum condensed droplet volume, *ml*

$$droplet\ vol. = 2/3\pi(r_{\max})^3 \qquad 6.50$$

3. The droplet lifetime (DLT) can be calculated according to Equation 6.51.

$$droplet\ lifetime = \frac{t}{No.drops}*60, \text{ min} \qquad 6.51$$

The correlations obtained from this study offer a practical way to estimate the lifetime of the condensed liquid. Table 6-2 shows the calculated DLT at different conditions, it can be seen that the shortest LDT of 3.38 minutes was

calculated at the highest WCR of 2.8 ml/m^2.s. While at the lowest WCR of 0.336 ml/m^2.s the longest LDT of 28 minutes was calculated.

Table 6-2. Water condensation rate (WCR) and droplet lifetime (DLT) at different gas and surface temperatures at a pressure of 1 bar.

Gas temperature, °C	**Surface temperature, °C**	**WCR, ml/m^2.s**	**DLT, min**
40	15	0.78	12.11
40	30	0.33	28.00
50	15	1.56	6.00
50	30	1.02	9.31
60	15	2.80	3.38
60	30	2.14	4.41
60	40	1.52	6.20

The obtained results of estimated droplet lifetime were validated against the experimental results obtained in this thesis. Figure 6-22 shows the comparison between the calculated and measured water droplet lifetime in the current work and the droplet lifetime determined experimentally by Islam [157] at atmospheric pressure. From this figure, it can be observed that a very good agreement is achieved between the calculated DLT and the experimentally measured DLT.

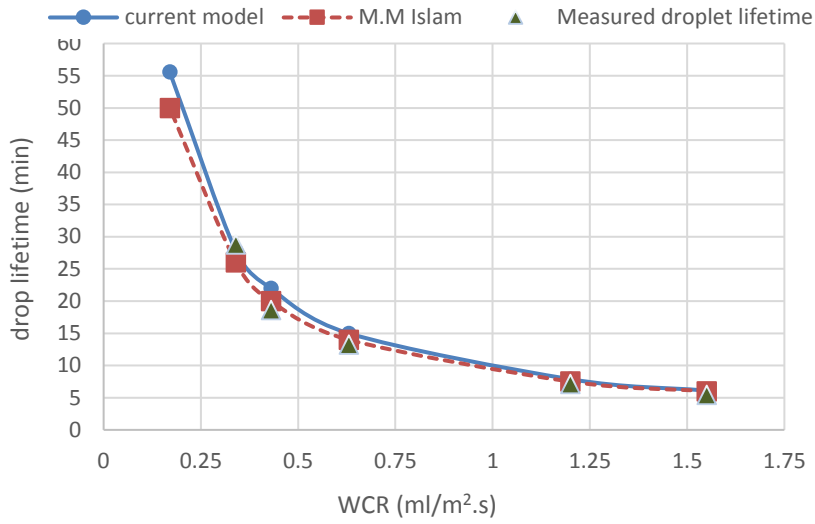

Figure 6-22. The comparison of the calculated water lifetime in the current work with the droplet lifetime determined experimentally by Islam [157] and measured droplet lifetime.

6.7 Summary

In the present study, Zhang et al.'s model of dropwise condensation in the presence of non-condensable gases was implemented in the Python computer language. The connection between heat transfer and mass transfer balance equations was established. In addition, a force analysis on a single droplet was conducted to determine the maximum droplet size and the criteria for droplet motion. In this study, by taking the buoyancy-driven force into consideration, the model is modified to predict the water condensation rate at stagnant conditions with low flow velocities.

Since the Zhang et al. condensation model has not been validated in detail, even in the original paper, a much more comprehensive validation and parameter study are carried out here for the first time. The model results have been compared with experimental and real field data which were found in the open literature. The performance of the new model, modified for static conditions, has been validated against experimental results which were obtained from a new customised experimental rig designed in this study.

Chapter 7. Numerical Modelling of CO_2-Top of Line Corrosion

7.1 Introduction

The experimental results explained previously clearly show that the top of line corrosion strong depends on the condensation rate. The competition between the corrosion process and the condensation process determines the species concentrations, and then the corrosion rate. Gaining a better understanding of the relation between all these parameters leads to a better understanding of the mechanisms of the TLC, which, in turns, provides more accurate predictions of the TLC.

This chapter describes the equations for the model of Top of Line CO_2 corrosion described in Zhang et al.[7] and Zhang [164], which is based on the Nordsveen et al. [44] multi-node numerical model for corrosion. These have been implemented in this thesis in a suite of Python software programs. The first component of the overall model is the prediction of the condensation rate which is due to dropwise condensation, a very complex physical process. The water condensation prediction model is described in detail in Chapter 6. The calculated condensation rate is then used as an input into a corrosion model in a growing water film, where the corrosion processes are modelled using the Nordsveen et al. [44] multi-node numerical analysis.

The three key processes that influence TLC, namely: condensation, chemistry, and corrosion must be considered in any attempt to model corrosion at the top of the line.

The dropwise condensation at the top of the line mechanistic model which was described earlier can meet the need for the development of a TLC model. The mechanistic model proposed by Nordsveen and Nesic in 2003 [44] which include corrosion, chemistry and iron carbonate film formation provide a powerful basis for further improvement and could be adapted to

match the TLC conditions. More details can be found in the original publication [44].

7.2 Equivalent Uniform Film Model

As dropwise condensation is a random process, the internal pipe surface can be considered to be covered by a distribution of condensed droplets of varying sizes. Hence, the condensation rate can be assumed to be constant over the entire surface. This means that calculations can be carried out as if the surface was covered by a uniform liquid layer, which follows a continuous cycle of growth and detachment – just like a single droplet.

A family of 2-D hemispherical droplets is represented with a 1-D liquid layer. Droplet/layer growth due to condensation is represented by the increase in the height of the water column until the maximum size of the droplet, r_{max}, is reached. At that point the droplet is dislodged and a new droplet starts growing in its place, this is simulated by reducing the size of the water column to the value corresponding to the minimum size of the droplet, r_{min}, and the cycle starts all over again.

If we have a hemispherical droplet of radius r then the volume is V(r) = $(2\pi r^3)/3$ and its footprint on the metal surface is πr^2, hence its equivalent 1-D film thickness, h(r), is given by

$$\pi\, r^2 h(r) = \frac{2\pi r^3}{3} \Rightarrow h(r) = \frac{2r}{3} \qquad 7.1$$

Now if the water condensation rate is WCR (kg/m^{2}s) then

$$\frac{dh}{dt} = \frac{WCR}{\rho_{water}}$$

where ρ_{water}=1000kg/m^3 is the density of water. Since the lifecycle of a droplet is between r_{min} and r_{max}, i.e. between $h_{min}=2r_{min}/3$ and $h_{max}=2r_{max}/3$, the droplet lifetime, t_{drop} is given by:

$$\frac{WCR}{\rho_{water}} \times t_{drop} = \frac{2(r_{max} - r_{min})}{3} => \ t_{drop} = \frac{2(r_{max} - r_{min})\,\rho_{water}}{3\,WCR} \qquad 7.2$$

7.3 Corrosion Rate Predictions

The model for Top of the Line CO_2 Corrosion developed by Zhang et al. [7] and Zhang [164] is a modified version of the 1-D multi-node CO_2 corrosion model developed by Nordsveen et al. [44] and later workers. In this case, rather than integrating through the boundary layer, it integrates across the 1-D equivalent droplet film thickness to calculate the concentration of each species at a series of points in the film.

In the top of line scenario, corrosion takes place between the birth time of the condensed droplet and its departure time. Indeed, the principles of the corrosion mechanisms are the same for both the top of the line and the bottom of the line.

The overall uniform CO_2 corrosion of carbon steel can be divided into three major processes occurring simultaneously as follows:

- Chemical reactions in the film, involving the dissolution of CO_2 in the aqueous solution to form the various reactive species which take part in the CO_2 corrosion reaction.
- Electrochemical reactions at the steel surface, which cause a flux of species there.
- Diffusive transport of species across the film – note that in this case there is no turbulent convection as there is no dominant velocity scale in the droplet.

Figure 7-1 represents a schematic of the CO_2 corrosion process of carbon steel. It is clear that all the three stages mentioned above are linked, and, the overall corrosion rate depends on the rate at which each of these individual processes takes place.

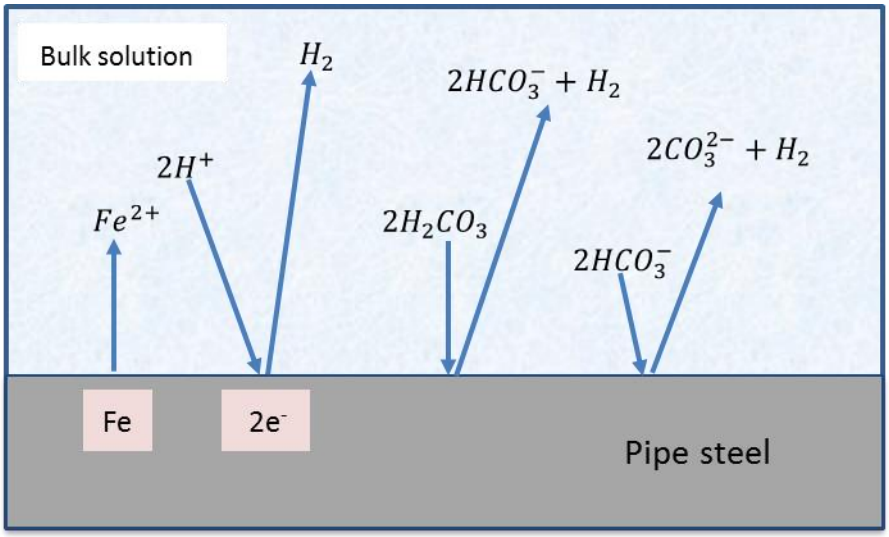

Figure 7-1. Schematic of CO_2 corrosion process of carbon steel.

The governing equation for the concentrations of species j, c_j, in mol/m^3 is:

$$\frac{\partial c_j}{\partial t} = -\frac{\partial N_j}{\partial x} + R_j \qquad 7.3$$

where R_j is the production of species j due to homogeneous chemical reactions and N_j is the flux of species j due to diffusion in the positive x direction (away from the steel surface), t is the time and x is the spatial coordinate (distance from the steel surface across the film). In this case at a time t, 0 ≤ x ≤ h(t). These equations also have to be solved subject to the charge balance equation:

$$c_{H^+} + 2\,c_{Fe^{2+}} = c_{OH^-} + c_{HCO_3^-} + 2c_{CO_3^{2-}} \qquad 7.4$$

Note that for the case of Top of the Line Corrosion, where the initial acidity of the condensing water depends on p_{CO_2}only, there are no major species, such as Na^+ and Cl^-. As described below, this equation is used to provide an explicit equation for c_{H^+}

7.3.1 Chemical Reactions in the Bulk Solution

In a uniform CO_2 corrosion process, the local sources of reactive species in the bulk is the chemical reactions that take place in the solution. The chemical reactions are often faster than other processes involved in corrosion, such us diffusion of species and electrochemical reactions, thus preserving chemical equilibria throughout the solution. On the other hand, when chemical reactions proceed slowly such as the CO_2 hydration reaction, other faster processes can lead to local non-equilibrium conditions at the corroding steel surface. Therefore, chemical reactions can significantly affect the rates of electrochemical processes at the steel surface and in turn the corrosion rate [230].

The method for calculating and solving the chemical reactions in the bulk together with the reaction constants are described in detail in Appendix A.

The calculation of concentrations of the various reactant species in the bulk (CO_2,H_2CO_3,H^+, OH^-,HCO_3^-, CO_3^{2-}) represents the first step in predicting the corrosion rate. The chemical reactions are given by the following equations.

1. $CO_{2(aq)}$ is created by dissolving Carbon Dioxide gas in water:

$$R_{CO_{2,s}} = \frac{d}{dt}\left(c_{CO_{2,s}}\right) = K_{b,hy}\, c_{H_2CO_3,s} - K_{f,hy} c_{CO_2,s} \quad 7.5$$

2. H_2CO_3 is created by carbonic acid hydration and carbonic acid dissociation:

$$R_{H_2CO_{3,s}} = \frac{d}{dt}\left(c_{H_2CO_{3,s}}\right) = -\left(K_{b,hy}\, c_{H_2CO_{3,s}} - K_{f,hy} c_{CO_{2,s}}\right) - \left(K_{f,ca}\, c_{H_2CO_{3,s}} - K_{b,ca} c_{H_s^+} c_{HCO_{3,s}^-}\right) \quad 7.6$$

3. Bicarbonate HCO_3^- ions are created by carbonic acid dissociation and bicarbonate ion dissociation:

$$R_{HCO_{3,s}^-} = \frac{dc_{HCO_{3,s}^-}}{dt} = \left(K_{f,ca}\, c_{H_2CO_{3,s}} - K_{b,ca} c_{H_s^+} c_{HCO_{3,s}^-}\right) - \left(K_{f,bi}\, c_{HCO_{3,s}^-} - K_{b,bi} c_{H_s^+} c_{CO_{3,s}^{2-}}\right) \quad 7.7$$

4. Carbonate CO_3^{2-} ions are created by bicarbonate ion dissociation:

$$R_{CO_{3,s}^{2-}} = \frac{dc_{CO_3^{2-}}}{dt} = \left(K_{f,bi}\, c_{HCO_{3,s}^-} - K_{b,bi} c_{H_s^+} c_{CO_{3,s}^{2-}}\right) \quad 7.8$$

5. Hydroxide OH^- ions are created from water dissociation:

$$R_{OH_s^-} = \frac{dc_{OH_s^-}}{dt} = K_{f,wa} - K_{b,wa} c_{H_s^+} c_{OH_s^-} \quad 7.9$$

6. H^+ ions are created by carbonic acid dissociation, bicarbonate ion dissociation and water dissociation:

$$R_{H^+.s} = \frac{dc_{H_s^+}}{dt} = \left(K_{f,ca}\, c_{H_2CO_{3,s}} - K_{b,ca} c_{H_s^+} c_{HCO_{3,s}^-}\right) + \left(K_{f,bi}\, c_{HCO_{3,s}^-} - K_{b,bi} c_{H_s^+} c_{CO_{3,s}^{2-}}\right) + (K_{f,wa} - K_{b,wa} c_{H_s^+} c_{OH_s^-}) \quad 7.10$$

7. Fe^{2+} ions are not created by the homogeneous chemical reactions.

$$R_{Fe_s^{2+}} = 0 \quad 7.11$$

The chemical reactions terms can be written as:

$$\frac{dx_1}{dt} = c_1 x_2 + c_2 x_1 \quad 7.12$$

$$\frac{dx_2}{dt} = -\frac{dx_1}{dt} = -c_1 x_2 - c_2 x_1 \quad 7.13$$

$$\frac{dx_3}{dt} = c_3 x_2 + c_4 x_3 x_6 + c_5 x_3 + c_6 x_4 x_6 \quad 7.4$$

$$\frac{dx_4}{dt} = c_7 x_3 + c_8 x_4 x_6 \quad 7.15$$

$$\frac{dx_5}{dt} = c_9 + c_{10} x_5 x_6 \quad 7.16$$

$$\frac{dx_6}{dt} = c_3 x_2 + c_4 x_3 x_6 - c_5 x_3 - c_6 x_4 x_6 + c_9 + c_{10} x_5 x_6 \quad 7.17$$

where c_1=$K_{b,hy}$, c_2= -$K_{f,hy}$, c_3=$K_{f,Ca}$, c_4= -0.001 $K_{b,Ca}$, c_5=-$K_{f,bi}$, c_6= 0.001 $K_{b,bi}$, c_7=$K_{f,bi}$, c_8= -0.001 $K_{b,bi}$, c_9=1000$K_{f,wa}$, c_{10}= -0.001$K_{b,wa}$.

7.3.2 Electrochemical Reactions at the Steel Surface

The electrochemical reactions which take place at the metal surface in CO_2 corrosion environment and accounted in the current model are presented in Table 7-1.

Table 7-1. Electrochemical reactions accounted in the model.

Reaction Type	Reaction	Reaction Description
Cathodic reactions	$2H_2CO_3 + 2e^- \rightarrow H_2 + 2HCO_3^-$	Direct reduction of carbonic acid
Cathodic reactions	$2H^+ + 2e^- \rightarrow H_2$	Hydrogen reduction
Cathodic reactions	$2\ H_2O_{(l)} + 2e^- \rightarrow H_{2(g)} + 2\ OH^-{}_{(aq)}$	Water reduction
Anodic reaction	$Fe \rightarrow Fe^{2+} + 2e^-$	iron dissolution

7.4 Flux of Species, N_j

The transport of species has three components: diffusion, convection, and electro-migration [22]. In the top of the line scenario, it can be assumed that the condensed water in the droplet is in a stagnant condition, and the species transportation happens under diffusion process only. Electro–migration is significant only for the transport of Na^+ and Cl^- [8], thus, this component can also be neglected in the mass transfer calculation at TLC conditions. Therefore, the mass transfer flux from the bulk solution to the steel surface N_j contains only a diffusion term and the mass transfer equation can be simplified as:

$$N_j = -D_j \frac{\partial c_j}{\partial x} \qquad 7.18$$

where D_j is the molecular diffusivity coefficient of species j in m^2/s and is calculated by

$$D_j = D_{j,ref} * \frac{T}{T_{ref}} * \frac{\mu_{ref}}{\mu} \quad 7.19$$

where $D_{j,ref}$ is the reference diffusion coefficient for species j in m^2/s, and their reference diffusion coefficients are shown in Table 7-2 [230]; μ is the dynamic viscosity, in kg/m.s and is determined by using equation 7.20; μ_{ref} is determined for a reference temperature T_{ref} of 20°C.

$$\mu = 0.001002 * 10^{\frac{1.3277*(293.15-T)-0.01053*((298.15-T)^2}{T+168.15}} \quad 7.20$$

Table 7-2. Species accounted for in the present model and their reference molecular diffusion coefficient, $D_{j,ref}$ [230].

Species	Diffusion coefficient (m^2/s), D_{ref}	Source
CO_2	$1.96*10^{-9}$	Perry [92]
H_2CO_3	$2.00*10^{-9}$	Kvarekva [231]
HCO_3^-	$1.105*10^{-9}$	Newman [232]
CO_3^{-2}	$0.92*10^{-9}$	Kvarekva [231]
H^+	$9.312*10^{-9}$	Newman [232]
OH^-	$5.26*10^{-9}$	Newman [232]
Fe^{2+}	$0.72*10^{-9}$	Kvarekva [231]

7.5 Calculation of Corrosion Currents

The total current density of H^+ reduction consists of two components, charge-transfer current and mass-transfer-limiting current [203]. Due to the absence of mass transfer from the bulk to the surface in Top of Line Corrosion, the mass-transfer limited corrosion currents are zero, hence the

total current density for each species is simply its charge transfer current density, as described below.

7.5.1 Charge Transfer Current Densities

The total current density rate for each species *j* can be obtained by using the Tafel equation [22]

$$i = i_o * 10^{\mp\frac{(E-E_0)}{b}} \quad 7.21$$

where i is the reaction current density of species *j* in A/m^2, i_o represents a reference or an exchange current density in A/m^2, E represent the corrosion potential of the steel in V, E_0 represent a reference potential in V and b represents the Tafel slope in V/decade. A negative sign is taken for cathodic reactions and a positive sign for anodic reactions.

The Tafel slope b for H^+ reduction can be calculated using the equation 7.22 [202] as :

$$b_c = \frac{2.3*R*T}{\alpha_c*F} \quad 7.22$$

where α_c represents charge transfer coefficient =0.5 and giving b_c=0.118V at 25°C [233]. In the current model, the current density for each electrochemical reaction depends on the surface concentration of each individual species *j*, which is not explicitly known and needs to be determined. The corrosion potential of the steel E, for a corrosion process, can be calculated from the charge balance equation at the steel surface [22]:

$$\sum_{cathodic} i = \sum_{anodic} i \quad 7.23$$

where $\sum_{cathodic} i$ is the sum of currents due to cathodic = $i_{H^+} + i_{H_2CO_3} + i_{H_2O}$ and $\sum_{anodic} i$ is the current due to the anodic reaction = $i_{Fe^{2+}}$ exchange current density.

The reference current density, i_o for each electrochemical reaction can be calculated using the following equation [230] :

$$i_0 = i_{0,ref}\left(\frac{c_{H+,s}}{c_{H+,s,ref}}\right)^{a1}\left(\frac{c_{CO_2,s}}{c_{CO_2,s,ref}}\right)^{a2}\left(\frac{c_{H_2CO_3,s}}{c_{H_2CO_3,s,ref}}\right)^{a3} e^{-\frac{\Delta H}{R}\left(\frac{1}{T}-\frac{1}{T_{ref}}\right)} \quad 7.24$$

where ΔH is activating energy in kJ/mol, a_1, a_2, a_3 are constants and, T_{ref} is the reference temperature, T_{ref} =25°C , where the concentrations are taken in molar (mol/litre). A detail about these constants and parameters are given in Table 7-3.

1. For the cathodic reaction $2\mathrm{H}^+ + 2\mathrm{e}^- \rightarrow \mathrm{H}_2$:

$i_0 = i_{0,H^+}$ with $i_{o,ref,H^+} = 0.05$, $c_{H+,s,ref}$=10^{-4}, a_1=0.5, a_2=a_3=0, ΔH=30,000J/mol, T and T_{ref} are in Kelvin and T_{ref}=298.15K (25°C) and the charge transfer current density is given by:

$$i_{H^+} = i_{0,H^+} \times 10^{-\left(\frac{E-E_{rev,H}}{b_H}\right)} \quad 7.25$$

where E represents the corrosion potential of the steel in V,

$b_H = \frac{2.303\ RT}{\alpha_c F}$ with α_c=0.5 and $E_{rev,H} = -\frac{2.303RT}{F}pH$.

2. For the cathodic reaction $2\mathrm{H_2CO_3} + 2\mathrm{e}^- \rightarrow \mathrm{H_2} + 2\mathrm{HCO_3^-}$:
From Nordsveen et al. [44]:

$$i_{0,H_2CO_3} = 0.018\left(\frac{c_{H_2CO_3,s}}{10^{-4}}\right)\left(\frac{c_{H^+,s}}{10^{-5}}\right)^{-0.5} e^{-\frac{50000}{R}\left(\frac{1}{T}-\frac{1}{293.15}\right)} \quad 7.26$$

From Zheng et al [22]:

$$i_{H_2CO_3} = i_{0,H_2CO_3} \times 10^{-\left(\frac{E-E_{rev,H_2CO_3}}{b_{H_2CO_3}}\right)} \quad 7.27$$

where $b_{H_2CO_3} = \frac{2.303\ RT}{\alpha_c F}$ with α_c=0.5, and $E_{rev,H_2CO_3} = -\frac{2.303RT}{F}pH$.

3. For the cathodic reaction $2H_2O + 2e^- \rightarrow H_2(g) + 2OH^-$:

From Fardisi et al [234]:

$i_{0,H_2O} = 0.002\, e^{-\frac{\Delta H}{R}\left(\frac{1}{T}-\frac{1}{T_{ref}}\right)}$, where ΔH=35,000 J/mol and T_{ref}=298.15 K.

The charge current density is given by

$$i_{H_2O} = i_{0,H_2O} \times 10^{-\left(\frac{E-E_{rev,H_2O}}{b_{H_2O}}\right)}. \quad 7.28$$

Since the reduction of H_2O is thermodynamically similar to reduction of H^+, the Tafel slope and reversible potential are taken to be the same. This gives the cathodic Tafel slope as:

$b_{H_2O} = \frac{2.303\ RT}{\alpha_c F}$ with α_c=0.5 and the reversible potential of water reduction is given by $E_{rev,H_2O} = -\frac{2.303RT}{F}pH$.

4. For the anodic reaction $\mathrm{Fe} \rightarrow \mathrm{Fe}^{2+} + 2\mathrm{e}^-$:

From Fardisi et al [234]: $i_{0,Fe} = \left(\frac{c_{H+,s}}{10^{-4}}\right)^{a1}\left(\frac{c_{CO_2,s}}{0.0366}\right)^{a2} e^{-\frac{37500}{R}\left(\frac{1}{T}-\frac{1}{298.15}\right)}$

where:

$a1$=2.0 if pH <= 4.0, $a1$ = 1.0 if 4.0 < pH < 5.0 and $a1$ = 0.0 if pH >= 5.0

$a2$ = 1.0 if P_{CO2} <= 1 bar, $a2$=0 if P_{CO2} >1 bar

$$i_{Fe} = i_{0,Fe} \times 10^{\left(\frac{E-E_{rev,Fe}}{b_{Fe}}\right)} \quad 7.29$$

where from Zheng et al [22] : $b_{Fe} = \frac{2.303\ RT}{1.5\ F}$ and $E_{rev,Fe}$=-0.488V.

The anodic corrosion current is given by i_{Fe}. The method for calculating the surface potential E is presented in Appendix B.

Table 7-3. Electrochemical constants and parameters for the reactions included in the current model which fit the Equations (7.24 and 7.25) adapted from [230].

Reaction	i_{oref} $\frac{A}{m^2}$	α_1	C_{H^+ref} M	α_2	C_{CO_2ref} M	α_3	$C_{H_2CO_3re}$ M	ΔH $\frac{KJ}{mol}$	T_{re} $°C$	E_{rev} V	b V
$2H^+ + 2e^- \rightarrow H_2$	0.05	0.5	10^{-4}	0	N/A	0	N/A	30	25	$-\frac{2.3RT}{F} PH$	$\frac{2.3RT}{2F}$
$2H_2CO_3 + 2e^- \rightarrow H_2 + 2HCO_3^-$	0.018	-0.5	10^{-5}	0	N/A	1	10^{-4}	50	20	$-\frac{2.3RT}{F} PH$	$\frac{2.3RT}{2F}$
$2\ H_2O_{(l)} + 2e^- \rightarrow\ H_{2(g)} + 2\ OH^-{}_{(aq)}$	0.002	0	10^{-4}	0	N/A	0	N/A	35	25	$-\frac{2.3RT}{F} PH$	$\frac{2.3RT}{2F}$
$Fe \rightarrow Fe^{2+} + 2e^-$	1	1 for P_{CO2}<1 bar 0 for P_{CO2}=1 bar	10^{-4}	2 for PH<4 1 for 4<PH<5 0 for pH>5	0.0366	0	N/A	37.5	25	-0.488	0.03 for pH<4 0.08 for 4<pH<5 0.12 for pH>

7.6 Initial and Boundary Conditions

7.6.1 Initial Conditions

Uniform concentrations of species as determined by chemical equilibria are used as initial conditions for all species. The calculation of the chemical equilibria conditions is described in Appendix C.

7.6.2 Boundary Conditions

On the outer boundary of the droplet, which is in contact with the gas, the boundary conditions are different for different species. For the 7 species considered in CO_2 corrosion: CO_2, H_2CO_3, HCO_3^-, CO_3^{2-}, OH^-, H^+, Fe^{2+}, the only volatile species is CO_2. Hence for CO_2 its concentration in mol/m^3 at the liquid/vapour droplet boundary is held constant and is calculated by Henry's Law:

$$c_{CO_2} = 1000\, p_{CO_2} K_{sol} \tag{7.30}$$

where p_{CO_2} is the partial pressure of CO_2 in the gas phase in bar and K_{sol} is defined in Appendix A. For all the other species, c_j, which are found only in the liquid phase, a zero flux condition ($\frac{\partial c_j}{\partial x} = 0$) representing zero flux of species normal to the liquid/vapour droplet boundary is imposed. As discussed below, at the metal surface the boundary conditions are specified by the electro-chemical reactions.

At the metal surface, zero flux is specified for the species not involved in the electrochemical reactions. For species j involved in electrochemical reactions at the metal surface, the flux at the metal surface can be determined from:

$$N_j = -\frac{i_j}{n_j F} \tag{7.31}$$

where i_j is the charge transfer current density for species j. Note that:

$$N_{H_2CO_3} = -\frac{i_{H_2CO_3}}{F} \quad 7.32$$

$$N_{HCO_3^-} = \frac{i_{H_2CO_3}}{F} \quad 7.33$$

$$N_{OH^-} = \frac{i_{H_2O}}{F} \quad 7.34$$

$$N_{H^+} = -\frac{i_{H^+}}{F} \quad 7.35$$

$$N_{Fe^{2+}} = \frac{i_{Fe}}{2F} \quad 7.36$$

Note that the corrosion rate in mm per year, CR_mmy, is given by

$$CR\_mmy = 1.16\, i_{Fe^{2+}} \quad 7.37$$

Note that if/when an equilibrium corrosion rate is attained then

$$N_{Fe^{2+}\_steady} \times droplet\ lifetime = c_{Fe^{2+}\_steady} \times (h_{max} - h_{min}) \quad 7.38$$

7.7 Numerical Method

The governing equations for the species concentrations in the film ($\frac{\partial c_j}{\partial t} = -\frac{\partial N_j}{\partial x} + R_j$) are solved using a Finite Volume (FV) approach in which there are a total of *nFV* FVs across the film (FVs 0 to nFV-1), which are located between 0 ≤ x ≤ h(t), with a total of *nFV+1* flux boundaries (boundaries 0 to nFV), since each FV has an upstream and downstream flux boundary. The unknown values of the concentration freedoms, c_j, are represented at the centres of the FVs and the species fluxes, N_j, are specified at the boundaries of the FVs. These are shown in the Figure 7-2 and Figure 7-3, where FV0 is adjacent to the steel surface and FV-1 is adjacent to the edge of the droplet at its liquid/vapour boundary.

For all internal Finite Volumes (i.e. FVs 1 to nFV-2) which are neither adjacent to the steel surface (FV0) or adjacent to the liquid/vapour droplet boundary (FV nFV-1), the governing equations are replaced by the charge balance equation:

$$c_{H^+} + 2c_{Fe^{2+}} = c_{OH^-} + c_{HCO_3^-} + 2c_{CO_3^{2-}} \quad 7.39$$

For FV nFV-1 (adjacent to the liquid/vapour droplet boundary) the governing equations are replaced by the required boundary conditions that c_{CO_2} is specified by the Henry's law condition while all other species concentrations there satisfy:

$$\frac{\partial c_j}{\partial x} = 0 \quad 7.40$$

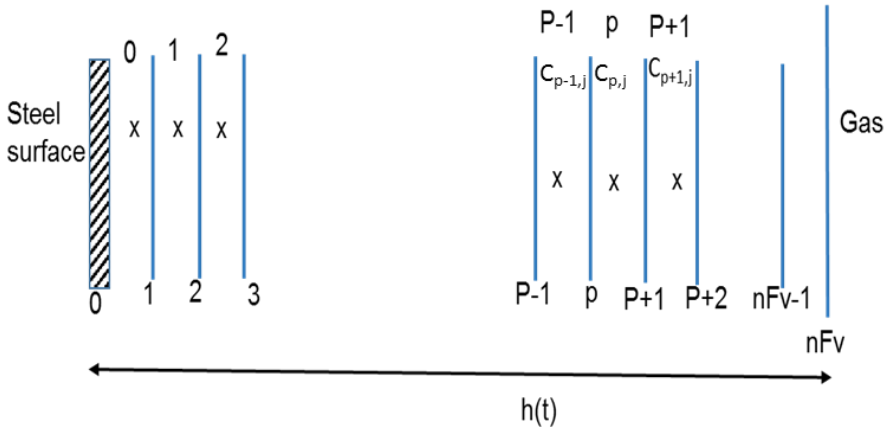

Figure 7-2. Finite Volume (FV) approach to calculate mass transfer across the water condensed droplet.

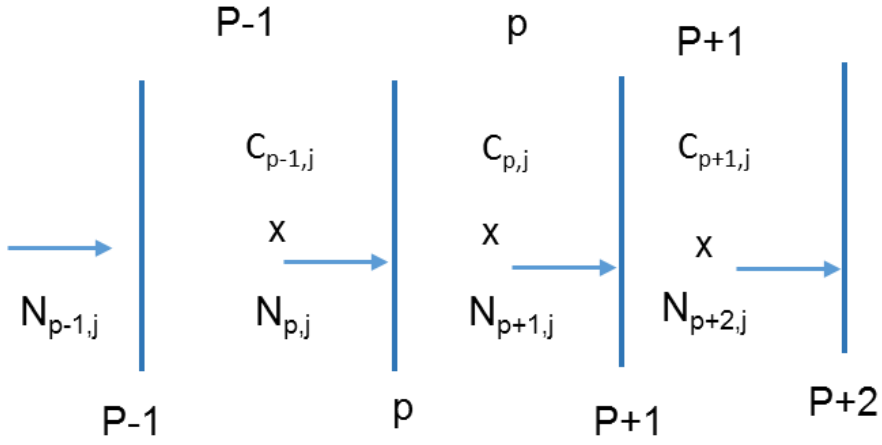

Figure 7-3. Mass flux through Finite Volumes in the condensed droplet.

Consider the pth FV which has concentration freedoms $c_{p,j}$, where $c_{p,j}$ represents the jth species concentration at the middle of the pth Finite Volume. The pth Finite Volume has concentration fluxes $N_{p,j}$ flowing into it

and $N_{p+1,j}$ flowing out of it. Since all the equations are strongly and non-linearly coupled through the chemical reaction and migration terms, they all have to be solved simultaneously, together with the boundary conditions including the non-linear surface charge balance. Note that due to the importance of the electro-chemical reaction terms, a non-uniform grid, with larger grid density near the steel surface, will be needed.

Integrating the transport equation over the pth Finite Volume of width Δx_p results in the following discretised equations:

$$\frac{\left(c_{p,j}^{n+1}-c_{p,j}^{n}\right)}{\Delta t}\,\Delta x_p = -N_{p+\frac{1}{2},j}^{n+1} + N_{p-\frac{1}{2},j}^{n+1} + R_{p,j}^{n+1}\Delta x_p \qquad 7.41$$

where:

$c_{p,j}^{n+1}$= concentration of species j in the pth Finite Volume at time step n+1

- $c_{p,j}^{n}$= concentration of species j in the pth Finite Volume at time step n
- $N_{p+\frac{1}{2},j}^{n+1}$ = flux of species j at the p+1st flux boundary at time step n+1
- $N_{p-\frac{1}{2},j}^{n+1}$ = flux of species j at the pth flux boundary at time step n+1
- $R_{p,j}^{n+1}$ = rate of change of species j in pth Finite Volume at time step n+1 due to homogeneous chemical reactions
- Δx_p = width of Finite Volume p
- $\Delta t = t_{n+1} - t_n$ is the nth time step (usually constant time steps are used)

This can be rewritten as:

$$c_{p,j}^{n+1} - c_{p,j}^{n} = r_p\left(-N_{p+\frac{1}{2},j}^{n+1} + N_{p-\frac{1}{2},j}^{n+1}\right) + \Delta t\, R_{p,j}^{n+1} \qquad 7.42$$

where $r_p=\Delta t/\Delta x_p$.

Using linearization of terms to create the equations to be solved, ignoring second order terms or higher, we can use:

$$N_{p+\frac{1}{2},j}^{n+1} = N_{p+\frac{1}{2},j}^{n\prime} + \frac{\partial N_{p+\frac{1}{2},j}^{n\prime}}{\partial c_{k,i}^{n\prime}} \left(c_{k,i}^{n+1} - c_{k,i}^{n\prime}\right) \quad 7.43$$

$$N_{p-\frac{1}{2},j}^{n+1} = N_{p-\frac{1}{2},j}^{n\prime} + \frac{\partial N_{p-\frac{1}{2},j}^{n\prime}}{\partial c_{k,i}^{n\prime}} \left(c_{k,i}^{n+1} - c_{k,i}^{n\prime}\right) \quad 7.44$$

$$R_{p,j}^{n+1} = R_{p,j}^{n\prime} + \frac{\partial R_{p,j}^{n\prime}}{\partial c_{k,i}^{n\prime}} \left(c_{k,i}^{n+1} - c_{k,i}^{n\prime}\right) \quad 7.45$$

where n' refers to the values of the freedoms at an intermediate time step $t_n \leq n' \leq t_{n+1}$. Hence the linearized form of the discretized equations becomes:

$$c_{p,j}^{n+1} + r_p \frac{\partial N_{p+\frac{1}{2},j}^{n\prime}}{\partial c_{k,i}^{n\prime}} c_{k,i}^{n+1} - r_p \frac{\partial N_{p-\frac{1}{2},j}^{n\prime}}{\partial c_{k,i}^{n\prime}} c_{k,i}^{n+1} - \Delta t \frac{\partial R_{p,j}^{n\prime}}{\partial c_{k,i}^{n\prime}} c_{k,i}^{n+1} = c_{p,j}^{n} + r_p \left(N_{p-\frac{1}{2},j}^{n\prime} - N_{p+\frac{1}{2},j}^{n\prime}\right) + r_p \left(\frac{\partial N_{p+\frac{1}{2},j}^{n\prime}}{\partial c_{k,i}^{n\prime}} c_{k,i}^{n\prime} - \frac{\partial N_{p-\frac{1}{2},j}^{n\prime}}{\partial c_{k,i}^{n\prime}} c_{k,i}^{n\prime} \right) + \Delta t R_{p,j}^{n\prime} - \Delta t \frac{\partial R_{p,j}^{n\prime}}{\partial c_{k,i}^{n\prime}} c_{k,i}^{n\prime} \quad 7.46$$

Note: that the left-hand side of this equation has unknown values at the end of the next time step (t=t_{n+1}) and the right-hand side of this equation is based on the known values at the intermediate time $t_{n'}$.

7.7.1 Chemical Reactions Terms and Derivatives

The rates of the chemical reactions within the pth Finite Volume only depend on the concentration of freedoms associated with that Finite Volume, i.e. $R_{p,j} = R_{p,j}(c_{p,k})$ only. Hence the only non-zero terms in the chemical reaction Jacobian are the $\frac{\partial R_{p,j}^{n\prime}}{\partial c_{p,i}^{n\prime}}$ terms. These can be calculated from the chemical reaction terms.

7.7.2 Flux Terms and Derivatives

The flux terms are:

$$N_j = -D_j \frac{\partial c_j}{\partial x} \quad 7.47$$

which means that we need a way of estimating the concentration gradients, $\frac{\partial c_j}{\partial x}$ at each flux boundary. To calculate the fluxes $N_{p-1/2,j}$ and $N_{p+1/2,j}$

associated with Finite Volume p, we use a quadratic representation of the concentration fields. In terms of the Figure 7-4 below:

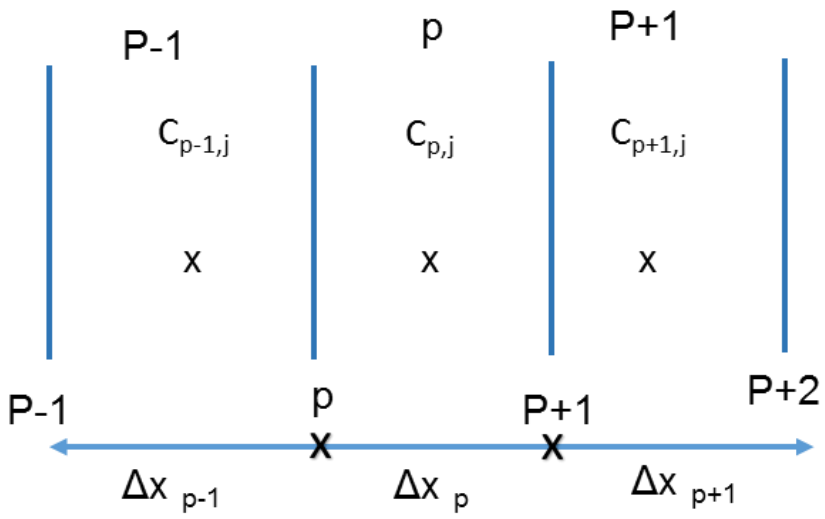

Figure 7-4. Concentration fields in finite volumes p-1, p and p+1.

For each species j fit a quadratic through the species concentration freedoms with x'=0 at the upstream boundary of FV p-1 and $x'=\Delta x_{p-1}+\Delta x_p+\Delta x_{p+1}$ at the downstream boundary of FV p+1, so that:

- $c_j = c_{p-1,j}$ at $x' = (\Delta x_{p-1})/2$
- $c_j = c_{p,j}$ at $x' = \Delta x_{p-1} + (\Delta x_p)/2$
- $c_j = c_{p+1,j}$ at $x' = \Delta x_{p-1} + \Delta x_p + (\Delta x_{p+1})/2$

Within FV p the derivatives of the fluxes $N_{p,j}$ and $N_{p+1,j}$ with respect to the freedoms $c_{p-1,j}$, $c_{p,j}$ and $c_{p+1,j}$ can be calculated analytically using the quadratic representation of the concentration field c_j within that FV.

At flux boundary 0, corresponding to the steel surface, $N_{0,j}$ fluxes and their derivatives are given in terms of the electrochemical reactions. At flux boundary 1, $N_{1,j}$ fluxes and their derivatives are calculated by derivatives at the upstream boundary of FV 1 in terms of the freedoms $c_{0,j}$, $c_{1,j}$, $c_{2,j}$

For internal flux boundaries where $2 \leq i \leq nFV-2$ then the fluxes and their derivatives $N_{i,j}$ can be calculated in two ways:

- by calculating concentration gradients and their derivatives at the upstream boundary of FV i: $\frac{dc_{i,j}}{dx}_u$ in terms of freedoms $c_{i-1,j}$, $c_{i,j}$, $c_{i+1,j}$
- by calculating concentration gradients and their derivatives at the downstream boundary of FV(i-1): $\frac{dc_{i,j}}{dx}_d$ in terms of freedoms $c_{i-2,j}$, $c_{i-1,j}$, $c_{i,j}$

As recommended by Nordsveen et al. [44], for flux boundaries 2 ≤ i ≤nFV-2 the concentration gradients and their derivatives are calculated by using the harmonic mean of these two gradients. This ensures that the non-uniform grid spacing does not lead to large concentration gradients that may cause numerical errors. Hence:

$$\frac{dc_{i,j}}{dx} = 2\frac{\frac{dc_{i,j}}{dx}_u \times \frac{dc_{i,j}}{dx}_d}{\left(\frac{dc_{i,j}}{dx}_u + \frac{dc_{i,j}}{dx}_d\right)} \quad \text{and} \quad N_{i,j} = -D_j \frac{\partial c_{i,j}}{\partial x}$$

where x_i is the location of the ith flux boundary in the boundary layer.

At flux boundary nFV-1, $N_{nFV-1,j}$ fluxes and their derivatives are calculated by derivatives at the downstream boundary of FV nFV-2 in terms of the freedoms $c_{nFV-3,j}$, $c_{nFV-2,j}$, $c_{nFv-1,j}$.

The derivatives of these fluxes need to be determined too, so that the corrosion equations can be solved using Newton iteration. These can be determined analytically and their harmonic means will be calculated numerically. The derivatives $\frac{\partial N^{n'}_{p-\frac{1}{2},j}}{\partial c^{n'}_{k,i}}$ and $\frac{\partial N^{n'}_{p+\frac{1}{2},j}}{\partial c^{n'}_{k,i}}$ are calculated using Finite Differences.

7.7.3 Numerical Solution of the Time-Dependent Equations

At each time step, the discretised form of the time-dependent equations (7.46) are solved to yield the concentration freedoms at time t=t_{n+1}, ${c_{p,j}}^{n+1}$. Due to the non-linearity of these equations, approximations of these freedoms are obtained at a series of intermediate times $t_n \leq t_{n'} \leq t_{n+1}$ until the difference between successive approximations is below a prescribed

error tolerance. In the solutions presented here, a tolerance of 0.01 is used since this provides a suitable compromise between accuracy and efficiency.

Under-relaxation normally needs to be used to get converged solutions. The solutions are obtained by linearising all terms and solving by Newton Iteration.

$$c_{p,j}^{n+1} + r_p \frac{\partial N^{n'}_{p+\frac{1}{2},j}}{\partial c^{n'}_{k,i}} c_{k,i}^{n+1} - r_p \frac{\partial N^{n'}_{p-\frac{1}{2},j}}{\partial c^{n'}_{k,i}} c_{k,i}^{n+1} - \Delta t \frac{\partial R^{n'}_{p,j}}{\partial c^{n'}_{k,i}} c_{k,i}^{n+1} = c_{p,j}^{n} + r_p \left(N^{n'}_{p-\frac{1}{2},j} - N^{n'}_{p+\frac{1}{2},j} \right) + r_p \left(\frac{\partial N^{n'}_{p+\frac{1}{2},j}}{\partial c^{n'}_{k,i}} c^{n'}_{k,i} - \frac{\partial N^{n'}_{p-\frac{1}{2},j}}{\partial c^{n'}_{k,i}} c^{n'}_{k,i} \right) + \Delta t R^{n'}_{p,j} - \Delta t \frac{\partial R^{n'}_{p,j}}{\partial c^{n'}_{k,i}} \quad 7.48$$

The numerical solution of the equations depends on a number of parameters, nFV, the number of Finite Volumes, the rate of expansion of the FV widths from the steel surface, the time-scale of the time-dependent integration and the size of the time steps used. If an incorrect combination is used this may lead to non-convergence of the equations, non-convergence to steady-state conditions etc. It is important to test the effect of each of these variables on the predictions of the model.

7.7.4 Modifications to Numerical Scheme

Note that for this problem the domain of calculation has to be adapted to take account of the growth and demise of the droplets with time. The growth of the droplet is simulated by controlling (moving) the position of the liquid/vapour interface, i.e. the outer boundary of the droplet. In reality, when the droplet reaches its maximum size and is removed from the top of the line, some liquid remains. This effect is included in the model. At the very beginning of the calculation when the first droplet with a minimum radius is generated, the initial concentrations in the droplet are set by equilibria for pure, freshly condensed water.

When this droplet grows, the outer boundary of the computational domain is shrunk back to match the initial (minimum) droplet size while the

concentrations of species in that small droplet are unchanged from what they were before detachment. The fact that the concentrations remain unchanged but the computational domain decreases instantaneously from h_{max} to h_{min} means that the concentration gradients are immediately increased by a factor of h_{max}/h_{min} everywhere in the droplet, leading to a surge in the corrosion rate. The new, freshly condensed droplet starts its lifetime with the minimum thickness, h_{min}.

7.8 Numerical Results

The first set of results show typical forms of output from the numerical model. This has been set up for the problem with WCR= 3 ml/m^{2}s, $T_{surface}$=20°C, P_{CO2}=0.97 bar with h_{max}=3.14 mm and h_{min}=0.0046 mm and the model is run for 3 droplet lifetimes. Figure 7-5 shows the average film height as a function of time throughout the 3 droplet lifetimes, while Figure 7-6 shows how concentrations across the droplet film differ with respect to the bulk equilibrium concentrations. Figure 7-7 shows the predicted corrosion rates throughout the 3 droplet lifetimes.

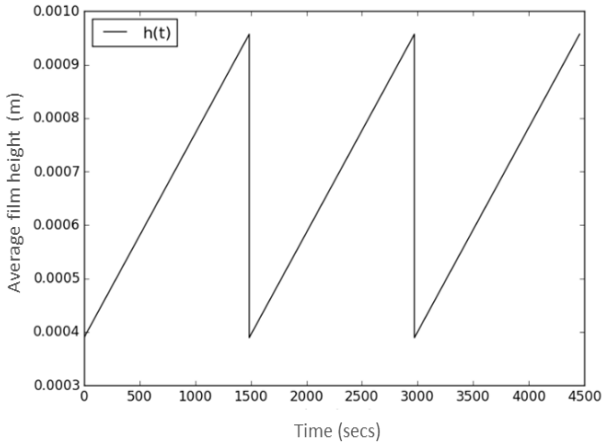

Figure 7-5. Droplet height change as a function of droplet lifetime at $T_{surface}$=20°C, P_{CO2}=0.97 bar and WCR of 3 ml/m^2.s

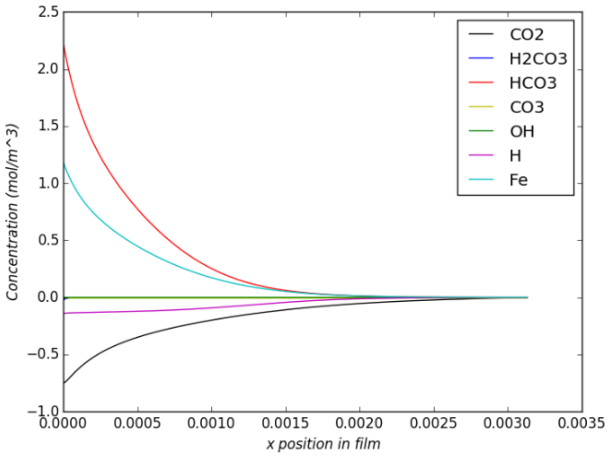

Figure 7-6. Concentration profiles for the main dissolved species as a function of distance from the steel surface at $T_{surface}$=20°, P_{CO2}=0.97 bar and WCR of 3 ml/m^2.s

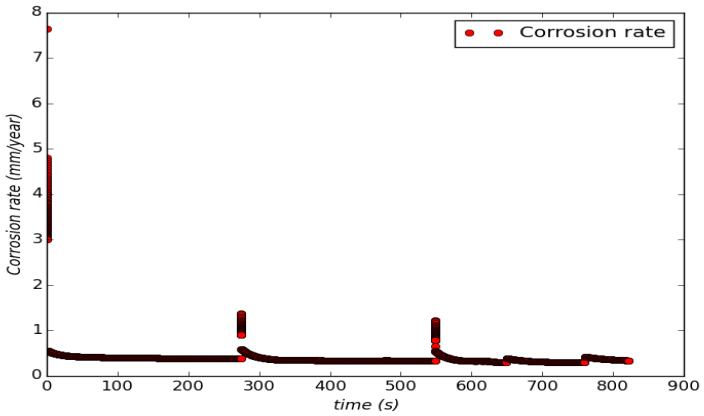

Figure 7-7. Predicted TLC rate as a function of time for 3 water droplet lifetimes at $T_{surface}$=20°C, P_{CO2}=0.97 bar and WCR=3 ml/m^2.s

Note:

The fact that the concentrations remain unchanged but the computational domain decreases instantaneously from h_{max} to h_{min} means that concentration gradients are immediately increased by a factor of h_{max}/h_{min} everywhere in the droplet, leading to a surge in the corrosion rate. This can be seen in the figure above.

7.8.1 Effect of Numerical Parameters

The calculations are extremely lengthy and require the use of small time steps and a large number of Finite Volumes in order the resolve the concentrations across the droplets. As noted by Zhang et al. [7] it necessary to use a more refined grid near the steel surface to resolve the electrochemical processes occurring near the corroding surface while a coarser grid will be adequate towards the liquid/gas interface. In the numerical calculations shown here the Finite Volume widths Δxp are increased progressively from the steel surface by a constant scale factor (typically between 1.01 and 1.03).

The following tables show the effect of the number of Finite Volumes, nFV, and time step, Δt, on the numerical predictions of corrosion rate in mm/year for the case of WCR=1 ml/m^2.s, P_{CO2}=0.97 bar, $T_{surface}$=20°C, h_{max}=4.695mm and h_{min}=0.0019mm. Corrosion rates are given at the time t=150 seconds, after which the corrosion rates have achieved an effective steady state, with a fixed time step of Δt=0.01s.

Table 7-4. TLC at different nFVs at surface temperature =20°C.

nFV (no)	TLC (mm/y)	WCR (ml/m^2.s)	P_{CO2} (bar)
75	0.502	1	0.97
100	0.476	1	0.97
150	0.486	1	0.97

This shows that the corrosion rate is not very sensitive to the value of nFV for nFV≥75.

Table 7-5 shows that the corrosion rate is not very sensitive to the value of Δt for $\Delta t \leq 0.01$s. Since the calculations are time-consuming all the following results are obtained using nFV=75 and Δt=0.01s, which is a suitable compromise between accuracy and numerical efficiency.

Table 7-5. TLC with different Δts at surface temperature =20°C and P_{CO2}= 0.97 bar.

Δt	TLC (mm/y)	WCR (kg/m^2.s)
0.01	0.502	0.001
0.005	0.505	0.001
0.0025	0.505	0.001

7.8.1 Comparison with Experiments for Static TLC Conditions

The corrosion rate predictions of the model were compared with the experimental measurements for static conditions obtained from the weight loss (WL) method. As seen in Figure 7-8 and Table 7-6, the model predictions show reasonable agreement with the experimental results. However, the experimental results are consistently higher than model's predictions, with a typical discrepancy of around (14-40%). The model's predictions are also more accurate for the lower condensation rates that are found in static conditions. It is important to recognise that the model conditions may differ from the experimental conditions in two important respect. The first is that the model is based on a uniform coverage of condensate whereas in the experimental conditions, corrosion occurs under a single droplet. The second difference may be attributed to the presence of an un-protective iron carbide (Fe_3C) scale. Since Fe_3C is an electronic

conductor, it is believed that its presence increases the corrosion rate by causing galvanic effect and acting as a cathodic site for the hydrogen evolution reaction [98, 187]. Hence, as the corrosion process continues, more iron carbide forms, increasing the cathodic reaction and therefore the corrosion rate. The including of the microstructure effect in the TLC modeling is outside the scope of the present study. In view of these differences, a typical discrepancy of around (14-40%) is reasonable and suggests that the model can be used to explore the effect of key parameters on the corrosion rates under the static top of line conditions.

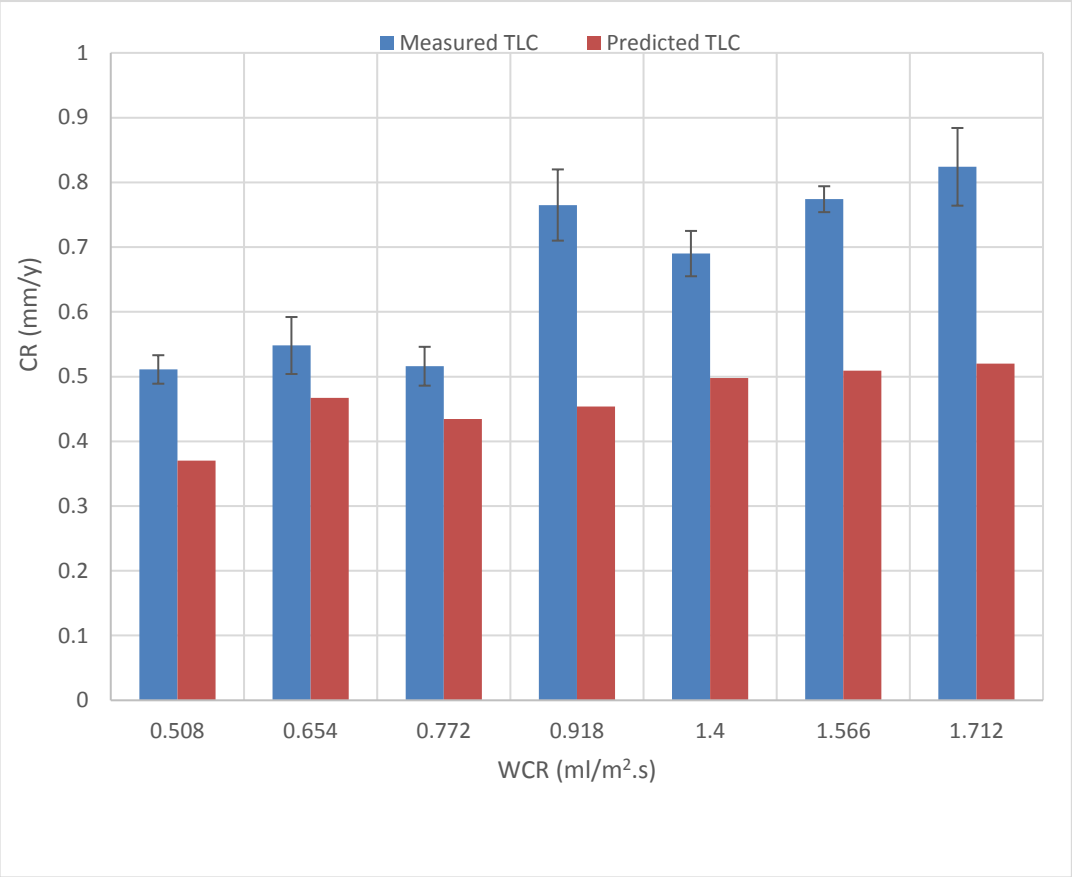

Figure 7-8. Predicted and measured TLC data comparison, at static conditions, atmospheric pressure and time= 24 hours.

Table 7-6. Predicted and measured TLC results at static conditions.

WCR ($kg/m^2.s$)	P_{CO2} (bar)	R_{min} (mm)	T_{gas} (°C)	$T_{surface}$ (°C)	TLC predicted (mm/y)	TLC measured after 24 hours (mm/y)	% Discrepancy
0.000508	0.989	0.0019	30	8	0.370	0.511	27.59
0.000654	0.976	0.00209	40	20	0.467	0.548	14.78
0.000772	0.983	0.0017	40	15	0.434	0.516	15.83
0.000918	0.952	0.00233	50	32	0.454	0.765	40.65
0.0014	0.983	0.0012	50	15	0.498	0.69	27.83
0.001566	0.976	0.00105	60	20	0.509	0.774	34.24
0.001712	0.983	0.00093	60	15	0.520	0.824	36.89

7.8.2 Effect of Key Parameters

7.8.2.1 Effect of Water Condensation Rate

Figure 7-9 illustrates how the TLC rates are affected by increasing the water condensation rates for static flow conditions. A number of previous studies have explored the effect of condensation rate on TLC rate in pipe flow conditions and, generally, these show that TLC rate increases with water condensation rate [12, 82, 84].

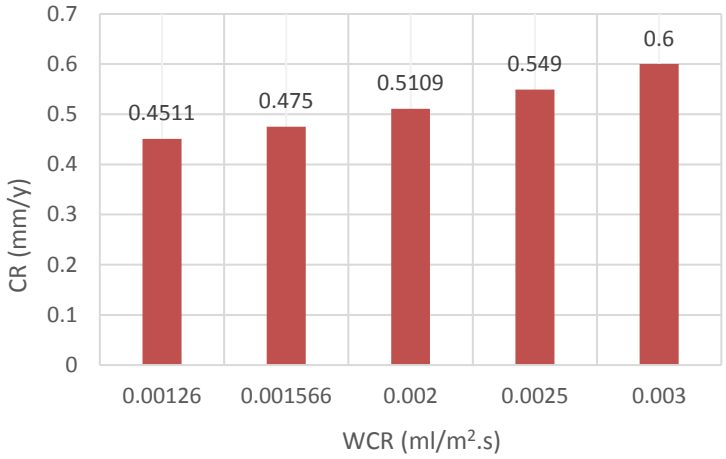

Figure 7-9. Predicted TLC at different water condensation rates at $T_{surface}$ =20°C, P_{CO2}=0.97 bar.

These results show that for static conditions, TLC increases in a monotonic, quasi-linear manner as water condensation rate increases.

7.8.3 Effect of CO_2 Partial Pressure

Figure 7-10 shows the effect of increasing CO_2 partial pressure on TLC for static TOLC conditions. It can be seen that corrosion rate increases when CO_2 partial pressure increases; this might be caused by increasing either the total pressure or the molar concentration of CO_2 in the gas phase. This means the concentrations of species are increased everywhere, in the droplet and at the steel surface, leading to a significant increase in the corrosion rate. Once again, the corrosion rate increases in a monotonic, linear manner as CO_2 partial pressure increases.

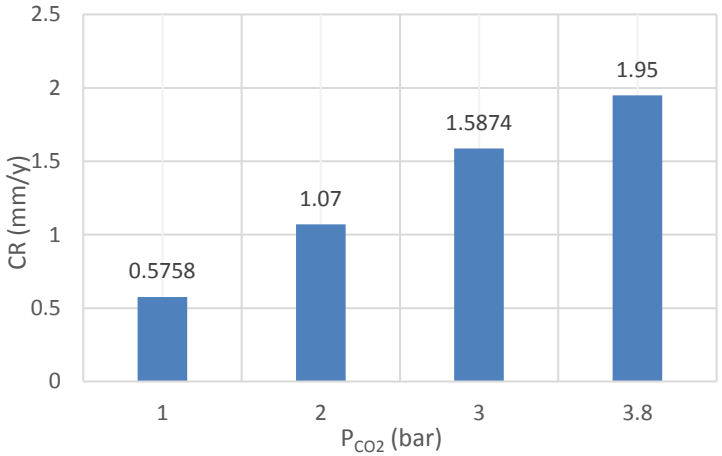

Figure 7-10. Predicted TLC at different CO_2 partial pressures and WCR=3 ml/m^2.s and $T_{surface}$ of 20°C.

7.8.3.1 Effect of Minimum Water Condensed Droplet Radius, r_{min}

The effect of the minimum droplet radius, for a fixed r_{max} =4.695mm, on the predicted TLC rate is illustrated in Table 7-7. The table shows that a decrease in r_{min} by a factor 10 gives an insignificant decrease in the predicted TLC rate. This shows that variations in r_{min} are much less influential than variations in water condensation rate and CO_2 partial pressure.

Table 7-7. Predicted TLC at different minimum droplet radius and surface temperature =20°C and P_{CO2}=0.97 bar

r_{min} (mm)	WCR (ml/m^2.s)	TLC (mm/y)
0.19	1	0.589
0.019	1	0.516
0.0019	1	0.503

7.9 Summary

Based on the basic principles of dropwise condensation theory, a mechanistic model for top of line corrosion model under static flow conditions has been developed and implemented to predict the effect of key parameters on TLC rates. The model takes into account the mechanisms of the CO_2 corrosion process, the rates of the different electrochemical reactions, the rates of the mass transfer processes, various equilibrium reactions in the system and the evolution of the droplet volume over a number of droplet lifetimes. The comparison between model predictions and experimental data has shown that the model can reasonably predict the corrosion rate at the top of the line for static conditions where corrosion products are not formed.

Chapter 8. Conclusions and Future Recommendations

This chapter summarises the main final findings and conclusions from the work undertaken during this PhD project. Also, this chapter suggests additional lines of research in order to improve understanding that will enable effective mitigation of the phenomenon of top of the line corrosion during oil and gas production and transportation.

8.1 Conclusions

A comprehensive study to investigate and understand the mechanism for top of the line corrosion in CO_2 dominated environments including experiments, modeling approaches and post-experiment surface analysis techniques has been carried out.

A new experimental setup was designed to simulate the top of the line corrosion process in an environment similar to field experience and to improve the quality of the experimental data. The unique setup is able to measure the real T_s, T_g and WCR, and enabling the corrosion rate of X65 steel coupons to be determined via weight change method and post-processing analysis. The apparatus holds many advantages as it involves very versatile and low-cost systems and also safety concerns related to high pressure and temperature setups are avoided and the issue of re-evaporation has been tackled.

The effects of the important factors on TLC such as operating temperatures and condensation rate were evaluated experimentally in 7-day term tests.

Hence, for the top of line corrosion, the question is, what is the relationship/synergy between the condensation rate and surface temperature and which is dominant under which conditions? One of the main objectives of the work presented in this study is to find the actual relation between the different factors that determine and affect TLC.

The extensive data obtained in this study gave an additional understanding of the actual relation between the different factors that determine and affect TLC, and which is dominant under which conditions. At the surface temperature lower than 32°C, the role of WCR is not substantial. But at the surface temperature higher than 32°C, both the WCR and pipe temperature influence the TLC, precipitation rate and scale film formation.

On the basis of the wide-ranging experimental data, a new empirical model to predict the TLC rate in the absence of $FeCO_3$ films is proposed. This model includes the most influential TLC variables, namely WCR and internal pipe temperature. The model enabled the effect of both T_s and WCR on CR to be isolated from one another and their contributions to be quantified.

The kinetic constant used in the precipitation equation which was proposed by Sun and Nesic is limited to the case of BLC. In this study, this constant was reviewed and a new constant was suggested for TLC scenario. This constant could give a more accurate calculation of iron carbonate precipitation rate in the case of top of line.

The localised corrosion investigation under different conditions was identified using surface profilometry technique. Understanding the kinetics of the $FeCO_3$ film formation, including when it does and does not form, is an important step towards identifying whether localised corrosion is likely to occur. Along of 7 days of exposure and at particular conditions of the condensation rate and the steel temperature, a partially protective corrosion film was formed, and localized corrosion was very clearly observed on the steel surface. Pits seemed to be growing in depth with time especially at higher steel temperatures.

To gain insight into the effect of the various influencing parameters on the water condensation rate, a parametric study has been done through implementing Zhang model using python code. In general, the results showed that all parameters that could promote heat and mass transfer

processes can increase the condensation rate. The main findings, and achievements in this study are summarized following:

- Due to increasing the driving forces (mass transfer and/or heat transfer) with an increase of the inlet temperature of the gas phase, the condensation rate is strongly enhanced.
- The results show a linear relationship between the gas velocity and condensation rate, as the gas velocity increases the condensation rate increases under all conditions of temperature and pressure.
- Two opposite impacts of the total pressure on the condensation rate have been seen, and no significant change was seen in the range of the investigated pressure.
- The effect of both total pressure and gas temperature on the droplet size has been studied by using this model. The gas pressure has a significant influence on the droplet motion and droplet size. Increasing gas pressure leads to increasing gas density, this increased the drag force dramatically, and the force balance in the horizontal direction can be reached at lower gas velocities. However, the gas temperature has an insignificant effect on the maximum droplet size and droplet motion.

In this PhD study, a mechanistic model was proposed for the prediction of the dropwise condensation rate at stagnant conditions in a top of the line corrosion scenario in the presence of non-condensable gases. The model is based on the analysis of heat transfer, mass transfer, hydrodynamics, and forces acting on a single droplet. The performance of the model to predict the condensation rate has been verified by experiments in a specially designed test setup. The verification results showed satisfactory performance in the prediction of condensation rate. The model can present a theoretical base for the development of a corrosion model at the top of the line.

A useful technique has been developed in this study to calculate the droplet lifetime (DLT). The results have been shown that the condensed droplets can stay on the surface at the top of the line depending on the water condensation rates. The DLT plays an important role in controlling the iron carbonate precipitation process, which in turn, can affect the TLC significantly.

In this thesis, on the basis of a wide range of the experimental data, an empirical model has been developed to predict the corrosion rate at the top of the line under static conditions.

A mechanistic model has been developed to predict TLC under static conditions. The model takes into account the mechanisms of the CO_2 corrosion process, the rates of the different electrochemical reactions, the rates of the mass transfer processes, various equilibrium reactions in the system and the evolution of the droplet volume over a number of droplet lifetimes. In comparison with experimental results, the model predictions have shown a reasonable agreement and the model can be used to provide insight with TLC under static conditions. The model does not account for the impact of the formation of a $FeCO_3$ film on the steel surface.

8.2 Recommendations for Future Work

The literature review carried out here has shown that the gas pipelines do not carry only water vapour but a certain range of hydrocarbons. The presence of the hydrocarbons with water vapour can cause a co-condensation process of hydrocarbons along with water vapour at the top of the pipelines. This process could change not only heat transfer behaviour for water vapour condensation but also the chemical speciation in water chemistry. Taking this factor into consideration will be useful to extend the ability of the present developed model to predict the water condensation rates during the oil and gas transportation process.

It has been widely reported that the presence of acetic acid in the wet gas can significantly increase TLC rate. Further experimental and theoretical works should focus on the effect of this corrosive species on pipeline corrosion. This can be done by using the relevant equations of mass and heat balance, adding additional terms to the charge balance equation, and using the applicable equations for the vapour/liquid equilibria for these additional species. Also, the mass transport of species in the droplet should be considered.

The duration of the present experimental work was seven days, for further study time-dependent of TOL localised corrosion mechanism, the duration of the experiments could be extended for a longer period such as 1 month or even up to 3 or 4 months.

The present study work is focused on the top of line corrosion in CO_2 dominated environments. However, H_2S-top of the line corrosion did not cover in this study and could be a focus of future research work.

The TLC model prediction procedure was developed in this study for predicting uniform CO_2 corrosion rates in the absence of corrosion scale on the metal surface, however, the model can be extended to conditions where iron carbonate scale formation takes place by taking in account the equations for scale formation.

References

1. Kermani, M. and A. Morshed, *Carbon dioxide corrosion in oil and gas production—a compendium.* Corrosion, 2003. **59**(8): p. 659-683.

2. Cheng, Y.F., *Pipeline Engineering.* Pipeline Engineering, Encyclopedia of Life Support System (EOLSS), Developed under the Auspices of the UNESCO, EOLSS Publishers, Oxford, UK, 2010.

3. Nyborg, R., *Controlling internal corrosion in oil and gas pipelines.* business briefing: exploration & production: the oil & gas review, 2005. **2**: p. 70-74.

4. Craig, B.D., *Practical oilfield metallurgy and corrosion*. 1993: Pennwell Corp.

5. Al-Hashem, A. and J. Carew. *Downhole Materials Optimization for Harsh Petroleum Production*. in *CORROSION 2003*. 2003. NACE International.

6. Edwards, M.A. and B. Cramer. *Top of line corrosion-Diagnosis, root cause analysis and treatment*. in *CORROSION 2000*. 2000. NACE International.

7. Zhang, Z., et al., *A mechanistic model of top-of-the-line corrosion.* Corrosion, 2007. **63**(11): p. 1051-1062.

8. Singh, S. and A. Mukherjee, *Kinetics of mild steel corrosion in aqueous acetic acid solutions.* Journal of Materials Science & Technology, 2010. **26**(3): p. 264-269.

9. Tran, T., et al., *Investigation of the mechanism for acetic acid corrosion of mild steel.* Corrosion/2013 paper, 2013(2487).

10. Nešić, S., *Key issues related to modelling of internal corrosion of oil and gas pipelines–A review.* Corrosion Science, 2007. **49**(12): p. 4308-4338.

11. Ajayi, F., Mitigating corrosion risks in oil and gas equipment by electrochemical protection: top of the line corrosion. 2015, PhD thesis, University of Manchester.

12. Larrey, D. and Y.M. Gunaltun. *Correlation of cases of top of line corrosion with calculated water condensation rates*. in *CORROSION 2000*. 2000. NACE International.

13. Dugstad, A., L. Lunde, and S. Nesic. *Control of internal corrosion in multi-phase oil and gas pipelines*. in *Proceedings of the conference Prevention of Pipeline Corrosion, Gulf Publishing Co*. 1994.

14. Shaw, B.A. and R.G. Kelly, *What is corrosion?* Interface-Electrochemical Society, 2006. **15**(1): p. 24-27.

15. Ossai, C., *Advances in asset management techniques: an overview of corrosion mechanisms and mitigation strategies for oil and gas pipelines. ISRN Corrosion, vol. 2012*.

16. Koch, G.H., et al., *Corrosion Cost and Preventative Strategies in the United States. Federal Highway Administration*. 2002, Report# FHWA-RD-01-156.

17. Cron, C. and G. Marsh, *Overview of economic and engineering aspects of corrosion in oil and gas production.* Journal of Petroleum Technology, 1983. **35**(06): p. 1,033-1,041.

18. Doctor, C. Corrosion cost to society 2017 [cited 2017 03/08/2017]; Available from: http://corrosion-doctors.org/Principles/Cost.htm.

19. Laboratories, G.M. Cost of Corrosion Annually in the US Over $1.1 Trillion in 2016. 2011 [cited 2017 03/08/2017]; Available from: http://www.g2mtlabs.com/corrosion/cost-of-corrosion/.

20. Kermani, M. and D. Harrop, *The impact of corrosion on oil and gas industry.* SPE Production & Facilities, 1996. **11**(03): p. 186-190.

21. Stansbury, E.E. and R.A. Buchanan, *Fundamentals of electrochemical corrosion*. 2000: ASM international.

22. Zheng, Y., et al., Advancement in Predictive Modeling of Mild Steel Corrosion in CO2-and H2S-Containing Environments. Corrosion, 2016. **72**(5): p. 679-691.

23. K, S. *Anti-corrosion Measures for Cable Bearers and Other Iron Fittings in Manholes*. 2008 [cited 2017 09/08/2017]; Available from: https://www.ntt-review.jp/archive/ntttechnical.php?contents=ntr200811sf3.html.

24. Shoham, O., Mechanistic modeling of gas-liquid two-phase flow in pipes. 2006.

25. Tiwari, A., *Characterization of mass transfer by condensation on a horizontal plate*. 2011, Université Blaise Pascal-Clermont-Ferrand II.

26. Beysens, D. and C. Knobler, *Growth of breath figures.* Physical review letters, 1986. **57**(12): p. 1433.

27. Chato, J., L.C. inside Horizontal, and I. Tubes, *American Society of Heating.* Refrigeration and Air Conditioning Engineering Journal, 1962. **4**: p. 52-60.

28. Vitse, F., *Experimental and theoretical study of the phenomena of corrosion by carbon dioxide under dewing conditions at the top of a horizontal pipeline in the presence of non-condensable gas*. 2002, Ohio University.

29. Minkowycz, W. and E. Sparrow, *Condensation heat transfer in the presence of noncondensables, interfacial resistance, superheating, variable properties, and diffusion.* International Journal of Heat and Mass Transfer, 1966. **9**(10): p. 1125-1144.

30. Vitse, F., et al., *Mechanistic model for the prediction of top-of-the-line corrosion risk.* Corrosion, 2003. **59**(12): p. 1075-1084.

31. Sardesai, R., R. Shock, and D. Butterworth, *Heat and mass transfer in multicomponent condensation and boiling.* Heat transfer engineering, 1982. **3**(3-4): p. 104-114.

32. Tanner, D., et al., *Heat transfer in dropwise condensation—Part I The effects of heat flux, steam velocity and non-condensable gas concentration.* International Journal of Heat and Mass Transfer, 1965. **8**(3): p. 419IN5421-420426.

33. Rose, J. and L. Glicksman, *Dropwise condensation—the distribution of drop sizes.* International Journal of Heat and Mass Transfer, 1973. **16**(2): p. 411-425.

34. Abu-Orabi, M., *Modeling of heat transfer in dropwise condensation.* International journal of heat and mass transfer, 1998. **41**(1): p. 81-87.

35. Sun, Y., T. Hong, and W. Jepson, *Pipeline corrosion under wet gas conditions.* Materials performance, 2001. **40**(10): p. 48-52.

36. Pojtanabuntoeng, T., *Influence of Water/Hydrocarbons Co-Condensation on Top of the Line Corrosion*. 2012: Ohio University.

37. Davis, J.R., *Corrosion: Understanding the basics*. 2000: ASM International.

38. Revie, R.W. and H.H. Uhlig, *Corrosion and corrosion control, An Introduction to corrosion science and engineering. A John Wiley & Sons.* INC., publication, 2008.

39. Barker, R.J., *Erosion-corrosion of carbon steel pipework on an offshore oil and gas facility*. 2012, PhD thesis, University of Leeds.

40. Ismail, A., *Seawater as a hydraulic fluid; corrosion mechanisms and rates of engineering materials*. 2014, PhD thesis, University of Leeds.

41. Talbot, D.E. and J.D. Talbot, *Corrosion science and technology*. 2007: CRC press.

42. Oldham, K., *JC MYLAND Fundamentals of electrochemical science*. 1994, London, Academic Press.

43. De Waard, C. and D. Milliams, *Carbonic acid corrosion of steel.* Corrosion, 1975. **31**(5): p. 177-181.

44. Nordsveen, M., et al., *A mechanistic model for carbon dioxide corrosion of mild steel in the presence of protective iron carbonate films—part 1: theory and verification.* Corrosion, 2003. **59**(5): p. 443-456.

45. Wang, S., *Effect of oxygen on CO2 corrosion of mild steel*. 2009, Ohio University.

46. Bockris, J.M., D. Drazic, and A. Despic, *The electrode kinetics of the deposition and dissolution of iron.* Electrochimica Acta, 1961. **4**(2-4): p. 325-361.

47. Dugstad, A., *The importance of FeCO 3 supersaturation on the CO 2 corrosion of carbon steels.* A. Dugstad, Paper, 1992(14).

48. Dugstad, A., *Mechanism of protective film formation during CO corrosion of carbon steel*. 1998, NACE International, Houston, TX (United States).

49. Li, T., et al., *Mechanism of protective film formation during CO2 corrosion of X65 pipeline steel.* Journal of University of Science and Technology Beijing, Mineral, Metallurgy, Material, 2008. **15**(6): p. 702-706.

50. Yang, Y., et al., *Mechanical strength and removal of a protective iron carbonate layer formed on mild steel in CO2 corrosion.* CORROSION 2010, 2010.

51. Gao, M., X. Pang, and K. Gao, *The growth mechanism of CO 2 corrosion product films.* Corrosion Science, 2011. **53**(2): p. 557-568.

52. Sun, W. and S. Nešic, *Kinetics of corrosion layer formation: part 1—iron carbonate layers in carbon dioxide corrosion.* Corrosion, 2008. **64**(4): p. 334-346.

53. Revie, R.W., *Corrosion and corrosion control*. 2008: John Wiley & Sons.

54. The Core of Corrosion. *[cited 2017 06/09/2017]; Available from: https://www.alcf.anl.gov/articles/core-corrosion.*

55. Romero, J., et al., *Localized corrosion of API X52 and API X65 pipeline steels in the presence of treated seawater used in the oil industry.* Corrosion, 2004. **60**(7): p. 689-696.

56. Nešic, S. and K.-L. Lee, *A mechanistic model for carbon dioxide corrosion of mild steel in the presence of protective iron carbonate films—part 3: film growth model.* Corrosion, 2003. **59**(7): p. 616-628.

57. Waseda, Y., S. Suzuki, and Y. Waseda, *Characterization of corrosion products on steel surfaces*. Vol. 1. 2006: Springer.

58. Papavinasam, S., A. Doiron, and R.W. Revie, *Model to predict internal pitting corrosion of oil and gas pipelines.* Corrosion, 2010. **66**(3): p. 035006-035006-11.

59. Zhu, Z., et al. *A mechanistic model for predicting localized pitting corrosion in a brine water-CO2 system*. in *CORROSION 2011*. 2011. NACE International.

60. Garber, J.D., et al. *Modeling Pitting Corrosion In A CO2 System Containing Bacteria*. in *CORROSION 2008*. 2008. NACE International.

61. Schmitt, G. and S. Feinen. *Effect of anions and cations on the pit initiation in CO2 corrosion of iron and steel*. in *CORROSION 2000*. 2000. NACE International.

62. Amri, J., *On growth and stifling of localized corrosion attacks in CO2 and acetic acid environments: Application to the Top-of-Line corrosion of wet gas pipelines operated in stratified flow regime*. 2009, PhD thesis, Institut National Polytechnique de Grenoble-INPG.

63. Sun, Y., *Localized CO 2 Corrosion in Horizontal Wet Gas Flow*. 2003, Ohio University.

64. *Pitting Corrosion & How To Treat It*. June 26, 2017 [cited 2018 30/04]; Available from: http://steelfabservices.com.au/pitting-corrosion-how-to-treat-it/.

65. Schmitt, G. and M. Horstemeier. *Fundamental aspects of CO2 metal loss corrosion-Part II: Influence of different parameters on CO2 corrosion mechanisms*. in *CORROSION 2006*. 2006. NACE International.

66. De Waard, C., U. Lotz, and D. Milliams, *Predictive model for CO2 corrosion engineering in wet natural gas pipelines.* Corrosion, 1991. **47**(12): p. 976-985.

67. Chen, Y., et al. *Effects Of Temperature On CO2 Top Of Line Corrosion Of Pipeline Steel*. in *CORROSION 2011*. 2011. NACE International.

68. Dugstad, A., *Mechanism of Protective Film Formation During CO2 Corrosion of Carbon Steel*. NACE International.

69. Linter, B. and G. Burstein, *Reactions of pipeline steels in carbon dioxide solutions.* Corrosion science, 1999. **41**(1): p. 117-139.

70. Zhang, G. and Y. Cheng, *On the fundamentals of electrochemical corrosion of X65 steel in CO 2-containing formation water in the presence of acetic acid in petroleum production.* Corrosion Science, 2009. **51**(1): p. 87-94.

71. Sun, W., *Kinetics of iron carbonate and iron sulfide scale formation in carbon dioxide/hydrogen sulfide corrosion*. 2006: ProQuest.

72. Cui, Z., et al., *Study on corrosion properties of pipelines in simulated produced water saturated with supercritical CO 2.* Applied Surface Science, 2006. **252**(6): p. 2368-2374.

73. Singer, M., S. Nesic, and Y. Gunaltun. *Top of the line corrosion in presence of acetic acid and carbon dioxide*. in *CORROSION 2004*. 2004. NACE International.

74. van Hunnik, E. and B. Pots, *Formation of Protective FeCO3 Corrosion Product Layers in CO2 Corrosion, Control*. CORROSION.

75. Gatlin, L., *Evaluation of Inhibitors for Wet, Sour Gas Gathering Systems.* Materials Performance, 1978. **17**(5): p. 9-15.

76. Dugstad, A. *Fundamental aspects of CO2 metal loss corrosion-part 1: mechanism*. in *CORROSION 2006*. 2006. NACE International.

77. Lotz, U. and T. Sydberger, *CO2 corrosion of carbon steel and 13Cr steel in particle-laden fluid.* Corrosion, 1988. **44**(11): p. 800-809.

78. Mishra, B., et al., *Development of a predictive model for activation-controlled corrosion of steel in solutions containing carbon dioxide.* Corrosion, 1997. **53**(11): p. 852-859.

79. Dougherty, J.A. *A review of the effect of organic acids on CO2 corrosion*. in *CORROSION 2004*. 2004. NACE International.

80. Garsany, Y., D. Pletcher, and B.M. Hedges. *The role of acetate in CO2 corrosion of carbon steel: has the chemistry been forgotten?* in *CORROSION 2002*. 2002. NACE International.

81. Olsen, S. and A. Dugstad, *Corrosion under dewing conditions.* S. Olsen, A. Dugstad, CORROSION 91/472, NACE, Houston, TX. Per Copy$ 5, 1991.

82. Vitse, F., et al., *Semi-empirical model for prediction of the top of the line corrosion risk.* CORROSION 2002, 2002.

83. Son, A.J. *Pitfalls in Monitoring Sweet Corrosion Inhibition Using Residual Analysis Techniques*. in *CORROSION 2004*. 2004. NACE International.

84. Nyborg, R. and A. Dugstad. *Top of line corrosion and water condensation rates in wet gas pipelines*. in *CORROSION 2007*. 2007. NACE International.

85. Han, J., et al., *Roles of passivation and galvanic effects in localized CO2 corrosion of mild steel.* CORROSION/2008, paper, 2008(08332).

86. Schmitt, G.A., et al., *Understanding Localized CO2 Corrosion of Carbon Steel from Physical Properties of Iron Carbonate Scales*. NACE International.

87. Davis, J., *Corrosion: understanding the basics. 2000.* Materials Park, Ohio: ASM International. x.

88. Singer, M., et al., *CO2 top-of-the-line corrosion in presence of acetic acid: a parametric study.* Corrosion, 2013. **69**(7): p. 719-735.

89. Amri, J., E. Gulbrandsen, and R.P. Nogueira, *Effect of acetic acid on propagation and stifling of localized attacks in CO2 corrosion of carbon steel.* CORROSION 2009, 2009.

90. Okafor, P. and S. Nesic, *Effect of acetic acid on CO2 corrosion of carbon steel in vapor-water two-phase horizontal flow.* Chemical Engineering Communications, 2007. **194**(2): p. 141-157.

91. Andersen, T.R., et al. *The influence of condensation rate and acetic acid concentration on TOL-Corrosion in multiphase pipelines*. in *CORROSION 2007*. 2007. NACE International.

92. Green, D.W. and R.H. Perry, *Perry's Chemical Engineers' Handbook/edición Don W. Green y Robert H. Perry*. 1973.

93. Garsany, Y., D. Pletcher, and B. Hedges, *Speciation and electrochemistry of brines containing acetate ion and carbon dioxide.* Journal of Electroanalytical Chemistry, 2002. **538**: p. 285-297.

94. Joosten, M.W., et al. *Organic acid corrosion in oil and gas production*. in *CORROSION 2002*. 2002. NACE International.

95. Nafday, O. and S. Nesic, *Iron carbonate scale formation and CO2 corrosion in the presence of acetic acid.* CORROSION 2005, 2005.

96. Crolet, J.-L. and M. Bonis. *Prediction of the Risks of CO Corrosion in Oil and Gas Wells*. in *Offshore Technology Conference*. 1990. Offshore Technology Conference.

97. Hinkson, D., et al., *A Study of the Chemical Composition and Corrosivity of the Condensate in Top of the Line Corrosion.* CORROSION 2008, 2008.

98. Lopez, D., T. Perez, and S. Simison, *The influence of microstructure and chemical composition of carbon and low alloy steels in CO 2 corrosion. A state-of-the-art appraisal.* Materials & Design, 2003. **24**(8): p. 561-575.

99. Akeer, E.S., *Effect of Carbon Steel Composition and Microstructure on CO 2 Corrosion*. 2014: Ohio University.

100. Dugstad, A., H. Hemmer, and M. Seiersten, *Effect of steel microstructure on corrosion rate and protective iron carbonate film formation.* Corrosion, 2001. **57**(4): p. 369-378.

101. Nyborg, R. and A. Dugstad, *Mesa corrosion attack in carbon steel and 0.5% chromium steel*. 1998, NACE International, Houston, TX (United States).

102. Nice, P.I. and M. Ueda, *The effect of microstructure and chromium alloying content to the corrosion resistance of low-alloy steel well tubing in seawater injection service*. 1998, NACE International, Houston, TX (United States).

103. Edmonds, D.V. and R.C. Cochrane, *The effect of alloying on the resistance of carbon steel for oilfield applications to CO2 corrosion.* Materials Research, 2005. **8**(4): p. 377-385.

104. Lopez, D., T. Perez, and S. Simison, *The influence of microstructure and chemical composition of carbon and low alloy steels in CO2 corrosion. A state-of-the-art appraisal.* Materials & Design, 2003. **24**(8): p. 561-575.

105. Lopez, D., et al., *The influence of carbon steel microstructure on corrosion layers: an XPS and SEM characterization.* Applied Surface Science, 2003. **207**(1-4): p. 69-85.

106. Lopez, D.A., S. Simison, and S. De Sanchez, *The influence of steel microstructure on CO2 corrosion. EIS studies on the inhibition efficiency of benzimidazole.* Electrochimica Acta, 2003. **48**(7): p. 845-854.

107. Crolet, J., N. Thevenot, and S. Nesic, *Role of conductive corrosion products in the protectiveness of corrosion layers.* Corrosion, 1998. **54**(3): p. 194-203.

108. Mora-Mendoza, J. and S. Turgoose, *Fe3C influence on the corrosion rate of mild steel in aqueous CO2 systems under turbulent flow conditions.* Corrosion Science, 2002. **44**(6): p. 1223-1246.

109. Gao, M., X. Pang, and K. Gao, *The growth mechanism of CO2 corrosion product films.* Corrosion Science, 2011. **53**(2): p. 557-568.

110. Farelas, F., et al., *Evolution of dissolution processes at the interface of carbon steel corroding in a CO2 environment studied by EIS.* Corrosion Science, 2010. **52**(2): p. 509-517.

111. Farelas, F., et al., *Evolution of dissolution processes at the interface of carbon steel corroding in a CO 2 environment studied by EIS.* Corrosion Science, 2010. **52**(2): p. 509-517.

112. Crolet, J.L., N. Thevenot, and S. Nesic, *Role of conductive corrosion products on the protectiveness of corrosion layers*. 1996, NACE International, Houston, TX (United States).

113. Sun, J., et al., *The formation mechanism of corrosion scale and electrochemical characteristic of low alloy steel in carbon dioxide-saturated solution.* Corrosion Science, 2012. **57**: p. 131-138.

114. Crolet, J.L., N. Thevenot, and A. Dugstad. *Role of free acetic acid on the CO2 corrosion of steels*. in *CORROSION 99*. 1999. NACE International.

115. Dugstad, A., H. Hemmer, and M. Seiersten. *Effect of steel microstructure upon corrosion rate and protective iron carbonate film formation*. in *CORROSION 2000*. 2000. NACE International.

116. Sun, W., et al. *A study of protective iron carbonate scale formation in CO2 corrosion*. in *AIChE annual meeting*. 2004.

117. Svenningsen, G. and R. Nyborg. *Modeling of top of line corrosion with organic acid and glycol*. in *CORROSION 2014*. 2014. NACE International.

118. Ruzic, V., M. Veidt, and S. Nešić, *Protective Iron Carbonate Films—Part 1: Mechanical removal in single-phase aqueous flow.* Corrosion, 2006. **62**(5): p. 419-432.

119. Nesic, S., et al., *A Mechanistic Model for Carbon Dioxide Corrosion of Mild Steel in the Presence of Protective Iron Carbonate FilmsPart 2: A Numerical Experiment.*

120. Sun, W., K. Chokshi, and S. Nesic, *Iron carbonate scale growth and the effect of inhibition in CO2 corrosion of mild steel.* CORROSION 2005, 2005.

121. Palumbo, O., et al., *Anelastic spectroscopy study of iron carbonate scales from CO 2 corrosion of steel.* Materials Science and Engineering: A, 2009. **521**: p. 343-346.

122. Pots, B.F. and E. Hendriksen. *CO2 corrosion under scaling conditions-the special case of top of line corrosion in wet gas pipelines*. in *CORROSION 2000*. 2000. NACE International.

123. Schmitt, G., M. Scheepers, and G. Siegmund. *Inhibition of the top-of-the-line corrosion under stratified flow*. in *CORROSION 2001*. 2001. NACE International.

124. Heidersbach, R., *Metallurgy and corrosion control in oil and gas production*. Vol. 14. 2010: John Wiley & Sons.

125. Ibrahim, T.H. and M.A. Zour, *Corrosion inhibition of mild steel using fig leaves extract in hydrochloric acid solution.* Int. J. Electrochem. Sci, 2011. **6**(12): p. 6442-6455.

126. Punpruk, S., M. Thammachart, and Y. Gunaltun. *Field Testing Of Volatile Corrosion Inhibitors And Evaluation Of Batch Treatment Efficiency By Cooled Probe*. in *CORROSION 2010*. 2010. NACE International.

127. Gunaltun, Y., et al., *Laboratory testing of volatile corrosion inhibitors.* CORROSION 2010, 2010.

128. Schmitt, G., et al., *Understanding Localized CO2 Corrosion of Mild steel from Physical Properties of Iron Carbonate Scales.* NACE CORROSION/99, paper, (38).

129. Gao, K., et al., *Mechanical properties of CO 2 corrosion product scales and their relationship to corrosion rates.* Corrosion Science, 2008. **50**(10): p. 2796-2803.

130. Pojtanabuntoeng, T., et al., *Assessment of corrosion control by pH neutralisation in the presence of glycol at low temperature.* Corrosion Science, 2017. **126**: p. 94-103.

131. Nalli, K., *Corrosion and its mitigation in the oil and gas industry.* An overview. PM-Pipeliner Report, 2010.

132. Singer, M., *Study and modeling of the localized nature of top of the line corrosion*. 2013, Ohio University.

133. Amri, J., *On growth and stifling of localized corrosion attacks in CO2 and acetic acid environments: Application to the Top-of-Line corrosion of wet gas pipelines operated in stratified flow regime*. 2009, Institut National Polytechnique de Grenoble-INPG.

134. Nalli, K., *Appendix VI: Corrosion and Its Mitigation in the Oil and Gas Industries.* Process Plant Equipment: Operation, Control, and Reliability, 2012: p. 673-679.

135. Popoola, L.T., et al., *Corrosion problems during oil and gas production and its mitigation.* International Journal of Industrial Chemistry, 2013. **4**(1): p. 35.

136. Jenkins, A. and I. Gilbert. *Development Of A Top-Of-Line Corrosion Inhibitor And A Top-Of-Line Corrosion Test Method*. in *CORROSION 2012*. 2012. NACE International.

137. Paillassa, R., M. Dieumegard, and M. Estevoyer. *Corrosion control in the gathering system at Lacq sour gas field*. in *2nd Intl. Congress of Metallic Corrosion, NACE*. 1963.

138. Bich, N.N. and K.E. Szklarz, *Crossfield corrosion experience.* N. N. Bich and K. E. Szklarz, Corrosion 88/196, NACE, Houston, TX, Per Copy$ 4. 00, 1988.

139. Singer, M. *Top of the line corrosion in sour environments–Study of the controlling parameters"*. in *Proc. International Corrosion Congress*. 2011.

140. Gunaltun, Y.M. and S. Achmad, *Top of line corrosion in multiphase gas lines: A case history*. 1999, NACE International, Houston, TX (United States).

141. Babakr, A. and A. Bairamov, *Top of line corrosion in industrial wastewater pipelines.* Hydrocarbon processing, 2003. **82**(9): p. 93-97.

142. Gunaltun, Y.M. and A. Belghazi. *Control of top of the line corrosion by chemical treatment*. in *CORROSION 2001*. 2001. NACE International.

143. Hinkson, D., et al., *A study of the chemical composition and corrosivity of the condensate in top of the line corrosion.* Corrosion/08, paper, 2008. **8466**.

144. Singer, M., et al., *Combined effect of carbon dioxide, hydrogen sulfide, and acetic acid on bottom-of-the-line corrosion.* Corrosion, 2011. **67**(1): p. 015004-1-015004-16.

145. Wanek, R. *Monitoring H2S to Meet New Exposure Standards*. 2011 [cited 2017 09/2017]; Available from: https://ohsonline.com/articles/2011/09/01/monitoring-h2s-to-meet-new-exposure-standards.aspx.

146. Singer, M., J. Al-Khamis, and S. Nešić, *Experimental study of sour top-of-the-line corrosion using a novel experimental setup.* Corrosion, 2013. **69**(6): p. 624-638.

147. Manuitt, A.C., *CO2 Top of the Line Corrosion in the Presence of H2S*. 2006, Ohio University.

148. Camacho, A., et al. *Top of the line corrosion in H2S/CO2 environment*. in *CORROSION 2008*. 2008. NACE International.

149. Pugh, D.V., et al. *Top-of-line corrosion mechanism for sour wet gas pipelines*. in *CORROSION 2009*. 2009. NACE International.

150. Nyborg, R., A. Dugstad, and T.G. Martin. *Top of line corrosion with high CO2 and traces of H2S*. in *CORROSION 2009*. 2009. NACE International.

151. Singer, M., et al., *Combined effect of CO2, H2S and acetic acid on bottom of the line corrosion.* CORROSION 2007, 2007.

152. SMART, J.S., *Wettability: A major factor in oil and gas system corrosion.* Materials performance, 2001. **40**(4): p. 54-59.

153. Pojtanabuntoeng, T., M. Singer, and S. Nesic. *Top-of-the-Line Corrosion in the presence of hydrocarbon Co-Condensation in Flowing Condition*. in *CORROSION 2012*. 2012. NACE International.

154. Pojtanabuntoeng, T., M. Singer, and S. Nesic, *Water/Hydrocarbon co-condensation and the influence on top-of-the-line corrosion.* CORROSION/11, paper, 2011(11330).

155. Asher, S.L., et al. *Top of the line corrosion prediction in wet gas pipelines*. in *CORROSION 2012*. 2012. NACE International.

156. Qin, H., et al. *Top of the line corrosion under low temperature and high condensation rate conditions*. in *CORROSION 2011*. 2011. NACE International.

157. Islam, M.M., T. Pojtanabuntoeng, and R. Gubner, *Condensation corrosion of carbon steel at low to moderate surface temperature and iron carbonate precipitation kinetics.* Corrosion Science, 2016. **111**: p. 139-150.

158. Kapusta, S.D., B.F. Pots, and I.J. Rippon. *The application of corrosion prediction models to the design and operation of pipelines*. in *CORROSION 2004*. 2004. NACE International.

159. Nyborg, R. *CO2 corrosion models for oil and gas production systems*. in *CORROSION 2010*. 2010. NACE International.

160. Fosbøl, P.L., E.H. Stenby, and K. Thomsen, *Carbon Dioxide Corrosion:: Modelling and Experimental Work Applied to Natural Gas Pipelines*. 2008: Technical University of DenmarkDanmarks Tekniske Universitet, CenterCenters, Center for Energy Resources EngineeringCenter for Energy Resources Engineering.

161. Fosbøl, P.L., K. Thomsen, and E.H. Stenby. *Improving mechanistic CO2 corrosion models*. in *CORROSION 2009*. 2009. NACE International.

162. De Waard, C. *Milliams DE Prediction of Carbonic Acid Corrosion in Natural Gas Pipelines*. in *First International Conference on the Internal and External Protection of Pipes, paper F1*. 1975.

163. De Waard, C. and U. Lotz, *Corrosion 93.* Huston, TX: NACE, 1993.

164. Zhang, Z., *A study of Top of the line corrosion under dropwise condensation*. 2008, Ohio University.

165. Remita, E., et al., *A kinetic model for CO2 corrosion of steel in confined aqueous environments.* Journal of the Electrochemical Society, 2008. **155**(1): p. C41-C45.

166. Amri, J., E. Gulbrandsen, and R. Nogueira, *The effect of acetic acid on the pit propagation in CO 2 corrosion of carbon steel.* Electrochemistry Communications, 2008. **10**(2): p. 200-203.

167. Ojifinni, R.A. and C. Li. *A parametric study of sweet top-of-line corrosion in wet gas pipelines*. in *CORROSION 2011*. 2011. NACE International.

168. Li, J., J. Chen, and S. Wang, *Introduction*, in *Risk Management of Supply and Cash Flows in Supply Chains*. 2011, Springer. p. 1-48.

169. Singer, M., Li, Chong, Achour, Mohsen, Jenkins, Alyn, *Top of the line corrosion – Part 1: Review of the mechanism and*

laboratory experience. NACE 2014.

170. Hua, Y., R. Barker, and A. Neville, *Effect of temperature on the critical water content for general and localised corrosion of X65 carbon steel in the transport of supercritical CO 2.* International Journal of Greenhouse Gas Control, 2014. **31**: p. 48-60.

171. Metals, A.C.G.-o.C.o., *Standard practice for preparing, cleaning, and evaluating corrosion test specimens*. 2011: ASTM International.

172. Sun, W., S. Nešić, and R.C. Woollam, *The effect of temperature and ionic strength on iron carbonate (FeCO 3) solubility limit.* Corrosion Science, 2009. **51**(6): p. 1273-1276.

173. Nesic, S. and W. Sun, *Corrosion in acid gas solutions.* Shreir's corrosion, 2010. **2**: p. 1270-1298.

174. Thomson, G.W., *The Antoine equation for vapor-pressure data.* Chemical reviews, 1946. **38**(1): p. 1-39.

175. Oddo, J.E. and M.B. Tomson, *Simplified calculation of CaCO3 saturation at high temperatures and pressures in brine solutions.* Journal of Petroleum Technology, 1982. **34**(07): p. 1,583-1,590.

176. Eldik, R. and D.A. Palmer, *Effects of pressure on the kinetics of the dehydration of carbonic acid and the hydrolysis of CO 2 in aqueous solution.* Journal of Solution Chemistry, 1982. **11**(5): p. 339-346.

177. Palmer, D.A. and R. Van Eldik, *The chemistry of metal carbonato and carbon dioxide complexes.* Chemical Reviews, 1983. **83**(6): p. 651-731.

178. Sun, W., *Kinetics of iron carbonate and iron sulfide scale formation in CO2/H2S corrosion*. 2006, Ohio University.

179. Goldstein, J., et al., *Scanning electron microscopy and X-ray microanalysis: a text for biologists, materials scientists, and geologists*. 2012: Springer Science & Business Media.

180. Yaakob, N., *Top of the Line Corrosion in CO2/H2S Environments*. 2015, Ohio University.

181. Fajardo, V., et al., *The effect of acetic acid on the integrity of protective iron carbonate layers in CO2 corrosion of mild steel.* CORROSION/2008, Paper, 2008(333).

182. Singh, D. and A. Kumar, *A fresh look at ASTM G 1-90 solution recommended for cleaning of corrosion products formed on iron and steels.* Corrosion, 2003. **59**(11): p. 1029-1036.

183. Estavoyer, M., *Corrosion problems at Lack sour gas field.* NACE publication “H2S corrosion in oil and gas production, 1981: p. 905.

184. Mendez, C., et al., *Effect of Acetic Acid, pH and MEG on the CO2 Top of the Line Corrosion.* CORROSION 2005, 2005.

185. Nusselt, W., *Die Oberflachenkondensationdes Wasserdamfes. Z*. Ver. deut. lng.

186. Stephan, K. and C.V. Green, *Heat transfer in condensation and boiling*. 1992: Springer.

187. Eliyan, F.F. and A. Alfantazi, *On the theory of CO 2 corrosion reactions–Investigating their interrelation with the corrosion products and API-X100 steel microstructure.* Corrosion Science, 2014. **85**: p. 380-393.

188. Wood, I., et al., *Thermal expansion and crystal structure of cementite, Fe3C, between 4 and 600 K determined by time-of-flight neutron powder diffraction.* Journal of Applied Crystallography, 2004. **37**(1): p. 82-90.

189. Effenberger, H., K. Mereiter, and J. Zemann, *Crystal structure refinements of magnesite, calcite, rhodochrosite, siderite, smithonite, and dolomite, with discussion of some aspects of the stereochemistry of calcite type carbonates.* Zeitschrift für Kristallographie-Crystalline Materials, 1981. **156**(1-4): p. 233-244.

190. Deganello, F., et al., *Cerium effect on the phase structure, phase stability and redox properties of Ce-doped strontium ferrates.* Journal of Solid State Chemistry, 2006. **179**(11): p. 3406-3419.

191. Smith, S.N. *A proposed mechanism for corrosion in slightly sour oil and gas production*. in *12th international corrosion congress, Houston, TX*. 1993.

192. Smith, S. and E. Wright, *Prediction of minimum H 2 S levels required for slightly sour corrosion.* S. N. Smith, and E. J. Wright, Paper, 1994(11).

193. Anderko, A. and P.J. Shuler, *A computational approach to predicting the formation of iron sulfide species using stability diagrams.* Computers & Geosciences, 1997. **23**(6): p. 647-658.

194. Anderko, A. and R.D. Young.Simulation of CO_2/H_2S corrosion using thermodynamic and electrochemical models. in corrosion -national association of corrosion engineers annual conference,199. NACE.

195. Anderko, A. Simulation of $FeCO_3/FeS$ scale formation using thermodynamic and electrochemical models. in corrosion -national association of corrosion engineers annual conference. 2000. NACE.

196. Smith, S.N. and J.L. Pacheco, *Prediction of corrosion in slightly sour environments.* CORROSION 2002, 2002.

197. Nesic, S., J. Lee, and V. Ruzic, *A mechanistic model of iron carbonate film growth and the effect on CO2 corrosion of mild steel.* CORROSION 2002, 2002.

198. Standard, A., *G46, Standard Guide for Examination and Evaluation of Pitting Corrosion.* ASTM International, West Conshohocken, PA, USA, 2005.

199. William, D., *Callister Jr.* Materials Science and Engineering an Introduction", John Wiley and Sons, 2007.

200. Pessu, F., R. Barker, and A. Neville, *Understanding Pitting Corrosion Behavior of X65 Carbon Steel in CO2-Saturated Environments: The Temperature Effect.* Corrosion, 2015. **72**(1): p. 78-94.

201. Han, J., B. Brown, and S. Nešic, *Investigation of the galvanic mechanism for localized carbon dioxide corrosion propagation using the artificial pit technique.* Corrosion, 2010. **66**(9): p. 095003-095003-12.

202. Nesic, S., J. Postlethwaite, and S. Olsen, *An electrochemical model for prediction of corrosion of mild steel in aqueous carbon dioxide solutions.* Corrosion, 1996. **52**(4): p. 280-294.

203. Zheng, Y., B. Brown, and S. Nešić, *Electrochemical study and modeling of H2S corrosion of mild steel.* Corrosion, 2013. **70**(4): p. 351-365.

204. Çengel, A., *HEHT TRANSFER.* 1998.

205. Yoshio, U., S. Akio, and Y. Hiroyuki, *On the mechanism determining the transition mode from dropwise to film condensation.* International journal of heat and mass transfer, 1988. **31**(5): p. 1113-1120.

206. Wu, Y.-T., C.-X. Yang, and X.-G. Yuan, A theoretical study of the effect of surface thermal conductivity on heat transfer coefficient in dropwise condensation. Numerical Heat Transfer: Part A: Applications, 2001. **40**(2): p. 169-179.

207. Gerner, F. and C. Tien, *Multi-component interfacial condensation.* International journal of heat and mass transfer, 1990. **33**(10): p. 2111-2120.

208. Wang, C.-Y. and C.-J. Tu, *Effects of non-condensable gas on laminar film condensation in a vertical tube.* International Journal of Heat and Mass Transfer, 1988. **31**(11): p. 2339-2345.

209. Shixue, W. and Y. Utaka, *Effect of non-condensable gas mass fraction on condensation heat transfer for water-ethanol vapor mixture.* JSME International Journal Series B Fluids and Thermal Engineering, 2004. **47**(2): p. 162-167.

210. Othmer, D.F., *The condensation of steam.* Industrial & Engineering Chemistry, 1929. **21**(6): p. 576-583.

211. Le Fevre, E. and J. Rose, *An experimental study of heat transfer by dropwise condensation.* International Journal of Heat and Mass Transfer, 1965. **8**(8): p. 1117-1133.

212. Citakoglu, E. and J. Rose, *Dropwise condensation—some factors influencing the validity of heat-transfer measurements.* International Journal of Heat and Mass Transfer, 1968. **11**(3): p. 523-537.

213. Tanner, D., et al., *Heat transfer in dropwise condensation—Part II surface chemistry.* International Journal of Heat and Mass Transfer, 1965. **8**(3): p. 427IN7429-428436.

214. Fatica, N. and D.L.V. Katz, *Dropwise condensation*. 1949: University of Michigan.

215. Sugawara, S. and I. Michiyoshi, *Dropwise condensation.* Mem. Fac. Eng., Kyoto Univ., Kyoto University, 1956. **18**: p. 84-111.

216. Gose, E.E., A. Mucciardi, and E. Baer, *Model for dropwise condensation on randomly distributed sites.* International Journal of Heat and Mass Transfer, 1967. **10**(1): p. 15-22.

217. Tanasawa, I. and F. Tachibana. *A synthesis of the total process of dropwise condensation using the method of computer simulation*. in *International Heat Transfer Conference 4*. 1970. Begel House Inc.

218. Rose, J., *Some aspects of condensation heat transfer theory.* International communications in heat and mass transfer, 1988. **15**(4): p. 449-473.

219. Graham, C. and P. Griffith, *Drop size distributions and heat transfer in dropwise condensation.* International Journal of Heat and Mass Transfer, 1973. **16**(2): p. 337-346.

220. Tanner, D., et al., *Heat transfer in dropwise condensation–Part1 & 2.* International Journal of Heat and Mass Transfer. **8**: p. 419-426.

221. WANG, S. and Y. UTAKA. *B308 EFFECT OF NON-CONDENSABLE GAS MASS FRACTION ON CONDENSATION HEAT TRANSFER FOR WATER-ETHANOL VAPOR MIXTURE*. in *Proceedings of the International Conference on Power Engineering: ICOPE*. 2003. 一般社団法人日本機械学会.

222. Dittus, F. and L. Boelter, *Public engineering, vol. 2.* University of California, Berkeley, 1930: p. 443.

223. Maa, J.R., *Drop size distribution and heat flux of dropwise condensation.* The Chemical Engineering Journal, 1978. **16**(3): p. 171-176.

224. Gunaltun, Y., et al., *Progress in the prediction of top of the line corrosion and challenges to predict corrosion rates measured in gas pipeline*. 2010, National Association of Corrosion Engineers, P. O. Box 218340 Houston TX 77084 USA.

225. Cengel, Y.A., *Heat transfer*, in *Encyclopedia of Energy Engineering and Technology-3 Volume Set (Print Version)*. 2007, CRC Press. p. 822-829.

226. Predel, B., M. Hoch, and M.J. Pool, *Phase diagrams and heterogeneous equilibria: a practical introduction*. 2013: Springer Science & Business Media.

227. Slegers, L. and R. Seban, *Laminar film condensation of steam containing small concentrations of air.* International Journal of Heat and Mass Transfer, 1970. **13**(12): p. 1941-1947.

228. Cengel, Y.A., *Introduction to thermodynamics and heat transfer*. 1997: McGraw-Hill New York.

229. WL McCabe, J.S., P Harriott *Unit Operations Of Chemical Engineering* Vol. 5th ed. 1993: McGraw-Hill, Inc.

230. Nesic, S., M. Nordsveen, and A. Stangel, *A Mechanistic Model for C02 Corrosion with Protective Iron Carbonate Films.* 2001.

231. Kvarekvål, J., *A kinetic model for calculating concentration profiles and fluxes of CO {sub 2}-related species across the Nernst diffusion layer*. 1997, NACE International, Houston, TX (United States).

232. Newman, J., *Electrochemical Systems, 2'nd edition Englewood.* New Jersey, Prentince-Hall, 1991: p. 378.

233. Bockris, I., *'M. The electrode kinetics of the deposition of iron/I. O'M. Bockris, D. Drazic, AR Despic.* Electrochimica Acta, 1961. **4**: p. 325-361.

234. Fardisi, S., N. Tajallipour, and P.J. Teevens. *Simulation And Analysis of the Effect of Different Design Parameters On the General Corrosion In the Annular Space of Flexible Pipes*. in *CORROSION 2012*. 2012. NACE International.

Appendix A: Homogeneous Chemical Reactions

In terms of concentrations given in molar (M) mol/litre the equations for the chemical reactions in the bulk liquid are given by the following chemical reactions:

1. Dissolution of CO_2: $CO_2(g) \Leftrightarrow CO_2(aq)$
2. Carbon dioxide hydration: $H_2O + CO_2 \Leftrightarrow H_2CO_3$
3. Carbonic acid dissociation: $H_2CO_3 \Leftrightarrow H^+ + HCO_3^-$
4. Bicarbonate ion dissociation: $HCO_3^- \Leftrightarrow H^+ + CO_3^{2-}$
5. Water dissociation: $H_2O \Leftrightarrow H^+ + OH^-$

$CO_{2(aq)}$ is created by carbonic acid hydration only:

The initial concentration of CO_2 (aq) in mol/litre can be calculated in terms of the partial pressure of CO_2 (in bar) via dissolution of CO_2: $K_{sol} = \frac{c_{CO_2}}{P_{CO_2}}$. Reaction rate of CO_2 is given by:

$$R_{CO_2} = \frac{d}{dt}\left(c_{CO_2}\right) = K_{b,hy}\, c_{H_2CO_3} - K_{f,hy} c_{CO_2}$$

H_2CO_3 is created carbon dioxide hydration and carbonic acid dissociation:

$$R_{H_2CO_3} = \frac{d}{dt}\left(c_{H_2CO_3}\right) = -\left(K_{b,hy}\, c_{H_2CO_3} - K_{f,hy} c_{CO_2}\right) - \left(K_{f,ca}\, c_{H_2CO_3} - K_{b,ca} c_{H^+} c_{HCO_3^-}\right)$$

Bicarbonate HCO_3^- ions are created by carbonic acid dissociation and bicarbonate ion dissociation:

$$R_{HCO_3^-} = \frac{dc_{HCO_3^-}}{dt} = \left(K_{f,ca}\, c_{H_2CO_3} - K_{b,ca} c_{H^+} c_{HCO_3^-}\right) - \left(K_{f,bi}\, c_{HCO_3^-} - K_{b,bi} c_{H^+} c_{CO_3^{2-}}\right)$$

Carbonate CO_3^{2-} ions are created by bicarbonate ion dissociation only:

$$R_{CO_3^{2-}} = \frac{dc_{CO_3^{2-}}}{dt} = \left(K_{f,bi}\, c_{HCO_3^-} - K_{b,bi} c_{H^+} c_{CO_3^{2-}}\right)$$

OH^- ions are created from water dissociation only:

$$R_{OH^-} = \frac{dc_{OH^-}}{dt} = K_{f,wa} - K_{b,wa} c_{H^+} c_{OH^-}$$

H^+ ions are created by carbonic acid dissociation, bicarbonate ion dissociation and water dissociation:

$$R_{H^+} = \frac{dc_{H^+}}{dt} = \left(K_{f,ca}\, c_{H_2CO_3} - K_{b,ca} c_{H^+} c_{HCO_3^-}\right) + \left(K_{f,bi}\, c_{HCO_3^-} - K_{b,bi} c_{H^+} c_{CO_3^{2-}}\right) + \left(K_{f,wa} - K_{b,wa} c_{H^+} c_{OH^-}\right)$$

<u>Fe^{2+} are not created by the homogenous chemical reactions.</u>

$$R_{Fe^{2+}} = 0$$

NOTE:

The molar concentrations need to be converted to mol/m^3. Hence if c_{molar} is concentration in molar and c_{SI} is concentration in mol/m^3 then $c_{molar} = c_{SI}/1000$. Hence the rates of the chemical production of species using concentrations in mol/m^3 are:

$$R_{CO_2} = \frac{d}{dt}\left(c_{CO_2}\right) = K_{b,hy}\, c_{H_2CO_3} - K_{f,hy} c_{CO_2}$$

$$R_{H_2CO_3} = \frac{d}{dt}\left(c_{H_2CO_3}\right) = -\left(K_{b,hy}\, c_{H_2CO_3} - K_{f,hy} c_{CO_2}\right) - \left(K_{f,ca}\, c_{H_2CO_3} - 0.001\, K_{b,ca} c_{H^+} c_{HCO_3^-}\right)$$

$$R_{HCO_3^-} = \frac{dc_{HCO_3^-}}{dt} = \left(K_{f,ca}\, c_{H_2CO_3} - 0.001\, K_{b,ca} c_{H^+} c_{HCO_3^-}\right) - \left(K_{f,bi}\, c_{HCO_3^-} - 0.001\, K_{b,bi} c_{H^+} c_{CO_3^{2-}}\right)$$

$$R_{CO_3^{2-}} = \frac{dc_{CO_3^{2-}}}{dt} = \left(K_{f,bi}\, c_{HCO_3^-} - 0.001\, K_{b,bi} c_{H^+} c_{CO_3^{2-}}\right)$$

$$R_{OH^-} = \frac{dc_{OH^-}}{dt} = 1000\, K_{f,wa} - 0.001\, K_{b,wa} c_{H^+} c_{OH^-}$$

$$R_{H^+} = \frac{dc_{H^+}}{dt} = \left(K_{f,ca}\, c_{H_2CO_{3,s}} - 0.001\, K_{b,ca} c_{H_s^+} c_{HCO_{3,s}^-}\right) + \left(K_{f,bi}\, c_{HCO_{3,s}^-} - 0.001\, K_{b,bi} c_{H_s^+} c_{CO_{3,s}^{2-}}\right) + \left(1000\, K_{f,wa} - 0.001\, K_{b,wa} c_{H_s^+} c_{OH_s^-}\right)$$

$$R_{Fe^{2+}} = 0$$

Reaction Rate Constants

- $K_{sol} = \frac{14.5}{1.00258}\ 10^{exp}$ where $exp = -(2.27 + 0.00565T_f - 8.06 \times 10^{-6}T_f^2 + 0.075I)$ moles/(litre. bar) (Oddo & Tomson, 1982). T_f is temperature in degrees Fahrenheit and I is the ionic strength in moles/litre.
- Carbonic acid never represents more than 1% of the total dissolved CO_2 as Kb,hy >> Kf,hy. Assume steady state Khy is constant with temperature and =0.00258 (Palmer and van Eldik (1983). $K_{f,hy} = 10^{exp}$ where $\exp = 329.85 - 110.541\ log_{10}(T_k) - (\frac{17265.4}{T_k})$ where T_k is the temperature in Kelvin. $K_{b,hy}=K_{f,hy}/K_{hy}$.
- $K_{f,ca}=10^{exp}\ s^{-1}$, where $exp=5.71+0.0526T_C-2.94x10^{-4}T_C^2+7.91x10^{-7}T_C^3$, in terms of temperature in degrees Celsius, Tc, (Comprehensive Chemical Kinetics, 1972). Steady-state $K_{ca}=387.6x10^{-exp}$ molar (Oddo & Tomson, 1982) where $exp=(6.41-1.594x10^{-3}T_f+8.52x10^{-6}T_f^2-3.07x10^{-5}p-0.4772I^{0.5}-0.118I)$ in terms of pressure p (in psi) and ionic strength I in molar. Backward reaction rate constant is given by the relationship: Kb,ca=Kf,ca/Kca.
- Steady-state $K_{bi}=10^{-exp}$ molar, Oddo & Tomson, 1982, where $exp=(10.61-4.97x10^{-3}T_f+1.331x10^{-5}T_f^2-2.624x10^{-5}p-1.166I^{0.5}+0.3466I)$. Forward reaction rate: $Kf,bi=10^9\ s^{-1}$ is assumed to be independent of temperature, Nordsveen et al (2003). Backward reaction rate given by Kb,bi=Kf,bi/Kbi.
- $K_{wa} = 10^{-exp}$ molar^2, where $exp =(29.3868-0.0737549T_K+7.47881x10^{-5}\ T_K^2)$ in terms of the absolute temperature in Kelvin, T_K, Kharaka et al (1989). Backward reaction rate constant independent of temperature: $Kb,wa=7.85x10^{10}M^{-1}s^{-1}$. Forward reaction rate constant Kf,wa=Kwa*Kb,wa.

Ionic Strength, I

In the above I is the ionic strength, which represents the strength of the electric field in a solution, equal to the sum of the molarities of each type of ion present multiplied by the square of the charges.

$$I = \frac{1}{2}\sum_{i=1}^{n} c_i z_i^2$$

where c_i = molar concentration of ion i (mol/litre) and z_i = charge number of ion i.

Example: To calculate the ionic strength of 0.05M Na_2SO_4 and 0.02M KCl solution:

$$I = \frac{1}{2}\begin{pmatrix} [Na_2SO_4] \times (\#Na\ ions) \times (charge\ of\ Na\ ion)^2 + \\ [Na_2SO_4] \times (\#SO_4\ ions) \times (charge\ of\ SO_4\ ion)^2 \\ + [KCl] \times (\#K\ ions) \times (charge\ of\ K\ ion)^2 + \\ [KCl] \times (\#Cl\ ions) \times (charge\ of\ Cl\ ion)^2 \end{pmatrix}$$

$$I = \frac{1}{2}\begin{pmatrix} 0.05 \times 2 \times 1^2 + \\ 0.05 \times 1 \times (-2)^2 \\ + 0.02 \times 1 \times 1^2 + \\ 0.02 \times 1 \times (-1)^2 \end{pmatrix} = 0.17M$$

Note that in the TLC cases considered here, I=0.

Appendix B: Exact Solution for the Surface Potential (Fardisi et al (2012))

The fundamental governing equation for the current density in electrochemistry can be represented by $i = \pm i_0\ 10^{\pm\frac{E-E_{rev}}{b}}$. E in this equation denotes the potential at the surface of the metal which assumes a value such that all the electrons released in the anodic reaction are consumed in the cathodic reactions. An exact solution for the surface potential, E, can be presented as:

$$\sum i_c + \sum i_a = 0$$

so that

$$i_{H^+} + i_{H_2CO_3} + i_{H_2O} + i_{Fe^{2+}} = 0$$

which leads to

$$-i_{o,H}\ 10^{-\left(\frac{E-E_{rev,H}}{b_H}\right)} - i_{o,H_2CO_3}\ 10^{-\left(\frac{E-E_{rev,H_2CO_3}}{b_{H_2CO_3}}\right)} - i_{o,H_2O}\ 10^{-\left(\frac{E-E_{rev,H_2O}}{b_{H_2O}}\right)} + i_{o,Fe}\ 10^{\left(\frac{E-E_{rev,Fe}}{b_{Fe}}\right)} = 0 \quad \text{(A1)}$$

Noting that the Tafel slope of all cathodic reactions are equal, let $b_c=b_H=b_{H2CO3}=b_{H2O}$, $b_a=b_{Fe}$, $m=b_c/b_a$ and $p = 10^{\frac{E}{b_c}}$. Then, $10^{\frac{E}{b_a}} = 10^{\frac{E\times m}{b_c}} = p^m$. Substituting $10^{\frac{E}{b_a}}$ and $10^{\frac{E}{b_c}}$ from the above into equation (A1) gives:

$$-i_{0,H}P^{-1}10^{\frac{E_{rev,H}}{b_c}} - i_{0,H_2CO_3}P^{-1}10^{\frac{E_{rev,H_2CO_3}}{b_c}} - i_{0,H_2O}P^{-1}10^{\frac{E_{rev,H_2O}}{b_c}} + i_{0,Fe}P^m10^{\frac{-E_{rev,Fe}}{b_a}} = 0$$

so that:

$$i_{0,H}\ 10^{\frac{E_{rev,H}}{b_c}} + i_{0,H_2CO_3}\ 10^{\frac{E_{rev,H_2CO_3}}{b_c}} + i_{0,H_2O}\ 10^{\frac{E_{rev,H_2O}}{b_c}} = i_{0,Fe}P^{m+1}10^{\frac{-E_{rev,Fe}}{b_a}}$$

hence:

$$P = \left[\left(i_{0,H}\ 10^{\frac{E_{rev,H}}{b_c}} + i_{0,H_2CO_3}\ 10^{\frac{E_{rev,H_2CO_3}}{b_c}} + i_{0,H_2O}\ 10^{\frac{E_{rev,H_2O}}{b_c}}\right)\frac{10^{\frac{E_{rev,Fe}}{b_a}}}{i_{0,Fe}}\right]^{\frac{1}{m+1}}$$

Appendix C: Steady State Bulk Chemistry Equations

If the partial pressure of CO_2 is specified, then start by calculating the initial bulk concentrations of CO_2 and H_2CO_3 in mol/m^3:

$$c_{CO_2} = 1000\, p_{CO_2} K_{sol}$$

$$c_{H_2CO_3} = 1000\, p_{CO_2} K_{sol}\, K_{hy}$$

Hence the rates of the chemical production of species using concentrations in mol/m^3 are:

$$0 = \frac{d}{dt}\left(c_{CO_2}\right) = K_{b,hy}\, c_{H_2CO_3} - K_{f,hy} c_{CO_2}$$

$$0 = \frac{d}{dt}\left(c_{H_2CO_3}\right) = -\left(K_{b,hy}\, c_{H_2CO_3} - K_{f,hy} c_{CO_2}\right) - \left(K_{f,ca}\, c_{H_2CO_3} - 0.001\, K_{b,ca} c_{H^+} c_{HCO_3^-}\right)$$

$$0 = \frac{dc_{HCO_3^-}}{dt} = \left(K_{f,ca}\, c_{H_2CO_3} - 0.001\, K_{b,ca} c_{H^+} c_{HCO_3^-}\right) - \left(K_{f,bi}\, c_{HCO_3^-} - 0.001\, K_{b,bi} c_{H^+} c_{CO_3^{2-}}\right)$$

$$0 = \frac{dc_{CO_3^{2-}}}{dt} = \left(K_{f,bi}\, c_{HCO_3^-} - 0.001\, K_{b,bi} c_{H^+} c_{CO_3^{2-}}\right)$$

$$0 = \frac{dc_{OH^-}}{dt} = 1000\, K_{f,wa} - 0.001\, K_{b,wa} c_{H^+} c_{OH^-}$$

$$0 = \frac{dc_{H^+}}{dt} = \left(K_{f,ca}\, c_{H_2CO_{3,s}} - 0.001\, K_{b,ca} c_{H_s^+} c_{HCO_{3,s}^-}\right) + \left(K_{f,bi}\, c_{HCO_{3,s}^-} - 0.001\, K_{b,bi} c_{H_s^+} c_{CO_{3,s}^{2-}}\right) + \left(1000\, K_{f,wa} - 0.001\, K_{b,wa} c_{H_s^+} c_{OH_s^-}\right)$$

The steady-state form of these equations yield:

$$1000\, K_{ca}\, c_{H_2CO_3} = c_{H^+} c_{HCO_3^-}$$

$$1000\, K_{bi}\, c_{HCO_3^-} = c_{H^+} c_{CO_3^{2-}}$$

$$1000000\, K_{wa} = c_{H^+} c_{OH^-}$$

Using the notation that: $x_1 = c_{HCO_3^-}$, $x_2 = c_{CO_3^{2-}}$, $x_3 = c_{OH^-}$, $x_4 = c_{H^+}$, and the concentration of $Fe^{2+} = c_{Fe^{2+}}$ these equations can be rewritten as:

$A = x_1 x_4$ where $A = 1000\, K_{ca}\, c_{H_2CO_3}$

$B\, x_1 = x_2 x_4$ where $B = 1000\, K_{bi}$

$C = x_3 x_4$ where $C = 1000000\, K_{wa}$

$x_4 + 2c_{Fe^{2+}} = x_1 + 2x_2 + x_3$

These equations can be written as a single charge balance equation for x_4:

$$x_4^3 + 2c_{Fe^{2+}} x_4^2 = (A + C)x_4 + 2AB$$

from which $x_1 = \frac{A}{x_4}, x_2 = \frac{Bx_1}{x_4}, x_3 = \frac{C}{x_4}$.

Appendix D: Water Condensation Rate Code at Static Conditions

```
@author: Khalid
"""
import numpy as np
# Rose droplet size distribution model
def Ndensity(nexp,rmax,radius):
Nr=(nexp/(np.pi*(rmax**nexp)))*radius**(nexp-3)
return Nr
# calculate saturated vapour pressure in bar using Anthoine equation
def Psat_bar(A,B,C,ToC):
exponent=A-B/(C+ToC)
Psat=(10**exponent)/750.0
return Psat # Bar
def find_Rmax(Kf,sigma,Cd,vg,rho_w,rho_g,gravity):
Rmax_sliding=(4.0*Kf*sigma)/(np.pi*Cd*rho_g*vg*vg)
a=(rho_w-rho_g)*gravity
b=(3.0*Cd*rho_g*vg*vg)/16.0
c=-3.0*sigma
Rmax_falling=(-b+np.sqrt(b**2-4.0*a*c))/(2.0*a)
Rmax=Rmax_sliding
if (Rmax_falling < Rmax_sliding):
Rmax=Rmax_falling
return Rmax,Rmax_sliding,Rmax_falling
# Calculate saturation temperature as a function of total pressure
```

```
# Ptot_bar = total gas pressure in bar
# Tsat is the saturation Temperature in K for this total pressure
def SatTemp(Ptot_bar):
Tsat=(1668.21/(5.09171-np.log10(Ptot_bar)))+45.15
return Tsat
# Function to evaluare Zhang integral
def FindIntegrals(nexp,N,rmin,rmax,kwater,hi,kwall,dwall):
r=np.linspace(rmin,rmax,N) # radius variable
deltar=(rmax-rmin)/(1.0*(N-1))
int1=0.0
int2=0.0
for i in range(1,N):
val1=1/(r[i]*kwater)
val2=2/(r[i]*r[i]*hi)
val3=dwall/(r[i]*r[i]*kwall)
denom=(val1+val2+val3)/(4*np.pi)
Nd=Ndensity(nexp,rmax,r[i])
int1=int1+Nd/denom
int2=int2+Nd/(r[i]*denom)
int1=int1*deltar
int2=int2*deltar
return int1,int2
# Function to find Tiw for given h_gas, Tbg, Tig, mdot and Hfg
def FindTiw(hg,Tbg,Tig,condrate,Hfg,kwall,dwall,Tow):
Qdot=hg*(Tbg-Tig)+Hfg*condrate
```

```
deltaT=Qdot*dwall/kwall

Tiw=Tow+deltaT

return Tiw

import matplotlib.pyplot as plt

# Specfy parameters to find maximum and minimum droplet radii as a function of

# gas velocity. Step 1 - find maximum droplet radii

Cd=0.44 # drag coefficient on drop

Kf=1.5 # friction coefficient

rho_water=1000.0 # water density kg/m3

kwater=0.58 # thermal conductivity of water W/mK

Tbg=40.0 # bulk gas temp oC

Ptot_bar=1.0 # total pressure (bar)

Mg=29.0 # average molecular weight of the gas

R=8.314 # universal gas constant J/mol/K

rho_gas=(100*Ptot_bar*Mg)/(R*(Tbg+273.15)) # gas density kg/m3

sigma = 0.072 # surface tension of water N/m

g=9.81 # m/s2

# now calculate condensation rates

# Anthoine saturated vapour pressures parameters

A=8.07131

B=1730.63

C=233.426

#pipe data

d_glass=0.095 # internal glass cell diamter m - used to calculate Gr

dwall=0.0025 # thickness of pipe wall m
```

```
kwall=54.0 # thermal conductivity of wall W/mK

Tow=15.0 # outside pipe temp oC

d=0.025 # sample diameter over which condensation measured,m - used in h_gas

# gas inlet conditions

mu_gas=1.749e-5 # viscosity Pas

Cp_gas=1000.0 # heat capacity of the gas J/kgK

k_gas=0.024 # gas thermal conductivity W/mK

b_t=1/(((Tow+273)+(Tbg+273))/2)# thermal expansion coefficient, k

d_t=Tbg-Tow # temperature difference , k

Gr=(d_glass**3*rho_gas**2*g*d_t*b_t)/(mu_gas**2) # Grashof number,Heat transfer to fluids without phase

#change, in Unit Operations Of Chemical Engineering, 5th ed. New York:McGraw-Hill, 1993, pp. 362-366.

Pr=(Cp_gas*mu_gas)/k_gas # Prandtl number

Nu=0.54*((Gr*Pr)**0.25) # Nusselt number, Heat transfer to fluids without phase

#change, in Unit Operations Of Chemical Engineering, 5th ed. New York:McGraw-Hill, 1993, pp. 362-366.

h_gas=(Nu*k_gas)/d # gas heat transer coeff W/m2K

rmax=(3*sigma/(g*(rho_water-rho_gas)))**0.5 # maximum droplet radius, m

print 'Gr=',Gr,'Pr=',Pr,'h_gas=',h_gas,'rho_gas=',rho_gas,'rmax=',rmax

# vapour properties

Hfg=2200970.0 # latent heat of condensation J/kg at Ptot

Mw=18.0 # Molecular mass of water vapour 18 g/mol

Le=1.0 # Lewis number of water vapour

Ts=SatTemp(Ptot_bar) # saturation temperature
```

```
#Ts=(1668.21/(5.09171-np.log10(Ptot_bar)))+45.15 # saturation temperature of water vapour

rho_vapour=(100*Ptot_bar*Mw)/(R*Ts) # Ptot_bar is bar and Ts in K rmin=(2*Ts*sigma)/(Hfg*rho_vapour*d_t) # minimum droplet radius

# water-vapour density

rho_wv=(rho_water*rho_vapour)/(rho_water-rho_vapour)

print 'rho_water=',rho_water,'rho_vapour=',rho_vapour,'rho_wv=',rho_wv,'rmin=', rmin

# interfacial heat transfer coefficient at droplet interface W/m2K

hi=2*np.sqrt(Mw/(2*np.pi*R*Ts))*(Hfg*Hfg*rho_vapour)/(Ts)

print 'Ptot=',Ptot_bar,'Ts=',Ts,'hi=',hi

# calculate Tig for each gas velocity

M=201 # number of subdivisions used to determine Tig

N=10001 # number of points used to determine Zhang integrals

nexp=1.0/3.0 # exponent of Rose droplet distribution

Temp=np.linspace(Tow,Tbg,M)

Temp_res=np.linspace(0,1,M)

Xsat_Tbg=(Mw/Mg)*Psat_bar(A,B,C,Tbg)/(Ptot_bar)

coeff2=(h_gas*Hfg*(Le**(2.0/3.0))*Mw)/(Cp_gas*Mg)

coeff3=(h_gas*(Le**(2.0/3.0)))/Cp_gas

# loop over temperature range to find Tig for this gas velocity

for j in range(M):

# calculate Tiw using current estimate of Tig (i.e. Temp[j])

Xsat_T=(Mw/Mg)*Psat_bar(A,B,C,Temp[j])/(Ptot_bar)

condrate=coeff3*(Xsat_Tbg-Xsat_T)

Tiw=FindTiw(h_gas,Tbg,Temp[j],condrate,Hfg,kwall,dwall,Tow)
```

```
# Delta T in denominator = Tig-Tiw but approximate with Tig-Tow
rmin=(2*Ts*sigma)/(Hfg*rho_wv*(Tbg-Tiw)) #????? temp[i] should be Tbg
int1,int2=FindIntegrals(nexp,N,rmin,rmax,kwater,hi,kwall,dwall)
Aint=int1-(2*sigma*int2)/(Hfg*rho_wv) #?????rho_water should be rho_wv
Bint=int1
# print 'Aint=',Aint,'Bint=',Bint
# set up the residual equation for Tig
coeff1=Aint+h_gas
rhs=h_gas*Tbg
rhs=rhs+(coeff2*Psat_bar(A,B,C,Tbg))/(Ptot_bar)+Bint*Tow
Temp_res[j]=coeff1*Temp[j]+ \
(coeff2*Psat_bar(A,B,C,Temp[j]))/(Ptot_bar)-rhs
# find Tig where equation residual = 0 using a simple bisection
for j in range(M-1):
prod=Temp_res[j]*Temp_res[j+1]
if (prod < 0):
Tig=Temp[j]
print 'Tig=',Tig
# calculate condensation rate
Xsat_Tig=(Mw/Mg)*Psat_bar(A,B,C,Tig)/(Ptot_bar)
Condrate=coeff3*(Xsat_Tbg-Xsat_Tig)
h_max = 2*rmax/9 # max ave film thickness, m
h_min= 2*rmin/9 # min ave film thickness, m
drop_lifetime = (((h_max - h_min)*rho_water)/Condrate)/60 # min
#print'drop_lifetime =',drop_lifetime,'min'
```

```
print 'condensation rate =',Condrate,'kg/m2.s'
Cond_Vol=(Condrate*24*3.8*1000)/2.77# vol of condensate per 24hours, ml
Dr_vol=(0.666*3.14*4.695*4.695*4.695)/1000# max droplet volume, ml
No_dr=Cond_Vol/Dr_vol# number of drops per total condensate water
DRLT=(24/No_dr)*60# droplet live time,min
print'DRLT=',DRLT,'min'
```

Appendix E: Program to Calculate Initial Species Concentrations (before corrosion process)

```
@author: Khalid

#input parameters

Tc=25 # bulk temperatur,°C

print'T(c)=',Tc,'Celsius'

# Antoine saturated vapour pressures parameters

A=8.07131

B=1730.63

C=233.426

P_tot=1

P_wv=(10**(A-(B/(C+Tc))))/760

pCO2= P_tot-P_wv

P=14.8

Tf=Tc*9/5 +32 # Fahrenheit

Tk=Tc+273.15 # Kelvin

print'pCO2=',pCO2

print 'P_wv=',P_wv

Ksol=(14.463)*10**-(2.27+0.00565*Tf-8.06*(10**-6)*(Tf**2)

+0.075*I)

Kwa= 10**-(29.3868-0.0737549*Tk+7.47881*(10**-5)*Tk**2)

Khy=2.58*(10**(-3))

Kca=387.6*10**-(6.41-1.594*(10**(-3))*Tf

+(8.52* 10**(-6) *Tf**(2))-3.07*10**(-5)*P-0.4772*(I**0.5)+0.118*I)

Kbi = 10**-(10.61-4.97*(10**-3)*Tf+1.331*(10**-5)*(Tf**2)-2.624*(10**-5)*P-
```

```
1.166*(I**0.5)+0.3466*I)
c_CO2 =pCO2*Ksol*1000
print'ksol=',Ksol
print'Kwa=',Kwa
print'Kca=',Kca
print'Kbi=',Kbi
ph=4
c_H2CO3=pCO2*Ksol*Khy*1000
c_H =10**(-ph)*1000
c_HCO3 =1000*(Kca*c_H2CO3)/(c_H)
c_CO3=1000*(Kbi*c_HCO3)/(c_H)
c_OH =(Kwa*(10**6))/c_H
print'[CO2]=', c_CO2 # Mol/ m3
print '[H2CO3]=',c_H2CO3 # Mol/ m3
print'[H]=',c_H # Mol/ m3
print '[HCO3-]=',c_HCO3 # Mol/ m3
print '[CO3]=',c_CO3 # Mol/ m3
print '[OH]=', c_OH # Mol/ m3
#math.log (c_H,10)
#pH=-1*math.log (c_H,10)
print 'pH1=',ph
c_Fe=(c_HCO3+2*c_CO3+c_OH-c_H)/2# mol/m3
print '[Fe]=',c_Fe
ksp=10**(-59.3498-(0.041377*Tk)-(2.1963/Tk)+(24.5724*2.5092025))
print'ksp=',ksp
```